frontiers | Research Topics

High-precision euv and x-ray optics for advanced photon source facilities

Edited by
Qiushi Huang, Hongchang Wang, Ming Li, Hongxin Luo
and Xiaohao Dong

Published in
Frontiers in Physics

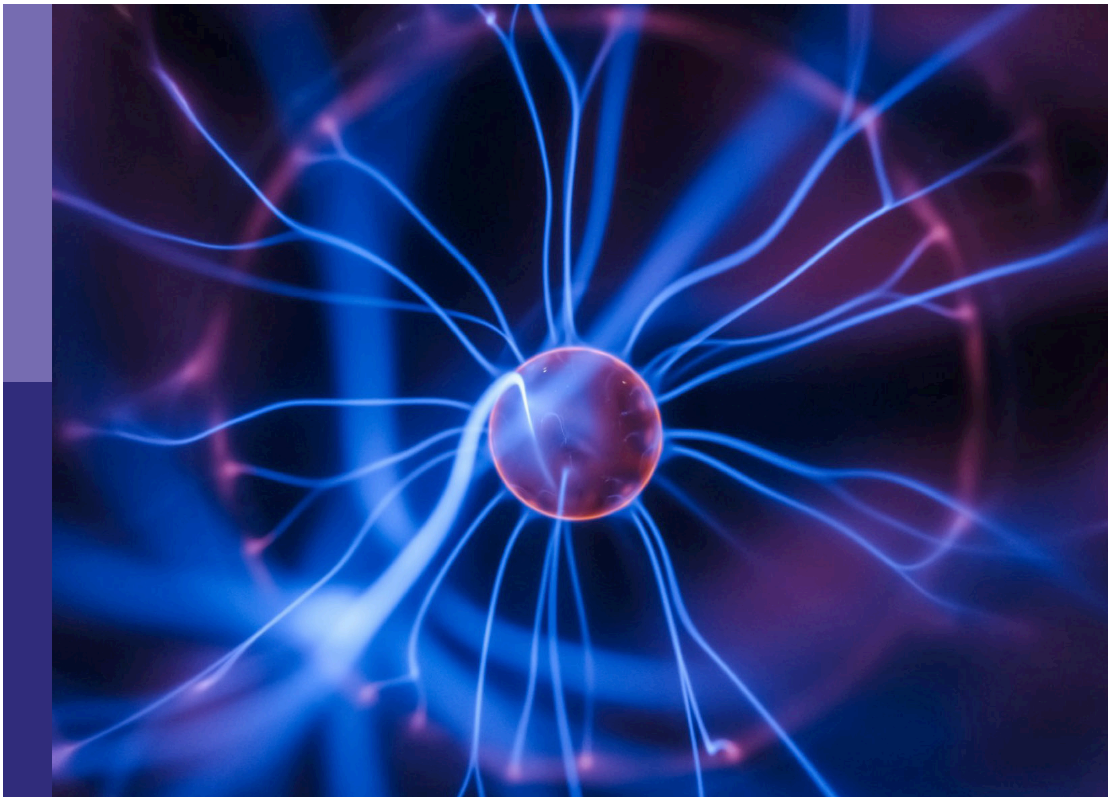

ISSN 1664-8714
ISBN 978-2-83251-318-7
DOI 10.3389/978-2-83251-318-7

About Frontiers

Frontiers is more than just an open access publisher of scholarly articles: it is a pioneering approach to the world of academia, radically improving the way scholarly research is managed. The grand vision of Frontiers is a world where all people have an equal opportunity to seek, share and generate knowledge. Frontiers provides immediate and permanent online open access to all its publications, but this alone is not enough to realize our grand goals.

Frontiers journal series

The Frontiers journal series is a multi-tier and interdisciplinary set of open-access, online journals, promising a paradigm shift from the current review, selection and dissemination processes in academic publishing. All Frontiers journals are driven by researchers for researchers; therefore, they constitute a service to the scholarly community. At the same time, the *Frontiers journal series* operates on a revolutionary invention, the tiered publishing system, initially addressing specific communities of scholars, and gradually climbing up to broader public understanding, thus serving the interests of the lay society, too.

Dedication to quality

Each Frontiers article is a landmark of the highest quality, thanks to genuinely collaborative interactions between authors and review editors, who include some of the world's best academicians. Research must be certified by peers before entering a stream of knowledge that may eventually reach the public - and shape society; therefore, Frontiers only applies the most rigorous and unbiased reviews. Frontiers revolutionizes research publishing by freely delivering the most outstanding research, evaluated with no bias from both the academic and social point of view. By applying the most advanced information technologies, Frontiers is catapulting scholarly publishing into a new generation.

What are Frontiers Research Topics?

Frontiers Research Topics are very popular trademarks of the *Frontiers journals series*: they are collections of at least ten articles, all centered on a particular subject. With their unique mix of varied contributions from Original Research to Review Articles, Frontiers Research Topics unify the most influential researchers, the latest key findings and historical advances in a hot research area.

Find out more on how to host your own Frontiers Research Topic or contribute to one as an author by contacting the Frontiers editorial office: frontiersin.org/about/contact

High-precision euv and x-ray optics for advanced photon source facilities

Topic editors

Qiushi Huang — Tongji University, China

Hongchang Wang — Diamond Light Source (United Kingdom), United Kingdom

Ming Li — Institute of High Energy Physics, Chinese Academy of Sciences (CAS), China

Hongxin Luo — Shanghai Synchrotron Radiation Facility, Shanghai Institute of Applied Physics, Chinese Academy of Sciences (CAS), China

Xiaohao Dong — Shanghai Advanced Research Institute, Chinese Academy of Sciences (CAS), China

Citation

Huang, Q., Wang, H., Li, M., Luo, H., Dong, X., eds. (2023). *High-precision euv and x-ray optics for advanced photon source facilities*. Lausanne: Frontiers Media SA. doi: 10.3389/978-2-83251-318-7

Table of contents

frontiers in Physics

ORIGINAL RESEARCH
published: 10 March 2022
doi: 10.3389/fphy.2022.837819

Background Pressure Induced Structural and Chemical Change in NiV/B_4C Multilayers Prepared by Magnetron Sputtering

Zhenbo Wei[1], Zhe Zhang[1]*, Li Jiang[1], Yang Yang[1], Chenyuan Chang[1], Yufei Feng[1], Runze Qi[1], Qiushi Huang[1], Wensheng Yan[2], Chun Xie[3] and Zhanshan Wang[1]

[1]MOE Key Laboratory of Advanced Micro-Structured Materials, Institute of Precision Optical Engineering (IPOE), School of Physics Science and Engineering, Tongji University, Shanghai, China, [2]National Synchrotron Radiation Laboratory, University of Science and Technology of China, Hefei, China, [3]Sino-German College of Applied Sciences, Tongji University, Shanghai, China

NiV/B_4C multilayers with a small d-spacing are suitable for multilayer monochromator working at a photon energy region from 5 to 8 keV, or photon energy region from 10 to 100 keV. To investigate the influence of background pressure during fabrication, NiV/B_4C multilayers with a d-spacing of 3.0 nm were fabricated by magnetron sputtering with different background pressures. The grazing incidence x-ray reflectivity (GIXR) and transmission electron microscopy (TEM) measurement illustrated the structural change that happened in NiV/B_4C multilayers when background pressure is high. The electron dispersive x-ray spectroscopy (EDX) of NiV/B_4C multilayer deposited with a high background pressure suggests a gradient distribution of oxygen, which corresponds to the gradient thickness change. The detailed x-ray absorption near edge spectroscopy (XANES) comparison of NiV/B_4C multilayers, NiV coating, and B_4C coating showed the chemical state change induced by background pressure. We concluded that during the deposition, vanadium oxide promoted the oxidation of boron. In order to fabricate a good performance of NiV/B_4C multilayers, the background pressure needs lower than 1×10^{-4} Pa.

Keywords: NiV/B_4C, multilayer, magnetron sputtering, XANES, background pressure

Edited by:
Xinping Zhang,
Beijing University of Technology,
China

Reviewed by:
Maheswar Nayak,
Raja Ramanna Centre for Advanced
Technology, India
Gregory Abadias,
UPR3346 Institut P' Recherche et
Ingénierie en Matériaux, Mécanique et
Energétique (Pprime), France

Correspondence:
Zhe Zhang
zzfight1226@foxmail.com

Specialty section:
This article was submitted to
Optics and Photonics,
a section of the journal
Frontiers in Physics

Received: *17 December 2021*
Accepted: *02 February 2022*
Published: *10 March 2022*

Citation:
Wei Z, Zhang Z, Jiang L, Yang Y, Chang C, Feng Y, Qi R, Huang Q, Yan W, Xie C and Wang Z (2022) Background Pressure Induced Structural and Chemical Change in NiV/B_4C Multilayers Prepared by Magnetron Sputtering.
Front. Phys. 10:837819.
doi: 10.3389/fphy.2022.837819

1 INTRODUCTION

Multilayer interference coating is an important optics in the hard x-ray region, which enables the reflection of the short-wavelength light beyond the total external reflection region, and chooses a narrow-band spectrum from the white light radiation. Thus, it is widely used in advanced imaging, spectroscopy, and monochromator systems for synchrotron radiation facilities and astronomical observation projects [1–3]. As photon energy requirement of synchrotron radiation facilities and space telescopes extends to several tens of kiloelectron volts, the multilayer working at such wavelength region requires an extremely small d-spacing which is less than 3.0 nm [4–7]. This makes the x-ray reflectance very sensitive to the interface and surface quality of the multilayer, which also needs the more precise control of fabrication and the more suitable selection of materials. As for fabrication, magnetron sputtering has been proved as an effective technique for fabricating small d-spacing multilayers, which has the good controllability of the process and the relatively low cost of the instrument [8]. For materials selection, more and more researchers began using a compound to replace the elementary substance [9, 10].

In the hard x-ray region, a multilayer monochromator has the advantage of a large spectral bandwidth and high reflectance, which can provide one or two orders of magnitude higher integral flux than a crystal monochromator [11]. Nickel is one of the ideal absorption materials in the whole hard x-ray region, except for 8.3 keV (Ni K-edge) [12, 13], but nickel is a magnetic material, which is not compatible with magnetron sputtering for small d-spacing multilayers. For solving this problem, a nonmagnetic alloy was made up of 93% nickel, and 7% vanadium has been proposed (in the following article, we will use NiV instead of the more correct $Ni_{93}V_7$). At the beginning, NiV has been suggested by Danish Space Research Institute as a potential candidate for hard x-ray telescope. [14] Because compared with tungsten and platinum, there was no absorption line for NiV at the photo energy range from 20 to 200 keV [9]. Until 2017, NiV was first used as a multilayer monochromator in European Synchrotron Radiation Facility (ESRF) [15]. Given the higher reflectivity and integral flux, the NiV/B_4C combination was thus chosen as the material of choice for a monochromator working at 8 keV and around 20 keV [16–18]. Apart from that, the detailed studies on NiV/B_4C multilayers were really limited, especially on how to fabricate this promising X-ray multilayer mirror.

During the magnetron sputtering process, there are a lot of factors that will influence the final performance of multilayers. For example, the pressure of working gas (typically argon) impacts stress and the layer density, and the speed of the spin motion of the substrate during deposition influences the uniformity of the coating. The background pressure is also one of the parameters that needs to be characterized and precisely controlled. It is reported that the background pressures affect the stress and layer morphology of layers [19, 20]. The residual gas in vacuum chamber will react with sputtering atoms and alter the refractive index contrast between multilayer materials, furthermore changing the film structure by the formation of compounds and impacting the interface quality [21, 22]. In order to understand the background pressure effect on the growth of the NiV/B_4C multilayer, a comparative study of the NiV/B_4C multilayers fabricated with different background pressures was performed in this paper. The multilayer structure, layer morphology, and chemical state of the multilayers were investigated and discussed systematically.

2 EXPERIMENTS

In order to realize the application of NiV/B_4C multilayers in hard x-ray telescope or multilayer monochromator, the multilayer d-spacing in this research was set to $d = 3.0$ nm and the thickness ratio $\gamma = d_{NiV}/d = 0.6$. The number of bilayers was $N = 60$ to test the period drift of multilayer. The NiV/B_4C multilayers were fabricated by direct current magnetron sputtering technique. The B_4C (purity 99.5%) target was used at a constant power of 80 W, the NiV target (Ni:V = 93:7, purity 99.99%) at 20 W. Both targets have a diameter of 4 inches. The distances from substrate to target are 8.5 and 9.0 cm, respectively to NiV and B_4C. During the deposition, high-purity argon (99.999%) was used as the working gas at a pressure of 0.16 Pa, for keeping a relatively high kinetic energy of the deposited atoms and, thus, to form smooth interfaces, and the flow rate for Ar is 8 sccm. The multilayers were deposited on superpolished Si (100) wafers (20 mm × 20 mm) with a root-mean-square roughness of 0.2 nm (1×1 μm^2 atomic force microscope scan). The individual layer thicknesses in the multilayer were, thus, adjusted by controlling the sputtering time independently over each target. The background pressures, which arise from residual air in the deposition chamber, were measured before inflating Ar. In each case, the chamber was pumped from the normal air condition to the background pressures of 4×10^{-4}, 2×10^{-4}, 1×10^{-4}, 8×10^{-5}, 4×10^{-5}, and 2×10^{-5} Pa, by using a combination of a turbomolecular pump and a mechanical pump. The fabricated multilayers are symbolized as S-4×10^{-4}, S-2×10^{-4}, S-1×10^{-4}, S-8×10^{-5}, S-4×10^{-5}, and S-2×10^{-5} Pa, respectively. Except for background pressure, all the deposition parameters were the same in all cases.

The grazing incidence x-ray reflectivity (GIXR) measurement used a laboratory-based diffractometer (Bede, Durham, UK) with the Cu Kα line as the source ($\lambda = 0.154$ nm). Fits of the GIXR curve were performed using the Bede Refs software [23]. The information of the individual layer thickness and interface width was determined from the fitting.

High-resolution transmission electron microscopy (TEM) measurements were made to compare the microstructure and layer morphology of the two samples deposited with different background pressures. The samples were prepared by focused ion beam and observed by FEI Talos F200X (FEI, Hillsboro, OR, United States). The elemental composition of the layers was further measured by energy dispersive x-ray spectroscopy (EDX) during the TEM measurements. Mapping and one-dimensional line scans across several bilayers were performed to measure the composition depth profiles of the different elements.

X-ray absorption near-edge structure (XANES) spectroscopy was commonly used to probe the local atomic structure around specific elements in films and often used as a fingerprint of the changes in the coordination numbers of elements [24–26]. XANES measurements were conducted after fabrication at the Beamline U12b at the National Synchrotron Radiation Laboratory (NSRL) in the total electron yield (TEY) mode by collecting sample drain currents under a vacuum, which was greater than 5×10^{-8} Pa. The beam from a bending magnet was monochromatized with a varied line-spacing plane grating and refocused using a toroidal mirror. An energy range from 100 to 1,000 eV was used with an energy resolution of approximately 0.2 eV. All XANES spectra were measured using the process of normalization by considering the low and high photon energy parts of the spectra far from the threshold [26, 27].

3 RESULTS AND DISCUSSION

3.1 Grazing Incidence X-Ray Reflectivity Measurement Analysis

The GIXR measurements of as-deposited samples are shown in **Figure 1A**. The different colors represent different background pressures. As the background pressure becomes lower, the Bragg

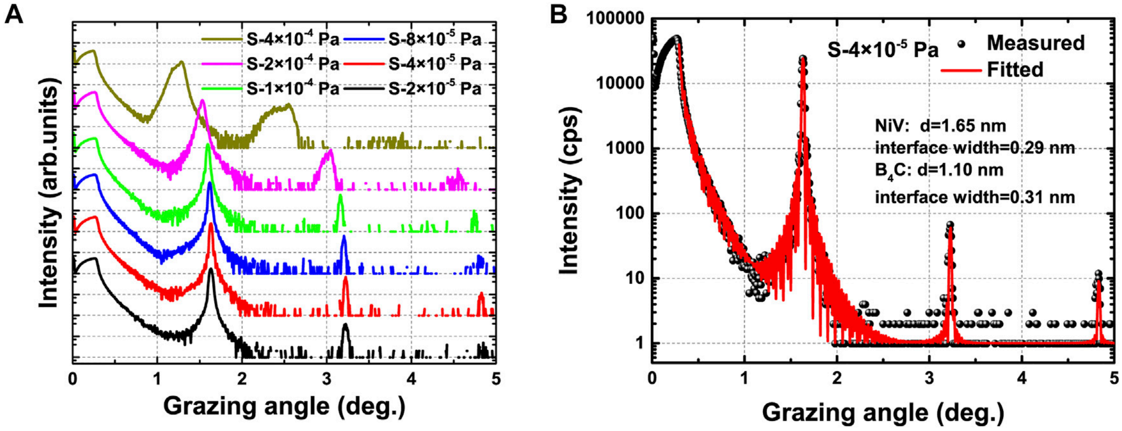

FIGURE 1 | (A) Grazing incidence x-ray reflectivity (GIXR) measurement of NiV/B_4C multilayer deposited with different background pressures. **(B)** GIXR measurement and fitted result of NiV/B_4C multilayer deposited with a background pressure of 4 × 10^{-5} Pa.

peaks become narrower, which indicates that the multilayer sample has less d-spacing drift from the surface to the substrate. Besides the width of Bragg peaks, the positions of Bragg peaks also changed with different background pressures. With the background pressure decreasing from 4 × 10^{-4} to 1 × 10^{-4} Pa, the grazing angles of Bragg peaks kept increasing, which means the d-spacing of multilayer becomes thinner. When the background pressure reached 8 × 10^{-5} Pa and further lower, the grazing angle of Bragg peaks did not change, indicating that the d-spacings of different samples became consistent with varied background pressures. **Figure 1B** shows the fitted result of NiV/B_4C multilayer deposited with background pressure of 4 × 10^{-5} Pa. The fitted curve matched very well with GIXR measurement result, which means the fitted model is in agreement with the deposited layer structure, and the bandwidth of the measured Bragg peaks is similar with the fitted curve, which indicates the good uniformity of 60 bilayers. The fitted values of two individual layers are also shown in this figure; the thicknesses of NiV and B_4C were 1.65 and 1.10 nm, respectively. The average interface width for the two kinds of materials were 0.29 nm (NiV) and 0.31 nm (B_4C).

Based on GIXR measurements, we can assume that the change in layer structure happened in NiV/B_4C multilayers when the background pressure was higher than 1 × 10^{-4} Pa because all of the parameters for GIXR measurement and deposition are the same except for background pressure. There are two most possible reasons for broader Bragg peaks, one is the gradient d-spacing change in a multilayer, and the other one is the gradient refractive index change. How did the background pressure induce a gradient change in multilayer? We need further analysis to investigate how the change happened in NiV/B_4C multilayers.

3.2 Transmission Electron Microscope Analysis

The cross-sectional TEM images and selected area electron diffraction (SAED) patterns of NiV/B_4C multilayer deposited with different background pressures are shown in **Figure 2**. The bright layers are B_4C, and the dark layers are NiV. Based on low-magnification images, we found that the total thickness of sample S-4 × 10^{-4} Pa was 47.7 nm thicker than that of sample S-4 × 10^{-5} Pa, which confirmed the structural change induced by background pressure. In **Figures 2A,B**, both samples have flat layers, but the interfaces of sample S-4 × 10^{-5} Pa are shaper. In the high-resolution images (**Figures 2C,D**), it can be easily found that the individual d-spacing of S-4 × 10^{-4} Pa was different from S-4 × 10^{-5} Pa, indicating the different positions of Bragg peak in **Figure 1A**. Based on further analysis of high-resolution images, we found that the d-spacing of sample S-4 × 10^{-4} Pa changed gradually from the surface to the substrate, which range from 3.38 to 4.18 nm. Such a gradient d-spacing will cause the broadened Bragg peak as shown in **Figure 1A**. The thicker layers were close to the substrate, and the B_4C layers changed much more than the NiV layers. As for sample S-4 × 10^{-5} Pa, the d-spacing was constant for the whole multilayer. The d-spacing was 2.79 nm measured from high-resolution images, which was close to the fitted result (shown in **Figure 1B**) of GIXR measurement and indicating that the fitted model was similar with the actual structure. SAED images were recorded with a large electron beam covering several tens of bilayers of the NiV/B_4C multilayers. **Figures 2E,F** display the SAED images of samples S-4 × 10^{-4} and S-4 × 10^{-5} Pa, respectively. Both of them only have a diffraction pattern coming from the multilayer structure indicating an amorphous layer structure in these samples [7]. However, compared with S-4 × 10^{-4} Pa, the electron diffraction pattern of S-4 × 10^{-5} Pa is more regular, which means that the layer structure in S-4 × 10^{-5} Pa is more uniform.

To our knowledge, the background pressure may cause the change in deposition rate for sputtering materials, but would not induce a gradient d-spacing in multilayers. Therefore, the only physical reason that can explain the formation of a gradient d-spacing is the element composition change in the multilayer due to the residual gas in the chamber [21, 22]. The element composition change will also cause the refractive index change.

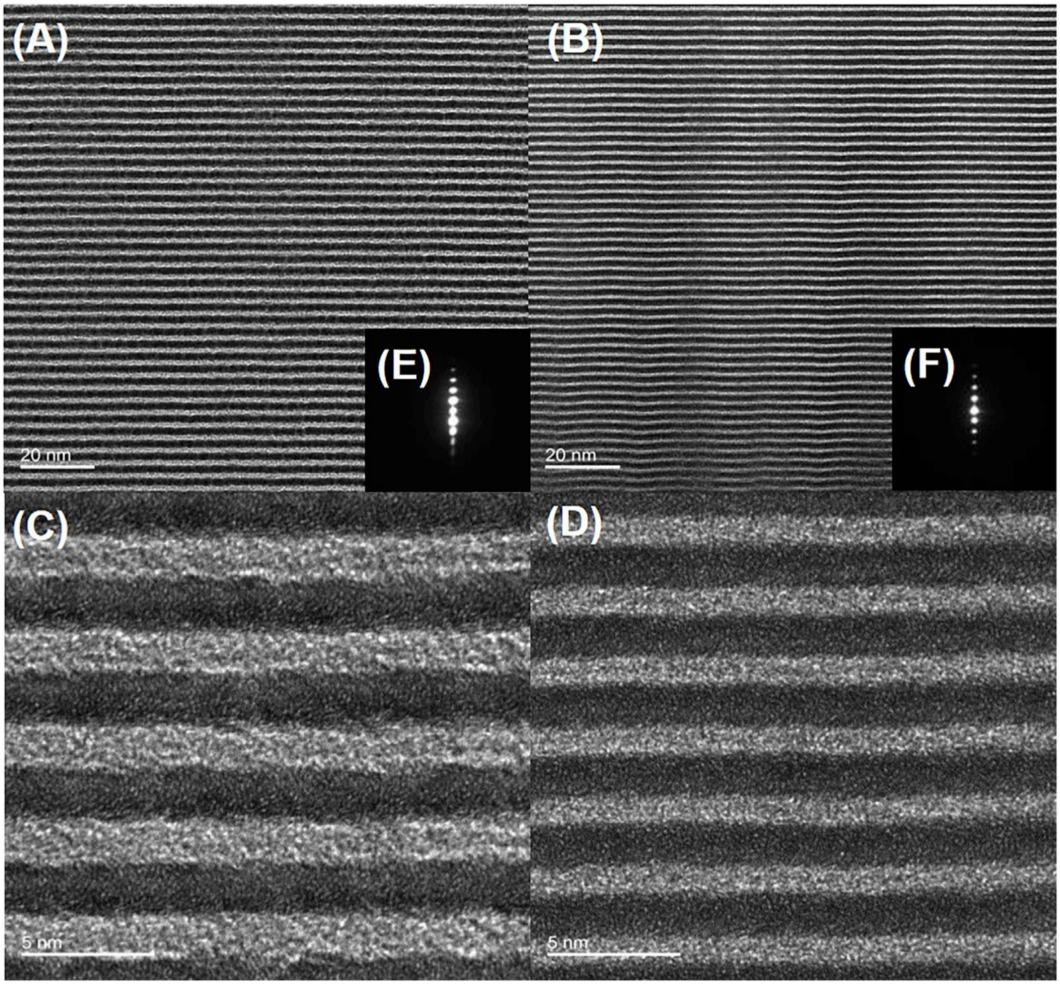

FIGURE 2 | Transmission electron microscopy (TEM) and selected area electron diffraction (SAED) images of the NiV/B_4C multilayers fabricated with background pressures of 4 × 10^{-4} Pa **(A,C,E)** and 4 × 10^{-5} Pa **(B,D,F)**.

Analysis of this hypothesis will be performed in the following section.

3.3 Energy-Dispersive X-Ray Spectroscopy Analysis

The higher background pressure means more residual gas stayed in the chamber. During the deposition process, some gas would be activated by plasma environment, then forming compounds with sputtering particles. In order to analyze the elemental composition of samples S-4 × 10^{-4} and S-4 × 10^{-5} Pa, EDX mapping and one-dimensional line scans across several bilayers were performed during the TEM measurement. In our work, the EDX measurements were performed to characterize elements of boron (B), carbon (C), nitrogen (N), oxygen (O), nickel (Ni), and vanadium (V).

The EDX measurement allowed to approximately determine the atomic concentration of different elements. In **Figures 3A,B**, the high angle annular dark field (HAADF) images are combined with element mapping images, for observing the element distribution in samples S-4 × 10^{-4} and S-4 × 10^{-5} Pa, respectively. Vanadium and nitrogen mapping images are not included in these figures because of the low atomic concentration (vanadium is only 7% in NiV target). In HAADF images, the bright layers are NiV and the dark layers are B_4C. As shown in **Figures 3A,B**, the Ni and C element distributions are both in accordance with HAADF images; the main difference happened in O and B elements distributions. In sample S-4 × 10^{-4} Pa, oxygen distribution exhibits the layer structure, and these layers are in keeping with B_4C layers, which means a lot of oxygen atoms stayed in the B_4C layers. On the contrary, the oxygen distribution in sample S-4 × 10^{-5} Pa does not have such an obvious layer structure. Because the sensitivity for boron detection in the EDX measurement is not good, the boron distributions in both samples are not as clear as the other elements, but in sample S-4 × 10^{-5} Pa, boron distribution seems to have a blurred layer structure compared with S-4 × 10^{-4} Pa.

The detailed one-dimensional line scans of samples S-4 × 10^{-4} and S-4 × 10^{-5} Pa are shown in **Figures 3C,D**. In sample S-4 ×

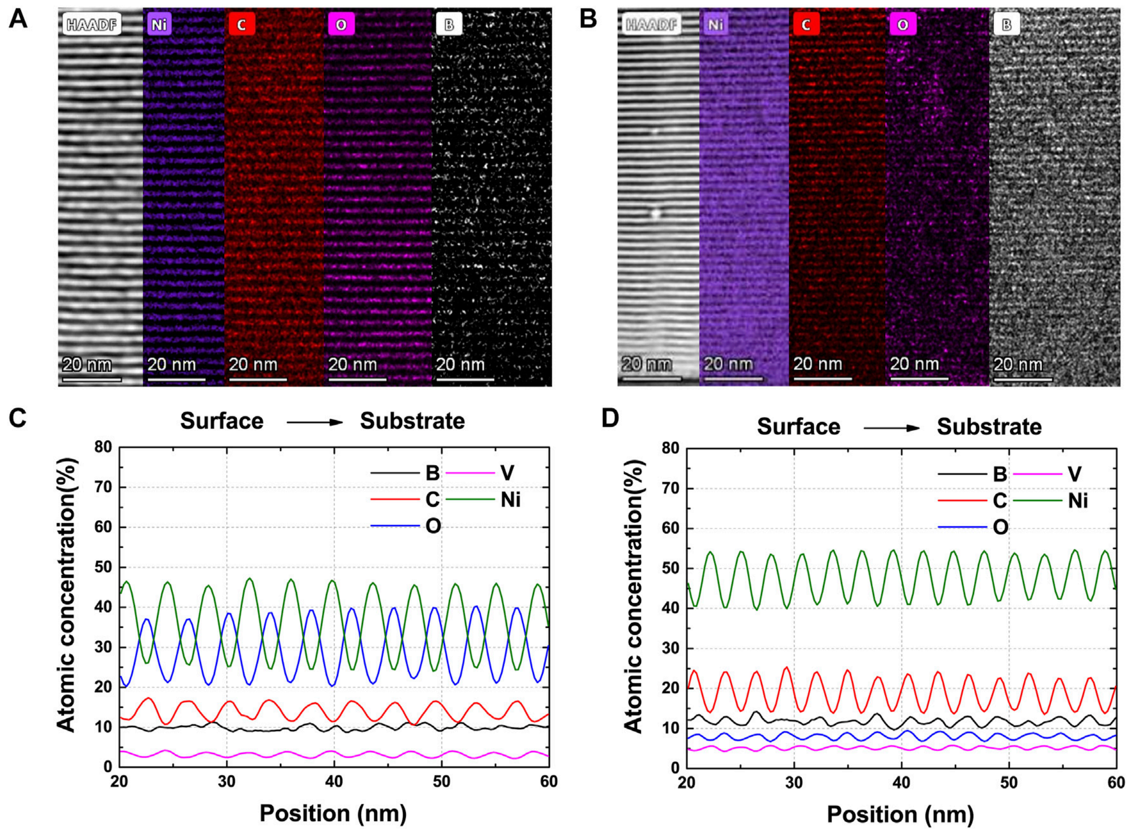

FIGURE 3 | Electron-dispersive x-ray spectroscopy (EDX) mapping-scan and line-scan (from surface to substrate) measurements of chemical elements in the NiV/B_4C multilayers fabricated with background pressures of 4 × 10^{-4} Pa **(A,C)** and 4 × 10^{-5} Pa **(B,D)**.

10^{-4} Pa (**Figure 3C**), except for boron, the other elements both have a periodic oscillation of concentration. The element with the most remarkable profile is oxygen, the average atomic concentration of oxygen in the whole scan area is more than 30%, and from the surface to substrate, the atomic concentration of oxygen keeps increasing, which is consistent with the d-spacing change in sample S-4 × 10^{-4} Pa. In sample S-4 × 10^{-5} Pa (**Figure 3D**), all measured elements have a periodic oscillation of concentration, which further illustrates that sample S-4 × 10^{-5} Pa has a uniform layer structure.

According to the EDX measurement results, we find that oxygen is the main reason for the gradient d-spacing in NiV/B_4C multilayer. When the deposition process happened with a higher background pressure, the oxygen in residual gas would interact with boron and carbon atoms. Then the tri-element compound layer replaces B_4C and causes the volume expansion. As the deposition time went by, the oxygen concentration in the chamber becomes lower, the tri-element compound layer also becomes thinner, which means the volume of the tri-element compound is proportion to the concentration of oxygen. Due to this phenomenon, the d-spacing of the multilayer is gradually thinning from the substrate to the surface. This gradient change is consistent with the results obtained from the GIXR and TEM measurements. Except for the volume change, the refractive index of this tri-element compound layer may also change with the oxygen concentration. When the deposition process happened with a lower background pressure, the oxygen concentration also lower in the residual gas. Although the oxygen still has the opportunity to interact with sputtering particles (which has been proved in our previous work [4]), the lower concentration of oxygen would not cause the obvious thickness change in the boron carbide layer, which promote the uniformity between bilayers (as shown in **Figures 1B**, **3D**).

3.4 X-Ray Absorption Near-Edge Structure Spectroscopy Analysis

In order to further explore the chemical change caused by different background pressures, XANES measurements have been implemented in several samples (S-4 × 10^{-4}, S-1 × 10^{-4}, S-8 × 10^{-5}, S-4 × 10^{-5}, S-2 × 10^{-5} Pa). Except for multilayer samples, we also fabricated two single-layer samples for comparison. One is NiV coating marked as S-NiV in the following part, and this sample was deposited with a background pressure of 1 × 10^{-4} Pa. Another one is B_4C coating marked as S-B_4C, which was deposited with a background pressure of 6 × 10^{-5} Pa. These two background pressure values were suggested by GIXR and TEM measurement results to mitigate the influence caused by residual gas. The thicknesses of S-NiV and S-B_4C are 16 and

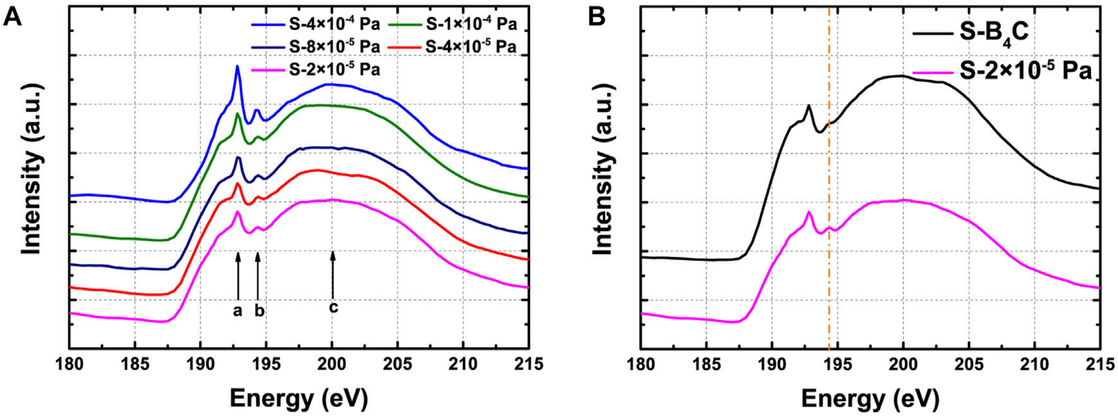

FIGURE 4 | The B K-edge X-ray absorption near-edge spectroscopy (XANES) spectra of different samples: **(A)** NiV/B$_4$C MLs deposited with different background pressures (S-4 × 10^{-4}, S-1 × 10^{-4}, S-8 × 10^{-5}, S-4 × 10^{-5}, and S-2 × 10^{-5} Pa). **(B)** NiV/B$_4$C ML deposited with 2 × 10^{-5} Pa and B$_4$C coating deposited with 6 × 10^{-5} Pa.

35 nm, respectively, which fitted the GIXR measurements. Because the purpose for this study is investigating the influence from background pressure, pre- and post-edge normalizations have not been carried out during the data analysis in this paper.

3.4.1 B K-Edge X-Ray Absorption Near-Edge Spectroscopy

The B K-edge absorption spectra of five NiV/B$_4$C MLs are presented in **Figure 4A**. There are three prominent features in the B-K absorption spectra, which are marked as a, b, and c, respectively. Features a and b are both narrow peaks appearing at photon energies of ~192.8 and ~194.2 eV. Feature c looks like a broad bump in the high-energy regime (195–205 eV). The narrow edge peak a (192.8 eV) occurs due to the transition of a B 1s electron to the unoccupied B 2p π^* state. According to Jiménez' s research, this feature seems related to inter-icosahedral B–B bonds [28]. The other narrow peak b (194.2 eV) is due to transition of a B 1s electron to the unoccupied B 2p π^* state in B in the presence of oxygen [29, 30]. The feature c is due to the transition of B 1s electrons to the unoccupied B σ^* states, which corresponds to bonding within the C–B–C chain structure [31, 32].

With the background pressure changing from 4 × 10^{-4} to 2 × 10^{-5} Pa, the relative intensities of features a and b become lower, but the intensity of feature c becomes higher. This result indicates the sputtered boron atoms tend to bond with carbon atoms to form a C–B–C chain with a lower background pressure in a vacuum chamber. These C–B–C chains mainly stay in boron carbide layers and make the boron carbide layer have a regular layer structure, which is proven by boron distribution in **Figure 3D**, but with a higher background pressure, the oxygen concentration becomes higher, the sputtered boron atoms seem to prefer to combine with oxygen atoms. Therefore, the oxygen atoms destroyed parts of the C–B–C chains and formed a lot of B–O bonds. These B–O bonds stayed in boron carbide layers and formed a tri-element compound layer, which is consistent with the oxygen distribution in **Figure 3C**. The increased B–B bonds may come from some dissociated boron in NiV/B$_4$C ML [33], which results in an aperiodic boron distribution shown in EDX measurements (**Figure 3C**).

In **Figure 4B**, the B K-edge absorption spectra of NiV/B$_4$C ML and B$_4$C coating are presented. The main difference between these two curves is the feature b, which is marked by an orange line. The background pressure during the deposition of S-B$_4$C (6 × 10^{-5} Pa) is higher than S6 (2 × 10^{-5} Pa), but S6 has a higher intensity at feature b, which means the boron in NiV/B$_4$C ML is easier to bond with oxygen. We suspect in NiV/B$_4$C ML that boron was excited by other elements then tend to combine with oxygen. There is a material worked as catalyst [34] during the deposition of NiV/B$_4$C ML.

3.4.2 V L-Edge and O K-Edge X-Ray Absorption Near-Edge Spectroscopy

The V L-edge and O K-edge XANES were measured to investigate the catalysis of the boron oxidation that happened in NiV/B$_4$C ML. The V L-edge and O K-edge absorption spectra of samples S-NiV, S-1 × 10^{-4} Pa and S-B$_4$C are presented in **Figure 5A**. S-NiV and S-1 × 10^{-4} Pa were deposited with the same background pressure. There are much more features in V L-edge and O K-edge XANES compared with B K-edge. Each feature is labeled with different letters shown in **Figure 5A**.

In the spectrum of S-NiV, the most distinct dual-peak feature (marked as e) at the region from 519.6 eV (left peak; known as L$_3$-edge) to 525.7 eV (right peak; known as L$_2$-edge), which correspond to the electronic transitions from the V 2p$_{3/2}$ and V 2p$_{1/2}$ core levels, respectively, to the unoccupied 3d levels [35]. Based on previous researches, the spectrum of S-NiV is similar with the V$_2$O$_5$, especially that they both have the small peak (peak d) besides the V L$_3$-edge [36]. This small peak (centered at 513.0 eV) can be assigned to the splitting of the unoccupied V 3d orbitals, which also indicates that the V$_2$O$_5$-liked structured formed in the S-NiV sample during the deposition. The features located at the energy region higher than 530.0 eV originated from the electronic transitions from O 1s to O 2p hybridized V 3d orbitals and are known to provide valuable information on the crystal structure, local symmetry of metal ions, and ligand-field

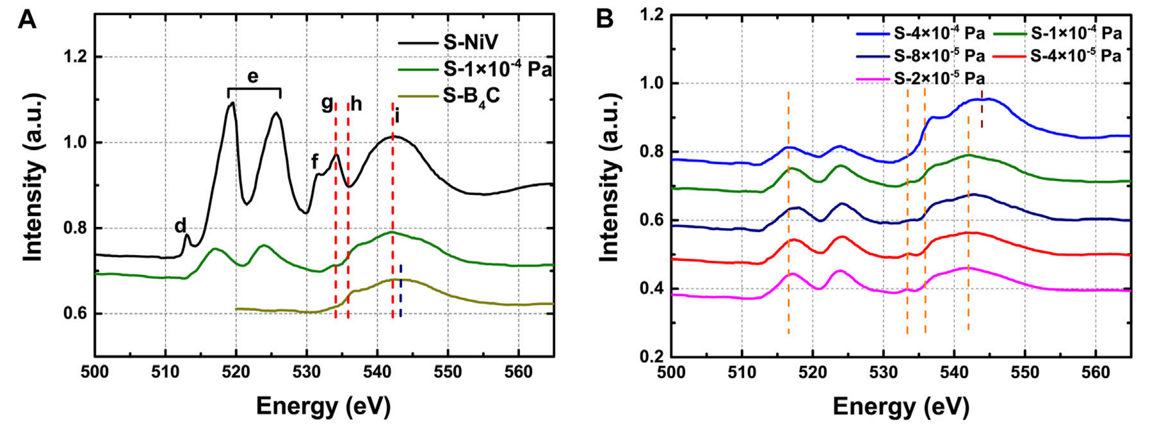

FIGURE 5 | The V L-edge and O K-edge XANES spectra of different samples. **(A)** NiV/B_4C ML and NiV coating deposited with 1×10^{-4} Pa, B_4C coating deposited with 6×10^{-5} Pa. **(B)** NiV/B_4C MLs deposited with different background pressures (S-4×10^{-4} , S-1×10^{-4}, S-8×10^{-5}, S-4×10^{-5}, and S-2×10^{-5} Pa).

effects [37, 38]. In an octahedral environment, the metal e_g (d_{z^2}, $d_{x^2-y^2}$) orbitals are pointed directly toward the O ligands to form strongly bonded σ bonds with the O p_z orbital. On the other hand, the metal t_{2g} (d_{xy}, d_{xz}, d_{yz}) orbitals point between the O ligands and make weak π bonds with O p_x and p_y [38]. In **Figure 5A**, peak f (531.7 eV) and peak g (534.1 eV) correspond to e_g and t_{2g}, respectively. The intensity of e_g is lower than t_{2g}, indicating that the V_2O_5-liked structured formed in S-NiV is closer to tetrahedrally coordinated compounds rather than octahedrally coordinated compounds [38, 39]. The broad feature i is due to the transition of O 1s electrons to the unoccupied O σ* states [38, 40].

Compared with S-NiV, the absorption spectrum of S-1×10^{-4} Pa shows less features. The dual-peak feature has a blue shift, L_2-edge centered at 517.0 eV, and L_3-edge changed to 523.9 eV, which means that the oxidation state of vanadium changed [41]. The position of features g and i are consistent with S-NiV, indicating that the coordinated structure around O atoms is similar, but the features d and f become absent, which means that the vanadium oxide in S-1×10^{-4} Pa is amorphous or highly disordered [36]. The O K-edge absorption spectrum of S-B_4C only has two features, one looks like a shoulder around 535.9 eV (labeled as h), which is also shown in the curve of S-1×10^{-4} Pa. The other one is also a broad feature, but peak has a little bit of shift compared with feature i in S-1×10^{-4} Pa and S-NiV. This shift is because the local atomic structure around O atoms was changed in different samples.

In **Figure 5B**, we compared NiV/B_4C MLs deposited with different background pressures. There are four orange dash lines corresponding to features e, g, h, and i (shown in **Figure 5A**), respectively. With the background pressure becoming lower, the L_3-edge has a gradual blue shift, which means that the oxidation state of vanadium keep changing toward a higher oxidation state. All the five curves both have feature h, and this feature is located at the same position, but the relative intensity of feature h also becomes lower as the background pressure changed. This is the same with feature b shown in B K-edge XANES because these two features are both related to B–O bonds. As for features g and i, the curve of S-4×10^{-4} Pa is totally different with other samples. The feature g in the curve of S-4×10^{-4} Pa is absent, and feature i has a shift compared with others. This shift is also shown in **Figure 5A**. Except for S-4×10^{-4} Pa, in the other samples, features g and i are both located at the same position. The relative intensity of feature i has a slight change with the changed concentration of oxygen in a vacuum chamber. On the contrary, the relative intensity of feature g seems to become higher when oxygen atoms become fewer, which means the structure of vanadium oxide tends to become ordered with less oxidation of boron.

Based on the comparison of the V L-edge and O K-edge XANES of different samples, we can conclude that several facts had happened during the magnetron sputtering deposition process: 1) Vanadium will form vanadium oxide during the deposition even with a background pressure of 2×10^{-5} Pa, and vanadium oxide is a well-known catalyst [34], which enhanced the combination of boron and oxygen. 2) As the combination of boron and oxygen has been catalyzed, the boron will grab more and more oxygen atoms, which will prevent the vanadium oxide from going to its highest oxidation state. 3) When the background pressure is lower than 1×10^{-4} Pa, the local atomic structure around O atoms does not change a lot, which means the chemical state and the layer structure are relatively stable in NiV/B_4C ML.

3.4.3 Nickel L-Edge X-Ray Absorption Near-Edge Spectroscopy

The Ni L-edge x-ray absorption near-edge structure spectra were measured to analyze the change in local atomic structure around the nickel atoms. The Ni L-edge absorption spectra of five NiV/B_4C MLs are presented in **Figure 6A**. There are two features in the measurement results, marked as j and k. The feature j centered at 857.3 eV (assigned at Ni L_3-edge) and the feature k located at 875.0 eV (assigned at Ni L_2-edge), which correspond to the electronic transitions from the Ni $2p_{3/2}$ and $2p_{1/2}$ ground states, respectively, to the unoccupied Ni 3d final states [42, 43]. As shown in **Figure 6A**, the relative intensities and positions of the different samples are the same, which means the background pressure does not cause any change in the Ni element in NiV/B_4C ML.

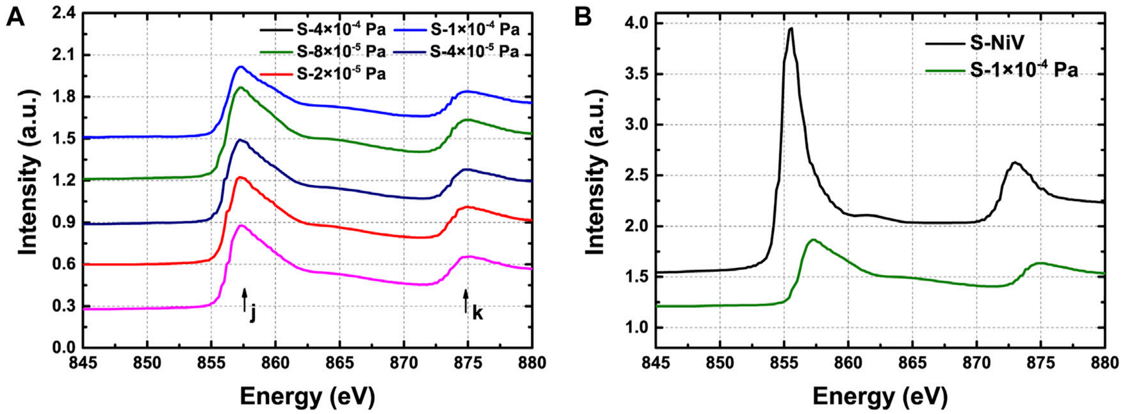

FIGURE 6 | The nickel (Ni) L-edge XANES spectra of different samples. **(A)** NiV/B$_4$C MLs deposited with different background pressures (S-4 × 10^{-4} , S-1 × 10^{-4}, S-8 × 10^{-5}, S-4 × 10^{-5}, and S-2 × 10^{-5} Pa). **(B)** NiV/B$_4$C ML and NiV coating both deposited with 1 × 10^{-4} Pa.

In **Figure 6B**, we compared the Ni L-edge absorption spectra of S-NiV and S-1 × 10^{-4} Pa. We found that features j and k both have a blue shift (~1.9 eV) in the curve of S-NiV. In the NiV coating, only vanadium and oxygen atoms are around Ni atoms, but in a multilayer, Ni atoms also adhere to the interface between NiV and B$_4$C layers. We suspected that the presence of interface caused the change in local atomic structure around Ni atoms, which caused the shift of Ni L-edge.

4 CONCLUSION

NiV/B$_4$C multilayers fabricated with different background pressures were studied comparatively. When the background pressure was higher than 1 × 10^{-4} Pa, an obvious structural change has been found in multilayers. This structural change is mainly shown in the thickness change in the B$_4$C layer. According to the EDX measurement, the thickness change is directly proportionate to the oxygen concentration in a vacuum chamber. Therefore, a gradient d-spacing change happened in a sample deposited with a high background pressure. Such a change will make the reflectivity spectrum broadened, which causes a severe performance loss when using an NiV/B$_4$C combination for a multilayer monochromator. XANES has been applied to further investigate the chemical change that happened in NiV/B$_4$C multilayers deposited with different background pressures. The oxidation of vanadium and boron has been found in all samples, which means the oxidation of active elements is inevitable during magnetron sputtering process, as long as the oxygen atoms stay in the vacuum chamber. After comparing the NiV/B$_4$C multilayer, NiV coating, and B$_4$C coating, an interesting phenomenon has been found. When the oxygen concentration is lower in the vacuum chamber, the vanadium oxidates work as a catalyst, which promotes the combination of boron and oxygen, but in the higher oxygen concentration environment, boron will "rob" the majority of oxygen atoms, which prevents the oxidation state of vanadium oxide toward its highest oxidation state. Besides the NiV/B$_4$C multilayers, a similar catalysis has been found in the Pd/B$_4$C multilayers [27]. Due to the catalysis, the ultrathin Pd/B$_4$C multilayers degraded rapidly when stored in air. Therefore, the lifetime and stability of NiV/B$_4$C multilayers is worth to be further studied. In this study, the structural and chemical changes both suggest that the NiV/B$_4$C multilayers need to fabricate with a background pressure lower than 1 × 10^{-4} Pa. Besides, the chemical state change found in this work can also provide useful guidance for further development and fabrication of NiV/B$_4$C multilayers.

DATA AVAILABILITY STATEMENT

The raw data supporting the conclusion of this article will be made available by the authors, without undue reservation.

AUTHOR CONTRIBUTIONS

ZZ and ZWa conceived and designed the research work. QH and RQ carried out the simulations. ZWe, YY and LJ prepared the samples. ZWe, ZZ, YF and CC analyzed the data. ZWe and ZZ wrote the paper. WY, CX and ZWa contributed to the helpful discussions for the research and modifications to the article. All authors have read and agreed to the published version of the manuscript.

FUNDING

This research was funded by the National Natural Science Foundation of China (Grant Nos. 12075170, 12003016 and U2030111(NSAF)).

ACKNOWLEDGMENTS

All authors would like to acknowledge the beamline MCD-A and MCD-B (Soochow Beamline for Energy Materials) at NSRL.

REFERENCES

1. Huang Q, Medvedev V, Van de Kruijs R, Yakshin A, Louis E, Bijkerk F. Spectral Tailoring of Nanoscale EUV and Soft X-Ray Multilayer Optics. *Appl Phys Rev* (2017) 4:011104. doi:10.1063/1.4978290
2. Barrett R, Baker R, Cloetens P, Morawe C, Tucoulou R, Vivo A. Reflective Optics for Hard X-Ray Nanofocusing Applications at the ESRF. *Synchrotron Radiat News* (2016) 29:10–5. doi:10.1080/08940886.2016.1198668
3. Windt DL. Advancements in Hard X-Ray Multilayers for X-Ray Astronomy. *Opt Euv, X-ray, Gamma-ray Astron* (2015) VII:960396031C. doi:10.1117/12.2187481
4. Huang Q, Liu Y, Yang Y, Qi R, Feng Y, Kozhevnikov IV, et al. Nitridated Ru/B4C Multilayer Mirrors with Improved Interface Structure, Zero Stress, and Enhanced Hard X-ray Reflectance. *Opt Express* (2018) 26:21803. doi:10.1364/oe.26.021803
5. Liu Y, Huang Q, Qi R, Xiao L, Zhang Z, Li W, et al. Microstructure Evolution and Hard X-Ray Reflectance of Ultrathin Ru/C Multilayer Mirrors with Different Layer Thicknesses. *Mater Res Express* (2021) 8:026401. doi:10.1088/2053-1591/abdf13
6. Windt DL, Donguy S, Hailey CJ, Koglin JE, Honkimaki V, Ziegler E, et al. Optical Constants for Hard X-Ray Multilayers over the Energy Range E = 35 - 180 KeV. *Proc SPIEOptics for EUV, X-Ray, and Gamma-Ray Astronomy* (2004) 5168:35–40. doi:10.1117/12.505886
7. Ni H, Huang Q, Liu G, Qi R, Zhang Z, Li X, et al. Comparative Study of Pd/B4C X-Ray Multilayer Mirrors Fabricated by Magnetron Sputtering with Kr and Ar Gas. *Materials* (2020) 13:4504–10. doi:10.3390/ma13204504
8. Louis E, Yakshin AE, Tsarfati T, Bijkerk F. Nanometer Interface and Materials Control for Multilayer EUV-Optical Applications. *Prog Surf Sci* (2011) 86:255–94. doi:10.1016/j.progsurf.2011.08.001
9. Jensen CP, Madsen KK, Christensen FE. Investigation of New Material Combinations for Hard X-Ray Telescope Designs. *Sp Telesc Instrum Ultrav Gamma Ray* (2006) 6266:626612. doi:10.1117/12.673180
10. Christensen FE, Jensen CP, Madsen KK, Pivovaroff MJ, Chen H, Dariel A, . Novel Multilayer Designs for Future Hard X-Ray Missions. *Sp Telesc Instrum Ultrav Gamma Ray* (2006) 6266:626611. doi:10.1117/12.673181
11. Rack A, Weitkamp T, Riotte M, Grigoriev D, Rack T, Helfen L, et al. Comparative Study of Multilayers Used in Monochromators for Synchrotron-Based Coherent Hard X-Ray Imaging. *J Synchrotron Radiat* (2010) 17:496–510. doi:10.1107/S0909049510011623
12. Dietsch R, Braun S, Holz T, Mai H, Scholz R, Bruegemann L. Multilayer X-ray Optics for Energies E > 8 keV and Their Application in X-ray Analysis. *Proc SPIE* (2000) 4144:137–47. doi:10.1117/12.405887
13. Ivan A, Bruni RJ, Byun KW, Gorenstein P, Romaine SE. Hard X-Ray Multilayers: A Study of Different Material Systems. *Proc Spie: Adv X-Ray Opt* (2001) 4145:72–9. doi:10.1117/12.411622
14. Chen CMH, Christensen FE, Harrison FA, Mao PH, Windt DL. Design of a Soft Gamma-Ray Focusing Telescope for the Study of Nuclear Lines. *X-ray Gamma-ray Telesc Instr Astron* (2003) 4851:1356. doi:10.1117/12.461419
15. Morawe C, Carau D, Peffen J-C. Double Multilayer Monochromators for Upgraded ESRF Beamlines. *Proc Spie: Adv X-Ray/EUV Opt Components* (2017) XII:103861038603. doi:10.1117/12.2273609
16. Carau D, Peffen J-C, Morawe C. Thickness Uniformity Study on the ESRF Multilayer Deposition System. *Proc Spie: Adv X-Ray/EUV Opt Components* (2017) XII:10386103860V. doi:10.1117/12.2273273
17. Leake SJ, Chahine GA, Djazouli H, Zhou T, Richter C, Hilhorst J, et al. The Nanodiffraction Beamline ID01/ESRF: A Microscope for Imaging Strain and Structure. *J Synchrotron Radiat* (2019) 26:571–84. doi:10.1107/S160057751900078X
18. Vaughan GBM, Baker R, Barret R, Bonnefoy J, Buslaps T, Checchia S, et al. ID15A at the ESRF - a Beamline for High Speed Operando X-ray Diffraction, Diffraction Tomography and Total Scattering. *J Synchrotron Radiat* (2020) 27:515–28. doi:10.1107/S1600577519016813
19. Qi R, Huang Q, Yang Y, Zhang Z, Wang Z. Effects of Sputtering Parameters and Separator Plates on the Structure and Stress of W/Si Multilayers in X-Ray Telescope Applications. *Opt Eng* (2017) 56:035103. doi:10.1117/1.oe.56.3.035103
20. Windt DL, Brown WL, Volkert CA, Waskiewicz WK. Variation in Stress with Background Pressure in Sputtered Mo/Si Multilayer Films. *J Appl Phys* (1995) 78:2423–30. doi:10.1063/1.360164
21. Wen M, Ma S, Huang Q, Jiang L, Li P, Zhang Z, et al. Effect of Background Pressure on Co/C Multilayers. *Appl Opt* (2017) 56:C16. doi:10.1364/AO.56.000C16
22. Jiang H, Zhu J, Huang Q, Xu J, Wang X, Wang Z, et al. The Influence of Residual Gas on Boron Carbide Thin Films Prepared by Magnetron Sputtering. *Appl Surf Sci* (2011) 257:9946–52. doi:10.1016/j.apsusc.2011.06.113
23. Li H, Zhu J, Wang Z, Song Z, Chen H. Asymmetrical Diffusion at Interfaces of Mg/SiC Multilayers. *Opt Mater Express* (2013) 3:546. doi:10.1364/ome.3.000546
24. Henderson GS, de Groot FMF, Moulton BJA. X-Ray Absorption Near-Edge Structure (XANES) Spectroscopy. *Rev Mineralogy Geochem* (2014) 78:75–138. doi:10.2138/rmg.2014.78.3
25. Sun Z, Liu Q, Yao T, Yan W, Wei S. X-Ray Absorption Fine Structure Spectroscopy in Nanomaterials. *Sci China Mater* (2015) 58:313–41. doi:10.1007/s40843-015-0043-4
26. Yan W, Liu Q, Wang C, Yang X, Yao T, He J, et al. Realizing Ferromagnetic Coupling in Diluted Magnetic Semiconductor Quantum Dots. *J Am Chem Soc* (2014) 136:1150–5. doi:10.1021/ja411900w
27. Feng Y, Qi R, Jiang L, Huang Q, Li T, Liu G, et al. Chemical Modification of B4C Films and B4C/Pd Layers Stored in Different Environments. *Materials* (2021) 14:1319. doi:10.3390/ma14051319
28. Jiménez I, Terminello LJ, Himpsel FJ, Grush M, Callcott TA. Photoemission, X-Ray Absorption and X-Ray Emission Study of Boron Carbides. *J Electron Spectros Relat Phenomena* (1999)(101–103) 611–5. doi:10.1016/s0368-2048(98)00342-9
29. Jia JJ, Underwood JH, Gullikson EM, Callcott TA, Perera RCC. Soft X-Ray Absorption Spectroscopy in 100 - 1000 EV Region at the ALS. *J Electron Spectrosc Relat Phenomena* (1996) 80:509–12. doi:10.1016/0368-2048(96)03028-9
30. Rao PN, Goutam UK, Kumar P, Gupta M, Ganguli T, Rai SK. Depth-resolved Compositional Analysis of W/B4C Multilayers Using Resonant Soft X-ray Reflectivity. *J Synchrotron Radiat* (2019) 26:793–800. doi:10.1107/S1600577519002339
31. Jiménez I, Sutherland DGJ, van Buuren T, Carlisle JA, Terminello LJ, Himpsel FJ. Photoemission and X-Ray-Absorption Study of Boron Carbide and its Surface Thermal Stability. *Phys Rev B* (1998) 57:13167–74. doi:10.1103/PhysRevB.57.13167
32. Zhang D, Mcilroy DN, O'Brien WL, De Stasio G. The Chemical and Morphological Properties of Boron-Carbon Alloys Grown by Plasma-Enhanced Chemical Vapour Deposition. *J Mater Sci* (1998) 33:4911–5. doi:10.1023/A:1004422016254
33. Rao PN, Gupta RK, Saravanan K, Bose A, Joshi SC, Ganguli T, . Investigation of Composition of Boron Carbide Thin Films by Resonant Soft X-Ray Reflectivity. *Surf Coat Techn* (2018) 334:536–42. doi:10.1016/j.surfcoat.2017.12.010
34. Bond GC, Tahir SF. Vanadium Oxide Monolayer Catalysts Preparation, Characterization and Catalytic Activity. *Appl Catal* (1991) 71:1–31. doi:10.1016/0166-9834(91)85002-D
35. Sharma A, Varshney M, Chae K-H, Won SO. Electronic Structure and Luminescence Assets in white-light Emitting Ca2V2O7, Sr2V2O7 and Ba2V2O7 Pyro-Vanadates: X-ray Absorption Spectroscopy Investigations. *RSC Adv* (2018) 8:26423–31. doi:10.1039/C8RA03347A
36. Lu Q, Bishop SR, Lee D, Lee S, Bluhm H, Tuller HL, et al. Electrochemically Triggered Metal-Insulator Transition between VO 2 and V 2 O 5. *Adv Funct Mater* (2018) 28:1803024–8. doi:10.1002/adfm.201803024
37. Lu Y-R, Hsu H-H, Chen J-L, Chang H-W, Chen C-L, Chou W-C, et al. Atomic and Electronic Aspects of the Coloration Mechanism of Gasochromic Pt/Mo-Modified V2O5 Smart Films: an *In Situ* X-ray Spectroscopic Study. *Phys Chem Chem Phys* (2016) 18:5203–10. doi:10.1039/c5cp06870c
38. Chen JG. NEXAFS Investigations of Transition Metal Oxides, Nitrides, Carbides, Sulfides and Other Interstitial Compounds. *Surf Sci Rep* (1997) 30:1–152. doi:10.1016/S0167-5729(97)00011-3

39. Chen CL, Dong CL, Ho YK, Chang CC, Wei DH, Chan TC, et al. Electronic and Atomic Structures of Gasochromic V 2 O 5 Films. *Epl* (2013) 101:17006. doi:10.1209/0295-5075/101/17006
40. Abbate M, de Groot FMF, Fuggle JC, Ma YJ, Chen CT, Sette F, et al. Soft-x-ray-absorption Studies of the Electronic-Structure Changes through theVO2phase Transition. *Phys Rev B* (1991) 43:7263–6. doi:10.1103/PhysRevB.43.7263
41. Chen JG, Frühberger B, Colaianni ML. Near-edge X-ray Absorption fine Structure Characterization of Compositions and Reactivities of Transition Metal Oxides. *J Vacuum Sci Techn A: Vacuum, Surf Films* (1996) 14:1668–73. doi:10.1116/1.580316
42. Ufuktepe Y, Akgül G, Aksoy F, Nordlund D. Thickness and Angular Dependence of the L-Edge X-Ray Absorption of Nickel Thin Films. *X-ray Spectrom* (2011) 40:427–31. doi:10.1002/xrs.1362
43. Gu W, Wang H, Wang K. Nickel L-Edge and K-Edge X-ray Absorption Spectroscopy of Non-innocent Ni[S2C2(CF3)2]2n Series (N = −2, −1, 0): Direct Probe of Nickel Fractional Oxidation State Changes. *Dalton Trans* (2014) 43:6406–13. doi:10.1039/c4dt00308j

Conflict of Interest: The authors declare that the research was conducted in the absence of any commercial or financial relationships that could be construed as a potential conflict of interest.

Frontiers in Physics

ORIGINAL RESEARCH
published: 07 April 2022
doi: 10.3389/fphy.2022.864985

Influence of Photon Beam and Motor Vibrations on At-Wavelength X-Ray Speckle Scanning Metrology

Naxi Tian[1], Hui Jiang[1,2,3]*, Lian Xue[1] and Jianan Xie[1,4]

[1]Shanghai Synchrotron Radiation Facility, Shanghai Advanced Research Institute, Chinese Academy of Sciences, Shanghai, China, [2]Shanghai Institute of Applied Physics, Chinese Academy of Sciences, Shanghai, China, [3]University of Chinese Academy of Sciences, Beijing, China, [4]School of Physical Science and Technlogy, ShanghaiTech University, Shanghai, China

Speckle scanning metrology is an effective tool to determine the X-ray wave front error in synchrotron radiation. By measuring wave front radii of curvature, X-ray optics can be high-precision aligned and adaptive optics can be used for compensating these wave front errors to pursue an aberration-free wave front. Photon beam and motor vibrations are the major limitations in characterizing the beam performances. An analytical model is presented in this article to reveal the influences of photon beams and motor vibrations on the measurements of the wave front radii of curvature. It is worth noting that the influence of low-frequency vibration is oscillatory and thus the selection of sampling frequency is strongly related. The experimental results verify the model and reveal the main dependency of the experimental deviations on the amplitude and frequency of vibrations.

Keywords: speckle scanning metrology, synchrotron radiation, vibration analysis, vibration frequency, wave front radius of curvature

Edited by:
Qiushi Huang,
Tongji University, China

Reviewed by:
Hongchang Wang,
Diamond Light Source,
United Kingdom
Simon Alcock,
Diamond Light Source,
United Kingdom

***Correspondence:**
Hui Jiang
jianghui@zjlab.org.cn

Specialty section:
This article was submitted to
Optics and Photonics,
a section of the journal
Frontiers in Physics

Received: 29 January 2022
Accepted: 11 March 2022
Published: 07 April 2022

Citation:
Tian N, Jiang H, Xue L and Xie J (2022)
Influence of Photon Beam and Motor
Vibrations on At-Wavelength X-Ray
Speckle Scanning Metrology.
Front. Phys. 10:864985.
doi: 10.3389/fphy.2022.864985

INTRODUCTION

As a novel X-ray wave front sensing technique, the near-field speckle-based technique has been successfully applied to X-ray imaging [1–3] and metrology [4–7]. Compared to the previous techniques such as the Hartmann wave front sensor [8], propagation iterative algorithm [9], and grating interferometry [10], the speckle-based technique has the advantages of high measurement accuracy, flexible experimental setup, and economical application cost. X-ray speckle scanning metrology utilizes the speckle pattern produced by the diffuser (such as sandpaper or membrane) as a wave front marker to modulate the X-ray wave front [11]. By analyzing a series of speckled patterns acquired during a diffuser scan, the wave front phase gradient or local curvature can be extracted [12].

Noise and vibration inevitably interact with synchrotron radiation facilities. For high-precision scanning-based metrology or an imaging experimental process, often, they have more influence than photon flux. Zhou discussed the noise properties on the speckle-based imaging and found a behavior similar to that of the grating-based method [13]. The signal-to-noise ratio was found to have a strong influence on the subset size choice in speckle-based imaging [14]. Photon beam vibrations from the electron beam orbit, insert devices [15], ground [16], optics (mechanical or thermal instability), mechanical pieces of equipment [17], and other human activities occur more unpredictably. Vibrations can be roughly divided into three frequency regimes: low (<1 Hz), intermediate (1–100 Hz), and high (>100 Hz) regimes [18]. Although the vibrations of intermediate and high frequencies can be greatly suppressed through the optimization of buildings and environment, as

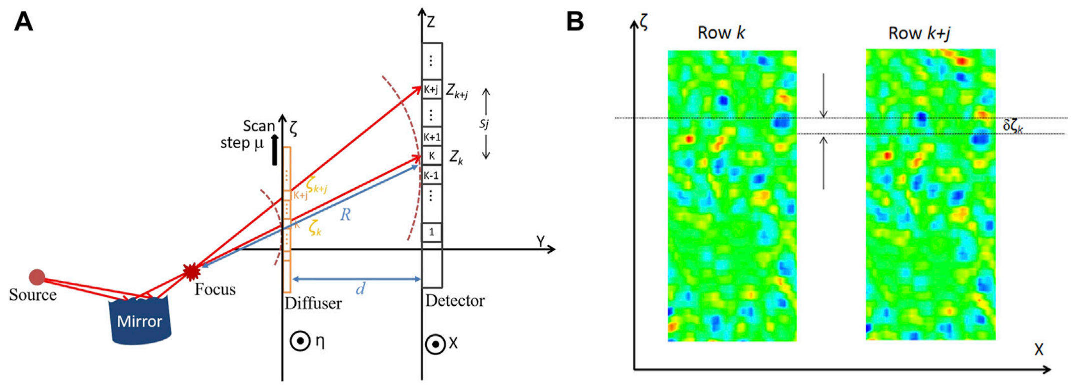

FIGURE 1 | (A) Measurement configuration for the speckle scanning metrology. **(B)** The new stitched speckle patterns built from the *k*th and $(k + j)^{\text{th}}$ rows of a stack of speckle patterns.

well as the beamline equipment and optics, the vibrations of intermediate and low frequencies in the submicron scale are widespread, which have a significant impact on the experiments of high spatial or temporal resolution. Optical vibrations have been revealed to have relations with beam coherence [19], beam size, and divergence [20]. Scanning motor vibrations or errors in different scan sequences that change the effective scan step size can also introduce artifacts in the measurement [21]. Berujon used the X-ray speckle tracking technique to measure the beam stability with a fast time-sampling resolution ~80 Hz [22]. However, rapid exposure requires a high beam flux, and this technique can only measure the vibrations below the sampling frequency. To the best of our knowledge, comprehensive studies discussing the influence of vibrations on beam quality or the accuracy of related metrology in the synchrotron radiation field are still lacking, which makes it difficult to accurately characterize the wave front and realize the stability adjustment with high-speed feedback. In contrast, a similar situation of laser propagation [23, 24] or sensor [25] in a turbulent atmosphere has been treated with an emphasis.

This article analytically analyzes and discusses the influence of photon beams and motor vibrations with various amplitudes and frequencies on the X-ray speckle scanning metrology.

THEORY

In speckle scanning metrology, X-rays pass through a diffuser and are collected on a pixel detector. As is shown in **Figure 1A**, the diffuser plane and detector plane are represented in the different coordinating systems. The diffuser can be scanned along the vertical direction driven by a high-precision motor at a constant step μ and a constant speed v. The line intensity profiles of the kth row $I_o(x, z_k)$ in a stack (n) of speckle patterns collected during a scan time t can be stitched as a new speckle pattern $I_o(x, z_k, \zeta_k(t))$, as shown in **Figure 1B**. Here, $\zeta_k(t) = \zeta_k(0) + vt$ and $vt < n\mu$. Since all images in the horizontal direction do not change, in order to simplify the expression, x will be omitted in the subsequent expressions.

The square difference between the kth and $(k + j)^{\text{th}}$ stitched speckle pattern can be expressed as follows:

$$\chi^2(\zeta) = \sum \left[I_o(z_k, \zeta_k - \zeta) - I_o\left(z_{k+j}, \zeta_{k+j}\right) \right]^2. \tag{1}$$

In this expression, with the change in ζ, a region of interest as the subset moves in the range of scan sequence for the square difference calculation. The location of the least-square difference at $\zeta = \delta\zeta_k$ can denote the best matching of two stitched speckle patterns, as shown in **Figure 1B**. **Equation 1** is equivalent to the cross-correlation function using a digital image correlation method [26]. In this situation, the kth and $(k + j)^{\text{th}}$ stitched speckle patterns have an approximate relational expression:

$$I_o(z_k, \zeta_k) = I_i(\zeta_k) T(\zeta_k) \simeq I_i\left(\zeta_{k+j}\right) T(\zeta_k + \delta\zeta_k), \tag{2}$$

where I_i is the incoming beam intensity at the diffuser plane and T is the transfer function of a diffuser. In the case where the focus is upstream of the diffuser, the local wave front radius of curvature R_k with respect to the kth row pixels can be calculated based on a geometrical relation given as follows:

$$\frac{R_k - d}{R_k} = \frac{\delta\zeta_k}{sj}, \tag{3}$$

where s is the detector pixel size and d is the diffuser-to-detector distance. The local wave front radius of curvature can be measured with higher angular resolution by analyzing the speckles using more neighboring pixels (smaller j), but too many neighboring pixel choices may result in an indistinguishable shift compared to the scan step.

Whether it is the vibration of a point source or a reflective mirror, the beam vibration mainly presents as the shift in position or angle. Actually, both linear and angular vibrations exist in any synchrotron beamline. In the small-angle approximation of a paraxial system, all vibration processes can be reflected on the linear position shift of speckles. Assuming the vibration occurs in the vertical direction, the vibration at the diffuser plane is described by a sinusoidal function of time and a random vibration τ_b in the form of

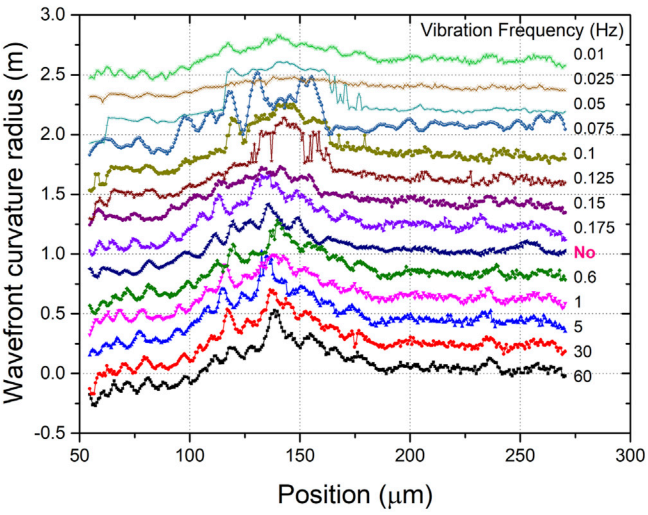

FIGURE 2 | Measured wave front radii of curvature with different vibration frequencies from 0.01 to 60 Hz and fixed vibration amplitude of 50 nm. When low-frequency vibrations below 0.15 Hz are added, the measured wave front curvature starts to diverge away from the no-vibration state.

$$\xi(t) = A\sin(2\pi f t) + \tau_b(t), \tag{4}$$

where A is the amplitude and f is the vibration frequency. τ_b normally satisfies Gaussian probability distributions with zero mean and a known standard deviation. The location of the irradiation on the diffuser changes with the vibration, therefore I_i in **Eq. 2** is no longer constant. Similarly, the scanning motor also has a random vibration or a step error, which can be denoted as τ_m. Defining a calculation error $\delta\zeta_{ek}$ of the shift $\delta\zeta_k$ resulting from a photon beam vibration $\xi(t)$ and a random motor vibration $\tau_m(t)$, **Eq. 2** can be changed as follows:

$$I_o(z_k, \zeta_k(t)) = I_i\left(\zeta_{k+j} + \Delta\zeta + \xi_k(t)\right)T\left(\zeta_k + \tau_{mk}(t) + \left(\delta\zeta_k + \delta\zeta_{e_k}\right)\right), \tag{5}$$

where $\Delta\zeta = A\sin(2\pi f\zeta_k/v)$ is the beam offset when the diffuser moves a displacement of $\delta\zeta_k$.

Since $\delta\zeta_e$ is far less than $\delta\zeta$, and the vibrations ξ and τ_m are small quantities, the first-order Taylor expansions can be used to express these disturbances. Combining **Eq. 1** and **Eq. 5**, the following equation is obtained:

$$\chi^2(\delta\zeta_k) = \sum[(M(\zeta_k)T(\zeta_k + \delta\zeta_k)\xi(t) + I_i(\zeta_{k+j} + \xi(t) + \Delta\zeta)h(\zeta_k)(\tau_m(t) + \delta\zeta_{e_k})]^2, \tag{6}$$

where $M(\zeta_k) = d^2I_i(\zeta_k)/d\zeta_k^2$ and $h(\zeta_k) = dT(\zeta_k)/d\zeta_k$. Minimizing **Eq. 6** by solving $d\chi^2/d\zeta = 0$ when $\zeta = \delta\zeta_k$, we can get the relationship between the error of shift and the different vibrations as follows:

$$\delta\zeta_e = \frac{\sum M(\zeta_k)T(\zeta_k + \delta\zeta_k)\xi(t)I_i(\zeta_{k+k} + \xi(t) + \Delta\zeta)h(\zeta_k) + \sum I_i^2\left(\zeta_{k+j} + \xi(t) + \Delta\zeta\right)h^2(\zeta_k)\tau_m(t)}{\sum I_i^2(\zeta_k + \xi(t) + \Delta\zeta)h^2(\zeta_k)}. \tag{7}$$

We assume that the motor vibration τ_m is Gaussian white noise. For a situation with only motor vibration, the variance of the error of shift can be expressed [27] in a simple form σ2ζ = σ2τm. For a situation with only beam vibration, the second summation term of the numerator in the **Eq. 7** equals zero. If the beam vibration obeys a Gaussian statistical relation $\xi(t) = \tau_b(t)$, the variance of the error of shift can be mathematically expressed as follows [27]:

$$\sigma^2_{\zeta_k} = \sigma^2_{\tau b}\sum\frac{T^2(\zeta_k)M^2(\zeta_k)}{h^2(\zeta_k)I_i^2\left(\zeta_{k+j} + \Delta\zeta\right)}. \tag{8}$$

When the beam vibration is described by a sinusoidal function, the situation is highly dependent on the vibration frequency. The beam intensity function can be expressed as the convolution of the probability density function P and its original intensity distribution [28]: $I_i(\zeta_k + \xi(t)) = P(\zeta_k) * I_i(\zeta_k)$, where * is the convolution operator. In a small range within the vibration amplitude A, the intensity can be regarded as a constant. In this case, the beam intensity function is equivalent to $I(\zeta_k + \xi(t)) = P(\zeta_k)I_i(\zeta_k)$. If the beam vibration $\xi(t) = A\sin(2\pi ft)$, the probability density function of $\xi(t)$ is $P(\zeta_k) = 1/[\pi(A^2 - \zeta_k^2)^{1/2}]$. The variance of the error of shift can be given as follows:

$$\sigma^2_{\zeta k} = \sigma^2_{\xi 1}\pi^2\sum_{i=0}^{nNf_s/f}\frac{T^2(\zeta_k)M^2(\zeta_k)\left(A^2 - \zeta_k^2\right)}{h^2(\zeta_k)I^2\left(\zeta_{k+j} + \Delta\zeta\right)} + \sigma^2_{\xi 2}\pi^2\sum_{i=nNf_s/f}^{n}\frac{T^2(\zeta_k)M^2(\zeta_k)\left(A^2 - \zeta_k^2\right)}{h^2(\zeta_k)I^2\left(\zeta_{k+j} + \Delta\zeta\right)}, \tag{9}$$

where $f_s = v/n\mu$ is the sampling frequency of the detector during a scan sequence in the range of any subset, i is the row order in the scan sequence, and $N = [f/f_s]$ is the integral value. In a sinusoidal period, the mean square $\sigma^2_{\xi 1} = A^2/2$. For extra beam offset beyond periodic vibrations, the mean square $\sigma^2_{\xi 2}$ is as follows:

$$\sigma^2_{\xi 2} = \frac{f_s^2\left[1 - \cos\left(\frac{2\pi f}{f_s}\right)\right]^2 A^2}{\left(f - Nf_s\right)^2}. \tag{10}$$

When the vibration frequency is much higher than the sampling frequency in a single exposure $f >> f_0 = f_s n$, the collected patterns are the statistical average of the speckle patterns in a sampling time, that is, low-contrast or blur speckle patterns. In this case, the second term can be neglected. Since the vibration period cannot be recorded by the detector, the frequency no longer affects the value of the first term. When the vibration frequency satisfies $f_s << f < f_0$, the stitched speckle image includes N reciprocating vibrations, which is the first item in the given expression. The vibrations with opposite directions in any vibration period produce reverse deviations $\delta\zeta_e$, which makes a relatively small competition error in the algorithm for searching out a maximum $\delta\zeta^{14}$. The weight of the first term **Eq. 9** is greater as N increases and the first term increases slowly with the increase of the vibration period and amplitude. The second term depicts the influence from the extra beam offset beyond these periodic vibrations. It is clear that if the vibration frequency f is exactly an integral multiple of f_s, the second term is equal to zero, so there is a relative minimum of the error of shift. If the vibration reaches maximum amplitude A,

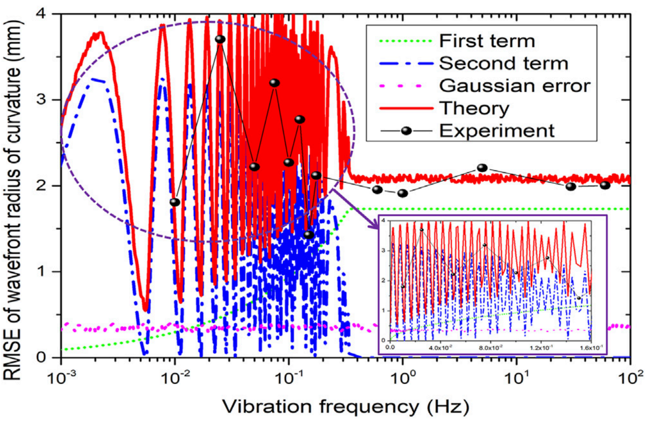

FIGURE 3 | Comparison of the experimental and the theoretical RMSE of the wave front radius of curvature. The solid red line represents the simulated curve based on **Eq. 11**. The green short dot, blue dash dot, and magenta dot, respectively, represent the first term, second term, and error term in **Eq. 11**. The black line and solid ball are the experiment data. The extra inserted figure is to expand the frequency range of 0–0.16.

there is a relative maximum of the error of shift. When the vibration frequency is close to or lower than the sampling frequency of the detector within the subset range, the effect of the vibration performs as the linear movement of the incoming beam. In this case, the first term is equal to zero and the low-frequency beam offset expressed in the second term determines the error of shift.

In consideration of the complex form of **Eq. 9**, we can simplify its expression based on the analysis in the last paragraph. Compared to the influence from multiple vibration periods on the correlation method, the influence from the statistical fluctuations of T, M, h, and I can be neglected so that a constant term can be used to replace the formula in summation term. **Eq. 9** and **Eq. 10** can be simplified as follows:

$$\sigma_{\zeta}^{2} = \sigma_{\xi 1}^{2}\pi^{2}\gamma(f)K_{1} + \sigma_{\xi 2}^{2}\pi^{2}\left(1-\gamma(f)\right)K_{1} + \sigma_{\tau b}^{2}K_{2}. \qquad (11)$$

where K_1 and K_2 are constants and the weight function $\gamma(f) = Nf_s/f$.

Based on **Eq. 3**, the root-mean-square error (RMSE) of the wave front radius of curvature has a relationship with that of the speckle shift, which is given as follows:

$$\Delta\bar{R} = \frac{\Delta\bar{\zeta}}{\left(sj-\bar{\zeta}\right)^{2}}. \qquad (12)$$

Combining **Eqs 9**, **10**, or using a simplified **Eq. 11**, the calculation error of the radius of curvature can be estimated from the vibration influence.

Except the calculation error of the wave front radius of curvature, the angular resolution of the measurement also changes. In theory, the angular resolution of the radius of curvature is sj/R. When the photon beam has a vibration with its frequency smaller than the sampling frequency, the angular resolution changes to $(sj+\Delta\zeta)/R$. For the position of a sudden change of curvature, $M(\zeta_k)$ in **Eqs 8**, **9** increases significantly and the vibration increases the error. For a high-frequency vibration, the angular resolution remains unchanged.

EXPERIMENTS

The X-ray speckle scanning metrology measurements were performed at the BL09B measurement beamline of the

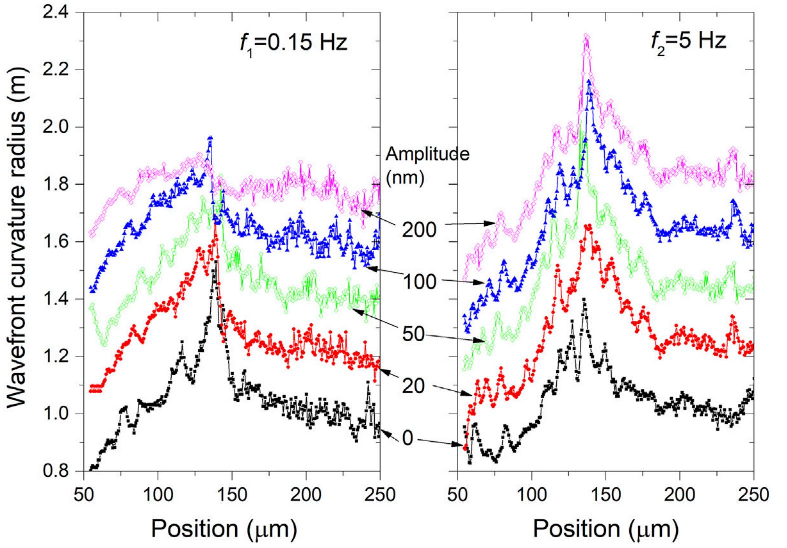

FIGURE 4 | Measured wave front curvature radius with different vibration amplitudes from 20 to 200 nm for a given frequency of 0.15 Hz (left) and 5 Hz (right). The measurement can tolerate a vibration amplitude of 200 nm at 5 Hz but much lower amplitude at 0.15 Hz.

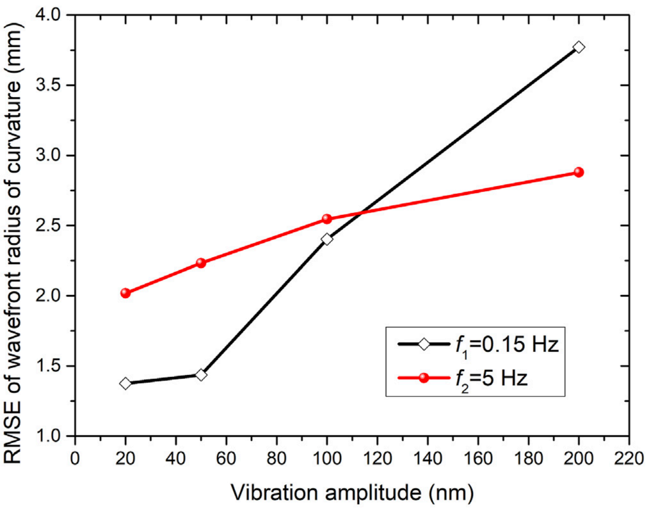

FIGURE 5 | Comparison of the RMSE of wave front radius of curvature at 0.15 and 5 Hz.

Shanghai Synchrotron Radiation Facility with an X-ray energy of 10 keV. As shown in **Figure 1**, the cylindrical mirror was mounted with the vertical deflection on the sample manipulator of $L_0 = 39$ m downstream of the source. The sandpaper with the pore size of 3 μm was $L_1 =$ 380 mm downstream of the mirror. The grazing-incidence angle of the mirror was at the total reflection $\theta = 0.18°$. The detection system, a microscope objective lens system (Optique Peter) with a magnification of 10 coupled to a CMOS camera (Hamamatsu) was placed at $d = 955$ mm behind the sandpaper. The effective pixel size was $s =$ 0.65 μm. The exposure time was 5 s for each capture. During scanning measurements, the sandpaper was driven at a nano-precision linear motion stage (PI) with a step size of $\mu = 200$ nm along the vertical direction and $m = 51$ speckle patterns were recorded during each scan. The movement time of each step is 0.2 s. The vibrations of a cylindrical mirror were simulated by a sinusoidal motion of another piezo linear motion stage (Coremorrow) along the vertical direction with different frequencies (0.01–60 Hz) and different amplitudes (20–200 nm). The subset width of 31 steps was used in the digital image correlation algorithm.

RESULTS AND DISCUSSIONS

Figure 2 shows the measured wave front radius of a curvature with different vibration frequencies from 0.01 to 60 Hz and fixed amplitude of 50 nm. It is clear that at the low-frequency regime, the vibration caused a significant influence. Based on the simplified analytical model of **Eq. 11**, the RMSE of these wave front radii of curvature versus the frequency can be simulated, as seen in **Figure 3**. The RSME curve can be regarded as the sum of the algorithm error from periodic vibration (first term), the extra deviation (second term), and the random errors. It is clear that when the vibration frequency is greater than $f_0 = 0.19$ Hz, the RSME tends to a constant, and in the low-frequency regime, the RSME shows a characteristic of oscillation. When the $f = 0.025$, 0.075, 0.125, and 0.175 Hz, the sinusoidal vibration almost reached the maximum amplitude. As seen in **Figure 3**, the RMSEs of the wave front radii of curvature are closer to the maximum. Whereas when the f/f_s is

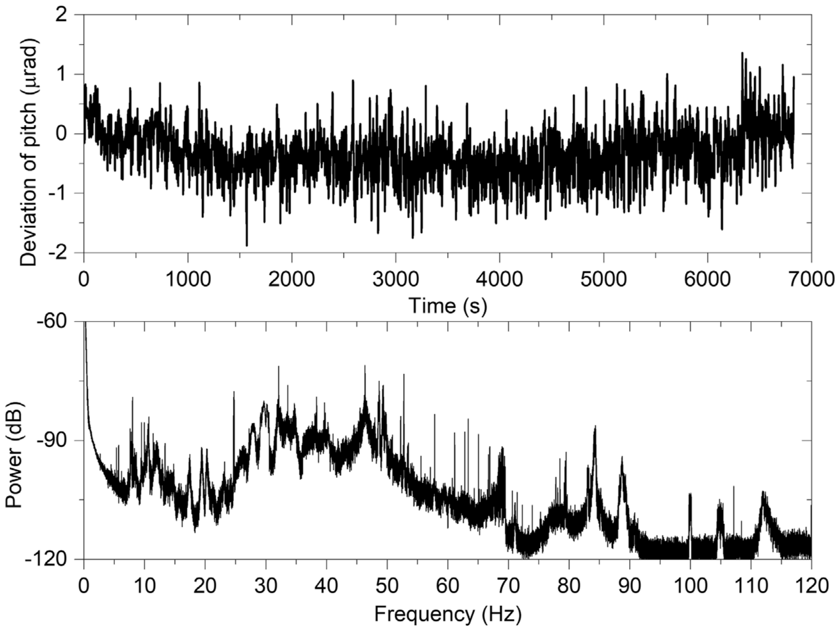

FIGURE 6 | Vibration of the pitch angle for the horizontal-deflecting collimating mirror (upper) and its power in the frequency domain (lower).

close to an integer such as $f = 0.1$ or 0.6 Hz, the RMSEs are relatively small. Based on the aforementioned results, it is obvious that if the sampling frequency is set lower than most of the vibration frequencies, to avoid the region of oscillation, relatively stable, and predictable experimental results can be obtained.

Figure 4 presents the measured wave front radii of curvature at the frequencies 0.15 and 5 Hz as the vibration amplitudes changed from 20 to 200 nm. Since the measurements for frequencies of 0.15 and 5 Hz were carried out on different days, the wave front curvature radii in cases of zero amplitude were a little different. In the case of 5 Hz, the measurement can tolerate a very large vibration amplitude and the curvature radius profile almost maintains the same shape. In contrast, the test data with 200 nm vibration amplitude at 0.15 Hz has significant errors and in some locations, the error is even more than 0.4 m. **Figure 5** compares the RMSE curves of the two frequencies. Since the amplitude changes, the summation terms in **Eq. 9** contain the variable A. In this case, the RMSE is a quartic increasing function of amplitude. Since the second term in **Eq. 9** has a certain weight at 0.15 Hz and the $\sigma_{\xi 2}^2$ is greater than $\sigma_{\xi 1}^2$, the RMSE at 0.15 Hz has a greater slope than that at 5 Hz as the amplitude increases. As the frequency decreases further, the weight of the first term in **Eq. 9** also decreases so that the RMSE increases significantly with the increase of amplitude.

Figure 6 presents a stability test of the pitch angle for the horizontal-deflecting collimating mirror with the water-cooling system at the Shanghai Synchrotron Radiation Facility. The relative pitch stability was measured using the Renishaw XL-80 laser interferometer, and the data were collected at a sampling frequency of 250 Hz. The lower figure reports the Fourier transform of vibration amplitudes with a bandwidth upper limit of 120 Hz. The eigenmodes below 50 Hz are always related to the support. For such a mirror longer than 800 mm, the low-frequency vibration of <0.5 Hz can be closed loop compensated by using a feedback system based on the beam position monitor because this low-frequency vibration has significant negative effects on X-ray speckle scanning metrology. The RMS vibration below 20 Hz is beyond 20 nrad. The sampling frequency of X-ray speckle scanning metrology needs to avoid higher than main frequency peaks or at least avoid the maximum of the second term in **Eq. 10**. The vibration of the frequency higher than 20 Hz cannot be compensated by a feedback system; hence, its influence on the metrology is almost a constant as demonstrated in **Figure 3**.

CONCLUSION

In conclusion, we presented an analytical model and experimental verification of the vibration-induced effect on the measurement of the wave front radius of curvature by using the X-ray speckle scanning technique. The proposed method can be used to estimate the experimental errors or optimize the sampling time in X-ray speckle scanning metrology based on the known eigenfrequency of the optics or the vibration frequency of the X-ray beam. It suggests that [1] the sampling frequency should be lower than most of the main vibration frequencies [2]; the rest of the lower vibration frequency should remain an integer multiple of the sampling frequency in a scan sequence within the range of a subset [3]; the low-frequency vibration should be eliminated as much as possible. When the aforementioned three conditions are satisfied, the test error of metrology can be considered as a constant and easily estimated.

DATA AVAILABILITY STATEMENT

The raw data supporting the conclusion of this article will be made available by the authors, without undue reservation.

AUTHOR CONTRIBUTIONS

NT: methodology, software, experiment, and writing. HJ: conceptualization, methodology, writing, and supervision. LX: experiment. JX: writing.

FUNDING

The study was funded by the National Natural Science Foundation of China (12175294, 11775295), Natural Science Foundation of Shanghai of China (21ZR1471500), and the Funds from the Youth Innovation Promotion Association, CAS (2018295).

ACKNOWLEDGMENTS

The authors would like to thank our colleague Dr. Zhongliang Li for helping with the set-up of experiments at the measurement beamline BL09B of SSRF.

REFERENCES

1. Berujon S, Wang H, Sawhney K. X-ray Multimodal Imaging Using a Random-phase Object. *Phys Rev.A* (2013) 86(6):1–9.
2. Morgan KS, Paganin DM, Siu KKW. X-ray Phase Imaging with a Paper Analyzer. *Appl Phys Lett* (2012) 100(12):124102. doi:10.1063/1.3694918
3. Zanette I, Zhou T, Burvall A, Lundström U, Larsson DH, Zdora M, et al. Speckle-Based X-Ray Phase-Contrast and Dark-Field Imaging with a Laboratory Source. *Phys Rev Lett* (2014) 112(25):253903. doi:10.1103/physrevlett.112.253903
4. Wang H, Sutter J, Sawhney K. Advanced *In Situ* Metrology for X-ray Beam Shaping with Super Precision. *Opt Express* (2015) 23(2):1605–14. doi:10.1364/oe.23.001605
5. Kashyap Y, Wang H, Sawhney K. Speckle-based At-Wavelength Metrology of X-ray Mirrors with Super Accuracy. *Rev Scientific Instr* (2016) 87(5):052001. doi:10.1063/1.4949004
6. Jiang H, Yan S, Tian N, Liang D, Dong Z, Zheng Y. Extraction of Medium-Spatial-Frequency Interfacial Waviness and Inner Structure from X-ray

Multilayers Using the Speckle Scanning Technique. *Opt Mater Express* (2019) 9(7):2878. doi:10.1364/ome.9.002878

7. Jiang H, Tian N, Liang D, Du G, Yan S. A Piezoelectric Deformable X-ray Mirror for Phase Compensation Based on Global Optimization. *J Synchrotron Radiat* (2019) 26:729–36. doi:10.1107/s1600577519003047
8. Idir M, Mercere P, Modi M, Dovillaire G, Sauvageot P. X-ray Active Mirror Coupled with a Hartmann Wavefront Sensor. *Nuc Instrum Meth A* (2010) 616(2-3):162–71. doi:10.1016/j.nima.2009.10.168
9. Kimura T, Mimura H, Handa S, Yumoto H, Yokoyama H, Imai S, et al. Wavefield Characterization of Nearly Diffraction-Limited Focused Hard X-ray Beam with Size Less Than 10 Nm. *Rev Scientific Instr* (2010) 81(12):123704. doi:10.1063/1.3509384
10. Zanette I, Weitkamp T, Donath T, Rutishauser S, David C. Two-Dimensional X-ray Grating Interferometer. *Phys Rev Lett* (2010) 105(24):248102. doi:10.1103/physrevlett.105.248102
11. Tian N, Jiang H, Li A, Liang D, Yan S, Zhang Z. Influence of Diffuser Grain Size on the Speckle Tracking Technique. *J Synchrotron Radiat* (2020) 27:146–57. doi:10.1107/s1600577519015200
12. Berujon S, Wang H, Alcock S, Sawhney K. At-wavelength Metrology of Hard X-ray Mirror Using Near Field Speckle. *Opt Express* (2014) 22(6):6438–46. doi:10.1364/oe.22.006438
13. Zhou T, Zdora M-C, Zanette I, Romell J, Hertz HM, Burvall A. Noise Analysis of Speckle-Based X-ray Phase-Contrast Imaging. *Opt Lett* (2016) 41(23):5490–3. doi:10.1364/ol.41.005490
14. Tian N, Jiang H, Li A, Liang D, Yu F. High-precision Speckle-Tracking X-ray Imaging with Adaptive Subset Size Choices. *Sci Rep* (2020) 10:14238. doi:10.1038/s41598-020-71158-9
15. Tsumaki K, Kumagai N. Vibration Measurement of the SPring-8 Storage Ring, Particle Accelerator Conference. *IEEE* (2001) 1482–4.
16. Wang X, Yan Z, Du H. Suppression of Ground Vibration for SSRF Foundation. *Appl Mech Mat* (2012) 105-107:30–3.
17. Li JW, Matias E, Chen N, Kim C-Y, Wang J, Gorin J, et al. Investigations of Mechanical Vibrations for Beamlines at the Canadian Light Source. *J Synchrotron Radiat* (2011) 18:109–16. doi:10.1107/s0909049510041075
18. Simos N. Synchrotron Facilities: Vibration and Stability challenge. *Synchrotron Radiat News* (2019) 32(5):2–3. doi:10.1080/08940886.2019.1654825
19. Grizolli W, Shi X, Assoufid L. Influence of Optics Vibration on Synchrotron Beam Coherence. *Opt Lett* (2019) 44(4):899–902. doi:10.1364/ol.44.000899
20. Goto S. Effect of Beamline Optics Vibration on the Source Size and Divergence for Synchrotron Radiation. *Proc SPIE* (2015) 9588:95880G. doi:10.1117/12.2191933
21. Zdora M-C. State of the Art of X-ray Speckle-Based Phase-Contrast and Dark-Field Imaging. *J Imaging* (2018) 4(5):60. doi:10.3390/jimaging4050060
22. Berujon S, Cojocaru R, Piault P, Celestre R, Roth T, Barrett R, et al. X-ray Optics and Beam Characterization Using Random Modulation: Experiments. *J Synchrotron Radiat* (2020) 27:293–304. doi:10.1107/s1600577520000508
23. Whiteley M. Compensation Efficiencies of Conventional Tracking and High-Order Beam Control in Extended Turbulence. *Proc.SPIE* (2000) 4125:21–101.
24. Frehlich R. Simulation of Laser Propagation in a Turbulent Atmosphere. *Appl Opt* (2000) 39(3):393–7. doi:10.1364/ao.39.000393
25. Kim JJ, Fernandez B, Agrawal B. Iterative Wavefront Reconstruction for strong Turbulence Using Shack-Hartmann Wavefront Sensor Measurements. *J Opt Soc Am A* (2021) 38(3):456–64. doi:10.1364/josaa.413934
26. Pan B, Xie H, Xu B, Dai F. Performance of Sub-pixel Registration Algorithms in Digital Image Correlation. *Meas Sci Technol* (2006) 17:1615–21.
27. Wang YQ, Sutton MA, Bruck HA, Schreier HW. Quantitative Error Assessment in Pattern Matching: Effects of Intensity Pattern Noise, Interpolation, Strain and Image Contrast on Motion Measurements. *Strain* (2009) 45:160–78. doi:10.1111/j.1475-1305.2008.00592.x
28. Hardy J. *Adaptive Optics for Astronomical Telescopes*. New York: CRC Press (1996).

Conflict of Interest: The authors declare that the research was conducted in the absence of any commercial or financial relationships that could be construed as a potential conflict of interest.

frontiers | Frontiers in Physics

ORIGINAL RESEARCH
published: 04 May 2022
doi: 10.3389/fphy.2022.821549

A Procedure for the Characterization of Monocapillary X-Ray Lenses as Condensers for Full-Field Transmission X-Ray Microscopes

Xuepeng Sun[1,2]*, Shangkun Shao*[1,2]*, Huiquan Li*[1,2]*, Xiaoyun Zhang*[1,2]*, Tianyu Yuan*[1,2]*, Fen Tao*[3] *and Tianxi Sun*[1,2]***

[1]Key Laboratory of Beam Technology of Ministry of Education, College of Nuclear Science and Technology, Beijing Normal University, Beijing, China, [2]Beijing Radiation Center, Beijing, China, [3]Zhangjiang Laboratory (SSRF, ZJLab), Shanghai Synchrotron Radiation Facility, Shanghai Advanced Research Institute, Chinese Academy of Science, Shanghai, China

Monocapillary x-ray lenses (MXRLs) are mostly used as condensers in full-field transmission x-ray microscopy (TXM) based on synchrotron radiation or laboratory x-ray tubes. The performance of the condenser has a significant impact on the imaging quality of the TXM. In this paper, a procedure for the characterization of the MXRL as a condenser is presented. The procedure mainly includes two parts: optical measurement and x-ray tests. From the test results of the characterization procedure, it can be seen that a relatively high-performance condenser can be screened out from a series of MXRLs drawn by an electric furnace. This is also fed back to the manufacturing process, and therefore, the technology of manufacturing the condenser can be gradually optimized. Moreover, the method of characterizing the performance of the condenser designed for synchrotron radiation TXM by laboratory x-ray tubes is proposed to be used in this procedure, which effectively reduces the manufacturing time of high-performance condensers for synchrotron radiation TXM.

Keywords: capillary condenser, zone plate, quality assessment, full-field transmission x-ray microscopy, optical measurement

Edited by:
Qiushi Huang,
Tongji University, China

Reviewed by:
P. S. Athiray,
University of Alabama in Huntsville, United States
Guibin Zan,
Stanford University, United States

****Correspondence:***
Tianxi Sun
stx@bnu.edu.cn

Specialty section:
This article was submitted to Optics and Photonics, a section of the journal Frontiers in Physics

Received: *24 November 2021*
Accepted: *08 April 2022*
Published: *04 May 2022*

Citation:
Sun X, Shao S, Li H, Zhang X, Yuan T, Tao F and Sun T (2022) A Procedure for the Characterization of Monocapillary X-Ray Lenses as Condensers for Full-Field Transmission X-Ray Microscopes. Front. Phys. 10:821549. doi: 10.3389/fphy.2022.821549

1 INTRODUCTION

Full-field transmission x-ray microscopy (TXM) is a powerful technique to observe the spatial structure of complex samples at nanoscale. TXM has a similar structure to visible light or electron microscopy. The resolution of TXM is superior to visible light microscopy because of the shorter wavelength of x-rays than visible light. Moreover, the powerful penetrating ability of x-rays enables TXM to nondestructively and three-dimensionally (3D) image complex structures compared to the either opaque to visible light microscopy or those that are too thick to be penetrated by electron microscopy. In the past decade, with the development of highly efficient x-ray optics and powerful x-ray sources, TXM working on the hard x-ray regime has been built at many synchrotron radiation facilities and in conventional laboratories using portable sources [1–9]. Besides, ZEISS in Germany offers commercial TXM, with a resolution down to 50 nm (ZEISS Xradia 800 Ultra). Because of its superior ability to nondestructively explore the internal structure of optically opaque solids with submicron resolution, TXM plays an important role in research in the fields of biology, medicine, minerals, and materials science [10–14].

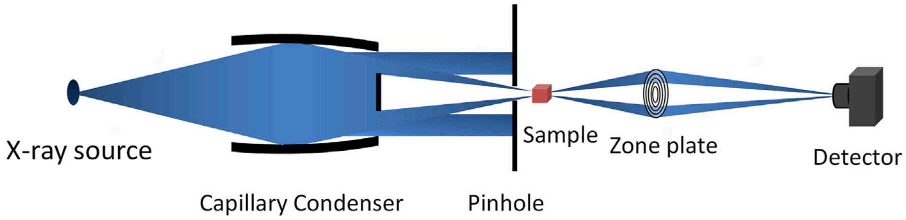

FIGURE 1 | Schematic diagram of the TXM system based on the capillary condenser.

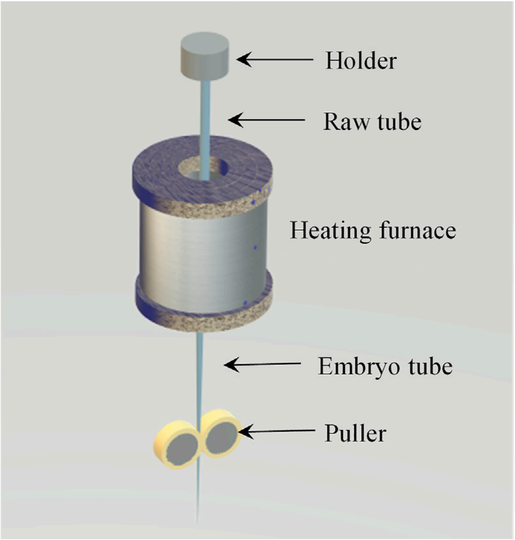

FIGURE 2 | Schematic diagram of the MXRL drawing using an optical fiber drawing machine.

The precision fabricated zone plate and the condenser are the key optical components of a TXM system. In the system, the zone plate works as an objective lens that receives the propagated image of the sample and produces a magnified image on a charge-coupled device (CCD) camera. TXM that has a zone plate as an objective lens needs a condenser to focus the x-ray beam onto the sample and increase the flux density while matching the numerical aperture (NA) with the zone plate [15]. So far, four main kinds of condenser optics for TXM have been reported in the studies: a zone plate, a multilayer mirror, a Kirkpatrick–Baez mirror, and a monocapillary x-ray lens (MXRL) [15–20]. The operating principle of the zone plate and the multilayer mirror confirms that they have a limited bandwidth, which is inconvenient for TXM to image at multiple wavelengths. In practice, to match the NA with the zone plate as an objective lens, the zone plate as a condenser is required to have a large diameter with a high number of zones and a small zone width, which is too difficult to manufacture, especially for hard x-rays. In addition, both types suffer from low efficiency, especially when used in TXM based on laboratory x-ray sources. Kirkpatrick–Baez mirrors and MXRLs based on total reflection are achromatic focusing optics. They have advantages such as being efficient, rugged, and achromatic, which is suitable for TXM systems. However, the illumination from the Kirkpatrick–Baez mirror is asymmetric, which generally generates inferior images when used in absorption contrast imaging and is not suitable for Zernike phase contrast imaging [21]. Besides the advantages of MXRLs mentioned above, they are symmetric, are easy to be aligned, and have a wide NA and bandwidth. This is clearly superior to other condensers used for TXM. In addition, MXRLs show good performance in focusing photons in the energy range of 5–25 keV. So far, a majority of tabletop and synchrotron hard x-ray TXM has chosen MXRL as the condenser. **Figure 1** shows the schematic diagram of the TXM system based on the capillary condenser.

Ellipsoidal or parabolic MXRLs used in tabletop and synchrotron TXM are drawn using an optical fiber drawing machine as shown in **Figure 2**. A straight raw glass tube with a fixed inner and outer diameter is placed in the heating furnace along its axle line, which ensures the raw glass tube is heated evenly in the furnace. The heating furnace is set at a certain temperature to maintain the glass tube in a softened state. The shape of the MXRL is formed by controlling the speed of the puller and holder, which is attached to a linear stepper motor and utilized to feed the raw tube into the heating furnace. The embryo tube that contains the desired MXRL takes shape between the heating furnace and the puller. To obtain a high-performance MXRL for TXM, characterizing the performance of the MXRL is an inevitable choice that can not only select the most appropriate MXRL as the condenser in the TXM system but also facilitate the parameter optimization of the optics during the capillary pulling process. The characterization procedure of the MXRL mainly includes optical measurement and x-ray tests. According to the previous studies [22], the optical measurement of the embryo tube provides the outer profile accurately, and the inner profile is calculated from the fixed ratio of the inner to outer profiles (the ID/OD ratio). However, there are some variations in the ID/OD ratio with regard to fabrication conditions, such as the capillary material, the temperature of the furnace, and the speed of the puller and holder. Therefore, optical measurement can only roughly assess the quality of the optics. In this paper, the measured characterization procedure of a certain designed MXRL as a condenser for TXM of the Shanghai Synchrotron Radiation Facility (SSRF) was presented. The MXRL was cut apart to measure the inner diameter so that a more accurate ID/OD ratio can be obtained. After cutting, the performance of the MXRL as a condenser was more intuitively tested using the x-ray source.

TABLE 1 | Main parameter of the designed MXRL.

Parameter	Value (mm)
Length	98
Input aperture	0.27
Output aperture	0.205
Major semiaxis	1,000
Minor semiaxis	0.437
Working distance	117

2 METHODS AND EXPERIMENT RESULTS

2.1 Optical Measurement

Table 1 lists the main parameters of the designed MXRL used as an example to demonstrate the condenser characterization procedure proposed in this study. In order to cut the designed MXRL from the embryo tube, a light microscope (LS-7030M, Keyence, Japan) with a motorized X stage as shown in **Figure 3** was used to measure the outer profile of the embryo tube. The detection precision and the diameter detectable range of the light microscope are ± 2 μm and 0.3–30 mm, respectively. The measurement step of the embryo tube is 200 μm.

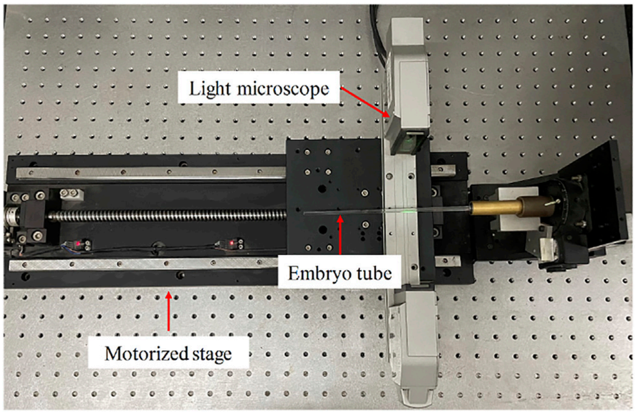

FIGURE 3 | Photograph of the optical test platform based on a light microscope.

Differently to the method used by Huang and Bilderback, in which the inner diameter (ID) is calculated by the constant ID/OD ratio of the embryo tube, varying ratios of OD/ID as shown in **Figure 4A** were used to infer the inner profile of the embryo tube [22]. In our manufacturing process, it was discovered that the OD/ID ratio of the embryo tube slightly varies with fabrication conditions, such as the glass tube material, glass tube diameter, temperature of the furnace, and speed of the holder. Therefore, to acquire an accurate inner profile, the OD/ID ratio of the embryo tube is needed to be measured before the MXRL drawing under specific conditions. To determine the OD/ID ratio of the embryo tube, the OD and ID of the embryo tube were measured using a micrometer and a high-powered digital microscope (VHX-500F, Keyence, Japan) after cutting at different positions. The designed MXRL was cut out referring to the inner profile of the embryo tube. **Figure 4B** presents the comparison of the measured and ideal inner profile of the designed MXRL, indicating that the measured curve of the inner profile is very close to the ideal one. To observe the deviation clearly, **Figures 4C and D** show the diameter error and straightness of the designed MXRL, respectively. The deviation in the diameter and the centerline of the designed MXRL as a condenser is < ±2 μm and < ±0.5 μm, respectively.

2.2 X-Ray Tests

2.2.1 NA of the MXRL as a Condenser

NA is an important parameter of the MXRL used as a condenser in the TXM system. NA match between the condenser and the objective zone plate is a prerequisite for the normal operation of TXM [15]. As for the condenser designed for the laboratory x-ray source, the NA of the ellipsoidal MXRL as a condenser can be easily measured by a series of far-field patterns captured at different distances from the exit of the condenser when the x-ray source was placed at the input focal spot of the ellipsoidal MXRL. However, due to the time limit of the synchrotron radiation, the NA of the condenser hardly directly tests in synchrotron radiation. In this study, we proposed using the microfocusing x-ray tube to measure the NA of the condenser used in synchrotron TXM. The major semiaxis of the MXRL designed as the condenser of synchrotron radiation TXM is usually much longer than the laboratory x-ray optical test platform. In practice, the NA of the condenser was measured with the x-ray source deviated from the input focal spot. As shown in **Figure 5**, the measured NA ($\theta^{'}$) for the x-ray source deviated from the input focal spot has a definite relationship with the designed NA (θ), which could be used to evaluate whether the NA of the newly drawn condenser meets the design. According to the total reflection of the x-ray transmitting in the condenser, we can know that the angle α is equal to β. From the geometric diagram shown in **Figure 5**, the following equations can be obtained:

$$\theta' = \theta + \beta \tag{1}$$

$$\alpha = \beta = \arctan\left(\frac{r_m}{d'_s + \frac{L}{2}}\right) - \arctan\left(\frac{r_m}{d_s + \frac{L}{2}}\right). \tag{2}$$

Therefore, the relationship of the NA of the condenser and the distance $d_s^{'}$ between the x-ray source and the condenser can be expressed as

$$\theta' = \theta + \arctan\left(\frac{r_m}{d'_s + \frac{L}{2}}\right) - \arctan\left(\frac{r_m}{d_s + \frac{L}{2}}\right). \tag{3}$$

Here, r_m is the inner radius at the middle of the condenser, $r_m = 0.2411$; L is the length of the condenser; and d_s is the input focal distance of the condenser. The corresponding measured working distance $d_f^{'}$ of the condenser can be expressed as

$$d_f^{'} = \frac{r_m}{\tan(\theta')} - \frac{L}{2}. \tag{4}$$

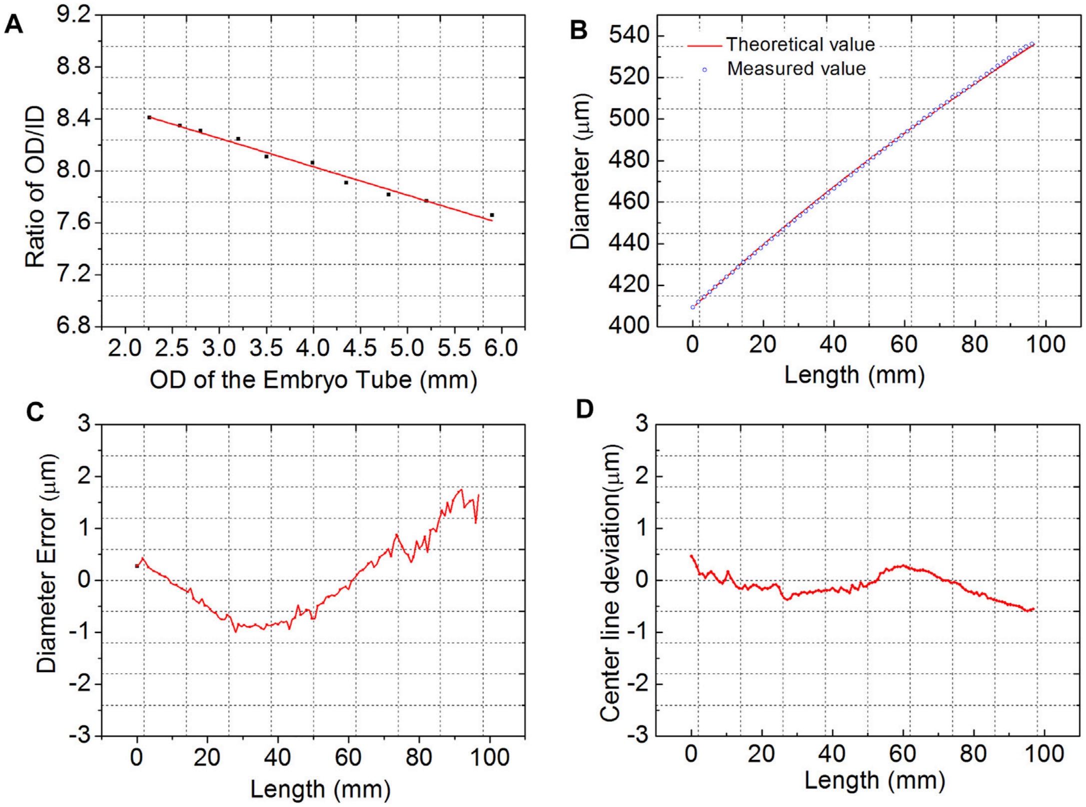

FIGURE 4 | Optical measurement results of an MXRL used as a condenser. **(A)** Ratio of OD/ID versus OD of the embryo tube. **(B)** Measured (dotted curve) and design ID (solid curve) profile of the MXRL. **(C)** Diameter error of the MXRL. **(D)** Center line deviation of the MXRL.

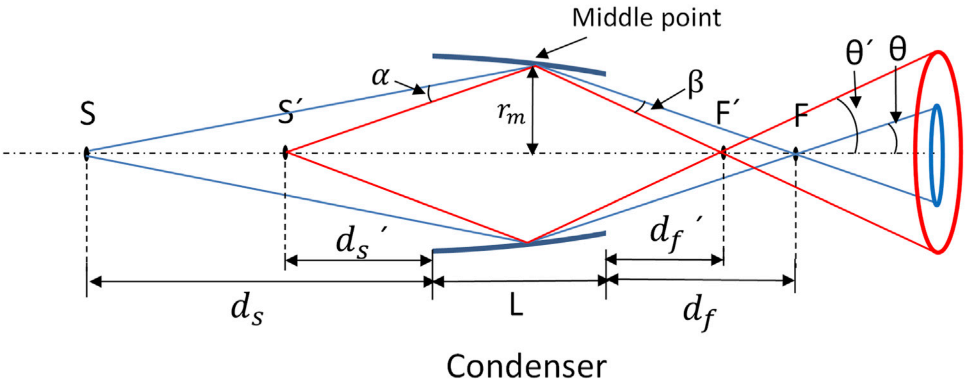

FIGURE 5 | Geometric sketch of the x-ray source deviating from the input focal spot of the ellipsoidal MXRL as a condenser for TXM (the blue line represents the transmitting light from the x-ray source to the input focal spot of the condenser, and the red line represents the transmitting light from the x-ray source deviating from the input focal spot).

A tungsten target micro-x-ray tube (L9631, Hamamatsu, Japan) with a focal diameter of 20 μm, operating at 30 kV and 800 μm, was employed in this experiment. An x-ray CCD (C11440-22CU, Hamamatsu, Japan) camera with a 13-μm pixel size was placed downstream of the condenser and was used to acquire the output far-field pattern of the condenser. The condenser was adjusted by a high-precision five-dimensional adjustment platform, which could ensure the lens can be accurately placed in a specific position. The photons from the x-ray tube are reflected from the inner surface of the condenser when the incident angle is smaller than the critical angle of total internal reflection and then are detected by the CCD camera. As shown in **Figure 5**, the incident angle and the location

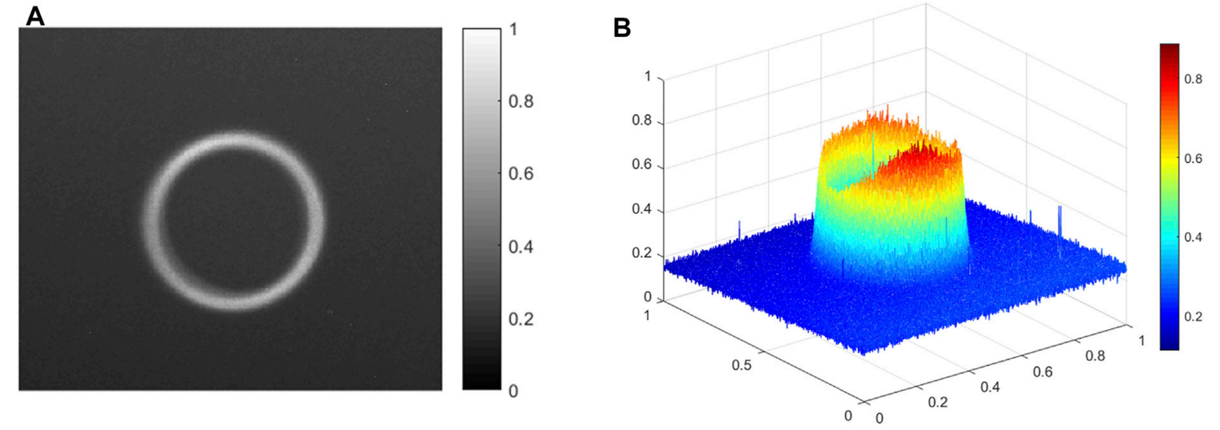

FIGURE 6 | (A) Far-field pattern of the condenser. **(B)** Intensity distribution of the far-field pattern.

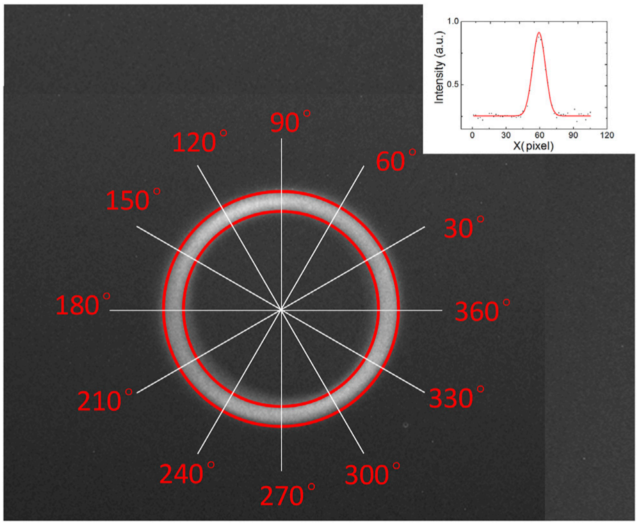

FIGURE 7 | Establishment of a polar coordinate system with the center of the far-field pattern of the condenser as the origin (the circle region with the red line is the ideal far-field pattern of the condenser, and the inset at the upper right shows the intensity profile along the white line).

where the photons are reflected are both determinants of the take-off angle. Thus, the far-field pattern of the condenser was produced. The distance between the MXRL and the micro-x-ray tube is about 80 cm. With the measured method mentioned above, the theoretical NA and the working distance (d_f) are 1.45 mrad and 117.0 mm, respectively, when the x-ray source is located in the input focal spot (S) of the condenser. After calculation, the theoretical NA and the working distance (d_f) are 1.60 mrad and 101.2 mm, respectively, when the condenser is placed 80 cm behind the micro-x-ray tube. The actual measured value of the NA and the working distance is 1.62 mrad and 102.5 mm, respectively. It is obvious that the measured value of the NA agrees well with the theoretical one, which proves the validity of the calculation method proposed in this paper.

2.2.2 Quality of the Far-Field Pattern of the Condenser

The ring shape region of the zone plate in the TXM system is an effective working area used to propagate and magnify the sample image to the CCD detector. In the TXM system, not only the NA of the condenser must match the zone plate but also the illuminating field of the hollow cone beam from the condenser must cover the effective working area of the zone plate. Therefore, the far-field pattern of the condenser is best when a standard ring shape is the effective working area of the condenser. Besides, the intensity distribution of the ring shape facula should be uniform to ensure the uniformity of the image field. The far-field pattern of the condenser mentioned above captured by the CCD detector placed 60 cm away from the condenser is shown in **Figure 6**. From the figure, we can intuitively observe the roundness and intensity uniformity of the ring shape facula of the condenser.

To quantitatively describe the suitability of the condenser and the zone plate, a polar coordinate system with the center of the far-field pattern of the condenser as the origin was established as shown in **Figure 7**. Three sets of data as shown in **Figure 8** show the quality of the far-field pattern of the condenser: intensity, proportion of the x-ray photons from the measured condenser irradiating on the theoretical region (the ring with the red line in **Figure 7**), and the ring width at different angles. The ring shape facula was divided into 12 30° parts . The uniformity of the intensity distribution of the ring shape facula is characterized by its standard deviation. In **Figure 8A**, the standard deviation of the intensity distribution of the ring shape facula is 0.0387, and the average value of the proportion of the x-ray photons from the measured condenser irradiating on the theoretical region is 91.525%. The standard deviation of “0.0387” indicates the degree to which the far-field pattern of the condenser deviates from the theoretical region, and the proportion of the x-ray photons shows that most photons transmitted from the MXRL can be employed for TXM. **Figure 8B** shows that the root mean square error of the ring width is 3.1 μm. The intensity distribution with the angle reflects the uniformity of the far-field pattern of the condenser. The higher the proportion of the output x-ray beam irradiating on the theoretical region, the higher the utilization rate of the output x-ray photons from the condenser.

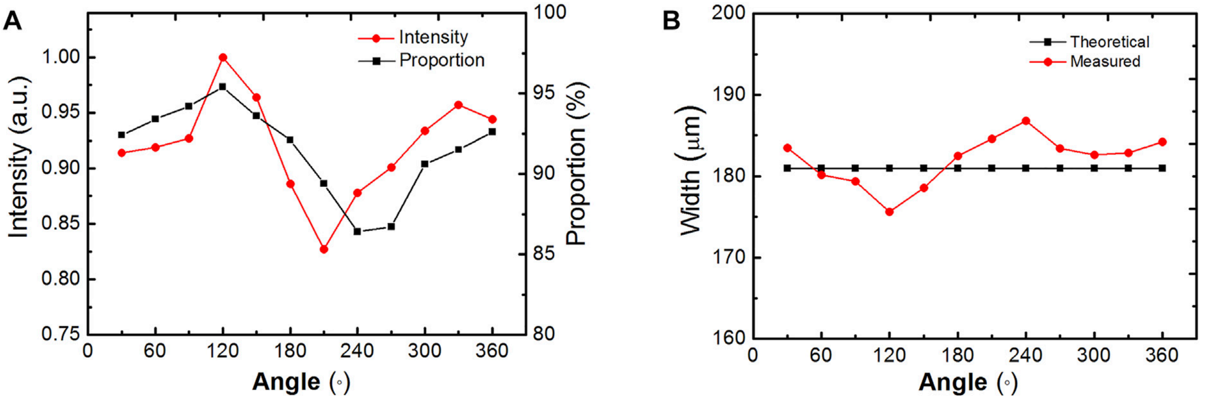

FIGURE 8 | (A) Intensity distribution with angle (red line) and proportion of the output x-ray beam irradiating on the theoretical region. **(B)** Annulus width of the ring shape facula from the condenser at different angles.

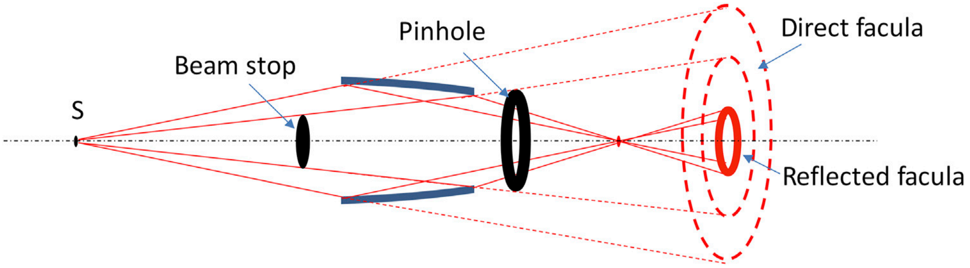

FIGURE 9 | Transmission efficiency of the condenser by the beam stop and pinhole.

2.2.3 Transmission Efficiency

The transmission efficiency of the MXRL used as a condenser is a significant parameter that influences the imaging efficiency of the TXM system. It is the ratio of all the reflected x-ray photons to the total incident photons intercepted by the condenser. In our experiment, the transmission efficiency of the condenser was measured by a beam stop and pinhole, as shown in **Figure 9**. With the assistance of the beam stop and pinhole, the incident x-ray beam can be regulated to only illuminate on the inner surface of the condenser. Using the CCD detector, a reflected and direct facula can be obtained with and without the condenser, respectively. Transmission efficiency can be calculated by dividing the intensity of the reflected and direct facula. The MXRL designed for the SSRF had a transmission efficiency of 81.4%, measured using the laboratory x-ray tube.

3 DISCUSSION

The performance of the condenser has a significant impact on the performance of the TXM system. The characterization procedure of the MXRL can not only pick out a relatively high-performance MXRL as the condenser in a TXM system but improve the optics manufacturing process according to the feedback of the measurement results. The characterization procedure of the MXRL designed for the condenser in the TXM system includes two parts: optical measurement and x-ray tests. The overall quality of the condenser can be inferred from the optical measurement results of the diameter error and centerline deviation of the condenser. Furthermore, according to the optical measurement results, we can adjust the drawing parameters of the optical fiber drawing machine to make the ID profile of the MXRL be more in line with the ideal one and cut the designed condenser in the proper position from the embryo tube. In the drawing process of the MXRL, the temperature of the heating furnace and the feeding speed of the holder remain unchanged, and the ellipsoidal ID profile of the MXRL is formed by changing the drawing speed. As shown in **Figure 10**, the ID profile deviates from the ideal one. For the measured ID profile of the MXRL greater and smaller than the design, as shown in **Figure 10**, we could correspondingly reduce and increase the drawing speed to correct the measured ID profile of the MXRL more close to the ideal profile in the next drawing procession.

The x-ray test with an x-ray source directly indicates the quality of the MXRL as a condenser. Imperfections in the far-field pattern of the condenser are mainly caused by the diameter error and centerline deviation, as mentioned above in the optical measurement. In the past research work, we have simulated that the inner surface imperfections of the condenser influence

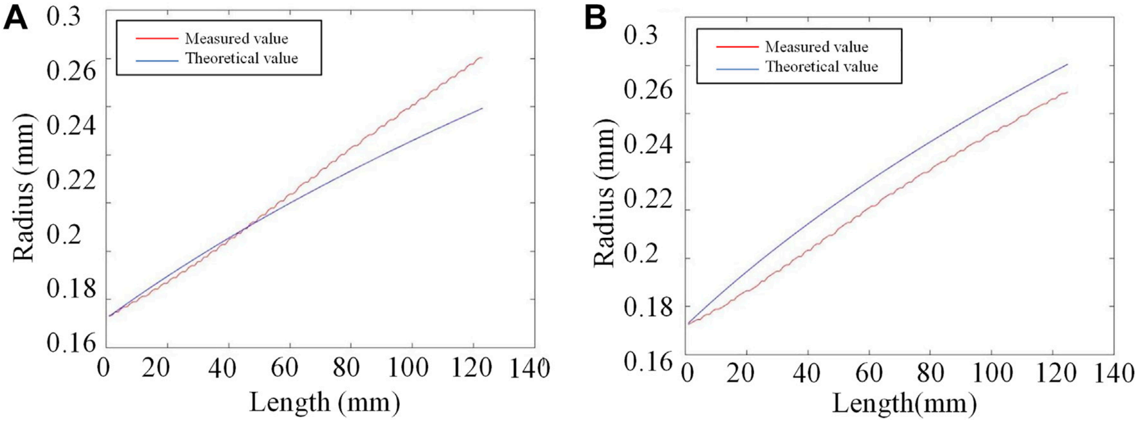

FIGURE 10 | ID profile of the embryo tube measured using a light microscope greater **(A)** and less **(B)** than the design

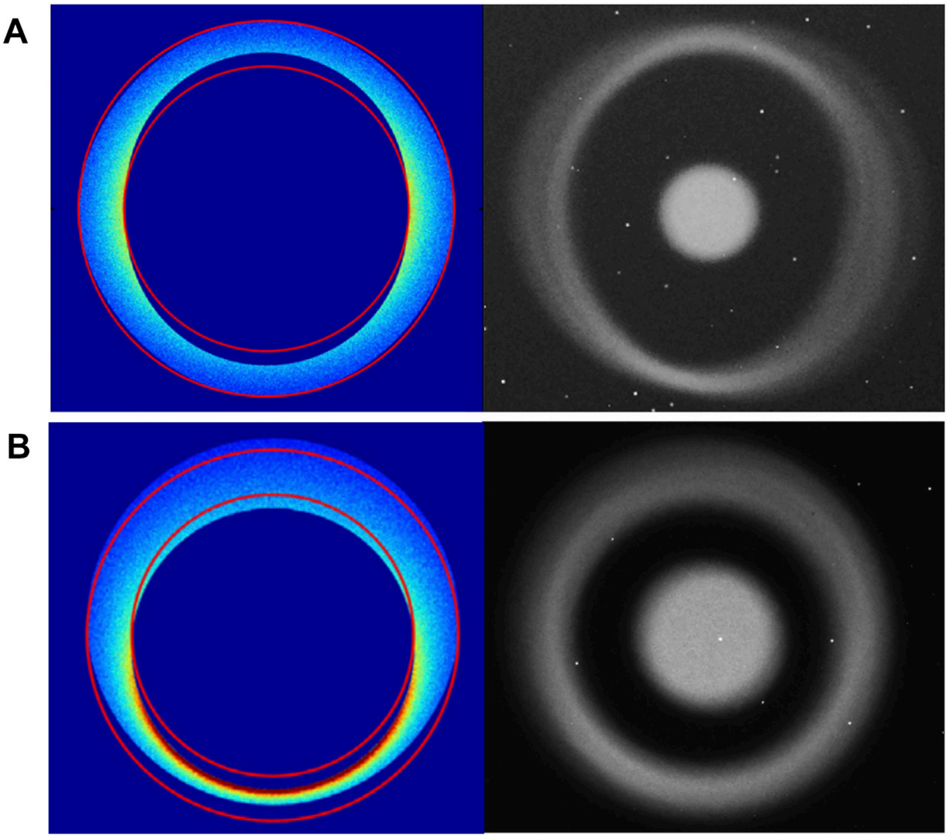

FIGURE 11 | Two main kinds of deformation of the condenser resulting in an imperfect far-field pattern. Simulated (left part) and measured (right part) distorted output facula of the condenser caused by elliptic deformation **(A)** and center line deviation **(B)** of the condenser (simulated figure cited from Ref. [23]).

its performance [23]. The imperfections of the inner surface of the condenser cause nonuniformity in the intensity and ring width of the far-field pattern, which greatly reduces condenser efficiency in the TXM system. **Figure 11** shows the simulated and measured deformation of the far-field pattern of the condenser caused by the elliptic deformation and the deviation in the centerline. In the manufacturing process, the main cause of condenser error can be inferred by analyzing the results of optical and x-ray tests. For instance, as shown in **Figure 11**, for the far-field pattern of the MXRL deformed by elliptic deformation and centerline deviation, we would optimize the manufacturing process by using high-quality glass tubes and rotating the embryo tube to ensure the tube is pulled evenly in the drawing process.

In addition, it should be noted that the characterization of the capillary condenser is related to the measuring condition, such as the energy of incident photons and the size of the x-ray source. Compared to monochromic beams from the synchrotron, the polychromic x-ray beams bring about changes in the intensity distribution of the far-field pattern of the condenser while the shape of the image is not affected. In addition, as the x-ray source size increases, the blurred area in the far-field pattern of the condenser and the NA are increasing, which can be calculated by geometrical optics [24].

4 CONCLUSION

In this study, the procedure for the characterization of the MXRL as a condenser in the TXM system was presented in detail. The procedure mainly includes optical measurement and x-ray tests. According to the results of the quality assessment procedure, we can not only screen out a high-quality MXRL that meets the design as a condenser of the TXM system but also find out the causes resulting in the mismatch between the condenser and the zone plate and then optimize the condenser manufacturing process. Besides, as for the x-ray test, we established a method that tests the condenser designed for synchrotron TXM using a laboratory x-ray source, which overcomes the limited access of the synchrotron source and accelerates the process of manufacturing high-performance condensers.

DATA AVAILABILITY STATEMENT

The original contributions presented in the study are included in the article/Supplementary Material, further inquiries can be directed to the corresponding author.

AUTHOR CONTRIBUTIONS

TS, XS, and SS developed the methodology, performed the experiments, analyzed the results, and wrote the article. HL, XZ, TY, and FT partially contributed toward implementing the conducted experiments.

FUNDING

This work was supported by the National Natural Science Foundation of China (Grant Nos 11675019 and 12105020) and the Project of Beijing Excellent Talents (2018400685627G334). This work was supported by the Bud project of the Beijing Academy of Science and Technology (BGS202106).

REFERENCES

1. Yuan Q, Zhang K, Hong Y, Huang W, Gao K, Wang Z, et al. A 30 Nm-Resolution Hard X-ray Microscope with X-ray Fluorescence Mapping Capability at BSRF. *J Synchrotron Radiat* (2012) 19:1021–8. doi:10.1107/S0909049512032852
2. Yin G-C, Tang M-T, Song Y-F, Chen F-R, Liang KS, Duewer FW, et al. Energy-tunable Transmission X-ray Microscope for Differential Contrast Imaging with Near 60nm Resolution Tomography. *Appl Phys Lett* (2006) 88:241115. doi:10.1063/1.2211300
3. Andrews JC, Brennan S, Patty C, Luening K, Pianetta P, Almeida E, et al. A High Resolution, Hard X-ray Bio-Imaging Facility at SSRL. *Synchrotron Radiat News* (2008) 21:17–26. doi:10.1080/08940880802123043
4. Chu YS, Yi JM, De Carlo F, Shen Q, Lee W-K, Wu HJ, et al. Hard-x-ray Microscopy with Fresnel Zone Plates Reaches 40nm Rayleigh Resolution. *Appl Phys Lett* (2008) 92:103119. doi:10.1063/1.2857476
5. Tian Y, Li W, Chen J, Liu L, Liu G, Tkachuk A, et al. High Resolution Hard X-ray Microscope on a Second Generation Synchrotron Source. *Rev Scientific Instr* (2008) 79:103708. doi:10.1063/1.3002484
6. Feser M, Duewer F, Wang S, Scott D, Lyon A, Yun W. 3-D X-ray Microscopy Using a Laboratory Source. *Microsc Microanal* (2004) 10:1036–7. doi:10.1017/S1431927604880292
7. Tkachuk A, Feser M, Cui H, Duewer F, Chang H, Yun W. High-resolution X-ray Tomography Using Laboratory Sources. In: *Developments in X-ray Tomography V*, 6318. San Diego: International Society for Optics and Photonics (2006). doi:10.1117/12.682383
8. Tkachuk A, Duewer F, Cui H, Feser M, Wang S, Yun W. X-ray Computed Tomography in Zernike Phase Contrast Mode at 8 keV with 50-nm Resolution Using Cu Rotating Anode X-ray Source. *Z Kristallogr* (2007) 222:650–5. doi:10.1524/zkri.2007.222.11.650
9. Zschech E, Löffler M, Krüger P, Gluch J, Kutukova K, Zgłobicka I, et al. Laboratory Computed X-Ray Tomography - A Nondestructive Technique for 3D Microstructure Analysis of Materials. *Prakt Metallogr* (2018) 55:539–55. doi:10.3139/147.110537
10. Andrews JC, Meirer F, Liu Y, Mester Z, Pianetta P. Transmission X-ray Microscopy for Full-Field Nano Imaging of Biomaterials. *Microsc Res Tech* (2011) 74:671–81. doi:10.1002/jemt.20907
11. Sun Y, Wang Y. Monitoring of Galvanic Replacement Reaction between Silver Nanowires and HAuCl4 by *In Situ* Transmission X-ray Microscopy. *Nano Lett* (2011) 11:4386–92. doi:10.1021/nl202538q
12. Chen J, Wu C, Tian J, Li W, Yu S, Tian Y. Three-dimensional Imaging of a Complex Concaved Cuboctahedron Copper Sulfide crystal by X-ray Nanotomography. *Appl Phys Lett* (2008) 92:233104. doi:10.1063/1.2943337
13. Hsu P-C, Chu Y, Yi J-M, Wang C-L, Wu S-R, Hwu Y, et al.Dynamical Growth Behavior of Copper Clusters during Electrodeposition. *Appl Phys Lett* (2010) 97:033101. doi:10.1063/1.3464550
14. Nelson GJ, Harris WM, Izzo JR, Jr, Grew KN, Chiu WKS, Chu YS, et al. Three-dimensional Mapping of Nickel Oxidation States Using Full Field X-ray Absorption Near Edge Structure Nanotomography. *Appl Phys Lett* (2011) 98:173109. doi:10.1063/1.3574774
15. Zeng X, Duewer F, Feser M, Huang C, Lyon A, Tkachuk A, et al. Ellipsoidal and Parabolic Glass Capillaries as Condensers for X-ray Microscopes. *Appl Opt* (2008) 47:2376–81. doi:10.1364/AO.47.002376
16. Stollberg H, Yulin S, Takman PAC, Hertz HM. High-reflectivity Cr/Sc Multilayer Condenser for Compact Soft X-ray Microscopy. *Rev Scientific Instr* (2006) 77:123101. doi:10.1063/1.2400665
17. Ge X, Wang ZL, Gao K, Wang DJ, Wu Z, Chen J, et al. Effects of the Condenser Fractal Zone Plate in a Transmission X-ray Microscope. *Radiat Phys Chem* (2014) 95:424–7. doi:10.1016/j.radphyschem.2013.03.026
18. Rau C, Crecea V, Richter CP, Peterson KM, Jemian PR, Neuhäusler U, et al. Imaging of Micro- and Nano-Structures with Hard X-Rays. *Micro Nano Lett* (2007) 2:1–5. doi:10.1049/mnl:20065060
19. Jiang B, Liu Z, Sun X, Sun T, Deng B, Li F, et al. Single Bounce Ellipsoidal Glass Monocapillary Condenser for X-ray Nano-Imaging. *Opt Commun* (2017) 398: 91–4. doi:10.1016/j.optcom.2017.04.035

20. Wang Y, Ren Y, Sun T, Tao F, Deng B, Xiao T. Single-bounce Ellipsoidal Capillary for X-ray Microscopes: Design and Measurements. *Microsc Microanal* (2018) 24:284–7. doi:10.1017/S1431927618013752
21. Zernike F. Phase Contrast, A New Method for the Microscopic Observation of Transparent Objects Part II. *Physica* (1942) 9:974–86. doi:10.1016/S0031-8914(42)80079-8
22. Huang R, Bilderback DH. Single-bounce Monocapillaries for Focusing Synchrotron Radiation: Modeling, Measurements and Theoretical Limits. *J Synchrotron Radiat* (2006) 13:74–84. doi:10.1107/S0909049505038562
23. Zhang S, Pan K, Wang Z, Zhou P, Liu Z, Sun X, et al. Simulation of Optical Properties of Ellipsoidal Monocapillary X-ray Optics with Inner-Surface Imperfections. *Opt Commun* (2021) 493:127028. doi:10.1016/j.optcom.2021.127028
24. Wang Y, Zhang X, Li Y, Sun X, Shao S, Liu Z, et al. Measuring the Average Slope Error of a Single-Bounce Ellipsoidal Glass Monocapillary X-Ray Condenser Based on an X-Ray Source with an Adjustable Source Size. *Nucl Instr Methods Phys Res Section A Acc Spectrometers Detectors Associated Eq* (2019) 934:36–40. doi:10.1016/j.nima.2019.04.049

Conflict of Interest: The authors declare that the research was conducted in the absence of any commercial or financial relationships that could be construed as a potential conflict of interest.

frontiers | Frontiers in Physics

ORIGINAL RESEARCH
published: 11 May 2022
doi: 10.3389/fphy.2022.880772

Measurement Uncertainty of Highly Asymmetrically Curved Elliptical Mirrors Using Multi-Pitch Slope Stitching Technique

Lei Huang[1]*, *Tianyi Wang*[1], *François Polack*[2], *Josep Nicolas*[3], *Kashmira Nakhoda*[1] and *Mourad Idir*[1]

[1]National Synchrotron Light Source II, Brookhaven National Laboratory, Upton, NY, United States, [2]Synchrotron SOLEIL, L'Orme des Merisiers, Gif-Sur-Yvette, France, [3]ALBA Synchrotron Light Source, Cerdanyola del Vallès, Spain

Soft X-ray off-axis elliptical mirrors bring new challenges for X-ray mirror metrology. These highly asymmetrically curved elliptical cylindrical mirrors with a total slope range >10 mrad are extremely challenging to measure. Their total slope range exceeds the measuring range of most angular sensors used for X-ray mirror inspection. To overcome this problem, it is possible to stitch partial slope data by measuring the mirror at different pitch angles (multi-pitch angles). By revisiting the theory of the multi-pitch Nano-accuracy Surface Profiler (NSP), we derive the sampling position error on the mirror surface as a function of the mirror height profile and the measurement error of the pitch rotation center. When measuring "extreme", highly asymmetrically curved, elliptical mirrors, the calculation of the mirror height profile with iterative reconstruction outperforms the classical "flat assumption" (i.e., assuming that the mirror sag is negligible). As demonstrated by our simulations, a proper tolerance evaluation on the measurement of pitch rotation center is needed to assess the measurement accuracy (systematic error) for these strongly aspherical mirrors using the multi-pitch NSP technique. Taking a real design of an "extreme" elliptical mirror as a case study, we conduct a Monte Carlo simulation to mimic the measurement and characterization process to analyze the impact of several error sources. With the measurement uncertainty of the pitch rotation center, the multi-pitch NSP measurement can estimate the grazing angle θ and the chief ray location x_o with their uncertainties, as well as the slope residuals.

Keywords: x-ray mirror, mirror metrology, multi-pitch NSP, mirror inspection, tolerance study

Edited by:
Qiushi Huang,
Tongji University, China

Reviewed by:
Shanyong Chen,
National University of Defense Technology, China
Maurizio Vannoni,
European X-Ray Free Electron Laser, Germany

Correspondence:
Lei Huang
huanglei0114@gmail.com

Specialty section:
This article was submitted to Optics and Photonics, a section of the journal Frontiers in Physics

Received: *21 February 2022*
Accepted: *20 April 2022*
Published: *11 May 2022*

Citation:
Huang L, Wang T, Polack F, Nicolas J, Nakhoda K and Idir M (2022) Measurement Uncertainty of Highly Asymmetrically Curved Elliptical Mirrors Using Multi-Pitch Slope Stitching Technique. Front. Phys. 10:880772. doi: 10.3389/fphy.2022.880772

INTRODUCTION

To match the evolution of the light source facilities (synchrotron radiation and free-electron lasers), X-ray optical elements must be at the diffraction limit to deliver the high-quality X-ray beam to the end station for scientific research. As a type of widely used X-ray optics, X-ray mirrors are required to be fabricated at the sub-100 nrad Root Mean Square (RMS) level for residual slope errors or the sub-nm RMS for residual height errors to preserve the wavefront of the incoming X-ray beam and produce a diffraction limited focal spot. Special dedicated optical metrology systems were developed to characterize such high-precision long rectangular X-ray mirrors. The Long Trace Profiler (LTP) [1] and the Nanometer Optical component measuring Machine (NOM) [2] are two classical optical slope profilers widely used in

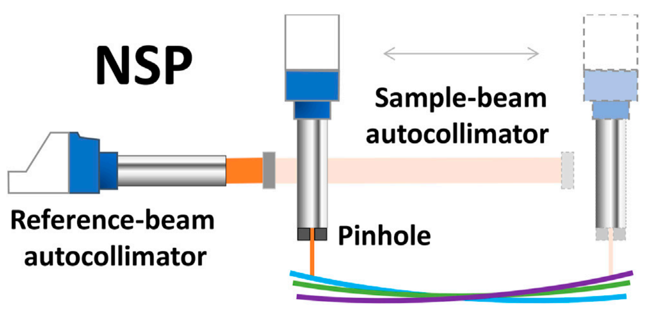

FIGURE 1 | The schematic diagram of the multi-pitch NSP setup.

the light source facilities all over the world [3–8]. With slightly different configuration, the Nano-accuracy Surface Profiler (NSP) [9] was developed with two separate beam arms. The sample beam arm (with the sample beam autocollimator) scans the test mirror surface (x-scan) with a fixed working distance, while the reference beam arm (with reference beam autocollimator) monitors the carriage wobble.

To meet the increasing need of the scientific research, more strongly curved focusing mirrors have been proposed for soft X-ray beamline. A soft X-ray nanoprobe will offer nano-imaging and spectroscopy tools non-destructive capabilities to study advanced materials using Nano ARPES and Nano RIXS experimental techniques [10]. To produce a diffraction-limited spot size for low energy (high λ), X-ray mirrors with high numerical aperture are required. These mirrors can have a total slope range larger than the current measuring range of the LTP/NOM/NSP (10 mrad). To overcome this problem, it is possible to stitch partial slope data recorded by measuring the mirror at different pitch angles. Based on this idea, Polack et al. proposed the Linearity Error Elimination Procedure (LEEP) algorithm [11]. This algorithm can reconstruct not only the mirror slope profile, but also the instrument error of the optical head at the same time. A modified LEEP algorithm was proposed for the NSP setup to reconstruct the instrument error of the sample-beam autocollimator [12]. The ambiguity in the algorithm was addressed by proposing several regularizations in the data acquisition and the algorithm constraints.

On the experimental side, when the LEEP algorithm or any other stitching algorithm is used where the pitch angle must be adjusted between different x-scans, the rotation center of the pitch needs to be known to a certain extent. The error on the position of the rotation center leads to pitch-dependent discrepancies of the sampling positions on the test mirror. For circular cylinders and shallow elliptical mirrors (few mrad total slope), the pitch rotation center does not need to be known with high accuracy, because the sampling position errors introduce little systematic slope errors in the final results (<10 nrad RMS). However, when highly curved and asymmetric elliptical mirrors must be measured, it becomes critical to know the pitch rotation center location with enough accuracy as this error leads to nonnegligible total systematic slope error contribution. In addition, the commonly applied “flat assumption” in the LEEP algorithm or the multi-pitch NSP technique as shown in **Figure 1**, assuming that the mirror sag is negligible, may no longer be valid when measuring such “extreme” ellipses.

In this work, the theory of the multi-pitch NSP technique is briefly reviewed, followed by the analysis of the influence of the pitch rotation center location with respect to the surface of the mirror under test. We propose a method to overcome the invalid “flat assumption” issue in the reconstruction of “extreme” ellipses. Then we focus on the measurement tolerance of the pitch rotation center location in the horizontal and the vertical directions. Series of simulations with different ellipse geometries are carried out to study the trend between the measurement tolerance of the pitch rotation center location and the curvature variation of the aspherical mirrors. We implement a Monte Carlo simulation with a real mirror design. Taking the uncertainty of the pitch rotation center measurement and the uncertainty of the angle measurement as two inputs, the multi-pitch NSP technique with the Monte Carlo simulation can give the slope residuals and an estimation of the grazing angle θ and the chief ray location x_o with their respective uncertainties.

THEORY OF THE MULTI-PITCH NSP TECHNIQUE

Based on the redundant dataset acquired from all the x-scans for different pitch angles, the multi-pitch NSP technique can simultaneously calculate the mirror surface slope, the instrument error of the sample-beam autocollimator, and the introduced pitch angles [12]. For simplicity, we define the origin of the world coordinate system $(x_w, z_w) = (0, 0)$ at the rotation center of the pitch angle α as shown in **Figure 2**. The direction of the x-translation in the NSP is defined as the direction of X_w axis in the world coordinate system, while the Z_w axis in the world coordinate system points upwards.

The center point of the x-scan range on the mirror surface is defined as the origin of the mirror coordinate system $(x_m, z_m) = (0, 0)$. The x-axis of the mirror coordinate system X_m is along its tangential direction and shares the same direction of X_w when the pitch angle $\alpha = 0$ as shown in **Figure 2A**, but they are different for other pitch angles as illustrated in **Figure 2B**. The Z_m axis of the mirror coordinate system is defined along the surface normal and pointing outwards the mirror surface. When the pitch angle $\alpha = 0$, the Z_m axis shares the same direction of Z_w. The coordinates of the pitch rotation center, expressed in the local frame of the mirror coordinate system, are given by $(x_m, z_m) = (x_c, z_c)$. It is illustrated in **Figure 2** that, for the same world abscissa x_w, the mirror abscissa x_m can be different at different pitch angles α. Moreover, as shown in **Figure 2B**, there is a clear difference in the x_m calculation with and without “flat assumption” which will be addressed in *Iterative Reconstruction*.

After a rotation in pitch with an angle α, one point (x_m, z_m) in mirror coordinate system can be transferred to the world coordinate system as

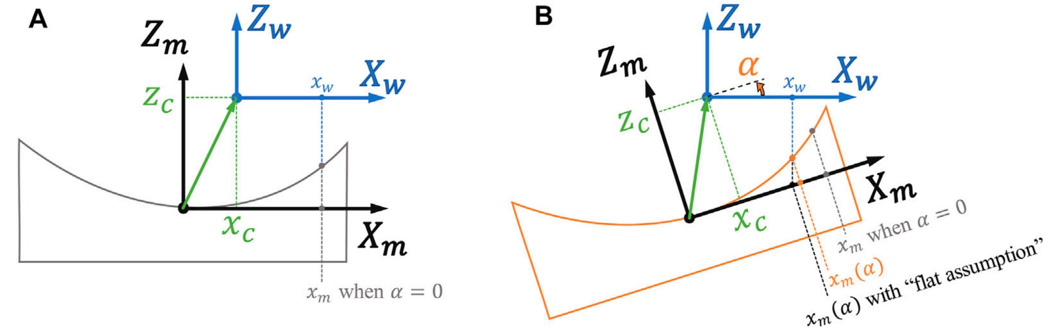

FIGURE 2 | The world coordinate system (X_w, Z_w) and the mirror coordinate system (X_m, Z_m) defined in the multi-pitch NSP technique when the pitch angle $\alpha = 0$ **(A)** and $\alpha \neq 0$ **(B)**.

$$\begin{bmatrix} x_w \\ z_w \end{bmatrix} = \begin{bmatrix} \cos\alpha & -\sin\alpha \\ \sin\alpha & \cos\alpha \end{bmatrix} \begin{bmatrix} x_m - x_c \\ z_m - z_c \end{bmatrix}. \tag{1}$$

The x position in world coordinate system can be calculated as

$$x_w = (x_m - x_c)\cos\alpha - (z_m - z_c)\sin\alpha. \tag{2}$$

For a particular measurement (x_c, z_c, and z_m are determinate), the x_m can be expressed as a function of x_w and α.

$$x_m(x_w, \alpha) = \frac{x_w + (z_m - z_c)\sin\alpha}{\cos\alpha} + x_c. \tag{3}$$

Under the n th actively-introduced pitch angle α_n, the angular signals captured in the sample-beam arm $s_n(x_w)$ and the reference-beam arm $r_n(x_w)$ can be explained by the mirror slope $m(x_m)$ at the actual sampling position x_m and the instrument error of the sample-beam autocollimator $e(s_n(x_w))$ at its current reading $s_n(x_w)$ as well as the uncorrelated additive random noise n_a.

$$\begin{aligned} s_n(x_w) + r_n(x_w) &\approx m(x_m(x_w, \alpha)) + e(s_n(x_w)) + \alpha_n \\ &+ n_a, \quad n \in [0, N-1]. \end{aligned} \tag{4}$$

Here the instrument error of the reference-beam autocollimator is ignored in our model, as the reference-beam angle $r_n(x_w)$ varies in a small range, usually <10 μrad, if an air-bearing translation stage is used.

The mirror slope $m(x_m)$ and the instrument error of sample-beam autocollimator $e(s_n(x_w))$ are then represented by two independent uniform cubic B-splines $\boldsymbol{M}(x_m)$ and $\boldsymbol{E}(s(x_w))$ as $m(x_m) = \boldsymbol{M}(x_m)\boldsymbol{c_m}$ and $e(s_n(x_w)) = \boldsymbol{E}(s_n(x_w))\,\boldsymbol{c_e}$, respectively, where $\boldsymbol{c_m}$ and $\boldsymbol{c_e}$ are column vectors containing the B-spline coefficients. Therefore, the mathematical model of multi-pitch NSP becomes

$$\begin{aligned} s_n(x_w) + r_n(x_w) &\approx \boldsymbol{M}(x_m(x_w, \alpha_n))\boldsymbol{c_m} + \boldsymbol{E}(s_n(x_w))\,\boldsymbol{c_e} + \alpha_n \\ &+ n_a, \quad n \in [0,\ N-1], \end{aligned} \tag{5}$$

Once the coefficients $\boldsymbol{c_m}$ and $\boldsymbol{c_e}$ are determined, we can reconstruct the mirror slope $m(x_m)$ and the sample-beam instrument error $e(s_n(x_w))$. The multi-pitch NSP algorithm is essentially to optimize the B-spline coefficients $\boldsymbol{c_m}$ and $\boldsymbol{c_e}$, and the pitch angles $\boldsymbol{\alpha} = [\alpha_0, \alpha_1, \ldots, \alpha_{N-1}]^\top$. In addition, to avoid the ambiguities in the optimized results, several regularizations are applied in the designs of the data acquisition and the constraints in algorithm [12]. Putting the constraints on the first pitch angle, the instrument error intercept, and the linear term, the optimization can be expressed as

$$\begin{aligned} \hat{\boldsymbol{c}}_{\boldsymbol{m}}, \hat{\boldsymbol{c}}_{\boldsymbol{e}}, \hat{\boldsymbol{\alpha}} = \underset{\boldsymbol{c_m},\, \boldsymbol{c_e},\, \boldsymbol{\alpha}}{\arg\min} \sum_{n=0}^{N-1} \sum_{x_w} &(s_n(x_w) + r_n(x_w) - \boldsymbol{M}(x_m(x_w, \alpha_n))\boldsymbol{c_m} - \boldsymbol{E}(s_n(x_w))\boldsymbol{c_e} - \alpha_n)^2 \\ s.t. \qquad \alpha_0 &= 0, \\ \boldsymbol{E}(0)\boldsymbol{c_e} &= 0, \\ \boldsymbol{s}^\top \boldsymbol{E}(\boldsymbol{s})\boldsymbol{c_e} &= 0. \end{aligned} \tag{6}$$

where the first pitch angle α_0 is constrained to 0. When the slope signal $s = 0$, the instrument error intercept is constrained as $e(0) = \boldsymbol{E}(0)\,\boldsymbol{c_e} = 0$. If we fit the instrument error $e(\boldsymbol{s})$ up to the linear terms, we have $e(\boldsymbol{s}) = \boldsymbol{E}(\boldsymbol{s})\,\boldsymbol{c_e} \triangleq e(0) + \varepsilon\boldsymbol{s}$, where $\boldsymbol{s}$ is the column vector of all slope sample values, the symbol $\triangleq$ stands for equal in a least squares sense. and ε is the linear term coefficient. Since we have constrained the instrument error intercept $e(0) = 0$, we have $\boldsymbol{E}(\boldsymbol{s})\,\boldsymbol{c_e} \triangleq \varepsilon\boldsymbol{s}$. As the third constraint, the linear term coefficient ε is also constrained to 0, so we have $\varepsilon = (\boldsymbol{s}^\top\boldsymbol{s})^{-1}\boldsymbol{s}^\top\boldsymbol{E}(\boldsymbol{s})\boldsymbol{c_e} = 0$. Because $\boldsymbol{s}^\top\boldsymbol{s} = |\boldsymbol{s}|^2 \neq 0$ is a nonzero scalar value, this constraint is simplified as $\boldsymbol{s}^\top\,\boldsymbol{E}(\boldsymbol{s})\,\boldsymbol{c_e} = 0$.

One thing to highlight is that nonuniform pitch steps $\Delta\alpha_n$ are necessary in data acquisition to avoid the periodic errors in the optimization results. Technical details on the ambiguities and the regularization can be found in Ref. [12] with more simulations and discussions.

To calculate the sampling position $x_m(x_w, \alpha_n)$ in the mirror coordinate system from the NSP x-scanning position x_w and pitch-scanning angle α by **Eq. 3**, we need to know the profile of the mirror height z_m and where the pitch rotation center (x_c, z_c) is in the mirror coordinate system. In the following sections, we are discussing the necessary accuracy of these different values.

THEORETICAL ANALYSIS OF THE SAMPLING POSITION ERROR AT DIFFERENT PITCH ANGLES CONSIDERING THE MIRROR HEIGHT PROFILE AND THE MEASUREMENT ERROR OF THE PITCH ROTATION CENTER LOCATION

The pitch rotation center (x_c, z_c) can be determined using additional metrology instruments. The measurement error of the pitch rotation center can be expressed as $e_{x_c} = \hat{x}_c - x_c$, and $e_{z_c} = \hat{z}_c - z_c$, where $(\hat{x}_c, \hat{z}_c)$ is the measured pitch rotation center. If the estimated mirror height profile is symbolized as $\hat{z}_m$, the estimation error is $e_{z_m} = \hat{z}_m - z_m$. In a real measurement, the dwell position of the x-stage $\hat{x}_w$ in the scans are defined as

$$\hat{x}_w = (x_m - \hat{x}_c)\cos\alpha - (\hat{z}_m - z_c)\sin\alpha. \tag{7}$$

If we have a measurement error of e_{x_c} when determining x_c, then the true dwell position x_w is

$$x_w = \hat{x}_w + e_{x_c} = \hat{x}_w + \hat{x}_c - x_c. \tag{8}$$

Based on **Eq. 3**, the estimated sampling position on the mirror $\hat{x}_m$ is

$$\hat{x}_m = \frac{\hat{x}_w + (\hat{z}_m - \hat{z}_c)\sin\alpha}{\cos\alpha} + \hat{x}_c, \tag{9}$$

And the true sampling position x_m is

$$x_m = \frac{x_w + (z_m - z_c)\sin\alpha}{\cos\alpha} + x_c. \tag{10}$$

The sampling position error $e_{x_m} = \hat{x}_m - x_m$ in the mirror coordinate system is

$$e_{x_m} = \hat{x}_m - x_m = \frac{(\hat{x}_w + (\hat{z}_m - \hat{z}_c)\sin\alpha)}{\cos\alpha} - \frac{(\hat{x}_w + \hat{x}_c - x_c + (z_m - z_c)\sin\alpha)}{\cos\alpha} + \hat{x}_c - x_c. \tag{11}$$

With some simplifications, it becomes

$$e_{x_m} = [(\hat{z}_m - z_m) - (\hat{z}_c - z_c)]\tan\alpha - (\hat{x}_c - x_c)\frac{1 - \cos\alpha}{\cos\alpha}. \tag{12}$$

Finally, we have the sampling position error as

$$e_{x_m} \approx e_{z_m}\alpha - e_{z_c}\alpha - \frac{e_{x_c}\alpha^2}{2}. \tag{13}$$

Considering the pitch angle $\alpha \ll 1$ rad, the error e_{z_c} will contribute a sampling position error of $-e_{z_c}\alpha$ in **Eq. 13**, while e_{x_c} only gives $-e_{x_c}\alpha^2/2$ error on x_m. It means that the error e_{z_c} has more impact on the multi-pitch NSP results than the error e_{x_c}.

By using a simple measurement tool, such as a metric ruler, and the mechanical tolerances of the pitch rotation system, it is not difficult to determine the pitch rotation center location with a few mm accuracy. For a circular cylinder, this level of uncertainty is enough. The slope profile of a circular cylinder is linear with x_m. In this case, the reconstruction is not sensitive to the measurement error e_{z_c}, because the slope error with a constant sampling error $-e_{z_c}\alpha_n$ at the n th pitch α_n due to e_{z_c} in **Eq. 13** will almost be equivalent to a slope offset on this linear slope profile. This slope offset will be treated as a pitch offset and will not affect the slope result by using the reconstruction algorithm. However, if the test mirror become strongly aspherical, the tolerance of the measurement on the pitch rotation center location becomes tighter, especially for the vertical distance z_c. Since the slope profile of an aspherical mirror has nonlinear terms, the sampling error e_{x_m} will lead to slope errors from these nonlinear terms. This becomes an important error source of the reconstruction in the multi-pitch NSP technique. A tolerance value is needed to control this type of error in the reconstruction result.

For simplicity, the mirror height profile z_m is usually assumed as a flat surface, *i.e.,* $\hat{z}_m = 0$. This “flat assumption” can be used when the mirror sag is much smaller than the tolerance of e_{z_c}. However, if the tolerance for e_{z_c} starts to be comparable to the mirror sag, its contribution $e_{z_m}\alpha$ to the sampling position error e_{x_m} in **Eq. 13** cannot be ignored and this will severely affect the reconstruction accuracy. A better estimate of the mirror height profile z_m is necessary. Two options can be used: the known mirror shape parameters or an iterative reconstruction with an initial guess.

Simulation Study on Multi-Pitch NSP With “Extreme” Ellipses

To study the influence of e_{z_m}, e_{x_c}, and e_{z_c} on the reconstruction results we have simulated the multi-pitch NSP data acquisition process as illustrated in **Figure 3**. This simulation features random variations of the pitch angles, the sample-beam instrument error that is an additive random noise n_a, and the measurement errors of e_{x_c} and e_{z_c}.

Descriptions of the Multi-Pitch NSP Simulations

In our simulations, as shown in **Figure 3A**, we used a default ellipse with the following parameters: the source distance p = 30 m, the image distance q = 0.3 m, the grazing angle θ = 30 mrad, and the tangential mirror length L = 0.3 m (total slope = 18.07 mrad). The mirror default parameters will be modified to make different comparisons.

To avoid the known periodic errors in the reconstruction [12], pitch steps with small random variations are implemented. For simplicity as shown in **Figure 3B**, we choose the average pitch step $\overline{\Delta\alpha}$ = 0.2 mrad and the standard deviation of the random variation on the pitch step is 30 μrad. The starting and ending pitch angles are determined by the slope range of the test mirror. The whole multi-pitch scan starts and finishes at angle values within (−1, 1) mrad at the two ends of the scanning range as shown in **Figure 3D**. The slope measuring range is set to be ± 5 mrad like the sample-beam autocollimator installed in our NSP instrument.

The instrument error used in the simulation shown in **Figure 3C** is a reconstruction of the instrument error from a real multi-pitch NSP experiment [12]. The measurement error of the pitch rotation center e_{x_c} and e_{z_c} are also considered in the data acquisition when calculating the sampling position on the mirror x_m. We add the normally distributed random angular noises n_a

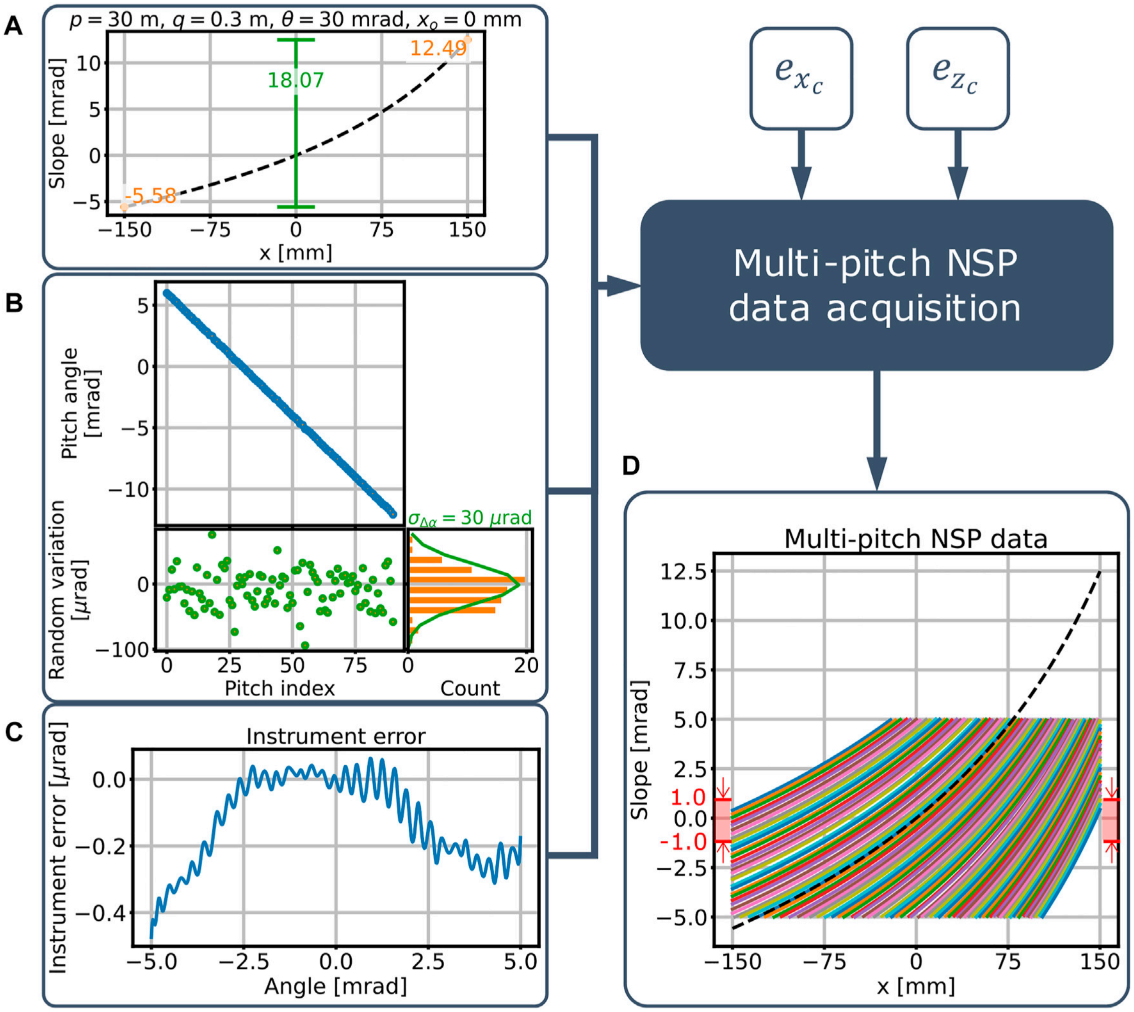

FIGURE 3 | The simulation of the multi-pitch NSP dataset. **(A)** the tangential slope of the elliptical cylinder with the default parameters, **(B)** the pitch angle and its random variations in step, **(C)** the instrument error of sample-beam autocollimator from a real multi-pitch NSP measurement, and **(D)** the simulated multi-pitch NSP data with the dashed curve showing the whole slope profile of the test mirror.

with a standard deviation σ_{n_a} = 70 nrad, which is a typical value based on our real NSP measurement. Finally, the multi-pitch NSP data is simulated as shown in **Figure 3D**.

Target Ellipse Fitting

For the characterization of synchrotron mirrors, the target ellipse fitting on slope is usually implemented with p, q, and θ fixed and the chief ray position x_o and the tilt (the slope bias) optimized. But in this work focusing on the extreme" ellipses, we include the grazing angle θ into the optimization with the following considerations:

1) The source and image distance values p and q are usually more constrained in most applications.
2) By changing the grazing angle θ with $\Delta\theta$, the corresponding focus displacement will be $2q\Delta\theta$. The q value for an "extreme" ellipse is commonly much shorter comparing to a "relaxed" ellipse. With the same restrict on the focus displacement, the tolerance of θ becomes larger when fit an "extreme" ellipse.

Therefore, we fit the reconstructed slope to the best ellipse with fixed p and q, while θ, x_o, and the tilt are optimized. As a fitting result, we can get the best fitted θ and x_o with their confidence intervals, and the associated slope residuals.

Iterative Reconstruction

Our first example is to demonstrate that the "flat assumption" ($\hat{z}_m = 0$) does not work for the ellipse with the default parameters: p = 30 m, q = 0.3 m, θ = 30 mrad, and L = 0.3 m (mirror sag = 777 μm), but it works well for some more "relaxed" ellipses (for example with the q = 0.6 m (mirror sag = 328 μm) as illustrated in **Figure 4A**). For this purpose, the measurement error of the pitch rotation center is set as $e_{x_c} = 0$ and $e_{z_c} = 0$. In this case, theoretically we should reconstruct the

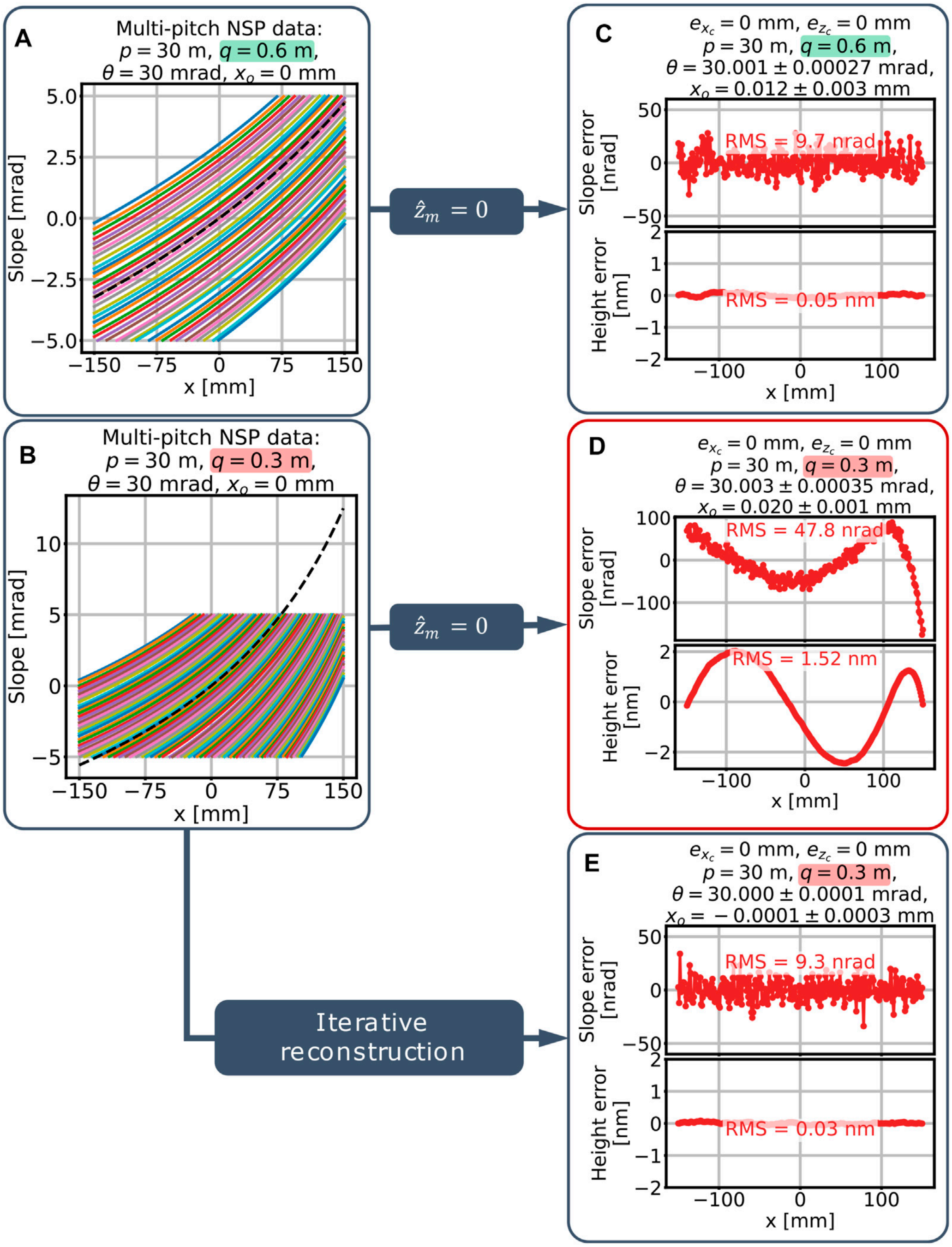

FIGURE 4 | The "flat assumption" ($\hat{z}_m = 0$) does not always work when reconstructing the "extreme" ellipse in multi-pitch NSP. It is demonstrated with the simulated multi-pitch NSP dataset for **(A)** a "relaxed" ellipse with $p = 30$ m, $q = 0.6$ m, $\theta = 30$ mrad (mirror sag = 328 μm), **(B)** the default ellipse with $p = 30$ m, $q = 0.3$ m, $\theta = 30$ mrad (mirror sag = 777 μm). By optimizing θ and x_o, the best fitting results of **(C)** the "relaxed ellipse" with the "flat assumption", **(D)** the default ellipse with flat assumption, and **(E)** the default ellipse with the proposed iterative reconstruction.

mirror slope "perfectly" with only the algorithm error and the random errors due to the slope noise.

However, as demonstrated in **Figure 4**, the "flat assumption" does not always give a perfect reconstruction. For the more "relaxed" ellipse with $q = 0.6$ m in **Figure 4A**, the reconstruction assuming $\hat{z}_m = 0$ ends up with an acceptable fitting result in **Figure 4C**: small slope residuals (due to the redundancy, the RMS of the slope residuals is much less than the standard deviation of the slope noises), about only 1 μrad grazing angle change, and 9 μm x_o adjustment. By contrast, the reconstruction error becomes much larger for a more "extreme" elliptical mirror in **Figure 4B** using the "flat

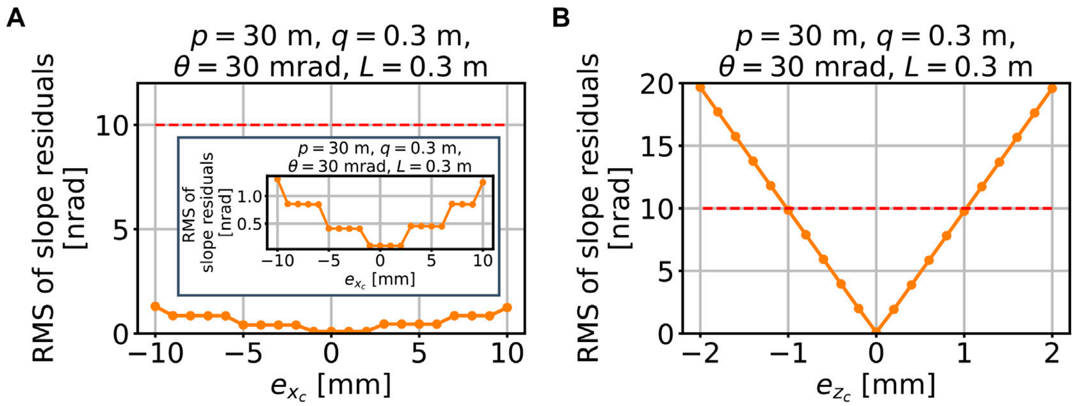

FIGURE 5 | Simulation with the default ellipse demonstrates the tolerance of e_{z_c} is much tighter than that of e_{x_c}:**(A)** the slope residuals due to e_{x_c} less than 10 nrad RMS within ± 10 mm range. **(B)** the slope residuals due to e_{z_c} across the red dash line (10 nrad RMS threshold) at $e_{z_c} \approx \pm$ 1 mm for this ellipse.

assumption" ($\hat{z}_m = 0$). As shown in **Figure 4D**, even after the best fit adjusting θ and x_o with 3 µrad and 20 µm, respectively, we still have more than 40 nrad RMS slope residuals giving about 1.5 nm RMS residuals in height as a systematic error from the metrology instrument. This is dominated by the algorithm error, which is too large for the X-ray mirror characterization. Therefore, the "flat assumption" ($\hat{z}_m = 0$) cannot always provide correct results even if we have no measurement errors on the pitch rotation center $e_{x_c} = 0$ and $e_{z_c} = 0$.

To measure "extreme" elliptical mirrors, we need to consider the mirror height profile $\hat{z}_m$. To solve this problem, we propose to use the "flat assumption" to get a reconstructed mirror slope first and then integrate the obtained slope to get the mirror height profile. This mirror height profile is then used as our estimation for $\hat{z}_m$ to recalculate the slope with the multi-pitch NSP approach. This iterative reconstruction process usually needs only one iteration to give a satisfactory result as shown in **Figure 4E**.

Using this approach, the $\hat{z}_m$ estimation issue is resolved for "extreme" elliptical mirrors. Since many of the mirrors in this study are extremely "extreme" ellipses which cannot be assumed as "flat", we apply the proposed iterative reconstruction method by default to enable the following study on the tolerance of the pitch rotation center location errors e_{x_c} and e_{z_c} for different elliptical mirrors.

SIMULATION STUDY ON THE MEASUREMENT TOLERANCE OF THE PITCH ROTATION CENTER

To conduct a tolerance study, we need to set a threshold. Here we set the threshold on the systematic slope error contributed from e_{x_c} and e_{z_c}. If 100 nrad slope accuracy is expected, the systematic slope error contribution from e_{x_c} and e_{z_c} should be less than 10 nrad RMS.

The error contribution due to e_{x_c} and e_{z_c} is isolated by setting the additive random noise on slope in the model to zero. Therefore, by meeting the reconstruction error <10 nrad RMS on the slope residuals, we can give a tolerance to the pitch rotation center error e_{x_c} and e_{z_c}.

Default Ellipse Case and Influence of Shape Parameters

Here we take the default ellipse ($p =$ 30 m, $q =$ 0.3 m, $\theta =$ 30 mrad, and $L =$ 0.3 m) as our sample mirror. When the measurement errors e_{x_c} changes from −10 to 10 mm, we can see in **Figure 5A** that the slope residuals is less than 10 nrad RMS (the red dash line in **Figure 5**) after θ and x_o optimization, so the tolerance of e_{x_c} is obviously much larger than ± 10 mm. It is easy to meet this tolerance requirement.

From **Figure 5B**, we can see that only when the measurement errors on the vertical distance e_{z_c} changes within ± 1 mm, after θ and x_o are optimized, the RMS value of the slope residuals are smaller than 10 nrad.

Following **Eq. 13** and **Figure 5**, the tolerance of e_{x_c} is much larger than the tolerance of e_{z_c} and it is easier to measure x_c with the required accuracy in practice. For this reason, we will focus on the tolerance of e_{z_c} in the following study.

Starting with the default ellipse parameters, we then modify one of the parameters q, θ, and L within a certain range while the others are maintained at their default values. We can then study the tolerance values of e_{z_c} with different ellipse geometries. First, we change the image distance q from 0.2 to 0.6 m with 0.1 m step, and the corresponding tolerance values of e_{z_c} are shown in **Figure 6A**. Then, we vary the grazing angle θ from 10 mrad up to 40 mrad with 5 mrad step and the tolerance values of e_{z_c} are shown in **Figure 6B**. Finally, the mirror length L is changed from 0.15 to 0.4 m with 0.05 m step. The tolerance values of e_{z_c} are shown in **Figure 6C**.

The results in **Figure 6** clearly reveal that the more "extreme" are the ellipses, with shorter image distance q, larger grazing angle θ, or longer optical length L, the tighter are the tolerance values of e_{z_c} (in orange in **Figure 6**). Therefore, measuring "extreme" ellipses using the multi-pitch NSP technique brings new

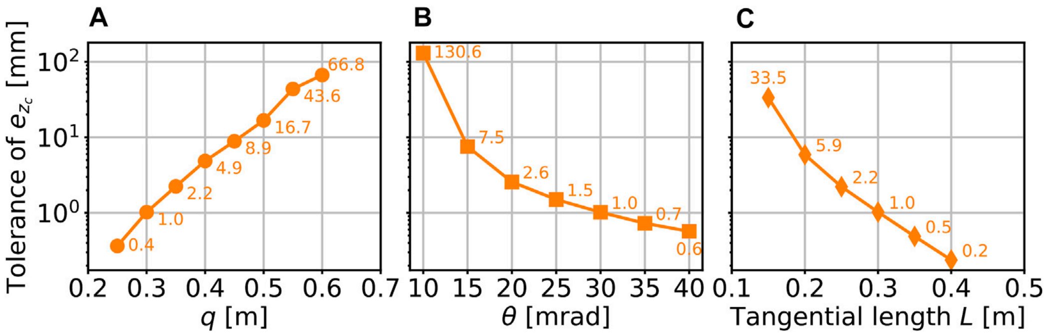

FIGURE 6 | Tolerance of e_{z_c} becomes tighter when the ellipse becomes more "extreme". From the default ellipse, change one parameter at a time: **(A)** the q value, **(B)** the θ value, **(C)** the length of the optical area.

TABLE 1 | Parameters of the two elliptical cylindrical mirrors.

Parameters	M1	M2
Object distance $\boldsymbol{p}$	28.176 m	28.167 m
Image distance $\boldsymbol{q}$	0.324 m	0.333 m
Grazing angle $\boldsymbol{\theta}$	1.76° ≈30.7178 mrad	5.13° ≈89.5354 mrad
Length of the optical area $\boldsymbol{L}$	290 mm	310 mm
Chief ray location $\boldsymbol{x_o}$	16 mm	17 mm

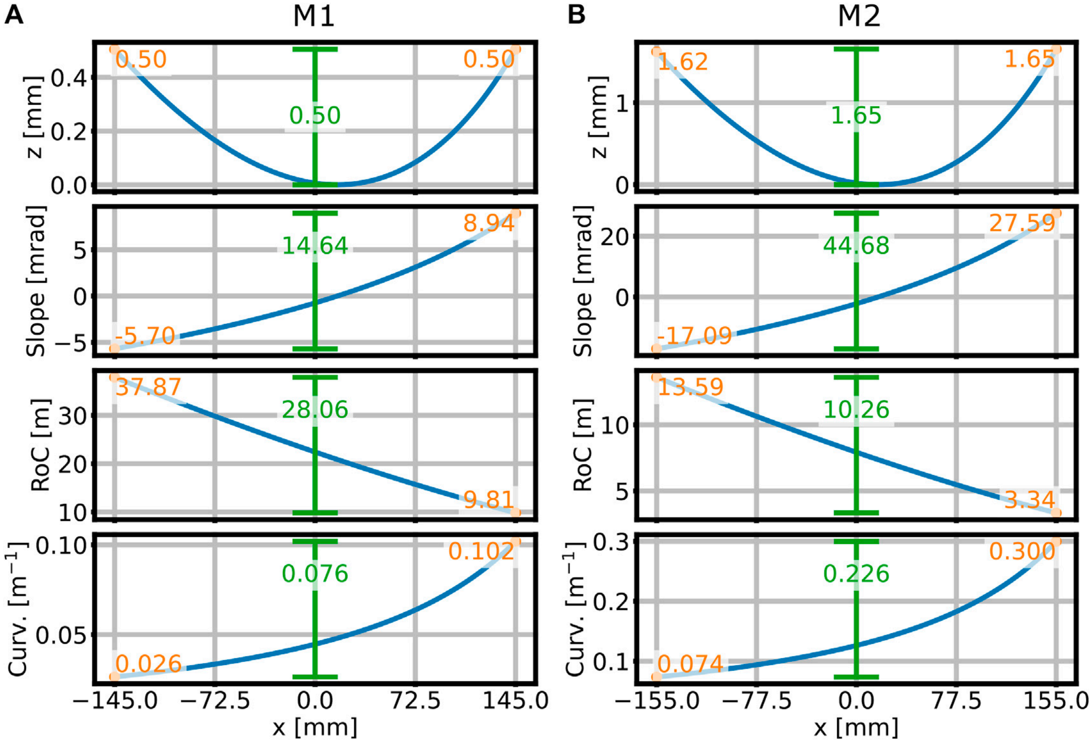

FIGURE 7 | The height, slope, RoC, and curvature profiles of M1 on the **(A)** and M2 on the **(B)**.

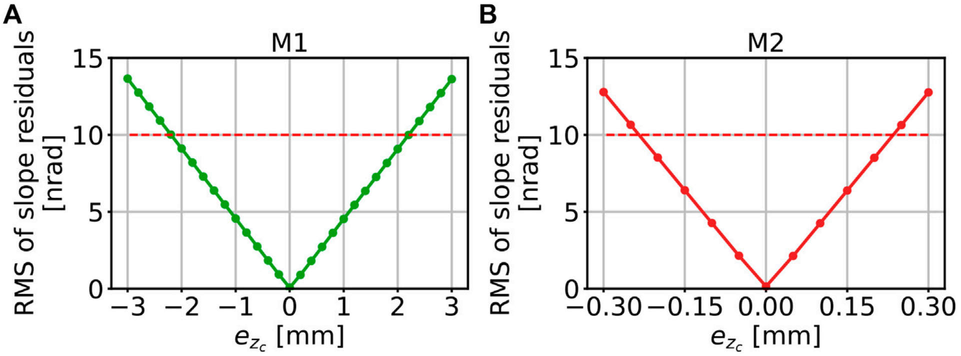

FIGURE 8 | The RMS value of the slope residuals varies along the measurement error of the vertical distance e_{z_c} for the M1 on the **(A)** and the M2 on the **(B)**.

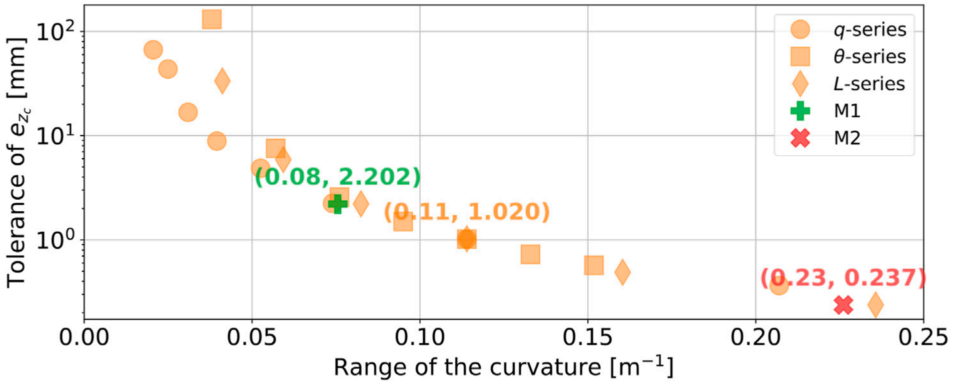

FIGURE 9 | The e_{z_c} tolerance values versus the curvature variation ranges of the ellipses of *q*-series, *θ*-series, *L*-series, M1, and M2. The tolerance of the e_{z_c} generally gets tighter when a mirror with a larger curvature range is under test.

challenges on the z_c measurement. In the next section, we present some results of the e_{z_c} tolerance calculations for two real "extreme" elliptical mirrors from an actual beamline optical design.

Two Ellipses From Beamline Optical Designs

The parameters of two elliptical cylindrical mirrors are listed in **Table 1**. These two mirrors are taken from two different sets of Kirkpatrick-Baez mirror systems proposed for the NSLS-II ARI beamlines.

To give a better description of these ellipse parameters, the height, slope, Radius of Curvature (RoC), and curvature variations of M1 and M2 are plotted in **Figure 7**. For M1, the mirror sag is about 0.5 mm, and its total slope range is almost 15 mrad, which is beyond the 10-mrad angular measuring range of the sampling-beam autocollimator in the NSP instrument. It is therefore necessary to change the pitch angle to measure the whole tangential profile of M1. Compared to M1, M2 is even more "extreme". The mirror sag is 1.65 mm and the total slope range is about 45 mrad.

These mirrors are intended to focus the incoming X-ray beam to a diffraction limited spot size at 1 keV and 250 eV for M1 and M2, respectively (the diffraction limited spot size of about 37 and 72.6 nm for M1 and M2). To satisfy the Maréchal criterion, the height error of the diffraction limited mirror should be less than $\lambda/(28\cdot\theta)$. This means that the mirror height error must be in the order of 1.16 nm RMS and 1.98 nm RMS for M1 and M2, respectively.

In this study, we disregard the RoC limit by the sample-beam autocollimator in our NSP instrument (around 7–8 m). We assume the optical head can measure the mirror surfaces with these RoC values. Our main objective is to evaluate the tolerance of the pitch rotation center location. The RMS values of the multi-pitch NSP reconstructed slope residuals are calculated when the e_{z_c} varies within ± 3 mm for M1 and ± 0.3 mm for M2 as shown in **Figure 8**.

Applying the 10-nrad-RMS threshold as the error budget analyzed above, the tolerance of the e_{z_c} for M1 is about ± 2.2 mm. The tolerance for the e_{z_c} for M2 is only around ± 0.23 mm, which is very tight and not easy to measure with simple approaches.

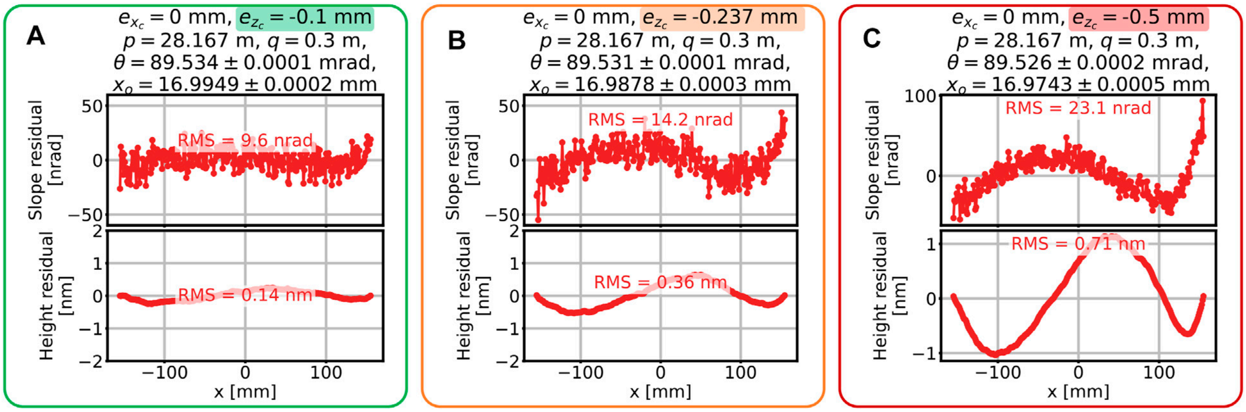

FIGURE 10 | The slope and height residuals when measuring M2 with σ_{n_a} = 70 nrad angular noise: **(A)** when e_{z_c} = −0.1 mm, **(B)** under a critical condition of e_{z_c} = −0.237 mm, and **(C)** when e_{z_c} = −0.5 mm.

By numerically searching the intersections between the curve of the RMS of slope residuals and the red dash line of 10-nrad-RMS threshold, we can determine the tolerance values of e_{z_c} for all ellipses of this study. If we use the variation range of the mirror curvature (1/RoC) as the horizontal axis, these different ellipses in series (q-, θ-, and L-series in **Figure 6**) and two real mirror designs (M1 and M2) can be included into one unified plot as shown in **Figure 9**.

An elliptical mirror becomes more "extreme" when its curvature varies in a larger range. The requirement on the pitch rotation center measurement becomes tight if the ellipse to test is very "extreme" as shown in **Figure 9**. The use the multi-pitch NSP technique to measure these kind of X-ray mirrors requires a precise auxiliary measurement of the pitch rotation center.

The vertical error of the pitch rotation center e_{z_c} introduces a systematic bias (or say a systematic error) on the reconstructed slope of the elliptical mirror under test from its true values. This systematic bias affects the fitting parameters (e.g., θ and x_o) and the fitting residuals (on slope and height), as well as their uncertainties.

Let's take a critical condition, M2 with $e_{z_c} = -0.237$ mm (the red cross marker in **Figure 9**), as an example. In presence of a 70 nrad RMS angular noise, as shown in **Figure 10B**, we get 14.2 nrad RMS slope residuals and the corresponding height residuals are 0.36 nm RMS after optimizing θ and x_o, though they only require a small adjustment. Since M2 should be characterized with a diffraction limited shape error below $\lambda/(28 \cdot \theta) = 1.98$ nm RMS, the 0.36 nm RMS bias added by an $e_{z_c} = -0.237$ mm estimation error in the rotation center location, is barely acceptable.

As shown in **Figure 10A**, the slope and height residuals are smaller when the center of rotation error is reduced to $e_{z_c} = -0.1$ mm, and the best fit parameters θ and x_o are closer to their nominal target values, compared to the critical condition $e_{z_c} = -0.237$ mm.

When $e_{z_c} = -0.5$ mm as shown in **Figure 10C**, the height residuals increase to 0.71 nm RMS which is more than 1/3 of the diffraction limited allowed shape error. In this case, the characterization of M2 would be significantly biased because the systematic error due to $e_{z_c} = -0.5$ mm is too large.

Framework to Determine the Measurement Tolerance of the Pitch Rotation Center

Before performing a multi-pitch NSP, it is required to ensure that the measurement of the pitch rotation center can meet the tolerance requirement. Therefore, we suggest a framework to determine the needed measurement accuracy of z_c:

1) Set the RMS threshold of slope residuals from the best fit. This RMS threshold should be 1/10 of the RMS value of the desired slope errors in total. For example, if 100 nrad RMS total slope error is pursued based on the mirror specification, the RMS threshold of slope residuals should be set as 10 nrad.
2) Calculate the tolerance of the e_{z_c} according to the target ellipse parameters and the preset RMS threshold of slope residuals.
3) The RMS value σ_{z_c} of the z_c measurement should be 1/6 of the range of the e_{z_c} tolerance, if we take the ± $3\sigma_{z_c}$ as the full range of the e_{z_c} tolerance.

Within this framework, one can estimate if the selected metrology tool is adequate to measure z_c for a particular elliptical mirror. Knowing the ellipse parameters and the uncertainty of the z_c measurement device, step 2 can be realized by simulating the multi-pitch NSP measurement without introducing any angular noise.

Moreover, we can also carry out Monte Carlo simulations considering both uncertainties of the angular sensor and of the z_c measurement device. As a result, it will give the uncertainties of the fit parameters, θ, x_o and of the slope residuals as well.

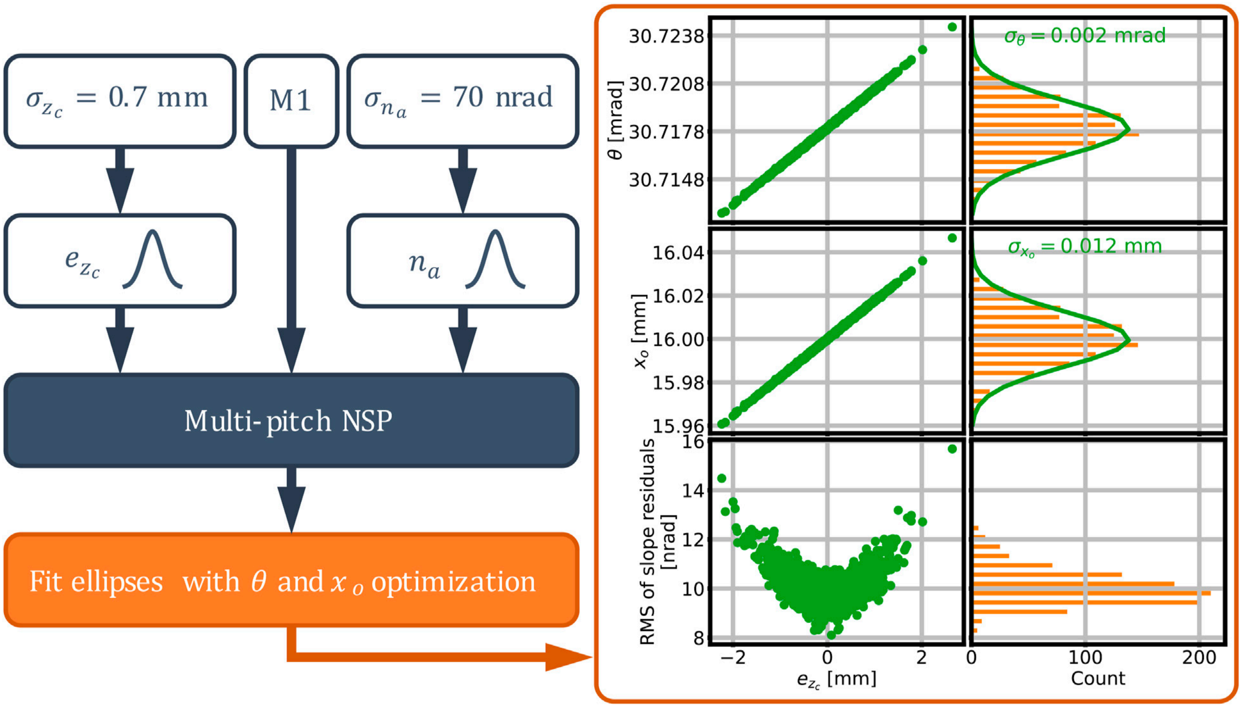

FIGURE 11 | The Monte Carlo simulation of measuring M1 using the multi-pitch NSP with a pitch rotation center measurement error e_{z_c} with a standard deviation σ_{z_c} = 0.7 mm and a normally-distributed angular noise with σ_{n_a} = 70 nrad gives the ellipse fitting results of the grazing angle θ in an uncertainty of ± $3\sigma_\theta$ = ± 6 μrad, the x_o with an uncertainty of ± $3\sigma_{x_o}$ = ± 36 μm, and the RMS of the slope residuals from the best fit around 10 ± 2 nrad RMS.

MONTE CARLO SIMULATION ON M1

From what precedes we can infer that a correlation exists between the error committed on z_c and the resulting errors in estimating the fit parameters. We use Monte Carlo simulations to study this correlation considering that the uncertainty of the two inputs, coming from the two separate metrology tools, are uncorrelated. The standard deviation of the additive angular noise σ_{n_a} is still set to 70 nrad, as previously.

M1 is selected as the test mirror in this Monte Carlo simulation. The average pitch steps are about 0.2 mrad, and 76 pitch angles are performed in the multi-pitch NSP simulation. As shown in **Figures 8**, **9**, the tolerance of the e_{z_c} for M1 is about ± 2.2 mm if the RMS threshold of slope residuals is set at 10 nrad, so we will need a metrology technique to measure z_c with an accuracy of $\sigma_{z_c} = 2.2/3 \approx 0.7$ mm. We simulated a sequence of 1,000 independent measurements of M1 mirror with the multi-pitch NSP technique, taking $\sigma_{z_c} = 0.7$ mm and $\sigma_{n_a} = 70$ nrad for standard deviation of the two random inputs, as shown in **Figure 11**.

After the best fit of ellipse (optimization of θ and x_o), as shown in the right panel of **Figure 11**, the Monte Carlo simulation can give the uncertainty of the measurement in θ and x_o, and the slope residuals from the best fit as the result of the measurement and data analysis. Taking this simulation as an example, if we measure the vertical distance z_c with $\sigma_{z_c} = 0.7$ mm and perform the angle acquisition for multi-pitch NSP with $\sigma_{n_a} = 70$ nrad, the slope residuals will end up at 10 nrad RMS level (the RMS of slope residuals due to e_{z_c} is less than 10 nrad RMS threshold). The grazing angle is estimated with a $\pm 3\sigma_\theta$ uncertainty as $\hat{\theta} = 30.7178 \pm 0.006$ mrad and the chief ray location, with a $\pm 3\sigma_{x_o}$ uncertainty, as $\hat{x}_o = 16 \pm 0.036$ mm. The Monte Carlo simulation offers a better picture of what we are expecting to get from the multi-pitch NSP measurement of a specific test mirror with a particular measurement of the pitch rotation center.

CONCLUSION

To take the challenge of measuring extreme off-axis elliptical mirrors, we revisit the multi-pitch NSP technique from its basic theory to the reconstruction algorithm. The true abscissa x_m of the measured position in the mirror coordinate system is needed in the reconstruction algorithm. This abscissa x_m in the mirror coordinate system is derived as a function of recorded position in the instrumental word coordinate system, the mirror height profile z_m and the measurement error on the pitch rotation center (x_c, z_c). We discuss the failure of the “flat assumption” $(\hat{z}_m = 0)$ when measuring “extreme” ellipses and propose a solution with iterative reconstruction in multi-pitch NSP system.

The tolerance of the measurement of the pitch rotation center location (x_c, z_c) is studied with simulations on a series of ellipse parameters. We find out from both theoretical analysis and simulations that the tolerance of the x_c measurement is large, and the requirement can easily be satisfied. When measuring "extreme" ellipses, the tolerance of the z_c measurement is much tighter. We proposed a practical framework to determine the needed measurement accuracy of the z_c measurement. For some extreme cases, the tolerance of the e_{z_c} is so small that the measurement of z_c can be a challenge.

A Monte Carlo simulation on a real design of an "extreme" elliptical mirror shows that, with a known accuracy of the pitch rotation center measurement, we can estimate θ and x_o with their uncertainties and get the slope residuals from the best fit. The RMS value of the slope residuals due to measurement error e_{z_c} is controlled by meeting the tolerance of the e_{z_c}.

This simulation study can guide the real multi-pitch NSP measurement for "extreme" elliptical mirrors. The tolerance of e_{z_c} can be calculated before the design of the measurement. A proper way to measure z_c becomes the key to the "extreme" elliptical mirror characterization with the multi-pitch NSP technique.

DATA AVAILABILITY STATEMENT

The original contributions presented in the study are included in the article/Supplementary Material, further inquiries can be directed to the corresponding author.

AUTHOR CONTRIBUTIONS

LH and MI contributed to conception, methodology and funding acquisition. LH wrote the first draft of the manuscript. TW and KN contributed to the review of the manuscript. FP reviewed and modified the manuscript. JN contributed to the review of the revised version. MI supervised the research. All authors discussed the results, revised the manuscript, and approved the submitted version.

FUNDING

This work was supported by NSLS-II Facility Improvement Project (21153) and DOE Office of Science (DE-SC0012704).

ACKNOWLEDGMENTS

This research used resources of the National Synchrotron Light Source II, a U.S. Department of Energy (DOE) Office of Science User Facility, operated for the DOE Office of Science by Brookhaven National Laboratory under Contract No. DE-SC0012704.

REFERENCES

1. Takacs PZ, Qian S-n., Colbert J. (1987). Design of A Long Trace Surface Profiler, *Metrol Fig Finish*, p. 59. Proc. SPIE 0749. doi:10.1117/12.939842
2. Siewert F, Noll T, Schlegel T, Zeschke T, Lammert H. The Nanometer Optical Component Measuring Machine: A New Sub-nm Topography Measuring Device for X-ray Optics at BESSY. *AIP Conf Proc* (2004) 705:847–50. doi:10.1063/1.1757928
3. Qian S, Jark W, Takacs PZ. The Penta-prism LTP: A Long-trace-profiler with Stationary Optical Head and Moving Penta Prisma). *Rev Scientific Instr* (1995) 66:2562–9. doi:10.1063/1.1145658
4. Ali Z, Yashchuk VV. Automated Suppression of Errors in LTP-II Slope Measurements of X-ray Optics .(2011) Part 2 : Specification for automated rotating/flipping/aligning system n.d.:1–8. Available at: https://www.osti.gov/servlets/purl/1170543. doi:10.2172/1170543
5. Siewert F, Buchheim J, Zeschke T. Characterization and Calibration of 2nd Generation Slope Measuring Profiler. *Nucl Instr Methods Phys Res Section A: Acc Spectrometers, Detectors Associated Equipment* (2010) 616:119–27. doi:10.1016/j.nima.2009.12.033
6. Nicolas J, Pedreira P, Šics I, Ramírez C, Campos J. Nanometer Accuracy with Continuous Scans at the ALBA-NOM. *Adv Metrol X-ray EUV Opt VI* (2016) 9962:996203. doi:10.1117/12.2238128
7. Alcock SG, Sawhney KJS, Scott S, Pedersen U, Walton R, Siewert F, et al. The Diamond-NOM: A Non-contact Profiler Capable of Characterizing Optical Figure Error with Sub-nanometre Repeatability. *Nucl Instr Methods Phys Res Section A: Acc Spectrometers, Detectors Associated Equipment* (2010) 616:224–8. doi:10.1016/j.nima.2009.10.137
8. Nicolas J, Martínez JC. Characterization of the Error Budget of Alba-NOM. *Nucl Instr Methods Phys Res Section A: Acc Spectrometers, Detectors Associated Equipment* (2013) 710:24–30. doi:10.1016/j.nima.2012.10.125
9. Qian S, Idir M. Innovative Nano-Accuracy Surface Profiler for Sub-50 Nrad Rms Mirror Test. *8th Int Symp Adv Opt Manuf Test Technol Subnanom Accuracy Meas Synchrotron Opt X-ray Opt* (2016) 9687:96870D. doi:10.1117/12.2247575
10. Avila J, Boury A, Caja-Muñoz B, Chen C, Lorcy S, Asensio MC. Optimal Focusing System of the Fresnel Zone Plates at the Synchrotron SOLEIL NanoARPES Beamline. *J Phys Conf Ser* (2017) 849:012039. doi:10.1088/1742-6596/849/1/012039
11. Polack F, Thomasset M, Brochet S, Rommeveaux A. An LTP Stitching Procedure with Compensation of Instrument Errors: Comparison of SOLEIL and ESRF Results on Strongly Curved Mirrors. *Nucl Instr Methods Phys Res Section A: Acc Spectrometers, Detectors Associated Equipment* (2010) 616:207–11. doi:10.1016/j.nima.2009.10.166
12. Huang L, Wang T, Nicolas J, Polack F, Zuo C, Nakhoda K, et al. Multi-pitch Self-Calibration Measurement Using a Nano-Accuracy Surface Profiler for X-ray Mirror Metrology. *Opt Express* (2020) 28:23060. doi:10.1364/oe.392433

Conflict of Interest: The authors declare that the research was conducted in the absence of any commercial or financial relationships that could be construed as a potential conflict of interest.

ORIGINAL RESEARCH
published: 24 May 2022
doi: 10.3389/fphy.2022.865411

High-Precision Ion Beam Figuring of X-Ray Plane Mirrors for the Bendable KB Focusing System

Yunyang Zhang[1], **Qiushi Huang**[1]*, **Shuai Yan**[2]*, **Jun Yu**[1], **Handan Huang**[1], **Yumei He**[2], **Hongxin Luo**[2], **Zhi Liu**[3], **Zhong Zhang**[1] **and Zhanshan Wang**[1]

[1]Key Laboratory of Advanced Micro-Structured Materials, MOE, Institute of Precision Optical Engineering (IPOE), School of Physics Science and Engineering, Tongji University, Shanghai, China, [2]Chinese Academy of Sciences, Shanghai Advanced Research Institute, Pudong, China, [3]Center for Transformative Science, ShanghaiTech University, Shanghai, China

Two trapezoidal plane mirrors of 240 mm in length were fabricated by ion beam figuring (IBF) technology for application in a bendable KB focusing system. The correction of surface height and slope errors in different spatial frequency ranges of the mirrors was studied systematically. After one to two iterations of IBF, the figure height errors of the vertical focusing mirror (VFM) and horizontal focusing mirror (HFM) were improved from 32.4 and 65.4 nm to 2.7 and 7.2 nm (RMS), respectively. If the best-fit sphere of the surface profile was subtracted, the residual two-dimensional height errors were only 1.1 and 1.2 nm (RMS). The slope errors in the low spatial frequency range were corrected much faster than the middle frequency ones ($f = \sim 1\ \mathrm{mm}^{-1}$), which make the low-frequency slope error much smaller. After IBF, the two-dimensional slope errors of the two mirrors calculated with a spatial interval of 1 and 10 mm were reduced to approximately 0.29 and 0.08 μrad, respectively. Full spatial frequency characterization of the VFM before and after IBF showed that the low-frequency figure errors ($f < 1\ \mathrm{mm}^{-1}$) were significantly reduced while the middle- and high-frequency morphologies ($f > 1\text{–}2\ \mathrm{mm}^{-1}$) remain almost the same as before figuring. The fabricated plane mirrors were applied in the hard X-ray micro-focusing beamline in the Shanghai Synchrotron Radiation Facility (SSRF), which realized a focal spot of 2.4 μm × 2.8 μm at 10 keV.

Keywords: ion beam figuring, X-Ray mirror, height error, slope error, focusing

Edited by:
Emmanouil P. Benis,
University of Ioannina, Greece

Reviewed by:
Giulia Festa,
Museo Storico della Fisica e Centro Studi e Ricerche Enrico Fermi, Italy
Simon Alcock,
Diamond Light Source, United Kingdom

Correspondence:
Qiushi Huang
huangqs@tongji.edu.cn
Shuai Yan
yanshuai@zjlab.org.cn

Specialty section:
This article was submitted to Optics and Photonics, a section of the journal Frontiers in Physics

Received: *29 January 2022*
Accepted: *19 April 2022*
Published: *24 May 2022*

Citation:
Zhang Y, Huang Q, Yan S, Yu J, Huang H, He Y, Luo H, Liu Z, Zhang Z and Wang Z (2022) High-Precision Ion Beam Figuring of X-Ray Plane Mirrors for the Bendable KB Focusing System. Front. Phys. 10:865411. doi: 10.3389/fphy.2022.865411

INTRODUCTION

The new generation synchrotron sources and free-electron laser can provide diffraction-limited X-ray beams with high coherence and a nearly perfect wavefront. This brings an extremely high requirement on the mirror figure accuracy, down to nanometer height error and hundreds to sub-hundred nanoradian slope error, to avoid any distortion of the wavefront. At the same time, the mirror roughness requirements also reached the sub-nanometer level. These requirements pose a great challenge for the manufacturing technology [1, 2].

At present, the deterministic methods for X-ray mirror fabrication include elastic emission machining (EEM) [3, 4], ion beam figuring (IBF) [5–8], and profile coating [9]. Among them, IBF is the most commonly used high-precision manufacturing method. It has a relatively high figuring efficiency with sub-nanometer accuracy and thus has been used by major suppliers such as Carl Zeiss and Thales SESO as the mirror finishing process. For example, Peverini et al. reported their achievements in the fabrication of

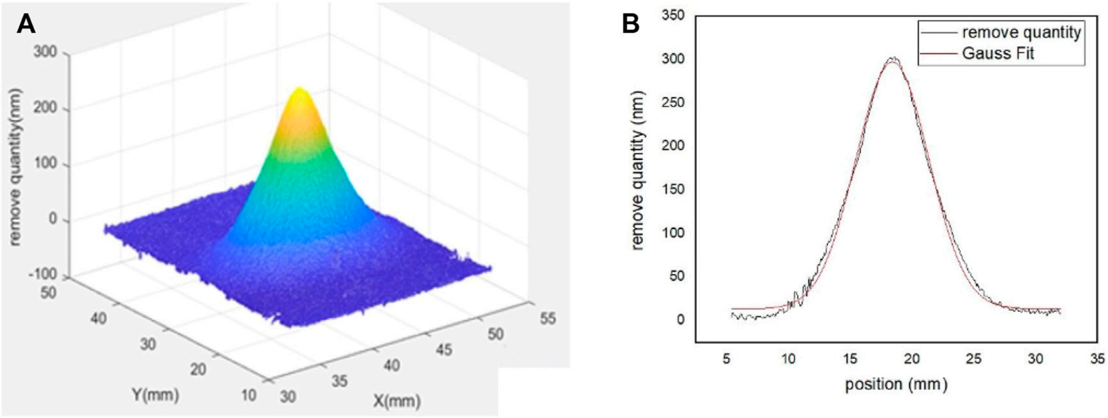

FIGURE 1 | (A) Measured ion beam removal function. **(B)** One-dimensional profile of the removal function and its Gaussian fit.

high-precision flat mirrors and ellipsoid mirrors using IBF. A very low figure error of 1 nm RMS was obtained on a 1.2 m long mirror, and a 0.2 μrad slope error has been achieved on a large ellipsoid mirror with highly curved surface [10].

Meanwhile, the optics groups within different synchrotron radiation facilities are also studying the IBF techniques to fabricate high-precision mirrors. Liu et al., from Advanced Photon Source, presented a method for pre-shaping mirror substrates through figuring with a broad-beam ion source and a contoured mask. A 100 mm-long elliptical cylinder substrate was obtained from a super-polisher flat Si substrate with a 48 nm root-mean-square (RMS) figure error and 0.15 nm roughness after one profile figuring process [11]. Hand et al., from Diamond Light Source, have designed and built an IBF system for the research and manufacture of high-quality X-ray mirrors [12]. Wang and Huang et al., from National Synchrotron Light Source II, have made significant progress in ion beam figuring of X-ray mirrors. They first proposed an effective 1D-IBF method with improved calibration of coordinate correspondence and dwell time calculation [13]. Several new dwell time calculations and optimization algorithms were further developed to reduce the estimated figure error residuals and enhance the computation efficiency [14, 15]. These methods were demonstrated in their own-built IBF system. Two elliptical mirrors of 80 mm in length were fabricated from cylinders which showed 0.62 and 0.71 nm RMS figure error, respectively [14]. The figure error of a flat mirror over an aperture of 92.3 mm × 15.7 mm was reduced from 6.32 to 0.2 nm RMS [15].

In these years, the synchrotron radiation and free-electron laser facilities in China are also undergoing a new wave of upgrading and construction [16, 17]. Driven by the increasing demand for high-precision X-ray mirrors, we are building a new platform in Institute Precision Optical Engineering (IPOE) combining ion beam figuring and interferometry measurement methods. Based on this platform, two trapezoidal plane mirrors have been fabricated as bendable mirrors for a hard X-ray KB focusing system in SSRF. Residual figure errors of only 1.1–1.3 nm RMS were achieved over the 240-mm length substrates. The slope errors were found to have a much faster convergence and smaller RMS value in the lower spatial frequency range after IBF. The two mirrors have been installed in the beamline for micro-focusing applications.

MATERIALS AND METHODS

The sizes of the two trapezoidal mirrors are 240 mm (length) × 34/20 mm (width) × 14 mm (thickness) and 240 mm × 67/20 m × 10 mm. The smaller one is for vertical focusing (VFM), and the larger one is for horizontal focusing (HFM). A commercial IBF machine (Trim 200) from SCIA company was used in this work. Ar gas was used in this experiment with a beam voltage of 1500 V. The beam removal function was calibrated in a small Si substrate, and the measurement result of the Fizeau interferometer is shown in **Figure 1**. It is very close to a two-dimensional Gaussian beam with full width at half maximum (FWHM) of 7.2 mm in both directions. The maximum removal rate at the center of the beam is 5.8 nm/s.

The Fizeau interferometer (model is DynaFiz™) from Zygo company was used to measure the low spatial frequency surface figure of the mirrors. During the test, the surface normals of the reference mirror remain parallel to those of the mirror under test. A camera resolution of 1,200 × 1,200 pixels with a pixel size of $0.2635 \times 0.2635\ \mathrm{mm}^2$ was employed. An optical profiler (model is ContourGT-X3) and atom force microscope (AFM, model is Icon Dimension) from Bruker company were used to measure the middle- and high-frequency surface morphologies. The optical profilometer used ×10 and ×50 magnification with test areas of $0.62 \times 0.47\ \mathrm{mm}^2$ and $0.13 \times 0.1\ \mathrm{mm}^2$, with minimum resolutions of $923\ \mathrm{mm}^{-1}$ and $103\ \mathrm{mm}^{-1}$, respectively. AFM used a $2 \times 2\ \mu\mathrm{m}^2$ test area and 256 × 256 pixels resolutions.

RESULTS AND DISCUSSION

Ion Beam Figuring of VFM

The surface figures of VFM before and after IBF are shown in **Figure 2**. The 2-mm edge area was removed from all sides of the

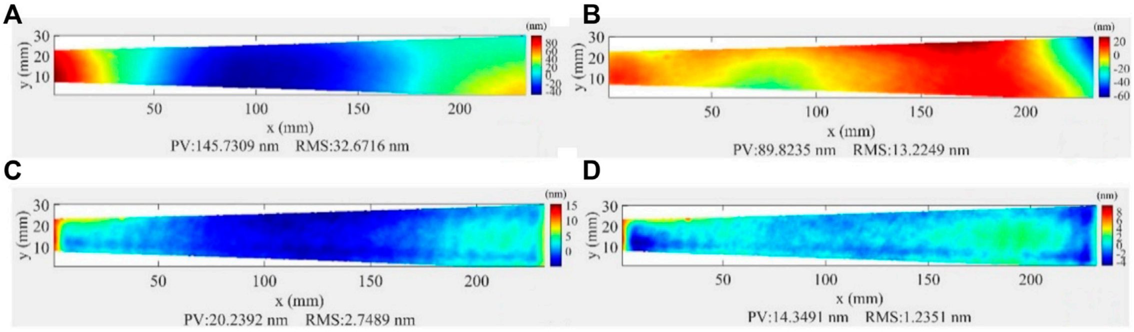

FIGURE 2 | (A) Initial surface figure of VFM. **(B)** Initial surface figure after subtracting the best-fit sphere. **(C)** Surface figure after IBF. **(D)** Surface figure after IBF with the best-fit sphere subtracted.

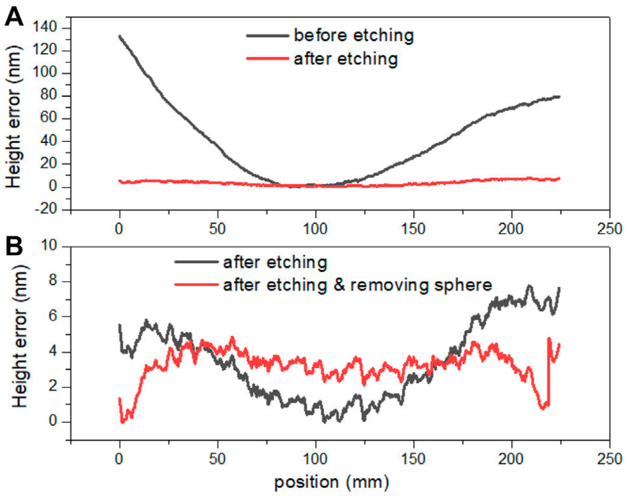

FIGURE 3 | (A) One-dimensional height profile along the length direction of VFM before and after IBF. **(B)** Height error after IBF without and with the best-fit sphere was subtracted.

mirror. The mirror was mechanically polished previously to a figure of 32.7 nm (RMS) with an ultrasmooth surface (roughness <0.3 nm). A small curvature existed in the surface profile which has a best-fit radius of 56.4 km (**Figure 2A**). If the best-fit sphere was subtracted, the residual figure error before IBF is 13.2 nm (RMS) (**Figure 2B**). The mirror surface profile (including the 2nd order spherical error) was figured by two iterations. After that, the radius of the best-fit sphere was increased to 603 km with a figure of 2.7 nm RMS (**Figure 2C**). Due to the small mirror thickness, it is difficult to completely remove the 2nd order curvature, and this extremely large radius of curvature will have negligible effect for application in the beamline. The residual height error after subtraction of the best-fit sphere was only 1.2 nm (RMS) (**Figure 2D**).

The one-dimensional height profile along the length direction at the center area of the mirror is shown in **Figure 3A**. The height error (including the 2nd order curvature) decreased dramatically from 132.9 to 7.8 nm (PV) and from 33.9 to 2.2 nm (RMS). The height error after IBF with the best-fit sphere subtracted is also shown in **Figure 3B**. The residual error is 4.8 nm (PV) and 0.88 nm (RMS) after subtracting the best-fit sphere, while some small oscillations can still be seen in the height profile. These middle-frequency errors will need to be removed in future work.

In order to further characterize the slope error of the figured surface topography, two-dimensional images of slope errors were made (as shown in **Figure 4**). The slope error was calculated along the length direction over the two-dimensional surface area, and the second-order curvature has been removed. Two different slope error maps with a spatial interval of 1 and 10 mm were calculated, and the RMS values were determined, respectively. In the case of a 1 mm interval (close to middle-frequency region), the slope error decreased from 0.77 to 0.28 μrad after two times figuring. In the case of the 10 mm interval, the slope error was smaller than in the 1 mm case in general, and it decreased from 0.65 to 0.08 μrad. A more detailed calculation of the slope error at different intervals (from 0.2635 to 42.16 mm) is shown in **Figure 5**.

In **Figure 5**, the slope error of the vertical axis is the root mean square of the slope error of the two-dimensional slope error maps, i.e., the root mean square value of slope error at different spatial frequencies. We calculated the slope error from pixel interval 1 to interval 160 (the interval is 1, and there are 160 groups of data points) and made the slope error-frequency graph. The spatial frequency of the horizontal axis is calculated from the selected interval (spatial frequency = 1/interval, pixel intervals range from 1 to 160, so the spatial frequencies range from 3.8 mm^{-1} to 0.0237 mm^{-1}). It is worth noting that in the two-dimensional image, in order to better compare the two images, we cut off the image to make them the same size, but this is not carried out in the spatial frequency error distribution, so there is a slight vertical difference between the two images.

It can be seen that the slope error gradually decreased as the spatial intervals increased. The reduction of slope error is significantly larger at the lower frequency region, indicating a stronger correction effect of IBF in this region. As a result, the slope error calculated with larger intervals exhibited a much

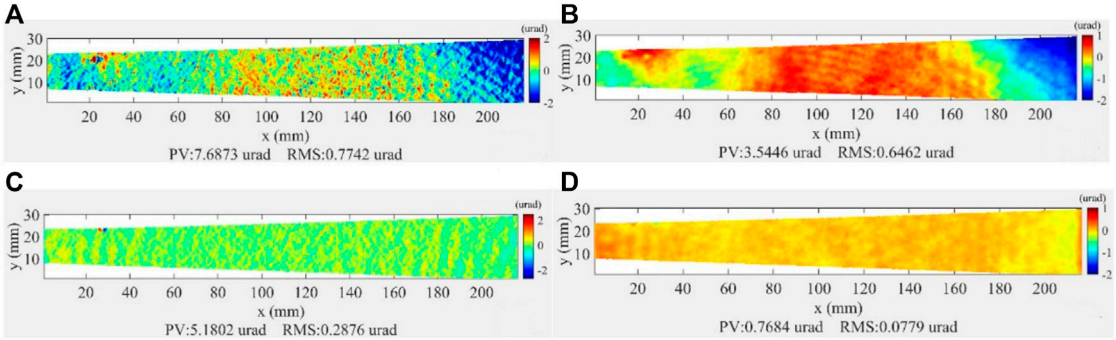

FIGURE 4 | (A) Initial slope error calculated with 1 mm interval. **(B)** Initial slope error calculated with 10 mm interval. **(C)** Slope error after IBF calculated with 1 mm interval. **(D)** Slope error after IBF calculated with 10 mm interval.

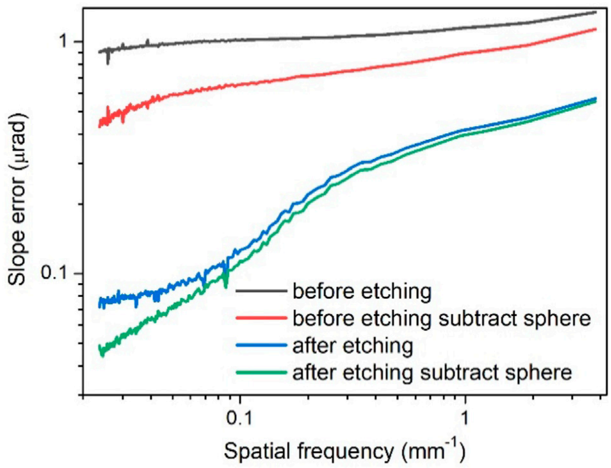

FIGURE 5 | RMS values of two-dimensional slope errors of VFM calculated at different spatial frequencies.

smaller value. Considering the different effects of the slope errors located in different frequencies on the X-ray wavefront [18], it is worth estimating the surface slope quality in a frequency-dependent way rather than using a fixed spatial interval.

Ion Beam Figuring of HFM

The surface figures of HFM before and after IBF are shown in **Figure 6**. A few millimeters of the edge area were removed from all sides of the mirror. A relatively large second-order curvature was observed in the mirror before IBF. After a single iteration figuring, the radius of curvature of HFM was increased from 26.7 to 267 km. The height error was reduced from 65.4 to 7.2 nm (RMS) (**Figures 6A, C**). If the best-fit sphere was subtracted, the residual figure before IBF was 13.2 nm (RMS) (**Figure 6B**), and the residual error after IBF was only 1.1 nm (RMS) (**Figure 6D**).

The one-dimensional height profile along the length direction of the center area of the mirror is shown in

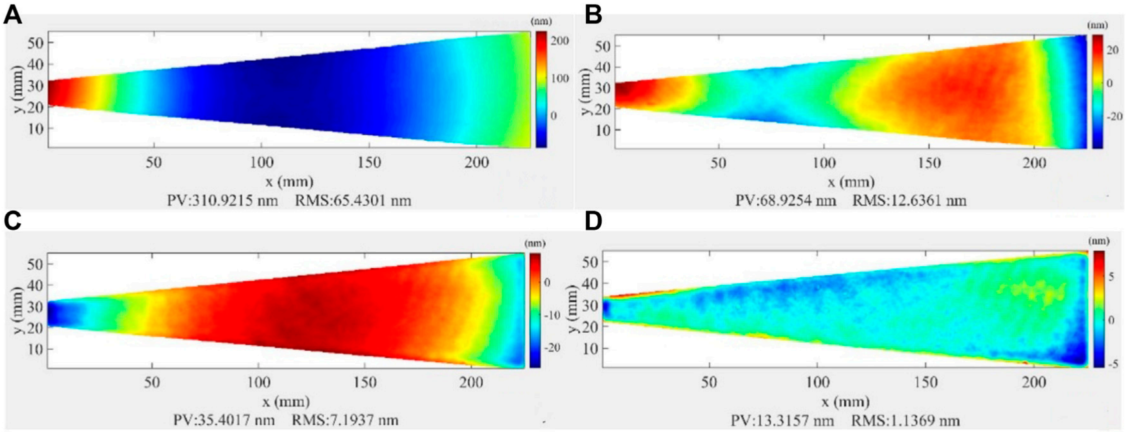

FIGURE 6 | (A) Initial surface figure of HFM. **(B)** Initial surface figure after subtracting the best-fit sphere. **(C)** Surface figure after IBF. **(D)** Surface figure after IBF with the best-fit sphere subtracted.

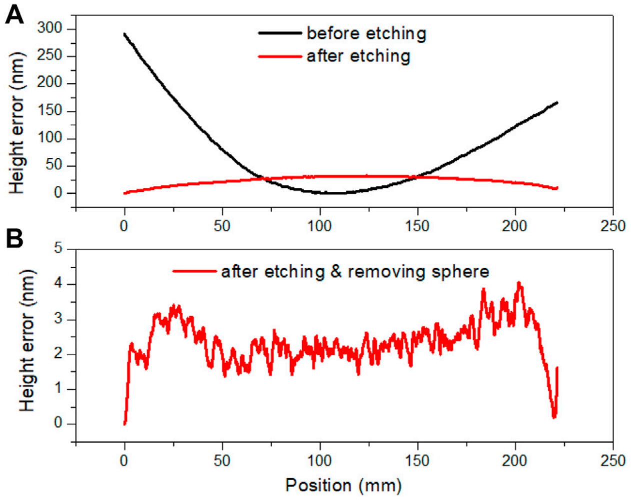

FIGURE 7 | (A) One-dimensional height profile along the length direction of HFM before and after IBF. **(B)** Height error after IBF with the best-fit sphere was subtracted.

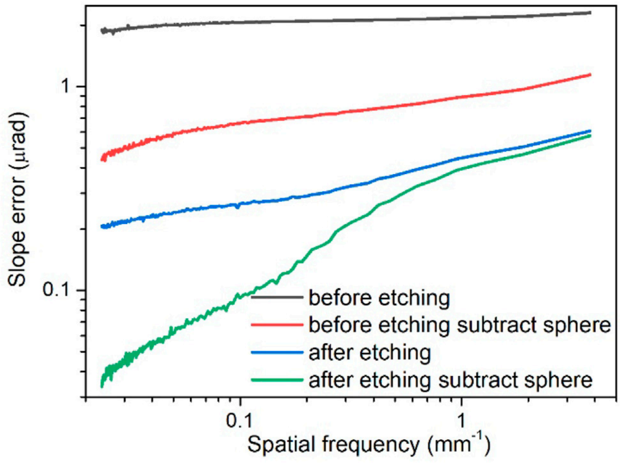

FIGURE 9 | RMS values of two-dimensional slope errors of HFM calculated at different spatial frequencies.

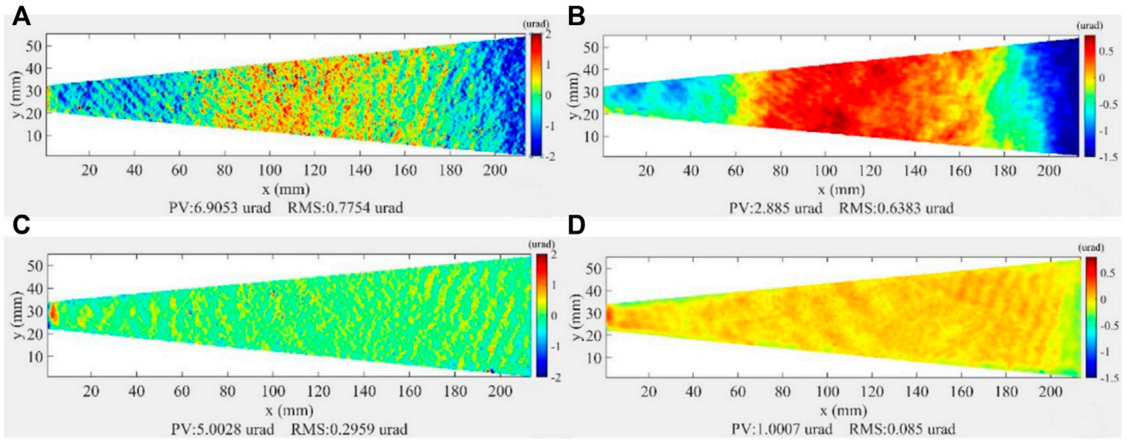

FIGURE 8 | (A) Initial slope error calculated with 1 mm interval. **(B)** Initial slope error calculated with 10 mm interval. **(C)** Slope error after IBF calculated with 1 mm interval. **(D)** Slope error after IBF calculated with 10 mm interval.

Figure 7. The height error (including the 2nd order curvature) decreased dramatically from 290.5 to 31.5 nm (PV) and from 74.1 to 8.0 nm (RMS). The height error with subtracting the best-fit sphere after IBF is further shown in the following diagram of **Figure 7**. The residual error is 3.9 nm (PV) and 1.1 nm (RMS) after subtracting the best-fit sphere, while some small oscillations can still be seen in the height profile. These middle-frequency errors will need to be removed in future work.

Figure 8 shows the two-dimensional slope error distribution of HFM. After figuring, the RMS of slope errors decreases from 0.78 to 0.29 μrad in the case of a 1-mm interval and from 0.64 to 0.08 μrad in the case of a 10-mm interval. Both VFM and HFM showed sub-hundred nanoradians slope error after IBF if a 10 mm spatial interval was used for estimation. **Figure 9** shows the slope error of HFM at different frequencies. It can be seen that the evolution of slope error is similar to VFM, while the effectiveness of IBF correction in the lower frequency region is much better.

To further estimate the absolute accuracy of our interferometer measurements, the HFM mirror was also measured by NOM in the optics group in SSRF. The trapezoidal mirror was mounted sideways in NOM, and a line profile indicated in **Figure 10A** was measured accordingly. The comparison of NOM and the interferometer results are shown in **Figures 10B, C**. The general trend of the height profiles of NOM and interferometer is similar while a difference of ±4 nm (PV) was observed. This can be caused

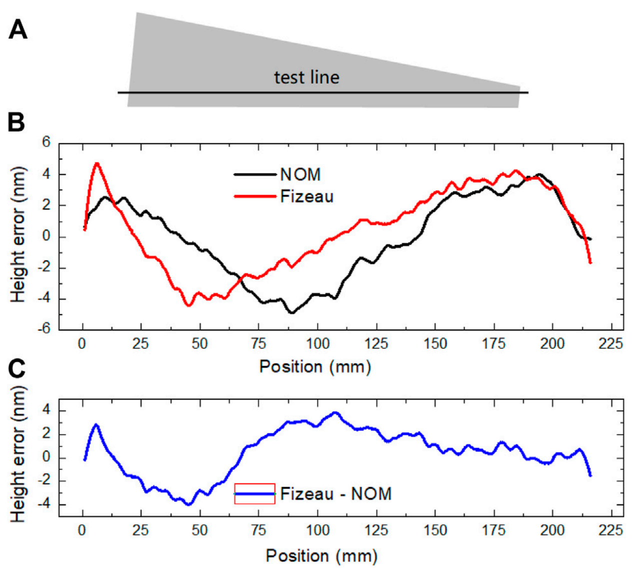

FIGURE 10 | (A) Schematic representation of the line position of HFM measured by NOM. **(B)** Comparison of the line profiles measured by NOM and Fizeau interferometer after IBF. **(C)** Difference between the height profiles of two measurements.

TABLE 1 | Surface roughness measured by using an optical profiler and AFM before and after IBF.

	10× (nm)	50× (nm)	AFM (nm)
Before	0.233	0.254	0.101
After	0.229	0.245	0.114

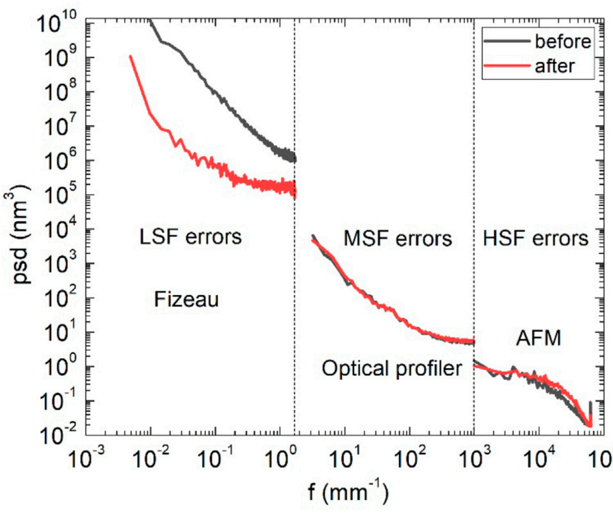

FIGURE 11 | PSD results of VFM before and after IBF as measured by the Fizeau interferometer, optical profiler, and AFM.

by the reference error of the interferometer that was not perfectly corrected. The slope error measured by NOM is 160 nrad, given the relatively large beam size of NOM. The consistent results proved the high figure accuracy of the trapezoidal plane mirrors fabricated by IBF.

Analysis of Surface Morphology in the Full Spatial Frequency Range

In addition, the low-frequency surface figure was measured by using the Fizeau interferometer; the middle and high spatial frequency morphologies of the mirrors were also measured before and after IBF by using an optical profiler and atom force microscope, respectively. The RMS values of VFM are listed in **Table 1**. The middle- and high-frequency roughness values after IBF are 0.23–0.25 and 0.11 nm (RMS), respectively, which are similar to before IBF.

The one-dimensional power spectral densities (PSDs) of the measured surface morphology of the interferometer, optical profiler, and AFM are calculated and shown together in **Figure 11**. It can be seen that in the low-frequency region of $f < 1\ \mathrm{mm}^{-1}$, the surface height errors were significantly reduced, whereas the height error convergence become slower as the frequency increased. In the higher frequency region of $f > 1–2\ \mathrm{mm}^{-1}$, the height errors remain almost the same as before, which indicates that the ion beam figuring process in this work has a negligible effect on the middle- and high-frequency errors.

Application in Hard X-Ray Micro-focusing Beamline in SSRF

After the high-precision ion beam figuring, a linear magnetron sputtering machine was used to coat both mirrors with 50-nm Rh film [19]. A thin Cr bonding layer was first deposited before the Rh layer. The coated mirrors were installed and applied in the bendable KB system in the end station of the hard X-ray micro-focusing beamline (XMF) in SSRF (**Figure 12**). The plane mirrors were bent into an elliptical shape by mechanical benders. The object distance of VFM is close to infinite, and the image distance is 42 cm; the object distance of HFM is 500 cm, and the image distance is 27 cm. Due to the toroidal mirror upstream providing collimation and pre-focusing in vertical and horizontal directions, respectively, the divergence angle of the incident beam is approximately 1 3 and 60 µrad for VFM and HFM. X-ray energy of 10 keV was used, and the grazing incidence is 3 mrad for both mirrors. The focal spot was measured by knife-edge scan to analyze the spot size and shape.

The focusing results are shown in **Figure 13**, and the simulation results performed by SHADOW software based on geometrical ray tracing were also added. The measured focal spot sizes (FWHM) are 2.8 and 2.4 µm in vertical and horizontal directions, respectively. The spot size in the horizontal direction is very close to the simulated result, while the one in the vertical direction is larger than the simulation. This can be caused by the surface errors of the upstream mirrors after long-term usage and the small error of the bender system in the vertical direction. The small figure error of the two mirrors has a negligible effect on the focusing result, according to simulation.

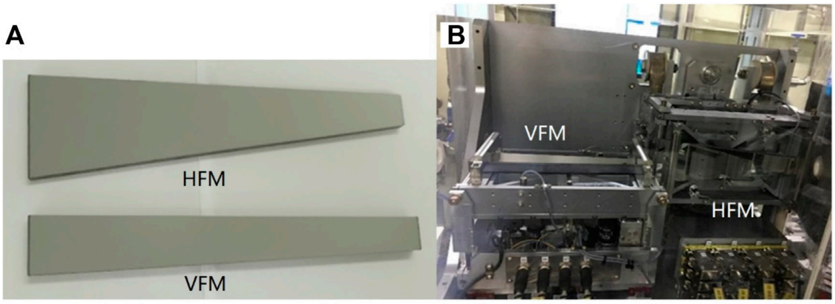

FIGURE 12 | (A) Pictures of two trapezoidal mirrors after coating and **(B)** after the installation in the bendable KB system.

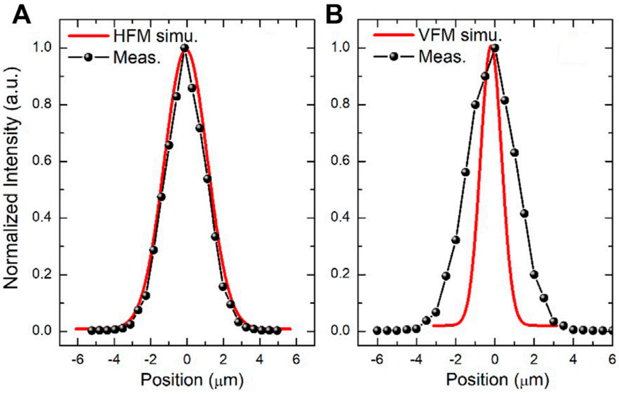

FIGURE 13 | (A) Measured focusing spot of the KB system in a horizontal direction and **(B)** in a vertical direction.

CONCLUSION

High-precision X-ray plane mirrors were fabricated by the developed IBF process. The figure errors of the 240 mm length mirrors were reduced down to 1.1–1.2 nm (RMS), and the ultrasmooth middle- and high-frequency morphologies were maintained the same as before IBF. The two-dimensional slope errors at different spatial frequency ranges were studied in detail. It was found that IBF has a much better correction effect on slope errors with a lower frequency, and a sub-hundred nanoradian slope error was obtained if a spatial period of 10 mm was used in estimation instead of the conventional 1 mm. The two mirrors were successfully installed in the hard X-ray micro-focusing beamline in SSRF, and a focusing spot of 2.4 μm × 2.8 μm was obtained. The KB focusing system has been opened to user applications.

Currently, the middle-frequency height errors still exist in the figured mirror surface. It needs to be further corrected by IBF, and even smaller slope errors can be expected. The IBF technology will also be developed for figuring curved mirrors and other more complex surface profiles to meet the different requirements in the beamlines.

DATA AVAILABILITY STATEMENT

The raw data supporting the conclusions of this article will be made available by the authors, without undue reservation.

AUTHOR CONTRIBUTIONS

YZ performed the IBF experiments, characterization, and contributed to writing of the manuscript, QH supervised the work and finalized the manuscript, SY performed mirror installation and focusing experiments, JY assisted the IBF experiments, HH assisted the IBF experiments, YH performed the NOM measurement, HL contributed to characterizations, ZL supported the IBF platform, ZZ contributed to fabrication and analysis, and ZW co-supervised the work.

FUNDING

This work is supported by the National Natural Science Foundation of China (12075170, U2032169, and 12027810) and the Shanghai Rising-Star Program (No. 19QA1409200).

REFERENCES

1. Eriksson M, van der Veen JF, Quitmann C. Diffraction-limited Storage Rings - a Window to the Science of Tomorrow. *J. Synchrotron Radiat.* (2015) 21(5): 837–42. doi:10.1107/S1600577514019286
2. Yamauchi K, Mimura H, Kimura T, Yumoto H, Handa S, Matsuyama S, et al. Single-nanometer Focusing of Hard X-Rays by Kirkpatrick-Baez Mirrors. *J. Phys Condens. Matter* (2011) 23(39):394206. doi:10.1088/0953-8984/23/39/394206
3. Takei Y, Mimura H. Effect of Focusing Flow on Stationary Spot Machining Properties in Elastic Emission Machining. *Nanoscale Res. Lett.* (2013) 8(1):237. doi:10.1186/1556-276x-8-237
4. Hirata T, Takei Y, Mimura H. Machining Property in Smoothing of Steeply Curved Surfaces by Elastic Emission Machining. *Procedia CIRP* (2014) 13: 198–202. doi:10.1016/j.procir.2014.04.034
5. Demmler M, Zeuner M, Allenstein F, Dunger T, Nestler M, Kiontke S. Ion Beam Figuring (IBF) for High Precision Optics. *Proc. SPIE* (2010) 7591:75910Y. doi:10.1117/12.840908

6. Yun L, Xing T, Xu J, Xu F, Lei N. Dwell Time Algorithm for the 3-axis Ion Beam Figuring System. *Infrared Laser Eng* (2012) 41(5):1300.
7. Chernyshev A, Chkhalo N, Malyshev I, Mikhailenko M, Toropov M. Matrix Based Algorithm for Ion-Beam Figuring of Optical Elements. *Precis. Eng.* (2021) 69(16). doi:10.1016/j.precisioneng.2021.01.006
8. Thiess H, Lasser H, Siewer F. Fabrication of X-Ray Mirrors for Synchrotron Applications. *Nucl. Instrum. Methods Phys. Res. A* (2010) 616(2-3):157–61. doi:10.1016/j.nima.2009.10.077
9. Shi Y, Huang Q, Qi R, Shen Z, Zhang Z, Wang Z. Theoretical and Experimental Study of Particle Distribution from Magnetron Sputtering with Masks for Accurate Thickness Profile Control. *Coatings* (2020) 10:357. doi:10.3390/coatings10040357
10. Peverini L, Guadalupi H, Michel T. Reflective Optics for EUV/x-ray Sources at Thales SESO: Possibilities and Perspectives. *Proc. SPIE* (2020) 11492:114920H. doi:10.1117/12.2570604
11. Liu C, Qian J, Assoufid L. Profile Etching for Prefiguring X-Ray Mirrors. *J. Synchrotron Radiat.* (2015) 22(2):458–60. doi:10.1107/s1600577515000624
12. Hand M, Alcock SG, Hillman M. Ion Beam Figuring and Optical Metrology System for Synchrotron X-Ray Mirrors. *Proc. SPIE* (2019) 11109:111090A. doi:10.1117/12.2528463
13. Wang T, Huang L, Vescovi M, Kuhne D, Tayabaly K, Bouet N, et al. Study on an Effective One-Dimensional Ion-Beam Figuring Method. *Opt. Express* (2019) 27(11):15368–81. doi:10.1364/oe.27.015368
14. Wang T, Huang L, Choi H, Vescovi M, Kuhne D, Zhu Y, et al. RISE: Robust Iterative Surface Extension for Sub-nanometer X-Ray Mirror Fabrication. *Opt. Express* (2021) 29(10):15114–32. doi:10.1364/oe.419490
15. Wang T, Huang L, Vescovi M, Kuhne D, Zhu Y, Negi VS, et al. Universal Dwell Time Optimization for Deterministic Optics Fabrication. *Opt. express* (2021) 29(23):38737–57. doi:10.1364/oe.443346
16. Shanghai-XFEL Beamline Project. *Shanghai-XFEL Beamline Project (SBP) and Shanghai Soft X-Ray Free Electron Laser Facility (SXEFL) Reach Another Milestone: First Light and First Data* (2021). Available at: https://www.shanghaitech.edu.cn/eng/2021/0626/c1260a66742/page.htm.
17. Jiang X, Wang J, Qing Q. The Chinese High-Energy Photon Source and its R&D Project. *Synchrotron Radiat. News* (2014) 27(6):27–31.
18. Pardini T, Cocco D, Hau-Riege SP. Effect of Slope Errors on the Performance of Mirrors for X-Ray Free Electron Laser Applications. *Opt. Express* (2015) 23(25):31889. doi:10.1364/oe.23.031889
19. Ni H, Huang Q, Shi Y, Qi R, Zhang Z, Feng Y, et al. Development of Large-Size Multilayer Mirrors with a Linear Deposition Facility for X-Ray Applications. *Opt. Eng.* (2019) 58(10):1. doi:10.1117/1.oe.58.10.104105

Conflict of Interest: The authors declare that the research was conducted in the absence of any commercial or financial relationships that could be construed as a potential conflict of interest.

frontiers | Frontiers in Physics

ORIGINAL RESEARCH
published: 08 June 2022
doi: 10.3389/fphy.2022.816981

Detailed Simulation of Single-Bounce Capillaries for Various X-Ray Sources

*Shangkun Shao[1,2], Huiquan Li[1,2], Tianyu Yuan[1,2], Xiaoyun Zhang[1,2], Lu Hua[1,2], Xuepeng Sun[1,2], Zhiguo Liu[1,2] and Tianxi Sun[1,2]**

[1]Key Laboratory of Beam Technology of the Ministry of Education, College of Nuclear Science and Technology, Beijing Normal University, Beijing, China, [2]Beijing Radiation Center, Beijing, China

In order to draw a high-quality single-bounce capillary (SBC) to meet various applications, there is an increasing demand for detailed simulations of the SBC. In this study, a code based on the ray-tracing method was developed to simulate SBCs in detail for various X-ray sources to optimize their performances by considering factors such as attenuation of X-rays, coating, X-ray source characteristics (spot-size, distribution of energy, and intensity), surface shape errors, centerline errors, surface roughness, and absorption edges of X-rays. This code has monochrome and polychrome modes which were usually used to simulate the monoenergetic and polyenergetic performances of the SBC.

Keywords: mono-capillary X-ray optics, single-bounce capillary, simulation, X-ray, mono-capillary

Edited by:
Ming Li,
Institute of High Energy Physics (CAS),
China

Reviewed by:
P. S. Athiray,
University of Alabama in Huntsville,
United States
Manish Sharma,
Pacific Northwest National Laboratory
(DOE), United States

Correspondence:
Tianxi Sun
stx@bnu.edu.cn

Specialty section:
This article was submitted to
Optics and Photonics,
a section of the journal
Frontiers in Physics

Received: *17 November 2021*
Accepted: *22 April 2022*
Published: *08 June 2022*

Citation:
Shao S, Li H, Yuan T, Zhang X, Hua L, Sun X, Liu Z and Sun T (2022) Detailed Simulation of Single-Bounce Capillaries for Various X-Ray Sources.
Front. Phys. 10:816981.
doi: 10.3389/fphy.2022.816981

1 INTRODUCTION

The capillary X-ray optics works on total external reflection. When the grazing incidence angle of X-rays is less than the critical angle of total reflection θ_c, X-rays can be transmitted on the inner surface of the wall of the capillary. This critical angle θ_c depends on the refraction attenuation of the reflective material, and it can be described as follows:

$$\theta_c = \sqrt{2\delta}, \tag{1}$$

where δ is the real part of X-ray reflection n.

According to the number of capillaries, capillary X-ray optics is divided into poly-capillary and mono-capillary X-ray optics. The poly-capillary X-ray optics is drawn from tens of thousands to hundreds of thousands of hollow glass fibers, and each capillary points to the same focal spot, as shown in **Figure 1A**. Generally, the focal spot size is in the range of tens of microns to hundreds of microns, and the gain in power density can reach the order of 10^3 [1, 2]. The poly-capillary X-ray optics has been widely used in X-ray fluorescence (XRF) [3], X-ray diffraction (XRD) [4, 5], and X-ray absorption fine structure spectroscopy (XAFS) [6].

The mono-capillary X-ray optics drawn by a hollow glass tube can be divided into the multi-bounce capillary (MBC) and single-bounce capillary (SBC) based on the number of total reflections of X-rays on its inner surface. The MBC is often made into tapered surface which is easier to manufacture than the SBC (e.g., parabolic and ellipsoidal capillaries), as shown in **Figure 1B**. However, the tapered surface capillary has smaller transmission efficiency due to the multiple reflections of X-rays on its inner wall. Compared with the tapered surface capillary, the parabolic and ellipsoidal capillaries can obtain a transmission efficiency larger than 95% by a single X-ray reflection [7], as shown in **Figures 1C, D**. In addition, the SBC has the advantages of long working distance and controllable divergence, and it is suitable for a larger

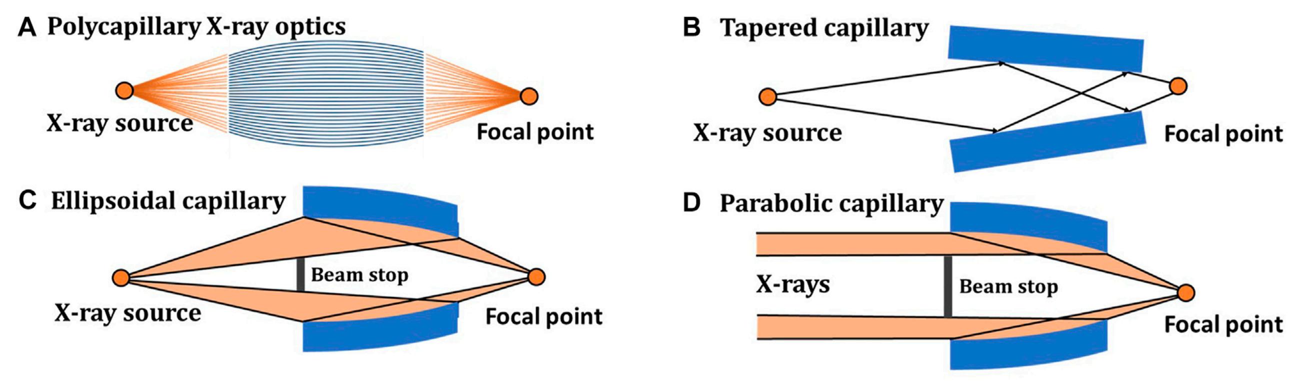

FIGURE 1 | Sketches of capillary X-ray optics focusing X-rays. **(A)** is poly-capillary X-ray optics. **(B)**, **(C)**, and **(D)** are tapered, ellipsoidal, and parabolic capillaries, respectively.

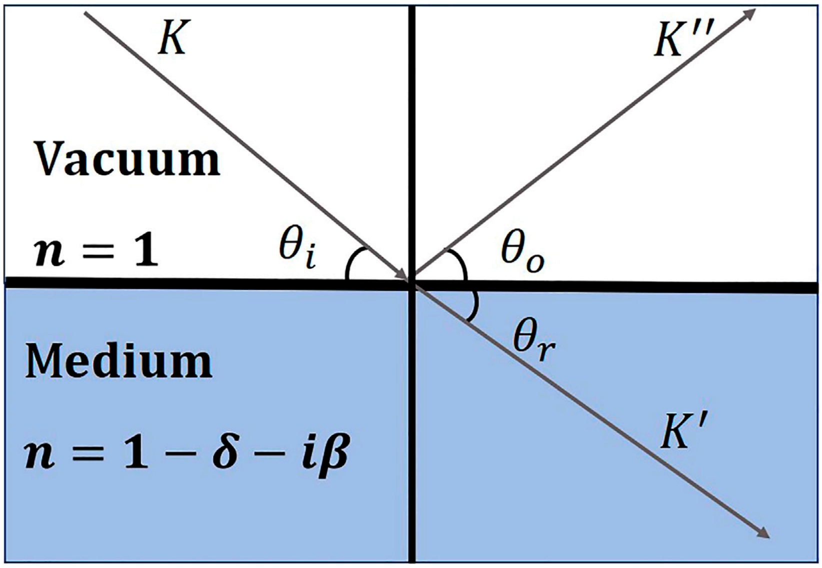

FIGURE 2 | X-ray reflection on a smooth surface.

variety of X-ray microbeam experiments such as X-ray crystallographic analysis [7], X-ray fluorescence imaging [8], and full-field transmission X-ray microscopy [9].

In practice, SBCs typically have centerline and surface shape errors. The centerline errors are the deviations of the actual centerline of the SBC from the theoretical centerline. Also, the surface shape errors are the deviations of the actual surface shape of the SBC from the theoretical surface shape. To draw a high-quality SBC to meet an application, the SBC should be designed specifically, and its various parameters, such as focal spot size, transmission efficiency, working distance, and divergence, should be optimized according to the special requirement of the application. There are some programs for simulating the SBC [10–12]; however, such programs cannot simulate the properties of an SBC with centerline and surface shape errors, and the attenuation of X-rays and X-ray source characteristics is not considered in their simulations. Therefore, a more detailed code should be designed to simulate the properties of an SBC.

In this study, a code based on the ray-tracing method was developed to simulate the SBC for various X-ray sources (e.g., synchrotron radiation source, laboratory source, and secondary X-ray source with focusing optical devices) by considering factors such as attenuation of X-rays, coating, X-ray source characteristics (spot-size, distribution of energy, and intensity), surface shape errors, centerline errors, surface roughness, and absorption edges of X-rays. To adapt to different applications, two working modes were designed. One was a monochrome mode which was usually used to simulate the mono-energetic performances of the SBC, and the other was a polychrome mode for simulating the polyenergetic performances by importing a primary spectrum of the X-ray source into the model.

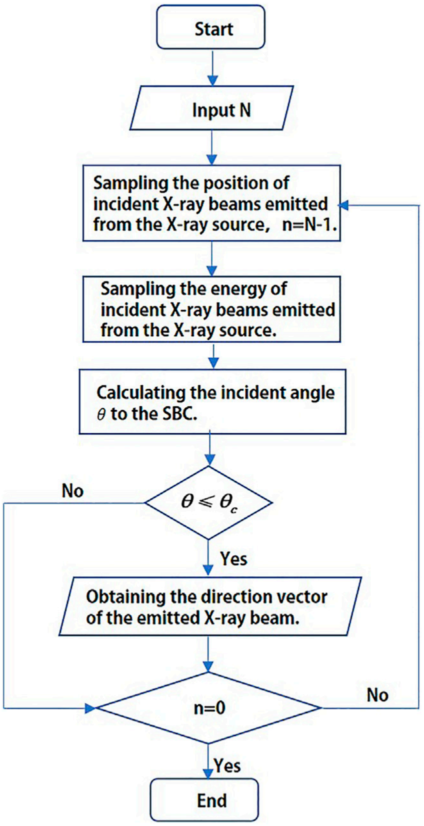

FIGURE 3 | Flow chart for simulating the SBC.

2 X-RAY TRANSMISSION THEORY

The smooth surface can totally reflect X-rays with a grazing incidence angle that is smaller than the critical angle θ_c for total external reflection (**Figure 2**).

For X-rays, the index of refraction can be written as follows:

$$n = 1 - \delta - \beta i, \tag{2}$$

where the real part δ is related to X-ray reflection and the imaginary part β has relations with X-ray absorption.

Relations between the reflectivity R and the incident angle θ can be given by the continuity conditions of the electric and magnetic fields at the interface [13]. The reflectivity R can be described as follows:

$$R = \frac{h - \left(\theta/\theta_c\sqrt{2(h-1)}\right)}{h + \left(\theta/\theta_c\sqrt{2(h-1)}\right)}, \tag{3}$$

where

$$h = \left(\frac{\theta}{\theta_c}\right)^2 + \left\{\left[\left(\frac{\theta}{\theta_c}\right)^2 - 1\right]^2 + \left(\frac{\beta}{\delta}\right)^2\right\}^{\frac{1}{2}}. \tag{4}$$

The inner wall of the SBC is not completely smooth, and the corrected reflectivity R_c by the roughness can be given by [14].

$$R_c = R \cdot \exp\left(-\frac{(4\pi\sigma\sin\theta)^2}{\lambda^2}\right), \tag{5}$$

where λ (nm) is the wavelength of incident X-rays and σ (nm) is the standard deviation of roughness.

Because of the photoelectric interaction, Rayleigh scattering, Compton scattering, and pair production (energy≥1.02 MeV, this effect can be neglected for SBC simulation), the intensity of X-rays passing through the air attenuates. When an X-ray beam with intensity I_0 propagates in the air, the intensity I of the X-rays transmitted along a length t in the air can be expressed as follows:

$$I = I_0 e^{-\mu t}, \tag{6}$$

where μ is the linear attenuation coefficient of the air.

3 SIMULATION MODEL

The code is built using MATLAB software. The simulation process is shown in **Figure 3**. First, the number N of X-ray beams emitted to the SBC was set. Then, the position coordinates, direction vectors, and the energy of the incident X-rays could be sampled. Finally, a series of ray-tracing processes were carried out. Since the ray-tracing method is a commonly used X-ray optical simulation method, it will not be repeated. The detailed description is given in reference [10].

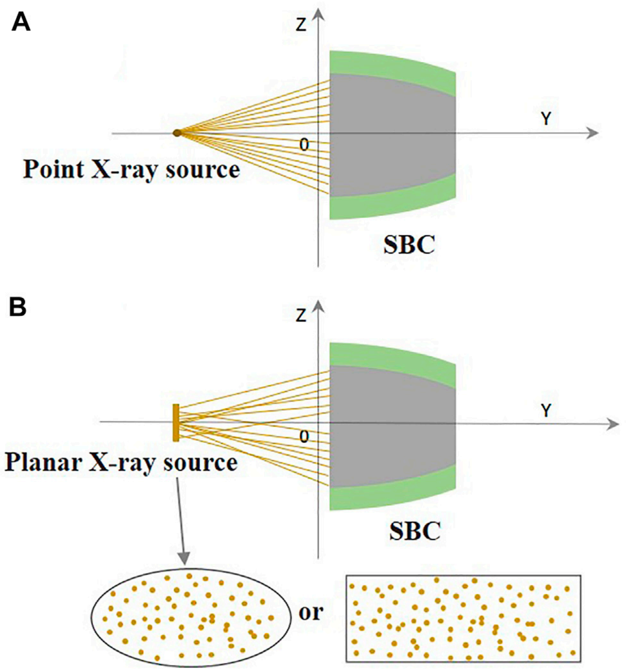

FIGURE 4 | Schematic diagram of X-rays incident on the SBC. **(A)** X-rays from the point source are incident on the SBC. **(B)** X-rays from the planar source are incident on the SBC.

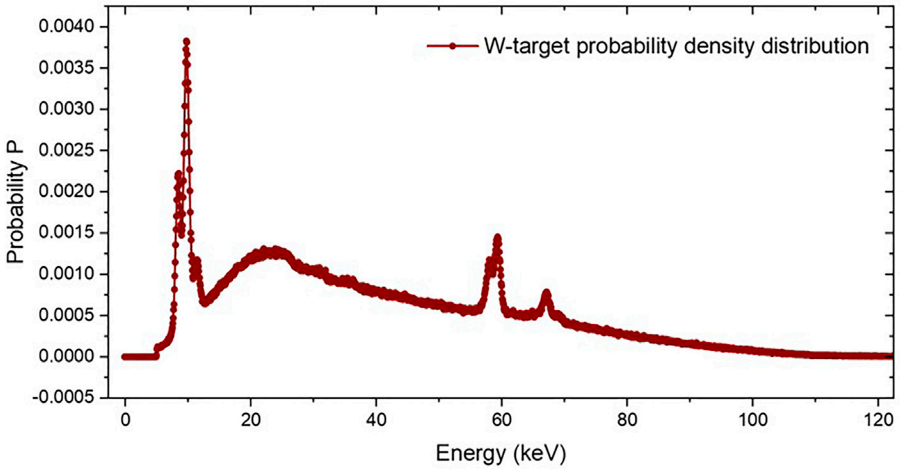

FIGURE 5 | Probability density distribution of the X-ray source. Probability density distribution converted from the primary spectrum of the X-ray source.

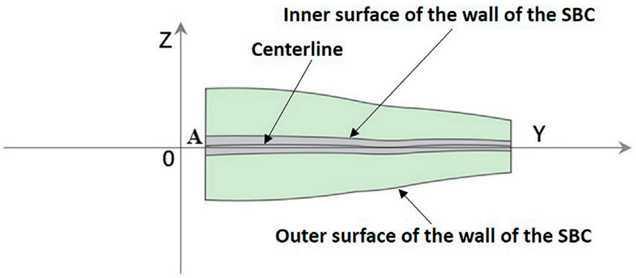

FIGURE 6 | Schematic diagram of the SBC with centerline and surface shape errors.

This simulation model has two types of X-ray simulation sources: point and planar X-ray sources (**Figure 4**). The planar X-ray source is more in accordance with the actual X-ray source than the point X-ray source. Therefore, elliptical and rectangular planar X-ray sources were provided to meet different simulation requirements. The model can utilize both uniform and Gaussian X-ray intensity distributions.

This simulation model has two modes: monochromatic and polychromatic. In the monochromatic mode, the mono-energetic performances of the SBC were simulated. Compared with the monochromatic mode, the primary spectrum of the X-ray source could be imported into the model to simulate the X-ray transmission in the polychromatic mode. In order to obtain the reflected energy spectrum, the primary spectrum was converted into a probability density distribution of energy E, as shown in **Figure 5**. The distribution law of the discrete random variable E can be given below:

$$P\{E = x_k\} = p_k, k = 1, 2, \cdots, \tag{7}$$

where x_k is a possible value of E.

$$p_k \geq 0, k = 1, 2, \cdots. \tag{8}$$

TABLE 1 | Parameters of the simulation X-ray sources.

X-ray source parameter	S₁	S₂	S₃
Type of planar source	Elliptic	Elliptic	Circular
Spot size (mm)	0.50 × 2.00	0.50 × 4.00	0.05 × 0.05
Intensity distribution	Gaussian	Gaussian	Gaussian
Energy distribution	Monoenergetic	Monoenergetic	W-target
Energy range	0.1–1 keV	5–20 keV	5–120 keV

$$\sum_k p_k = 1. \tag{9}$$

In practice, the centerline error is an important factor affecting the simulation results of the SBC. The ideal centerline of the SBC is a straight line along the y-axis; however, the actual centerline is a three-dimensional space curve, as shown in **Figure 6**. We assume that $A(0, y0, 0)$ is the first centerline data point at the entrance of the SBC and the centerline offsets along the x-axis and z-axis are $c_x(y)$ and $c_z(y)$, respectively. Therefore, the centerline errors of the SBC can be expressed as $\vec{C}(y) = c_x(y) \cdot \vec{x} + c_z(y) \cdot \vec{z}$. Due to the complexity of the perturbation of the surface shape of the SBC, we simplified the expression of surface shape errors and assumed that the cross-section of the SBC at the coordinate y could be expressed as follows:

$$\frac{(x - c_x(y))^2}{\left(a + s_x(y)^2\right)} + \frac{(z - c_z(y))^2}{\left(a + s_z(y)^2\right)} = 1, \tag{10}$$

where a was the semi-axis of the ideal ellipsoid in the x- and z-axis directions.

Surface shape errors can be given by $\vec{S}(y) = s_x(y) \cdot \vec{x} + s_z(y) \cdot \vec{z}$. In order to simplify the calculation process, the centerline and surface shape perturbation of the SBC can be fit by polynomial functions $f(y) = a_n y^n + a_{n-1} y^{(n-1)} + \cdots + a_2 y^2 + a_1 y + a_0$. Then, the

TABLE 2 | Design parameters of SBCs.

Design parameter	El_1	Pa_1	El_2
Semi-major axis b (mm)	300.00	-	260.00
Semi-minor axis a (mm)	3.00	-	0.30
Semi-latus rectum (p)	-	0.00022	-
Length (mm)	59.24	100	51.00
Input focal distance (mm)	523.59	34000	381.87
Working distance (mm)	17.14	50	88.03
Input diameter (mm)	4.00	0.5138	0.53
Output diameter (mm)	2.00	0.2966	0.45
Cut-off energy (keV)	1	20	60
Coating material	-	-	Ir

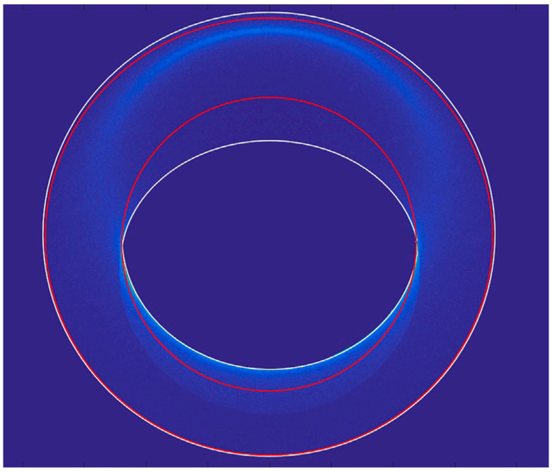

FIGURE 7 | Simulated far-field image of the ellipsoid capillary El_1. The two red circles represent the inner and outer boundaries of the ideal focusing ring. The two white irregular circles represent the inner and outer boundaries of the ideal focusing ring with the centerline and the surface shape errors.

model of the ellipsoid capillary with centerline and surface shape errors can be expressed as follows:

$$\frac{(x-c_x(y))^2}{(a+s_x(y))^2}+\frac{(y)^2}{b^2}+\frac{(z-c_z(y))^2}{(a+s_z(y))^2}=1, \tag{11}$$

where b is the semi-axis of the ideal ellipsoid in the y-axis direction.

The model of the parabolic capillary with centerline and surface shape errors is built as follows:

$$\frac{(x-c_x(y))^2}{(a+s_x(y))^2}+\frac{(z-c_z(y))^2}{(a+s_z(y))^2}=y+d, \tag{12}$$

where d is any real number.

4 SIMULATION

To verify the validity of the code, SBCs for three different X-ray sources were simulated by using polychromatic and monochromatic modes. We studied such parameters of the SBCs, that is, transmission efficiency, focal spot size, and divergence. The transmission efficiency η of X-rays through the SBC can be defined as follows:

$$\eta=\frac{I_{out}}{I_{in}}, \tag{13}$$

where I_{in} is the beam flux entering the SBC with a beam stop (**Figures 1C, D**) and I_{out} is the beam flux emitted from the outlet of the SBC.

The parameters of the simulation X-ray sources are presented in **Table 1**. Sources S_1 and S_2 are synchrotron X-ray sources with focusing optical devices, and S_3 is a W-target laboratory X-ray source.

The design parameters of SBCs are shown in **Table 2**. The El_1 is an ellipsoid capillary used for the synchrotron radiation soft X-ray source S_1, and Pa_1 is a parabolic capillary for the synchrotron radiation hard X-ray source S_2 with a quasi-parallel beam. The laboratory X-ray source has relatively less beam flux than synchrotron radiation sources. The coated SBC has a large solid angle for receiving incident X-rays than the uncoated SBC, which improves the beam flux at the focal spot. El_2 is an Ir-coated ellipsoidal capillary for the W-target laboratory X-ray source $S_{3,}$ with an energy range of 5–120 keV.

5 RESULTS AND DISCUSSION

The simulated far-field image of the ellipsoid capillary El_1 is presented in **Figure 7**. The distortion of the focusing ring is related to the centerline and the surface shape errors. If the focusing ring of the SBC has larger distortion, the SBC is of low quality and its parameters (transmission efficiency, focal spot size, and divergence) will have a large deviation from the theoretical design parameters.

The divergence angle and focal spot size of SBCs are shown in **Table 3**. The focal spot size was obtained by fitting the simulated

TABLE 3 | Divergence angle and focal spot size of SBCs.

Parameter	The types of SBC		
	El_1	Pa_1	El_2
Minimum divergence angle (mrad)	53.21	3.50	3.78
Maximum divergence angle (mrad)	116.78	6.05	5.13
Focal spot size (μm)	30.01 ± 1.50	2.66 ± 0.51	11.98 ± 0.60

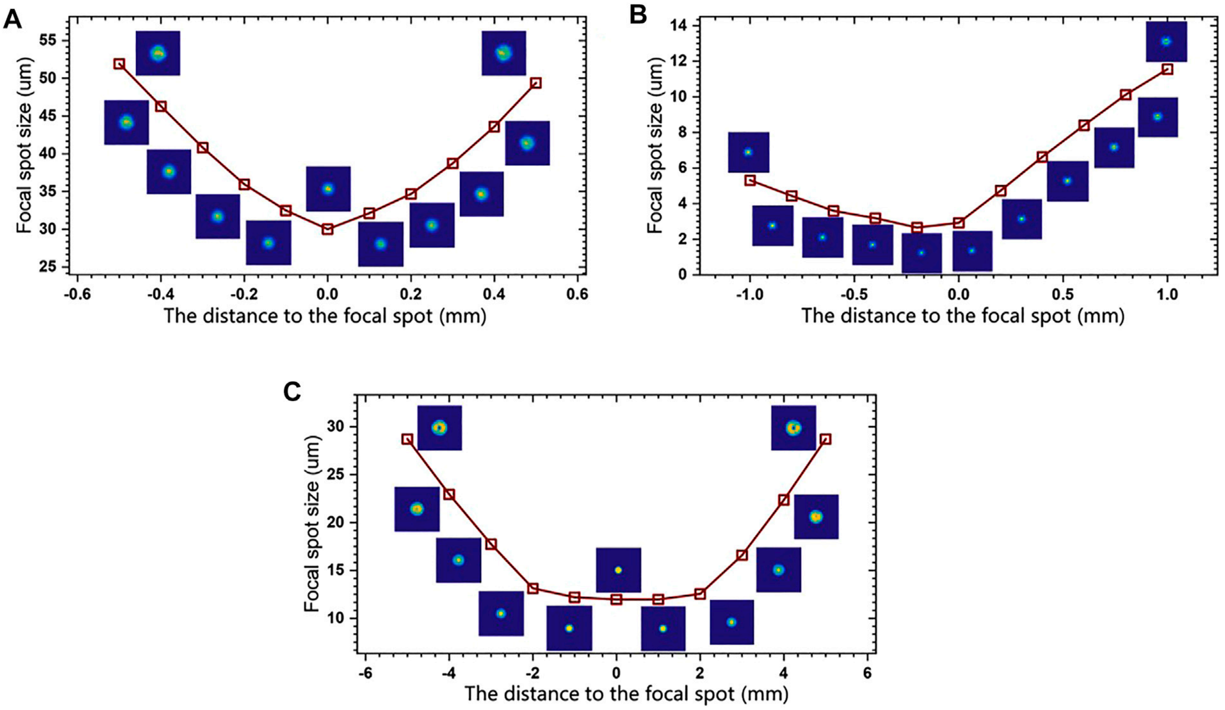

FIGURE 8 | Evolution of the focal spot size with the distance to the focal spot. **(A)** and **(C)** are the ellipsoid capillaries El_1 and El_2, respectively. **(B)** is the parabolic capillary Pa_1.

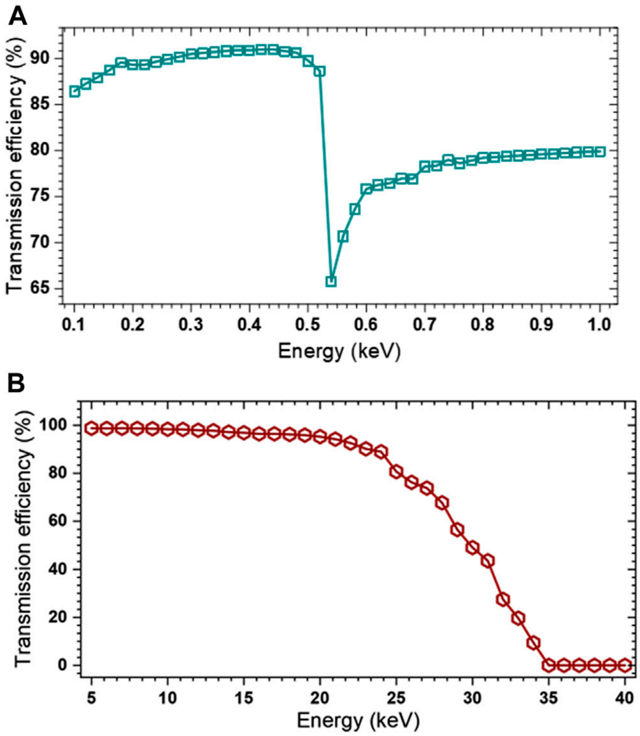

FIGURE 9 | Energy dependence of the transmission efficiency. **(A)** and **(B)** are the transmission efficiency curves of the ellipsoid capillary El_1 and parabolic capillary Pa_1, respectively.

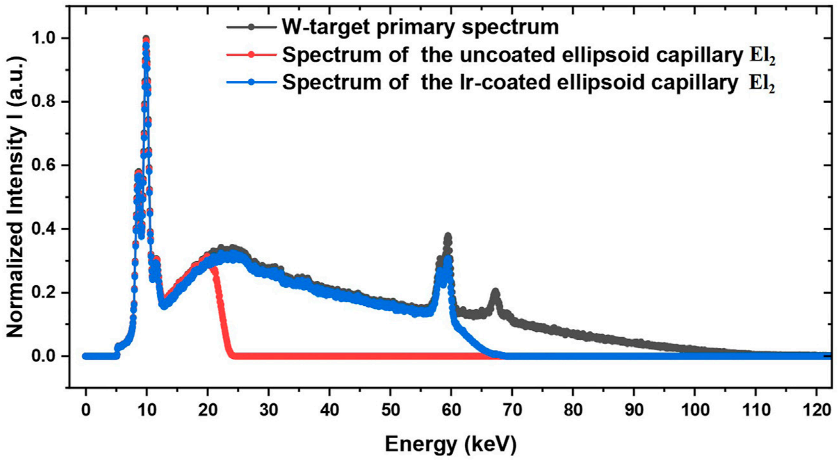

FIGURE 10 | Normalized spectrums of the reflected X-rays of the ellipsoid capillary El$_2$. The gray curve is the W-target primary normalized spectrum. The red and blue curves are the normalized reflected energy spectrums of the uncoated and Ir-coated ellipsoid capillaries, respectively.

focal spot data with a Gaussian function, and it is the full width at half maximum (FHWM) of the Gaussian fitting function. The synchrotron radiation hard X-ray source S$_2$ has high collimation properties so that the focal spot size of the parabolic capillary Pa$_1$ is smaller than that of the other two SBCs. Due to the large critical total reflection angle θ_c of soft X-rays, the SBC used for soft X-rays usually has large acceptance and divergence angles. Therefore, the divergence angles of the ellipsoid capillary El$_1$ are much larger than those of the other two SBCs.

Figure 8 shows the evolution of the focal spot size with the distance to the focal spot. When the incident X-ray energy is less than the cut-off energy, the focal spot characteristics are energy-independent [15]. Therefore, it was only necessary to study the focal spot characteristics of a certain energy. As shown in **Figure 8A**, the X-ray beams exited from the ellipsoid capillary El$_1$ were first focused to a minimum focal spot size, and then they were rapidly defocused so that the ellipsoid capillary El$_1$ had a shorter focal depth. The non-strictly parallel incident X-rays resulted in an asymmetry in a focal spot size of the parabolic capillary Pa$_1$ between 0.0 and 1.0 mm and 0.0 and 1.0 mm, as shown in **Figure 8B**.

Figure 9 shows the energy dependence of the transmission efficiency for the ellipsoid capillary El$_1$ and parabolic capillary Pa1. Since the SBC is usually made of borosilicate glass with a large amount of oxygen, X-rays at the absorption edge of oxygen are strongly absorbed, which can lead to lower transmission efficiency of the ellipsoid capillary El$_1$ at an energy of 0.543 keV, as shown in **Figure 9A**. The transmission efficiency of the parabolic capillary Pa$_1$ was greater than 95% in the energy range of 5–20 keV, as shown in **Figure 9B**. Therefore, it is necessary to consider the absorption edge effect in the simulation of the SBC for soft X-rays.

Figure 10 shows normalized spectrums of the reflected X-rays of the ellipsoid capillary El$_2$. We compared the polyenergetic performances of the Ir-coated ellipsoid capillary and uncoated ones for the W-target laboratory X-ray source S$_3$. The transmission efficiency of the uncoated ellipsoid capillary El$_2$ rapidly decreased to zero at the energy of 20 keV. The critical angle of total reflection θ_c of the Ir-coated capillary was increased by 1.77 times. Hence, in the energy range greater than 20 keV, the transmission efficiency of the Ir-coated ellipsoid capillary El$_2$ had a significant increase compared to that of the uncoated ones. In addition, when the energy is greater than 60 keV, the incident angle of the Ir-coated capillary was smaller than the critical angle of total reflection θ_c, which leads to the transmission efficiency decreasing to zero quickly. Therefore, the coating could enhance the performance of the SBC to reflect high-energy X-rays.

6 CONCLUSION

To meet the rapid development of the SBC, a code for various types of X-ray sources was proposed to optimize their performance by considering such factors (e.g., attenuation of X-rays, roughness, coating, X-ray source characteristics, surface shape error, centerline error, surface roughness, and absorption edges of X-ray). Also, we have given two different modes: monochrome and polychrome modes. The monochromatic mode is usually used for the simulation of the SBC of the synchrotron radiation source. For the polychrome mode, the primary spectrum of the practical X-ray source can be imported into the program to simulate the SBC parameters, which is more in accordance with reality. In addition, the reflected energy spectrum can be obtained in the polychromatic mode, which can help scientists design the SBC that is most suitable for their application.

Although only the ellipsoid and parabolic capillary models are established in Sec.3, they can be easily extended to other types of capillaries, such as hyperbolic, double parabolic, and Walter-1. Relevant investigations on these topics will be carried out in the near future.

DATA AVAILABILITY STATEMENT

The original contributions presented in the study are included in the article/Supplementary Material; further inquiries can be directed to the corresponding authors.

AUTHOR CONTRIBUTIONS

SS: simulation, methodology, and writing. HL: investigation. XZ: investigation. TY: investigation. LH: investigation. XS: supervision. ZL: supervision. TS: methodology and supervision.

FUNDING

This work was supported by the National Natural Science Foundation of China (Grant Nos 11875087 and 12105220), the Chinese National Key Research and Development Plan (No. 2018YFF0109100), the Chinese Academy of Sciences Key Technology Research and Development Team (No. GJJSTD20170005), and the Beijing Academy of Science and Technology (No. BGS202106).

REFERENCES

1. Guilherme A, Buzanich G, Carvalho ML. Focusing Systems for the Generation of X-ray Micro Beam: An Overview. *Spectrochimica Acta B: At Spectrosc* (2012) 77:1–8. doi:10.1016/j.sab.2012.07.021
2. MacDonald CA. Focusing Polycapillary Optics and Their Applications. *X-ray Opt Instrumentation* (2010) 2010:17. doi:10.1155/2010/867049
3. Peng S, Liu Z, Sun T, Ma Y, Ding X. Spatially Resolved *In Situ* Measurements of the Ion Distribution Near the Surface of Electrode in a Steady-State Diffusion in an Electrolytic Tank with Confocal Micro X-ray Fluorescence. *Anal Chem* (2014) 86:362–6. doi:10.1021/ac403188k
4. Sun T, Liu H, Liu Z, Peng S, Ma Y, Sun W, et al. Application of Confocal Technology Based on Polycapillary X-ray Optics in Three-Dimensional Diffraction Scanning Analysis. *Nucl Instr Methods Phys Res Section B: Beam Interactions Mater Atoms* (2014) 323:25–9. doi:10.1016/j.nimb.2014.01.013
5. Yamanashi M, Tsuji K. Development of Full-Field XRD (FFXRD) Imaging Method Realized in the Laboratory Using a Straight Polycapillary and *In Situ* Observation of the Oxidation Process of Cu by Heat Treatment. *E-j Surf Sci Nanotec* (2020) 18:1–7. doi:10.1380/ejssnt.2020.1
6. Sun T, Liu Z, Ding X. Characterization of a Polycapillary Focusing X-ray Lens for Application in Spatially Resolved EXAFS Experiments. *Chem Phys Lett* (2007) 439:412–4. doi:10.1016/j.cplett.2007.03.105
7. Bilderback DH, Huang R. X-ray Tests of Microfocusing Mono-Capillary Optic for Protein Crystallography. *Nucl Instr Methods Phys Res Section A: Acc Spectrometers, Detectors Associated Equipment* (2001) 467-468:970–3. doi:10.1016/s0168-9002(01)00543-5
8. Woll AR, Mass J, Bisulca C, Huang R, Bilderback DH, Gruner S, et al. Development of Confocal X-ray Fluorescence (XRF) Microscopy at the Cornell High Energy Synchrotron Source. *Appl Phys A* (2006) 83:235–8. doi:10.1007/s00339-006-3513-4
9. Zeng X, Duewer F, Feser M, Huang C, Lyon A, Tkachuk A, et al. Ellipsoidal and Parabolic Glass Capillaries as Condensers for X-ray Microscopes. *Appl Opt* (2008) 47:2376–81. doi:10.1364/ao.47.002376
10. Lin X, Liu A, Li Y, Wu P. A MATLAB Programming for Simulation of X-ray Capillaries. *Appl Math Comput* (2006) 172:188–97. doi:10.1016/j.amc.2005.01.150
11. Liu A. Simulation of X-ray Propagation in a Straight Capillary. *Mathematics Comput Simulation* (2004) 65:251–6. doi:10.1016/j.matcom.2004.01.001
12. Liu A, Lin Y. Simulation of X-ray Transmission in Capillaries with Different Profiles. *Math Comput Simulation* (2004) 66:577–84. doi:10.1016/j.matcom.2004.05.001
13. Takano A, Maehata K, Iyomoto N, Hara T, Mitsuda K, Yamasaki N, et al.Simulation Model of Transmitted X-Rays in Polycapillary Optics for TES Microcalorimeter EDS System on Scanning Transmission Electron Microscope. *IEEE Trans Nucl Sci* (2018) 65:758–65. doi:10.1109/tns.2017.2786703
14. Zymierska D. Determination of Surface Roughness Bu Grazing Incidence X-ray Reflectivity. *Acta Phys Pol A* (1996) 89:347–52. doi:10.12693/aphyspola.89.347
15. Huang R, Bilderback DH. Simulation of Microfocused Image Size from a One-Bounce Glass Capillary. *Nucl Instr Methods Phys Res Section A: Acc Spectrometers, Detectors Associated Equipment* (2001) 467-468:978–81. doi:10.1016/s0168-9002(01)00546-0

Conflict of Interest: The authors declare that the research was conducted in the absence of any commercial or financial relationships that could be construed as a potential conflict of interest.

frontiers | Frontiers in Physics

ORIGINAL RESEARCH
published: 28 June 2022
doi: 10.3389/fphy.2022.908380

Feasibility Analysis of Sapphire Compound Refractive Lenses for Advanced X-Ray Light Sources

Yunzhu Wang[1,2], *Xiaohao Dong*[2,3]* *and Jun Hu*[1,3]

[1]School of Physical Science and Technology, ShanghaiTech University, Shanghai, China, [2]Shanghai High Repetition Rate XFEL and Extreme Light Facility, Shanghai, China, [3]Shanghai Advanced Research Institute, Chinese Academy of Sciences, Shanghai, China

The compound refractive lens (CRL) is a commonly used X-ray optical component for photon beam conditioning and focusing on the beamlines of the X-ray facilities. The normal preparation materials are beryllium, aluminum, silicon of current lenses, and they all suffered from high heat load fatigue and short pulse damage risks. Hard materials based CRL is engaged attention for the advanced X-ray application. Sapphire crystal has the advantages of high density, high melting point, low thermal expansion coefficient. In this paper, properties of the refraction and absorption ratio of Sapphire and parameters of Sapphire lenses of effective aperture, transmittance, resolution, number of lenses needed for a certain focus, are taken into account for the CRL design, comparing with those of several common materials as well. The calculation results show that the performance of the sapphire lens is better than that of the aluminum lens and silicon lens, and inferior to that of the beryllium lens and diamond lens, but the number of lenses used is less. In the meantime, performances of sapphire lenses focusing are simulated and thermal effects on lenses are analyzed. Analysis and discussion are carried out under the same conditions as the metal Aluminum ones. The focusing simulation shows that the sapphire lenses can obtain a smaller spot with more intensity. The thermal analysis indicates that the temperature during use of the sapphire lens is much lower than the melting point of sapphire, and the thermal deformation is negligible.

Keywords: compound refractive lens, sapphire, x-ray optics, focusing, photon beam conditioning

Edited by:
Jifeng Liu,
Dartmouth College, United States

Reviewed by:
Airan Rodenas,
University of La Laguna, Spain
Xiangping Li,
Jinan University, China

****Correspondence:***
Xiaohao Dong
dongxiaohao@zjlab.org.cn

Specialty section:
This article was submitted to Optics and Photonics, a section of the journal Frontiers in Physics

Received: *30 March 2022*
Accepted: *08 June 2022*
Published: *28 June 2022*

Citation:
Wang Y, Dong X and Hu J (2022) Feasibility Analysis of Sapphire Compound Refractive Lenses for Advanced X-Ray Light Sources. Front. Phys. 10:908380. doi: 10.3389/fphy.2022.908380

INTRODUCTION

With the development of the forth-generation synchrotron radiation sources and X-ray free electron lasers facilities, beamlines with high energy, high intensity, low divergence have been produced, and X-ray analysis technology has been more widely used in material structure and material dynamics, biophysics and protein crystallography, geophysics and environmental science and the research in other subject areas [1]. With the deepening of these researches, the requirements for X-ray resolution are getting higher and higher. At the same time, higher standards are put forward for X-ray optical devices, and X-ray nano-focusing devices have also caused more and more focus.

Since the refractive index of material for X-rays is less than 1, the focusing of X-rays could only be done employing reflection and diffraction. Until 1996, researchers such as Snigirev demonstrated focusing capabilities of the refractive optics, so called compound refractive lens (CRL) [2]. They machined 30 circular holes with a diameter of 600 μm on an aluminum plate, focused X-rays with an energy of 14 keV at 1.8 m, and obtained a spot of 8 μm. Compared with other X-ray optics, compound refractive lenses have many advantages. CRL has low requirements on the surface roughness of the lens, does not change the direction of the optical path, can work at high temperature, and is easy to align. Therefore, CRL has developed rapidly. Therefore, it has been developed rapidly. At present, compound refractive lenses include cylindrical, parabolic [3], planar [4], saw-tooth [5], spherical [6], etc. Among them, the parabolic lens is the most widely used due to its small aberration.

At present, the most commonly used X-ray compound refractive lenses are made from elements of beryllium (Be) [7], diamond (C) [8], aluminum (Al) [2], silicon (Si) [9]. Be is the earliest applied lens material and is widely used in wide-spectrum X-rays ranging from 3 to 60 keV. However, Be is highly toxic. And after processing and manufacturing, the single crystal Be will be transformed into polycrystalline, and the single crystal Be lens cannot be obtained. Imperfections of Be leads to the increase of small-angle scattering, which is easy to produce spots, and spoil the focusing. The resolution of Be lens is only about 100 nm [10]. In addition, the thermal expansion coefficient of Be is relatively large, and the long-term high thermal load operation makes the Be lens prone to recrystallization behavior, resulting in fatigue damage and thermal deformation [11].

Diamond has the advantages of high density, low X-ray absorption, low thermal expansion coefficient, high thermal conductivity coefficient, and high thermal damage threshold [12]. Therefore, diamond has been the material of choice for several crucial high-heat component applications in X-ray optics, including double-crystal monochromators [13] and high-reflectivity Bragg mirrors [14]. Using single crystal diamond to prepare a composite refractive lens can improve the uniformity of electron density, small angle scattering signal, less speckle, and more conducive to focusing. A resolution of about 40 nm can be obtained [15]. However, the hardness of the diamond is relatively high, and the processing is complex. At present, diamond composite refractive lenses can be manufactured by ion beam lithography [15] and laser pulse technology [8] can be used to manufacture diamond composite refractive lenses at present. The surface roughness of the processed diamond lens can currently reach about 20 nm [16].

Another popular material for compound refractive lenses are polymer materials, such as polymethyl methacrylate (PMMA). Lenses are often prepared in combination with 3D printing technology [17]. A resolution of around 100 nm can be obtained [18]. It has many advantages. However, the lens made of this material has low thermal conductivity, low melting point, strong small-angle scattering signal, and poor resistance to thermal damage and radiation.

Alumina is a compound material of Aluminum Oxide (Al_2O_3) with high hardness, high density, high temperature resistance and low thermal expansion coefficient. In the past, alumina was not used for compound refractive lenses due to the limitation of processing techniques, since that it was difficult to manufacture a lens with sub-nanometer surface roughness and sub-microradian shape errors of hard materials. But at present, advanced processing techniques, such as ultrafast laser ablation, offers a higher level of surface quality (that is, low surface roughness values). Alumina has a variety of structures, commonly alpha-alumina (α-alumina) and gamma-alumina. Among them, α-alumina has the densest structure and the highest density, and at high temperature, all crystalline aluminas will be converted into α-alumina. Sapphire is α-alumina, doped with a small amount of titanium and iron, has been increasingly used in optical components for high heat load optics of light sources like powerful lasers, bright synchrotron radiation, etc.

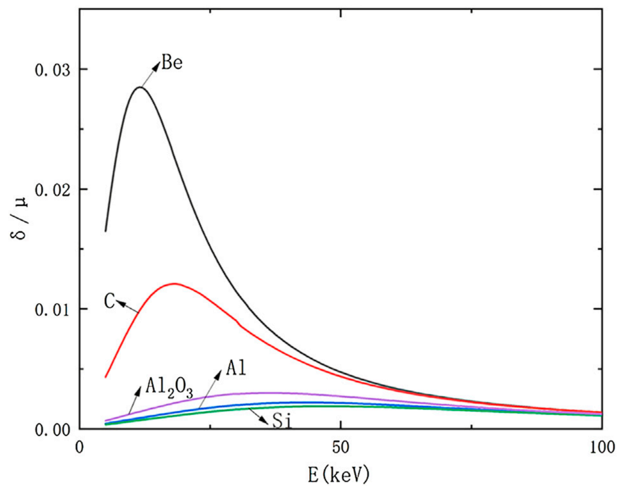

FIGURE 1 | The δ/μ ratio of several common materials at 5–100 keV.

In this article, we analyze the optical parameters, machinability, uniformity, etc. of sapphire material for X-ray compound refractive lenses, and the focusing simulation of the sapphire X-ray compound refractive lenses as designed is carried out compared to the ones made of metal Aluminum. As an addition, we also considered the thermal stability of the sapphire lenses proposed to be used for high heat load X-ray source as free electron lasers as well.

MATERIAL SELECTION CONSIDERATION

The refractive index of X-rays in the material is:

$$n = 1 - \delta + i\beta$$

where δ is the refractive indices, which is positively related to the atomic number and density. And β is the absorption coefficient, which is also positively related to the atomic number and density [7, 19]. In the process of using the lens, it is hoped that the refraction effect of the material is good and the absorption is small. Therefore, the higher the ratio of the refractive index to the absorption coefficient (δ/β) of the material, the better. That is, it is better that the atomic number of the material is small. At the same time, the higher the density of the material, the stronger the refracted electromagnetic wave, so it is hoped that the material has a lower atomic number and a higher density to achieve a better focusing effect. And $\beta = \mu\lambda/4\pi$, so δ/μ can be also used to represent the refraction absorption ratio. **Figure 1** shows the δ/μ

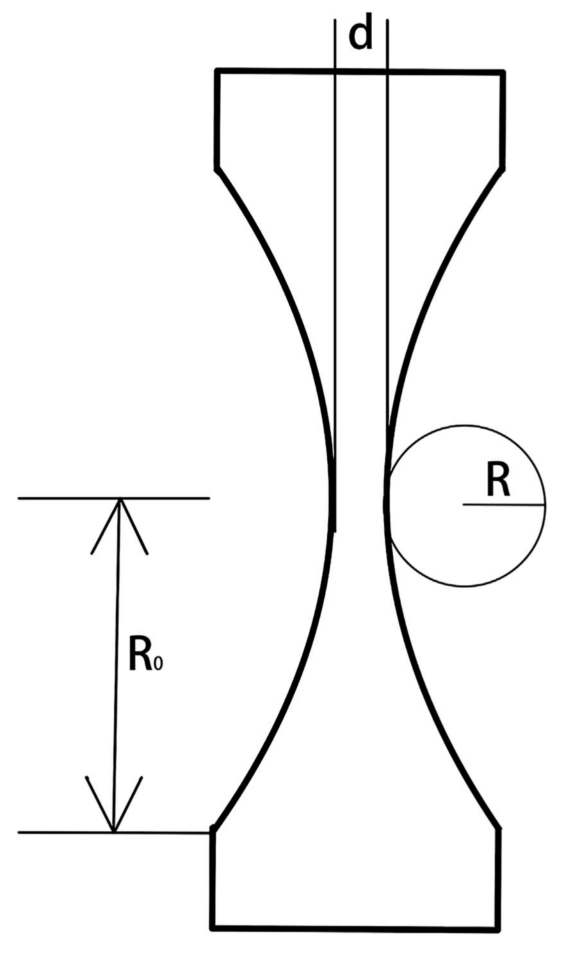

FIGURE 2 | Geometrical scheme of a single lens.

value of several common compound refractive lens materials within 5–100 keV (the calculation data and the following are from the website [20]). As shown in **Figure 1**, below 50 keV, compared with beryllium and diamond, the refractive absorption of sapphire is relatively small. Still, it is better than that of materials such as silicon and aluminum. Above 50 keV, the refraction and absorption ratios of several materials are not much different. Although the refractive absorption ratio of beryllium and diamond is relatively large, as we mentioned in the Introduction, beryllium and diamond have limitations. Beryllium lenses are always polycrystalline, and diamond lenses are difficult to process, so we choose sapphire as the material of the lens.

The focal length of the lens is:

$$f = R/2N\delta$$

where R is the radius of curvature at the vertex of the lens (**Figure 2**), and N is the number of lenses. The number of lenses used can be determined after determining the required focal length, working energy, and materials used. Calculate the number of lenses as are necessary for several common materials within 5–100 keV. The radius of curvature is set to 50 μm. The focal length is set to 10m, and the calculation results are shown in **Figure 3** (The result is not rounded). Compared with other materials, under the condition of achieving the same focusing effect, the number of sapphire lenses used is the least, even half the number of lenses required by other materials. Then, in the process of actual engineering use, can reduce the cost of the lenses. Certainly that, it can reduce alignment errors caused by the many-groups lenses stacks.

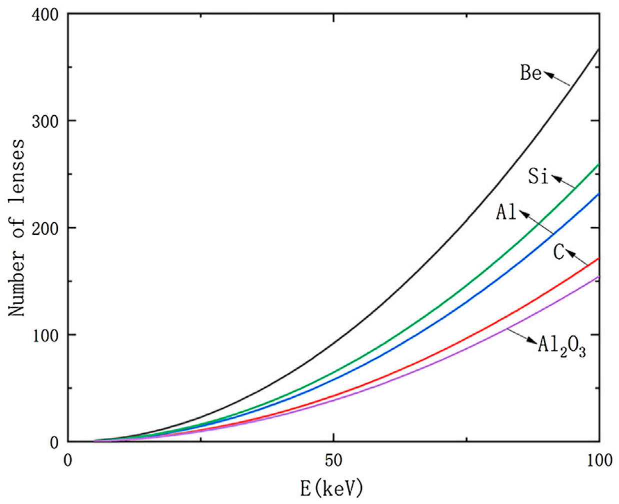

FIGURE 3 | The number of lenses required for several common materials at 5–100 keV.

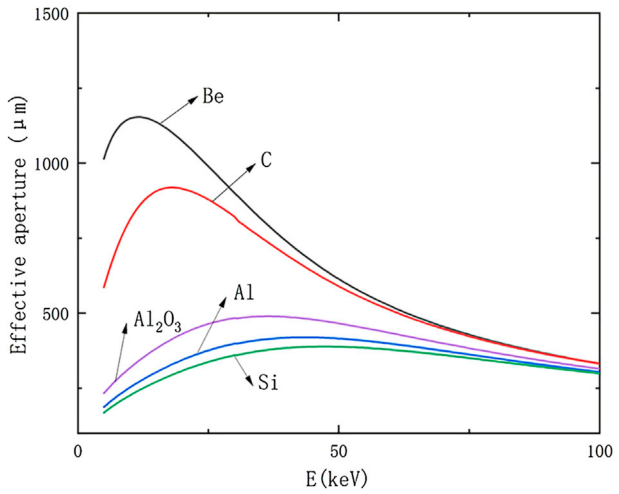

FIGURE 4 | Effective aperture of several common materials at 5–100 keV.

Considerations of sapphire lenses will be discussed from the following aspects.

i) Consideration of the effective aperture of the sapphire lens. Due to the absorption and scattering effects of X-rays in

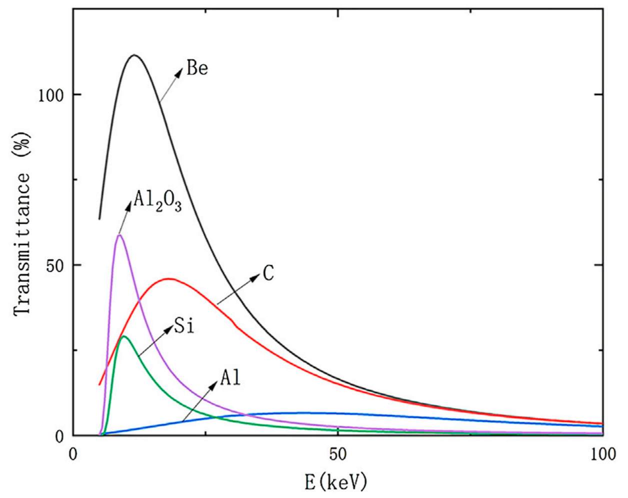

FIGURE 5 | Transmittance of several common materials at 5–100 keV.

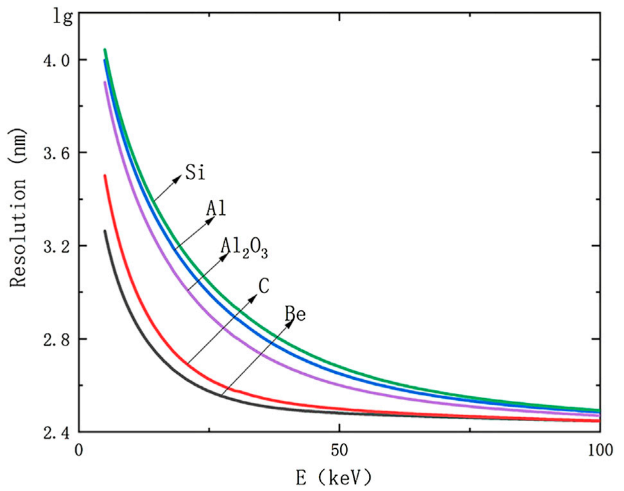

FIGURE 6 | 5–100 keV lateral resolution for several common materials.

materials, only part of the photons of X-rays can pass through the lens. Assuming that the intensity of the transmitted X-rays is evenly distributed on a circle, the diameter of the circle is the effective diameter of the lens. The effective aperture of the lenses is:

$$D_{eff} = 2\sqrt{R/\mu N}\sqrt{1 - \exp(-a)}$$

where $a = \frac{\mu N R_0^2}{R}$. Calculate the effective aperture of several common materials within 5–100 keV. Refer to **Figure 3** for the setting of the number of lenses. The radius of curvature is set to 50 μm. The effective aperture is set to 1000 μm. The focal length is set to 10m. The calculation results are shown in **Figure 4**. Compared with beryllium and diamond, the effective aperture of sapphire is smaller under the same conditions, but compared with materials such as silicon and aluminum, the sapphire lens has advantages.

ii) Consideration of the transmittance of the sapphire lens during use, it is the ratio of the total light intensity passing through the lens to the full light intensity that the lens can receive. The transmittance of the lens is:

$$T_p = \frac{1 - \exp(-a)}{a}\exp(-\mu N d)]$$

It can be clearly seen from the formula that the transmittance. It is related to the choice of material and the distance between the two vertices of the lens. The transmittance of several common materials in the range of 5–100 keV is calculated. The distance between the two paraboloids is set to 50 μm. Other settings are the same as **Figure 3** and **Figure 4**. The calculation results are shown in **Figure 5**. In the range of low energy, the transmittance of sapphire is higher, even better than that of the diamond; in the middle energy range, the transmittance of sapphire is lower than that of diamond, etc. In the high energy range, there is little difference between several materials.

iii) Consideration of the resolution of the sapphire lens. Resolution is divided into horizontal resolution and vertical resolution, which refers to the distance between the smallest two points that can be distinguished through the lens. That is to say, when the distance between two points is smaller than the resolution, it cannot be discerned. The resolution of the lens is $d_h = 0.75\lambda L_1/D_{eff}$ in the horizontal direction and $d_l = \frac{8\lambda}{\pi}\frac{4L_1^2}{D_{eff}^2}$ in the vertical direction, where L_1 is the object distance. Both lateral and vertical resolution are negatively related to the effective aperture. The larger the effective aperture, the smaller the resolution of the lens. The lateral resolution of several common materials within 5–100 keV is calculated. The parameter settings are the same as before. The calculation results are shown in **Figure 6** (For comparison purposes, we log the results). The results are similar to the refraction and absorption ratio and the effective aperture. Compared with beryllium and diamond, sapphire is weaker, but compared with materials such as silicon and aluminum, the sapphire lens has advantages.

Consideration of the uniformity of the lens. The uniformity of the material will affect the wavefront of the X-ray, which will affect the refraction and focusing effect of the lens. The better the uniformity of the material, the better the refraction and focusing effect of the lens. Density variations, stacking faults, dislocations, inclusions, and voids affect the uniformity of the material. These cause intensity variations across the beam cross-section, halos from small-angle X-ray scattering, and different phase shifts in the beam's wavefront, all expressed as wavefront distortion. To evaluate the uniformity of the material, it can be measured by small-angle scattering [21]. For the same material, the small-angle scattering signal of single-crystal is smaller than that of polycrystalline material. Sapphire crystal has two forms of single-crystal and polycrystalline. Single-crystal sapphire will not be transformed into polycrystalline after mechanical processing

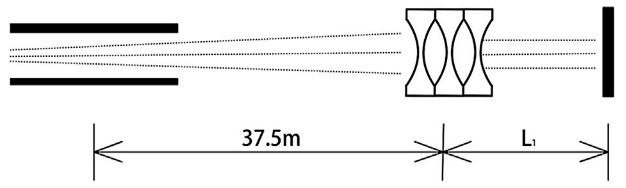

FIGURE 7 | Optical configuration for Simulation.

or special processing, which can reduce the small-angle scattering signal, reduce the wavefront distortion, and is more conducive to focusing. A lens made of a single crystal material may cause Bragg diffraction when specific incident photon energies are satisfied, resulting in a decrease in the transmission intensity. Still when only one set of crystal planes is met, the diffraction can be ignored [22]. In addition to single crystal polycrystals affecting the uniformity of sapphire, the growth method of the sapphire also affects the uniformity. Tsai et al. [23] found that optical-grade sapphire grown by the heat exchange method (HEM) had a much lower dislocation density than sapphire grown by the Kylopoulos method (KYM). Obviously, the sapphire grown by the HEM method has better uniformity and is more suitable as a material for sapphire lenses.

iv) Consideration of the machinability of the sapphire lenses. The material of the lens needs to be capable of mechanical processing or special processing, and the properties of the material remain basically unchanged before and after processing. Lenses need to have a good surface profile and surface roughness but are much less demanding than mirrors. This is because the beam propagates almost perpendicular to the interface, rather than at grazing incidence, so high surface precision is not required [7]. Due to the advantages and characteristics of high-resolution processing capability, arbitrary designability, and a wide range of processing materials, femtosecond laser micro-nano processing technology has been widely used in micro-mechanics, micro-optics, optical sensing, and bionic devices. Any complex three-dimensional micro-nano structures preparation. Using femtosecond laser processing technology can realize the preparation of the micro-nano structure of the sapphire crystal. After fabrication, the surface roughness of sapphire can reach several tens of nanometers. The surface roughness of the sapphire-based Fresnel zone plate prepared by Li et al. achieved 12 nm [24]; Wang et al. found that the surface roughness can reach about 15 nm in the anisotropy study of sapphire [25].

SAPPHIRE LENS FOCUSING SIMULATION AND THERMAL ANALYSIS

Focusing Performance Simulation

After comprehensively considering optical performance parameters of the sapphire lenses, the SRW (Synchrotron Radiation Workshop) code [26] is used to perform a case of focusing simulation. The parameter settings are the same as the previous calculation. The simulation layout is shown in **Figure 7**. The simulation results are shown in **Figure 8**.

Simulations were performed at 10 keV for sapphire and aluminum lenses. The radii of curvature of the sapphire lens and the aluminum lens were both set to 250 μm, and the geometric apertures were both set to 1000 μm. To obtain the same focal length, the number of sapphire lenses is set to 2. And the number of aluminum lenses is set to 3. The calculated focus of the sapphire lens is about 7.66 m and the effective aperture is 279 μm. The calculated focus of the sapphire lens is about 7.64 m and the effective aperture is 221 μm. **Figure 8A** is the simulation result of the aluminum compound refracting lens, which is the light spot near the focal point. **Figure 8B** is the simulation result of the sapphire compound refracting lens, which is the light spot near the focal point. **Figure 8C** is the aluminum lens and the sapphire lens at x = The intensity at 0, **Figure 8D** is the intensity of the aluminum lens and the sapphire lens at y = 0. It can be seen from Figures (A) and (B) that the light spot formed by the aluminum lens is slightly smaller than that formed by the sapphire lens. The focal spot formed by the sapphire lens is significantly smaller than that formed by the aluminum lens. From Figure (C), the light spot passing through the sapphire lens has a longitudinal half-width of about 50 μm; the light spot passing through the aluminum lens has a longitudinal half-height width of about 47 μm. From Figure (D), the light spot passing through the sapphire lens has a lateral half-height width of about 54 μm; the light spot passing through the aluminum lens has a lateral half-height width of about 38 μm. Under the condition of obtaining the same focal length, the effective aperture of the sapphire lens is larger, and the required number is smaller, and the obtained beam intensity is higher.

Thermal Effects Analysis

The brightness of the third-generation synchrotron radiation source is significantly improved, and the thermal load is also considerably increased, which may cause related deformation. Therefore, the compound refractive lens material needs to have good thermal properties, high-temperature resistance, and low thermal expansion coefficient. For refractive parabolic lenses, the change of focal length with temperature is $\Delta f/f = \alpha\Delta T$ [9], where α is the thermal expansion coefficient. So the thermal expansion coefficient is too large, which will affect the focusing effect. The melting point of sapphire is higher, reaching 2050°C, the thermal expansion coefficient is small, the deformation at high temperature is small, and the influence on the refraction is also tiny. Therefore, it can maintain relatively good working performance at high temperatures. In order to observe the temperature distribution of the sapphire lens under illumination, the finite element thermal analysis of the sapphire lens was carried out using ANSYS software

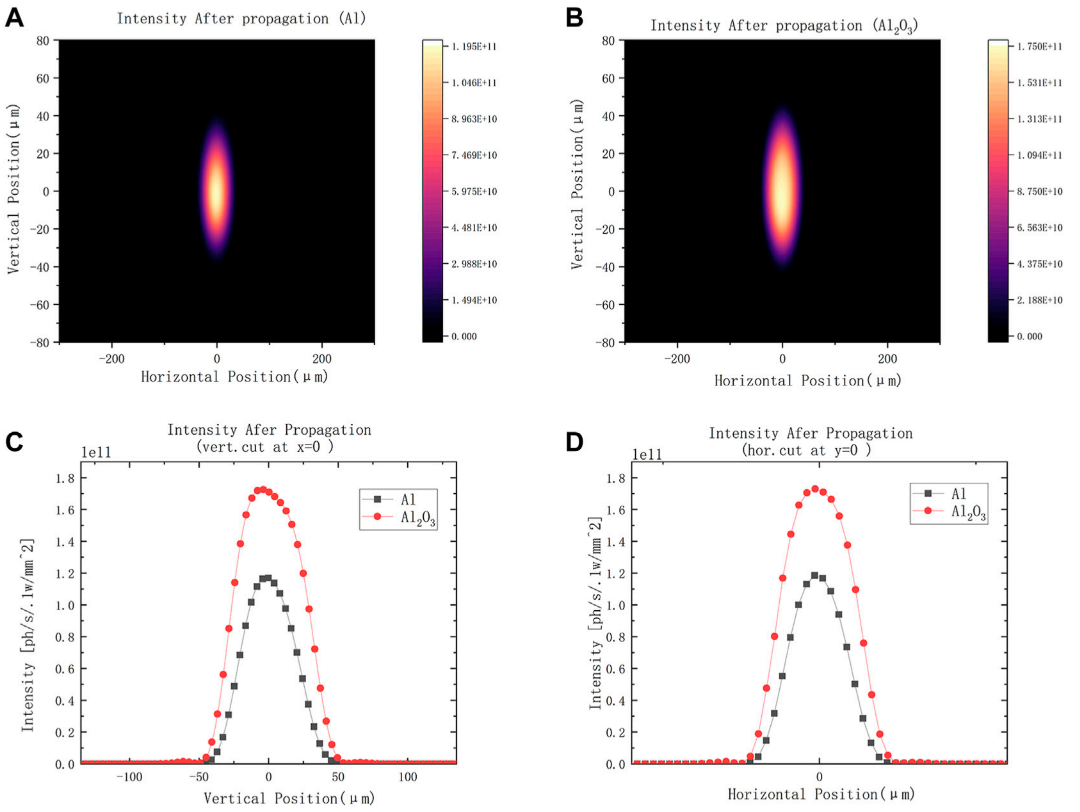

FIGURE 8 | (A) Intensity distribution of ~10 keV X-ray focused with aluminum lens. **(B)** Intensity distribution of ~10 keV X-ray focused with sapphire lens. **(C)** The intensity after propagation at $x = 0$. **(D)** The intensity after propagation at $y = 0$.

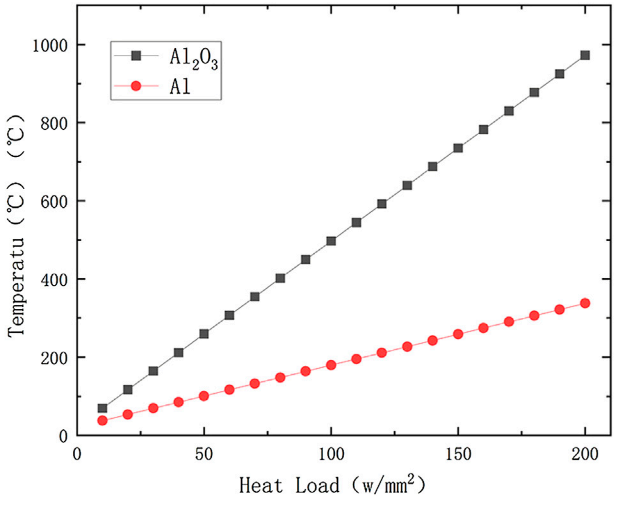

FIGURE 9 | Thermal analysis temperature comparison of sapphire lens and aluminum lens.

[27]. During the simulation, the thermal load range is 0–200 w/mm^2, and the cooling coefficient of water cooling is around 2000–10,000 w/m^2/°C [11]. A simple preliminary simulation is carried out according to this condition.

Figure 9 shows the thermal analysis results of the sapphire lens and the aluminum lens. Under the same conditions, the temperature of the sapphire lens is always higher than that of the aluminum lens. But aluminum is a metal with a melting point of 660°C. When the temperature reaches about 200°C, recrystallization begins to occur. And the higher the purity of aluminum, the lower the recrystallization start temperature. Therefore, when the thermal load reaches 110, the aluminum lens will recrystallize, affecting the uniformity inside the lens, and even leading to the formation of cracks. Simulation calculations also show that, due to the small thermal expansion coefficient of sapphire, the stress and strain caused by temperature gradients in the lens are small and can be ignored.

CONCLUSION

The parameters of several commonly used X-ray compound refractive lens materials are calculated and compared, including refraction and absorption ratio, number of lenses, effective aperture, transmittance, resolution, etc. Most calculations show that sapphire is superior to materials such as aluminum and silicon and inferior to materials such as beryllium and diamond. However, in the case of reaching the same focal length, the number of sapphire lenses used is the least, which can reduce the error caused by the length of the lens group. At the same time, the possible cost of the lens during actual use is reduced. Through the lens simulation, it can be found that under the same focal length, the number of sapphire lenses is less, and the transmitted X-ray light is stronger. Through thermal analysis of sapphire, it is found that the highest temperature that may be generated is much lower than the melting point of sapphire, and the resulting thermal stress can also be ignored. In actual use, the processing difficulty of sapphire lens is far less than that of diamond. Considering these factors, the use of sapphire lenses is feasible in future X-ray optics engineering.

In future work, we will conduct further simulations and calculations on the sapphire lens, including the phase defect of the sapphire lens based on X-ray wave optics for diffraction-limited synchrotrons and free-electron lasers [28]. Currently, Sapphire lenses are being fabricated by ultra-fast laser ablation. Experiments will be conducted soon for quality characterization of the sapphire lenses and focusing performances as well.

DATA AVAILABILITY STATEMENT

The original contributions presented in the study are included in the article/Supplementary Material, further inquiries can be directed to the corresponding author.

AUTHOR CONTRIBUTIONS

YW is responsible for calculations and writing paper. XD is responsible for guidance and revision. JH is responsible for providing guidance.

FUNDING

This work was supported by the National Natural Science Foundation of China (Grant No.U1832172), and the Science and Technology Major Project of Shanghai (Grant No.2017SHZDZX02), and grants from Talent Program (2018) and R&D program of optics (2021) for large scientific infrastructures of the Chinese Academy of Sciences.

REFERENCES

1. Ice GE, Budai JD, Pang JWL. The Race to X-Ray Microbeam and Nanobeam Science. *Science* (2011) 334(6060):1234–9. doi:10.1126/science.1202366
2. Snigirev A, Kohn V, Snigireva I, Lengeler B. A Compound Refractive Lens for Focusing High-Energy X-Rays. *Nature* (1996) 384(6604):49–51. doi:10.1038/384049a0
3. Lengeler B, Schroer CG, Benner B, Gerhardus A, Günzler TF, Kuhlmann M, et al.Parabolic Refractive X-Ray Lenses. *J Sync. Radiat* (2002) 9(Pt 3):119–24. doi:10.1107/s0909049502003436
4. Aristov V, Grigoriev M, Kuznetsov S, Shabelnikov L, Yunkin V, Weitkamp T, et al.X-Ray Refractive Planar Lens with Minimized Absorption. *Appl Phys Lett* (2000) 77(24):4058–60. doi:10.1063/1.1332401
5. Cederström B, Cahn RN, Danielsson M, Lundqvist M, Nygren DR. Focusing Hard X-Rays with Old Lps. *Nature* (2000) 404(6781):951. doi:10.1038/35010190
6. Beguiristain HR, Anderson IS, Dewhurst CD, Piestrup MA, Cremer JT, Pantell RH. A Simple Neutron Microscope Using a Compound Refractive Lens. *Appl Phys Lett* (2002) 81(22):4290–2. doi:10.1063/1.1524698
7. Lengeler B, Schroer C, Tümmler J, Benner B, Richwin M, Snigirev A, et al.Imaging by Parabolic Refractive Lenses in the Hard X-Ray Range. *J Sync. Radiat* (1999) 6(6):1153–67. doi:10.1107/s0909049599009747
8. Terentyev S, Blank V, Polyakov S, Zholudev S, Snigirev A, Polikarpov M, et al.Parabolic Single-Crystal Diamond Lenses for Coherent X-Ray Imaging. *Appl Phys Lett* (2015) 107(11):111108. doi:10.1063/1.4931357
9. V Aristov, M Grigoriev, S Kuznetsov, L Shabelnikov, V Yunkin, C Rau, et al.Silicon Planar Parabolic Lenses. X-Ray Mirrors, Crystals, and Multilayers Conference; 2000 Aug 02-04; San Diego, Ca (2001).
10. I Snigireva, GBM Vaughan, A Snigirev, editors. High-Energy Nanoscale-Resolution X-Ray Microscopy Based on Refractive Optics on a Long Beamline. 10th International Conference on X-ray Microscopy; 2010 Aug 15-20. Chicago, IL: Univ Chicago (2011).
11. L Zhang, A Snigirev, I Snigireva, G Naylor, A Madsen, F Zontone, et al.Thermo-Mechanical Analysis and Design Optimization of Front-End Compound Refractive Lens. Conference on Design and Microfabrication of Novel X-Ray Optics II; 2004 Aug 05-06; Denver, CO (2004).
12. Medvedev N, Jeschke HO, Ziaja B. Nonthermal Graphitization of Diamond Induced by a Femtosecond X-Ray Laser Pulse. *Phys Rev B* (2013) 88(22). doi:10.1103/PhysRevB.88.224304
13. Fernandez PB, Graber T, Lee WK, Mills DM, Rogers CS, Assoufid L. Test of a High-Heat-Load Double-Crystal Diamond Monochromator at the Advanced Photon Source. *Nucl Instr Methods Phys Res Section a-Accelerators Spectrometers Detectors Associated Equipment* (1997) 400(2-3):476–83. doi:10.1016/s0168-9002(97)01014-0
14. Shvyd'ko Y, Stoupin S, Blank V, Terentyev S. Near-100% Bragg Reflectivity of X-Rays. *Nat Photon* (2011) 5(9):539–42. doi:10.1038/nphoton.2011.197
15. Medvedskaya P, Lyatun I, Shevyrtalov S, Polikarpov M, Snigireva I, Yunkin V, et al.Diamond Refractive Micro-lenses for Full-Field X-Ray Imaging and Microscopy Produced with Ion Beam Lithography. *Opt Express* (2020) 28(4):4773–85. doi:10.1364/oe.384647
16. Celestre R, Antipov S, Gomez E, Zinn T, Barrett R, Roth T. Polished Diamond X-Ray Lenses. *J Sync. Radiat* (2022) 29(3):629–43. doi:10.1107/s1600577522001795
17. Mirzaeimoghri M, Morales Martinez A, Panna A, Bennett EE, Lucotte BM, DeVoe DL, et al.Nano-Printed Miniature Compound Refractive Lens for Desktop Hard X-Ray Microscopy. *Plos One* (2018) 13(8):e0203319. doi:10.1371/journal.pone.0203319
18. Lyubomirskiy M, Koch F, Abrashitova KA, Bessonov VO, Kokareva N, Petrov A, et al.Ptychographic Characterisation of Polymer Compound Refractive Lenses Manufactured by Additive Technology. *Opt Express* (2019) 27(6):8639–50. doi:10.1364/oe.27.008639
19. Serebrennikov D, Clementyev E, Semenov A, Snigirev A. Optical Performance of Materials for X-Ray Refractive Optics in the Energy Range 8–100 Kev. *J Synchrotron Radiat* (2016) 23:1315–22. doi:10.1107/S1600577516014508
20. X-Ray Optics Calculator. X-Ray Optics Calculator. Available at: http://purple.iptm.ru/xcalc/xcalc_mysql/ref_index.php (Accessed December 4, 2021).
21. T Roth, L Helfen, J Hallmann, L Samoylova, P Kwasniewski, B Lengeler, et al.X-Ray Laminography and Saxs on Beryllium Grades and Lenses and Wavefront Propagation through Imperfect Compound Refractive Lenses. Conference on Advances in X-Ray/EUV Optics and Components IX held as part of the SPIE 2014 International Symposium on Optics + Photonics; 2014 Aug 18-20; San Diego, CA (2014).
22. Terentyev S, Polikarpov M, Snigireva I, Di Michiel M, Zholudev S, Yunkin V, et al.Linear Parabolic Single-Crystal Diamond Refractive Lenses for Synchrotron X-Ray Sources. *J Sync. Radiat* (2017) 24:103–9. doi:10.1107/s1600577516017331
23. Tsai Y-W, Wu Y-H, Chang Y-Y, Liu W-C, Liu H-L, Chu C-H, et al.Sapphire Hard X-Ray Fabry-Perot Resonators for Synchrotron Experiments. *J Sync. Radiat* (2016) 23:658–64. doi:10.1107/s1600577516004999

24. Li Q-K, Yu Y-H, Wang L, Cao X-W, Liu X-Q, Sun Y-L, et al.Sapphire-Based Fresnel Zone Plate Fabricated by Femtosecond Laser Direct Writing and Wet Etching. *IEEE Photon Technol Lett* (2016) 28(12):1290–3. doi:10.1109/lpt.2016.2538270
25. Wang J, Guo B, Zhao Q, Zeng Z, Zhai W, Chen H, et al.Investigation into the Anisotropy of Cross-Grinding Surface Quality in C- and M-Planes of Sapphire. *Proc Inst Mech Eng B: J Eng Manufacture* (2019) 233(1):44–54. doi:10.1177/0954405417718596
26. Chubar O, Elleaume P. Accurate and Efficient Computation of Synchrotron Radiation in the Near Field Region. In: Proceedings, 6th European conference, EPAC'98; June 22-26, 1998; Stockholm, Sweden, 1-3 (1998). p. 1177–9.
27. Ansys. Ansys. Available from: https://www.ansys.com/ (Accessed October 25, 2021).
28. Celestre R, Berujon S, Roth T, Sanchez del Rio M, Barrett R. Modelling Phase Imperfections in Compound Refractive Lenses. *J Sync. Radiat* (2020) 27: 305–18. doi:10.1107/s1600577519017235

Conflict of Interest: The authors declare that the research was conducted in the absence of any commercial or financial relationships that could be construed as a potential conflict of interest.

frontiers | Frontiers in Physics

TYPE Original Research
PUBLISHED 30 August 2022
DOI 10.3389/fphy.2022.977957

Check for updates

OPEN ACCESS

EDITED BY
Qiushi Huang,
Tongji University, China

REVIEWED BY
Manoj Tiwari,
Raja Ramanna Centre for Advanced Technology, India
Yinpeng Zhong,
Institute of Advanced Science Facilities, Shenzhen, China

*CORRESPONDENCE
Huaidong Jiang,
jianghd@shanghaitech.edu.cn

SPECIALTY SECTION
This article was submitted to Optics and Photonics,
a section of the journal
Frontiers in Physics

RECEIVED 25 June 2022
ACCEPTED 02 August 2022
PUBLISHED 30 August 2022

CITATION
Tong Y, Fan J, Nie Y, Guo Z, Gao Z, Yuan X, He B, Chen J, Zhang D, Luan H, Zhang J, Lu D, Xie M, Cheng P, Feng C, Liu T, Deng H, Liu B, Liu Z and Jiang H (2022), Kirkpatrick-Baez mirrors commissioning for coherent scattering and imaging endstation at SXFEL. *Front. Phys.* 10:977957.
doi: 10.3389/fphy.2022.977957

Kirkpatrick-Baez mirrors commissioning for coherent scattering and imaging endstation at SXFEL

Yajun Tong[1], Jiadong Fan[1], Yonggan Nie[1], Zhi Guo[2], Zichen Gao[3], Xinye Yuan[3], Bo He[3], Jiahua Chen[2], Difei Zhang[3], Hui Luan[3], Jianhua Zhang[1], Donghao Lu[3], Minghan Xie[3], Peng Cheng[3], Chao Feng[2], Tao Liu[2], Haixiao Deng[2], Bo Liu[2], Zhi Liu[1,3] and Huaidong Jiang[1,3]*

[1]Center for Transformative Science, ShanghaiTech University, Shanghai, China, [2]Shanghai Synchrotron Radiation Facility, Shanghai Advanced Research Institute, Chinese Academy of Sciences, Shanghai, China, [3]School of Physical Science and Technology, ShanghaiTech University, Shanghai, China

Shanghai Soft X-ray Free-Electron Laser (SXFEL) is the first X-ray free-electron laser facility in China. The initial commissioning of the beamline was carried out in May 2021. Herein, we present a status report and the first experimental results obtained during the early commissioning of Kirkpatrick-Baez (KB) mirrors for the Coherent Scattering and Imaging (CSI) endstation, including three types of diagnostics. A bright X-ray focal spot of less than 3 μm was achieved by using edge-scan and silicon ablation imprint measurements. In order to confirm the spot size, the attenuated beam and full beam are used respectively for the two measurement methods.

KEYWORDS

x-ray optics, diagnostics, free electron laser, KB mirrors, beamline

Introduction

Shanghai Soft X-ray Free-Electron Laser (SXFEL) [1, 2], as the first XFEL in China, consists of two established beamlines. One is a self-amplified spontaneous emission (SASE) beamline, and the other is echo enabled harmonic generation (EEHG) beamline. So far, there are five constructed endstations, focusing on dynamic and radiation damage-free imaging, ultrafast physical phenomena, surface and ultrafast chemical processes, and atomic and molecular physics. Among the five endstations, the Coherent Scattering and Imaging (CSI) endstation is designed for high temporal and spatial imaging with coherent diffraction imaging (CDI) and Fourier transform holography (FTH). Furthermore, other methods based on forward scattering geometry can also be available, such as time-resolved small-angle X-ray scattering (Tr-SAXS). To achieve high spatial resolution at the CSI endstaiton, a high flux density at sample position is required. A Kirkpatrick-Baez (KB) system was installed at the upstream of the CSI endstation to focus the beam down to a few micrometers [3]. The KB mirrors for CSI

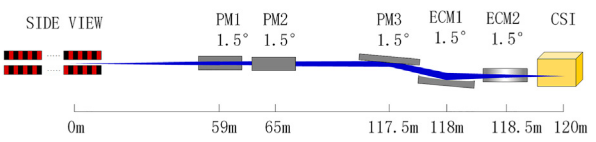

FIGURE 1
Layout of the beamline for CSI.

endstation were commissioned, and the first coherent diffraction imaging experiment of samples was successfully demonstrated.

Various appropriate diagnostics at the focusing position are required to obtain good focusing in the shortest time during the commissioning process. The pioneers of FEL have shown different diagnostics, such as a YAG screen with a microscope, PMMA ablation imprints, wire (or edge) scan, wavefront sensor, etc. The YAG screen method [4, 5] is a convenient way to characterize the focus spot. But to obtain a high spatial resolution, such as sub-micrometer, an in-vacuum high numerical aperture (NA) objective is essential and more space is needed. A low-resolution microscope is also very useful for rough alignment as it has a large field of view (FOV). Beam attenuation is required to avoid radiation damage to the YAG screen. The PMMA ablation imprints are usually used to obtain the actual beam shape. It has been widely used to determine the focus spot size and the focus position at FLASH, FERMI, LCLS and SACLA ([4, 6–10]). However, it can not give a fast online determination, as it takes time to remove the PMMA from vacuum and image it with a microscope or scan it with a AFM. The wire (edge) scan [9, 11–14] is a common method used to measure the beam size. Similar to YAG screen imaging, the XFEL pulse energy needs to be attenuated to avoid radiation damage to wire (edge). On the other hand, the wire (edge) scan is an accumulation of multi-shot, thus, the stability of the beam is convoluted to the beam size. It can not identify the tilt of the spot, but it is suitable for the final measurements. The wavefront sensor [6, 13, 15–19] is a very useful method, especially for bendable mirrors. A bendable KB system with a wavefront sensor was developed at FERMI [5, 7]. It is an ideal method, as the wavefront error can be decomposed into Zernike coefficients which represent the possible source of errors. It can give the direction of the alignment. However, the FOV of the wavefront sensor is limited, and a rough commissioning is still necessary beforehand. In summary, although each method has its own advantages and limitations, combining various characterization methods can accelerate the commissioning process and get optimized focus results during the KB mirrors commissioning.

In this paper the KB system alignment process and focusing result at the CSI endstation of SXFEL are reported. The different characterization methods for rough commissioning, fine commissioning, and final characterization are presented.

Beamline and focus diagnostics

Figure 1 shows the beamline layout of the CSI endstation. The first and second plane mirrors are offset mirrors, which are located at 59 and 65 m downstream of the source respectively, and generate a horizontal offset of 314 mm to block the high energy radiations easily. A plane mirror PM3 located at 117.5 m, is parallel with the vertical focusing mirror ECM1, so it can make the exit beam in the horizontal plane. The last mirror is the horizontal focusing mirror ECM2. The image distances of ECM1 and ECM2 are 2 and 1.5 m, respectively. These three mirrors are in the same chamber. A gas attenuator is positioned in front of PM1 to adjust the pulse energy. Two gas monitors are installed in front and back of the gas attenuator to monitor the pulse energy. A solid attenuator is located in front of PM3 to supply further attenuation abilities. The grazing angles of all mirrors are 1.5°, and all mirrors are coated with B_4C for the energy range of 100–1,000 eV (except for the carbon K edge and boron K edge). The mirrors were made by Jtec. According to the Maréchal criterion, the height errors were calculated with Eq. 1, where h is height error, λ is the wavelength, θ is the grazing angle, and N is the number of optics. It should be smaller than 0.76 nm RMS for 5 mirrors at 1,000 eV, and 1.46 nm RMS at 520 eV. Table 1 shows the requirements of the mirrors. The theoretical beam size is about 1.8 μm (H) × 2.4 μm (V) from the simulation.

$$\boldsymbol{h} \approx \frac{\lambda}{\mathbf{14}\times\ \mathbf{2}\times\ \theta\times\sqrt{\boldsymbol{N}}} \tag{1}$$

The CSI endstation is shown in Figure 2. The main components are sample chamber and detector chamber. To characterize the KB focusing properties, various diagnostic tools were installed inside and on the sample chamber. First, a large FOV imaging system was mounted on the sample chamber cover as shown in Figure 2. It includes a camera (Basler a2A5328-15 um BAS, 2.74 μm pixel size) and a 75 mm focal length lens (Computar V7531-MPZ). Through a 45° view window which points to the focusing position, a YAG screen mounted on the sample stage could be imaged by the large FOV imaging system. Such a configuration can offer a pixel resolution of about 15 μm with a FOV of about 78 mm × 67 mm. Because the YAG screen is not perpendicular to the optical axis of the lens, the image out of focal depth is blurred. The second is an inline microscope, which is designed for locating the fixed target sample and XFEL beam position. It consists of a long working distance (LWD) microscope (UWZ400F), a view window, and a 45° mirror. The LWD microscope has a fixed working distance of 400 mm and allows samples to be viewed through an observation window with the help of a 45° lens. On the 45° mirror, a 2 mm hole was drilled to enable it to work online. It has inline illumination, its spatial resolution is 6.71 μm, and its pixel resolution is about 1 μm. Due to the numerical aperture (NA) limitation, it is difficult to catch the focusing spot with enough signal-to-noise ratio (SNR). The edge scan system includes a knife-edge (silicon edge) and an X-ray sensitive photodiode (XUV100), which is achieved by scanning the knife-edge mounted on the sample stages and recording the signal of the photodiode behind the frame

TABLE 1 Requirements of mirrors.

Mirrors	PM1	PM2	PM3	ECM1	ECM2
Shape	Plane	Plane	Plane	Elliptical	Elliptical
Optical area (mm)	400 × 30	400 × 30	400 × 30	400 × 30	400 × 30
Distance to source(m)	59.0	65.0	117.5	118.0	118.5
Image distance(m)	—	—	—	2.0	1.5
Coating/thickness (nm)	B_4C/40	B_4C/40	B_4C/40	B_4C/40	B_4C/40
Height error (RMS/PV) (nm)	0.75/3	0.75/3	0.75/3	0.75/3	0.75/3
Roughness (nm)	0.3	0.3	0.3	0.3	0.3

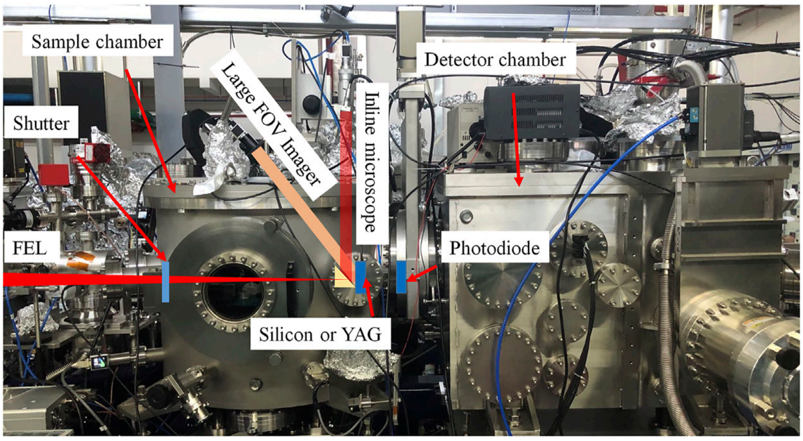

FIGURE 2
Photo of the CSI endstation.

step by step. The signal is recorded by an oscilloscope. The X-ray detector was used to confirm the full beam entering to the sample chamber. A shutter was installed at the beam entrance of the chamber to select single pulses. All of the devices are controlled with the EPICS and triggered by the White Rabbit based timing system. The data acquisition is realized with PyEpics. The commissioning of the KB system was performed at 520 eV with a repetition of 2 Hz.

The commissioning of KB system

Before commissioning, all the components of the beamline were aligned with a laser tracker. A number of apertures were mounted in front of important components to avoid damage. Especially, there are two 8 mm apertures in the differential pumping system between the KB mirror chamber and the sample chamber. These apertures make the online alignment complicated. Therefore, an X-ray detector was used initially to ensure that the entire beam entered to the sample chamber.

Rough alignment

The main purpose of rough alignment is to focus the beam to a size that can easily damage the silicon. It was performed with the large FOV imaging system. A 10 mm × 10 mm YAG screen mounted on the sample stages was placed at the theoretical focusing position. From the large FOV imaging system, a bright spot of hundreds of micrometers was observed. The beam was focused from hundreds of micrometers to tens of micrometers by tuning the KB mirrors. In order to avoid radiation damage of the YAG screen, the pressure of the gas attenuator was increased as the spot size diminishing. A Python script was used to track and display the spot area for convenience. It can display the spots in an image with pixel values as shown in Figure 3. When the spot size is big, the image can show the special shape of the beam, such as tilt and tails. When the beam size is small and only few pixels are bright, the pixel value is very useful. Figure 4 shows the ratio of the maximum pixel value of the Gaussian beam to neighbor pixel value changed with the full width at half height (FWHM) beam size. For example, the

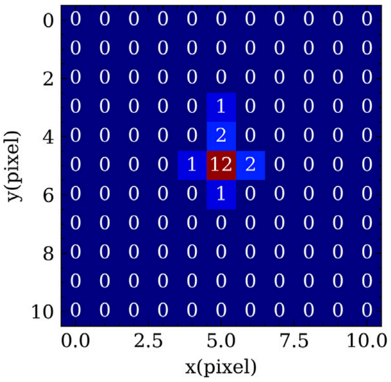

0	0	0	0	0	0	0	0	0	0	0
0	0	0	0	0	0	0	0	0	0	0
0	0	0	0	0	0	0	0	0	0	0
0	0	0	0	0	1	0	0	0	0	0
0	0	0	0	0	2	0	0	0	0	0
0	0	0	0	1	12	2	0	0	0	0
0	0	0	0	0	1	0	0	0	0	0
0	0	0	0	0	0	0	0	0	0	0
0	0	0	0	0	0	0	0	0	0	0
0	0	0	0	0	0	0	0	0	0	0
0	0	0	0	0	0	0	0	0	0	0

FIGURE 3
The spot image displayed in a matrix way.

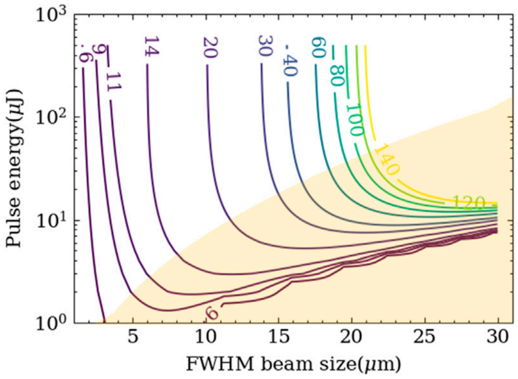

FIGURE 5
The contour of ablation area diameter changed with FWHM beam size and pulse energy.

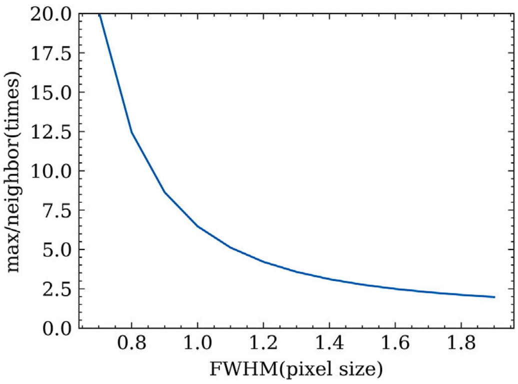

FIGURE 4
The ratio of the max pixel value to the neighbor pixel value changed with the FWHM beam size.

maximum pixel value is 12, and the maximum neighbor pixel value is 2 in Figure 3, the ratio is 6. According to Figure 4, the FWHM beam size is about 1 pixel. This is a rough estimation, as the beam is not an ideal Gaussian shape, especially during commissioning. After this step, the beam size was about 15 μm.

Micrometers focusing with silicon ablation imprint

The silicon ablation imprint imaged by the inline microscope was used for further tuning of the KB system. The aim of this step was to decrease the coupling of the horizontal and vertical beam sizes caused by the spot tilt and to focus to less than 10 μm. The silicon ablation imprint is not as sensitive as PMMA, but it can also be used as an indicator of beam shape and size. The silicon frame of the sample holder was used as the ablation target. It was well polished, with good reflectivity. When the silicon surface is perpendicular to the optical axis of the inline microscope, the image is very bright. Because the inline illumination directly reflects back to the microscope. Any defect larger than the pixel resolution of the microscope can be imaged as a dark spot under this condition. When the silicon surface is not perpendicular to the optical axis of the inline microscope, the image is dark, and the defects on the silicon can be imaged as a bright spot. This phenomenon was used to adjust the contrast of the image.

After the rough alignment, the spot was small enough for ablating the silicon. Here, the damage threshold of silicon is about 0.88 eV/atom [20], corresponding to an energy density 0.007 μJ/μm^2 at 520 eV and 90° incidence. Assuming a Gaussian distribution of focus spot, Figure 5 shows that the ablation area diameter changed with the pulse energy and FWHM beam size in theory. For the yellow area, the pulse energy is relatively low, and the beam size is big. The ablation area diameter is sensitive to the pulse energy. In the other area, the ablation area diameter is not sensitive to the pulse energy.

The silicon ablation imprint was performed with the full beam of about 10–100 μJ. The shutter at the entrance of the sample chamber was used to select a single pulse to shoot the silicon frame for each scan step. During tuning of the KB mirrors, the focus profile was detected by imaging the silicon ablation imprint. Figure 6A shows a typical commissioning process. The tilt of the spot or the coupling of the horizontal and vertical beam size was decreased during the process. The silicon was moved after index 21, so the index is not continuous. Figure 6B shows the silicon ablation imprint after adjusting KB mirrors. Finally, the shape looks round and small. But it is not the real beam shape because the spatial resolution of the inline microscope is 6.71 μm. The shape is the convolution of the beam shape and the point spread function of the microscope. The diameter of the damage area is about 10 pixels. With the silicon ablation imprint, the beam size was focused down to 10 μm.

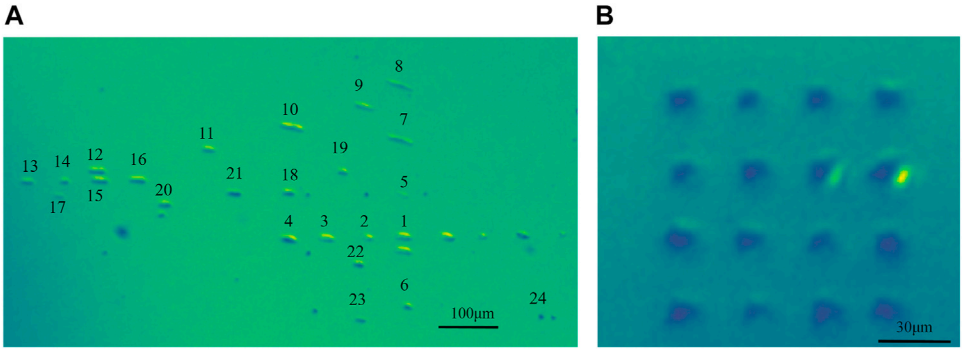

FIGURE 6
(A) Typical commissioning process. **(B)** Silicon ablation imprint.

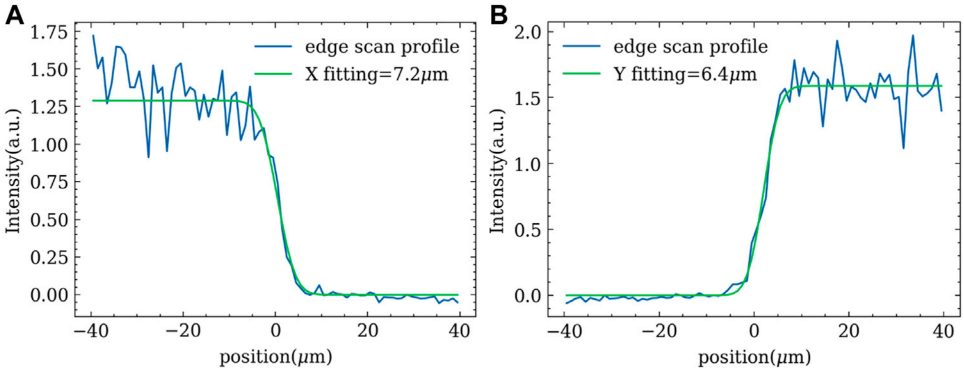

FIGURE 7
The edge scan result after silicon ablation imprint. **(A)** The horizontal beam size is 7.2 μm. **(B)** The vertical beam size is 6.4 μm.

Edge scan and final silicon ablation imprint

To further optimize the KB system and check the focus spot size, the edge scan was used for finer alignment. The pulse energy was attenuated 3–4 orders of magnitude with the gas attenuator to avoid radiation damage to silicon. A photodiode was mounted downstream of the silicon edge to record the transmitted pulse energy. The X-ray beam was cut step by step by moving the silicon edge, the transmitted pulse energy was recorded by the oscilloscope. For the rough edge scan, 10 pulses were recorded per step. The averaged photodiode signals were normalized to the averaged pulse energy. Figure 7 shows the edge scan result after silicon ablation imprint. Due to the poor SNR, it was difficult to differentiate and fit. To solve this problem, one way is to record more pulses and then average them. It is effective, but it will take a long time to record enough pulses considering the repetition rate of 2 Hz. Alternatively, the edge scan results were fitted with the integral of the Gaussian function. Although it cannot distinguish the side peak, it can give an estimation of beam size and trend without requiring a high SNR. Figure 7 shows the fitting results with a beam size of about 7.2 μm in the horizontal direction and about 6.4 μm in the vertical direction. Then, we adjusted the mirror and performed the edge scan each time. Finally, to accurately measure the beam size, 20 pulses per step were recorded and averaged to improve the SNR. Figure 8 shows the final result by fitting the differentiation of edge scan result with the Gaussian function. The beam size is about 2.2 μm × 2.5 μm (FWHM). Compared to the theoretical beam size, the horizontal beam size is slightly larger. The stability and figure errors of PM1, PM2 and horizontal focusing mirror ECM2 are the main factors to the horizontal beam size. The spot tilt is also a possible reason, which requires more experiments and analysis.

After the edge scan, the silicon ablation imprint was performed again. To examine the detailed profile and measure the accurate size of the crater, the silicon was removed from the vacuum chamber and imaged with a high NA microscope. Figure 9A shows a representative 4 by 4 silicon ablation imprint image. Figures 9B,C are the enlarged view of the red and blue rectangular

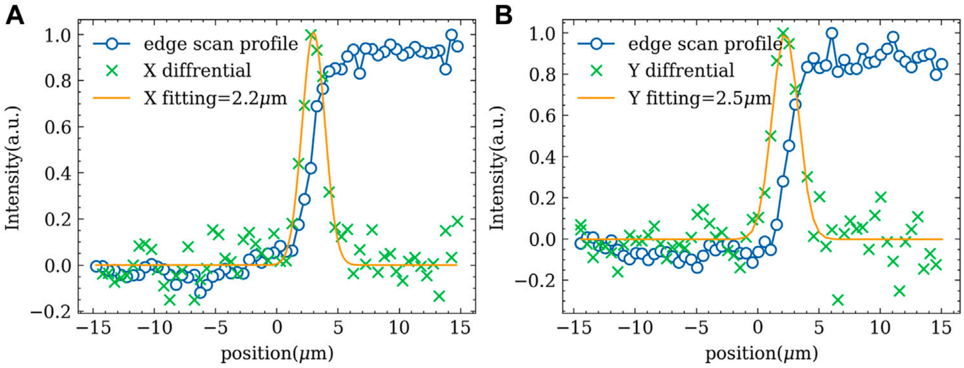

FIGURE 8
The final edge scan result. **(A)** The horizontal beam size is 2.2 μm. **(B)** The vertical beam size is 2.5 μm.

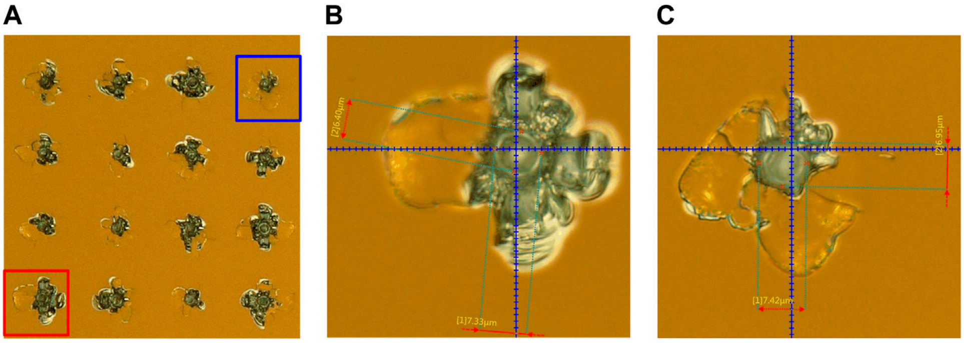

FIGURE 9
Image of the final silicon ablation imprint. **(A)** 4 by 4 silicon ablation imprint image. **(B)** Enlarged view of the red rectangular area. **(C)** Enlarged view of the blue rectangular area.

area. The FEL pulse not only ablated the central region, but also destroyed the surrounding region. Spallation and cracks could be found around the crater. The size of the craters ranges from 6 to 10 μm, which is consistent with Figure 5. When the focus spot size is 2–3 μm, and the pulse energy is 10–100 μJ, the central ablation diameter is about 6–10 μm.

Conclusion

In this paper, the first commissioning results of the KB system at SXFEL were reported. A focused X-ray spot of 2.2 μm × 2.5 μm was achieved, which was characterized by edge scan and silicon ablation imprint. To obtain better focusing performance, three methods were used for the commissioning of the KB system at different stages. A large FOV camera was used for rough alignment in the first stage, and a rough estimation method of beam size was described. When the ratio of the maximum value to the neighbor value is 6, the FWHM beam size is about 1 pixel. Then the inline microscope was used to characterize the silicon ablation imprint. With the help of this method, the beam tilt was corrected. The beam was focused to about 8 μm. Finally, the method of edge scan was used for fine alignment. By adjusting the KB mirrors, the focal spot size of less than 3 μm was achieved. The final result was confirmed with the silicon ablation imprint. In the future, the wavefront sensor at the CSI endstation, which is being commissioned, will be optional for further alignment of KB mirrors and better focusing performance.

Data availability statement

The raw data supporting the conclusion of this article will be made available by the authors, without undue reservation.

Author contributions

ZL and HJ directed the project. HJ, JF, YT, and YN designed and installed the CSI endstation. ZG and JC designed and ran the beamline. CF, TL, HD, and BL designed and ran the accelerator parts. JF, YT, YN, ZG, XY, JZ, BH, DZ, HL, DL, MX, and PC performed the commissioning process. JF, XY, BH, and YT contributed to the sample preparation and sample measurement. YT, JF, ZG, and XY contributed to the data analysis. YT, JF, and HJ wrote the manuscript. All authors discussed the results and commented on the manuscript.

Funding

This work was supported by the Shanghai soft X-ray free-electron laser Beamline Projection. The research was funded by the Strategic Priority Research Program of Chinese Academy of Sciences (Grant No. XDB 37040303), the National Natural Science Foundation of China (Grant No. 21727817), and the major state basic research development program of China (2017YFA0504802).

Acknowledgments

The authors would like to acknowledge all the SXFEL engineering team for their enormous assistance and cooperation.

Conflict of interest

Publisher's note

References

1. Liu B, Feng C, Gu D, Gao F, Deng HX, Zhang M, et al. The sxfel upgrade: From test facility to user facility. *Appl Sci (Basel)* (2022) 12(1):176. ARTN 176. doi:10.3390/app12010176

2. Zhao ZT, Wang D, Gu Q, Yin LX, Gu M, Leng YB, et al. Status of the sxfel facility. *Appl Sci (Basel)* (2017) 7(6):607. ARTN 607. doi:10.3390/app7060607

3. Zhang X, Xiangyu M, Zhang X, Jin Z, Wang Y. Research on the influence of slope error on free-electron laser focusing spot. *Nucl Tech* (2020) 43(6): 60101–060101. doi:10.11889/j.0253-3219.2020.hjs.43.060101

4. Raimondi L, Svetina C, Mahne N, Cocco D, Abrami A, De Marco M, et al. Microfocusing of the Fermi@Elettra fel beam with a K–B active optics system: Spot size predictions by application of the wise code. *Nucl Instr Methods Phys Res Section A: Acc Spectrometers, Detectors Associated Equipment* (2013) 710:131–8. doi:10.1016/j.nima.2012.11.039

5. Raimondi L, Svetina C, Mahne N, Cocco D, Capotondi F, Pedersoli E, et al. "Status of the K-B bendable optics at Fermi@Elettra fel," in Proc. SPIE 9208, Adaptive X-Ray Optics III, 920804, San Diego, CA, September 17, 2014. doi:10.1117/12.2062326

6. Flöter B, Juranić P, Kapitzki S, Keitel B, Mann K, Plönjes E, et al. Euv hartmann sensor for wavefront measurements at the free-electron laser in hamburg. *New J Phys* (2010) 12(8):083015. doi:10.1088/1367-2630/12/8/083015

7. Khounsary A, Raimondi L, Svetina C, Mahne N, Cocco D, Capotondi F, et al. K-B bendable system optimization at Fermi@Elettra fel: Impact of different spatial wavelengths on the spot size. *Adv X-Ray/EUV Opt Components* (2013) 8848. doi:10.1117/12.2023024

8. Gerasimova N, Dziarzhytski S, Weigelt H, Chalupsky J, Hajkova V, Vysin L, et al. *In situ* focus characterization by ablation technique to enable optics alignment at an XUV FEL source. *Rev Scientific Instr* (2013) 84(6):065104. doi:10.1063/1.4807896

9. Yumoto H, Mimura H, Koyama T, Matsuyama S, Tono K, Togashi T, et al. Focusing of X-ray free-electron laser pulses with reflective optics. *Nat Photon* (2013) 7(1):43–7. doi:10.1038/Nphoton.2012.306

10. Chalupsky J, Juha L, Kuba J, Cihelka J, Hajkova V, Koptyaev S, et al. Characteristics of focused soft X-ray free-electron laser beam determined by ablation of organic molecular solids. *Opt express* (2007) 15(10):6036–43. doi:10.1364/Oe.15.006036

11. Kim J, Kim HY, Park J, Kim S, Kim S, Rah S, et al. Focusing X-ray free-electron laser pulses using kirkpatrick-baez mirrors at the nci hutch of the pal-xfel. *J Synchrotron Radiat* (2018) 25:289–92. doi:10.1107/s1600577517016186

12. Yumoto H, Koyama T, Matsuyama S, Kohmura Y, Yamauchi K, Ishikawa T, et al. Ellipsoidal mirror for two-dimensional 100-nm focusing in hard X-ray region. *Sci Rep* (2017) 7(1):16408. Epub 2017/11/29. doi:10.1038/s41598-017-16468-1

13. Matsuyama S, Inoue T, Yamada J, Kim J, Yumoto H, Inubushi Y, et al. Nanofocusing of X-ray free-electron laser using wavefront-corrected multilayer focusing mirrors. *Sci Rep* (2018) 8(1):17440. doi:10.1038/s41598-018-35611-0

14. Yumoto H, Inubushi Y, Osaka T, Inoue I, Koyama T, Tono K, et al. Nanofocusing optics for an X-ray free-electron laser generating an extreme intensity of 100 ew/Cm(2) using total reflection mirrors. *Appl Sci (Basel)* (2020) 10(7):2611. ARTN 2611. doi:10.3390/app10072611

15. Keitel B, Plonjes E, Kreis S, Kuhlmann M, Tiedtke K, Mey T, et al. Hartmann wavefront sensors and their application at flash. *J Synchrotron Radiat* (2016) 23: 43–9. doi:10.1107/s1600577515020354

16. Berujon S, Ziegler E, Cojocaru R, Martin T "Development of a hard X-ray wavefront sensor for the EuXFEL," in Proc. SPIE 10237, Advances in X-ray Free-Electron Lasers Instrumentation IV, 102370K, Prague, Czech Republic, 24 May 2017 (2017). doi:10.1117/12.2269452

17. Nagler B, Aquila A, Boutet S, Galtier EC, Hashim A, Hunter MS, et al. Focal spot and wavefront sensing of an X-ray free electron laser using ronchi shearing interferometry. *Sci Rep* (2017) 7, 13698. doi:10.1038/s41598-017-13710-8

18. Liu Y, Seaberg M, Zhu D, Krzywinski J, Seiboth F, Hardin C, et al. High-accuracy wavefront sensing for X-ray free electron lasers. *Optica* (2018) 5(8):967. doi:10.1364/optica.5.000967

19. Seaberg M, Cojocaru R, Berujon S, Ziegler E, Jaggi A, Krempasky J, et al. Wavefront sensing at X-ray free-electron lasers. *J Synchrotron Radiat* (2019) 26: 1115–26. doi:10.1107/S1600577519005721

20. Koyama T, Yumoto H, Senba Y, Tono K, Sato T, Togashi T, et al. Investigation of ablation thresholds of optical materials using 1-µm-focusing beam at hard X-ray free electron laser. *Opt Express* (2013) 21(13):15382–8. Epub 2013/07/12. doi:10.1364/OE.21.015382

frontiers | Frontiers in Physics

TYPE Original Research
PUBLISHED 01 September 2022
DOI 10.3389/fphy.2022.933301

Structural and optical properties of narrowband Sc/Si multilayer at 46.5 nm

Jiali Wu, Runze Qi*, Zhong Zhang and Zhanshan Wang

MOE Key Laboratory of Advanced Micro-Structured Materials, Institute of Precision Optical Engineering (IPOE), School of Physics Science and Engineering, Tongji University, Shanghai, China

OPEN ACCESS

EDITED BY
Hongchang Wang,
Diamond Light Source, United Kingdom

REVIEWED BY
Anil Kumar Malik,
Chaudhary Charan Singh University, India
P. S. Athiray,
University of Alabama in Huntsville, United States
Surendra Singh,
Bhabha Atomic Research Centre, India
François Polack,
Soleil Synchrotron, France

*CORRESPONDENCE
Runze Qi,
qrz@tongji.edu.cn

SPECIALTY SECTION
This article was submitted to Optics and Photonics,
a section of the journal
Frontiers in Physics

RECEIVED 30 April 2022
ACCEPTED 25 July 2022
PUBLISHED 01 September 2022

CITATION
Wu J, Qi R, Zhang Z and Wang Z (2022), Structural and optical properties of narrowband Sc/Si multilayer at 46.5 nm.
Front. Phys. 10:933301.
doi: 10.3389/fphy.2022.933301

The Ne VII line is an intense solar line emitted from the solar transition region located at 46.5 nm with a temperature of approximately 0.5 MK. The observation of a Ne VII line is important to deepen the understanding of solar physics. For observing the Ne VII line at 46.5 nm, we have proposed a narrowband Sc/Si multilayer that could avoid the other solar emission lines going to the observatory instrument. In this article, Sc/Si multilayers with a Sc thickness ratio of 0.35 (conventional design) and 0.65 (narrowband design) were deposited. The microstructures of both multilayers were measured by grazing incidence X-ray reflectometry, X-ray diffraction, and transmission electron microscopy. The results showed that the interdiffusion at the Si-on-Sc interface was more significant than that at the Sc-on-Si interface in both multilayer. Compared with the conventional multilayer, the narrowband multilayer had a thinner Si-on-Sc interface width. The measured reflectivity of the Sc/Si multilayer with a Sc thickness ratio of 0.65 was 37.9% at 45.5 nm with a near-normal incident angle of 4.60°. The bandwidth was 3.68 nm, which is narrow enough to observe the Ne VII solar line.

KEYWORDS

Ne VII line, Sc/Si, multilayer, narrowband, thickness ratio

1 Introduction

The solar transition region (TR) is a highly dynamic and nonuniform area between the chromosphere and corona [1]. Within this region, the temperature rapidly increases from roughly 0.02 to 0.8 MK, and the collisional and partially ionized plasma transforms into the less collisional and fully ionized plasma [2]. Emission lines from the TR cover approximately 40–160 nm in the extreme ultraviolet (EUV) and far ultraviolet (FUV) regions and contain physical information about the TR. In this spectral range, the imager and spectrograph are mostly used as observing devices [3–5]. An intense Ne VII emission line is formed at a temperature of 0.5 MK in the upper TR, which is important for monitoring solar eruptions [6]. The Ne VII line is located at 46.5 nm, and in order to realize the observation of this specific emission line, a solar EUV telescope operating at 46.5 nm has been proposed. Because the Ne VII line is surrounded by other solar emission lines, such as Mg VIII at 43.7 nm and the Ne V line at 48.0/48.3 nm, the EUV telescope requires a narrow spectral bandpass to avoid the influence of other lines [7]. The EUV telescope is designed using a Ritchey–Chrétien structure [8], and the narrow spectral bandpass for this instrument is achieved by multilayer mirrors. The telescope requires the bandwidth of multilayer mirror less than 4 nm to ensure performance, and the narrowband multilayer mirror can be achieved by optimizing the multilayer structure.

Sc/Si multilayers show a high reflectivity in the 35–50 nm wavelength range and have been used for 46.9 nm Ne-like Ar X-ray tabletop lasers, spectroheliography, and X-ray microscopy [9–11]. Yulin obtained the asymmetrical interface width as $d_{Sc\text{-}on\text{-}Si}$ = 2.6 nm and $d_{Si\text{-}on\text{-}Sc}$ = 1.6 nm using the four-layer model (Sc/ScSi/Si/ScSi) [12]. At a Sc layer thickness ratio of 0.42 ($\Gamma_{Sc} = d_{Sc}/d$, where Γ_{Sc} represents the thickness ratio of the Sc layer, d_{Sc} represents the thickness of Sc, and d represents the d-spacing of the multilayer), the sample with a d-spacing of 25.45 nm had the highest reflectivity of 52% at 45.9 nm, and the bandwidth was 4.4 nm. At a constant d-spacing of 24.50 nm, the sample with Γ_{Sc} = 0.37 had the highest reflectivity. However, the microstructure of these multilayers with different Γ_{Sc} values has not been investigated. Gautier optimized the thickness of the top Si layer to 3.2 nm, whereby the reflectivity improved from 37 to 46% at 46 nm [13]. In the Sc/Si multilayer with a Sc ratio of 0.5, an asymmetrical interface was also found. The Si-on-Sc interlayer thickness was 2.5 nm, which was wider than the Si-on-Sc interlayer. Zhu indicated that the critical crystalline Sc layer thickness was about 5.68 nm [14]. However, previous work has usually focused on improving the reflectivity, and the Sc thickness ratio was between 0.37 and 0.5. The narrowband Sc/Si multilayer is important for 46.5 nm line imaging observations. Increasing the Sc layer thickness ratio is expected to achieve a narrow bandwidth of the Sc/Si multilayer, which is confirmed in the Mo/Si multilayer [15].

In this article, we designed the narrowband Sc/Si multilayer working at 46.5 nm. The narrowband Sc/Si multilayer with Γ_{Sc} = 0.65 and the conventional Sc/Si multilayer with Γ_{Sc} = 0.35 are deposited. These multilayers are characterized by different methods. The microstructures of both multilayers are measured by grazing incidence X-ray reflectometry (GIXR), X-ray diffraction (XRD), and transmission electron microscopy (TEM). The EUV reflectivity is measured by normal incidence reflectometry.

2 Design of a narrowband Sc/Si multilayer at 46.5 nm

Taking into account the diffusion in periodic Sc/Si multilayers, a four-layer structure (Sc/ScSi/Si/ScSi) was set up for simulation, where ScSi was the diffusion interlayer at the Sc-on-Si interface and the Si-on-Sc interface. In the design, the density of the ScSi layers was assumed to be 3.30 g/cm^3 [12]. The interlayer thickness at the Sc-on-Si and Si-on-Sc interfaces was set to 2.60 and 1.60 nm, respectively [16]. The surface and interface roughness were set to 0.30 nm. The reflectivity was computed at a near-normal incidence of 4.60°. To study the impact of Γ_{Sc} on the bandwidth and reflectivity of the Sc/Si multilayer, the reflectivity curves with different Γ_{Sc} values were calculated by the software IMD [17], as shown in Figure 1. Figure 1A shows the theoretical reflectivity of Sc/Si multilayers with a fixed d-spacing of 24.50 nm. With increasing the ratio from 0.35 to 0.75, the peak position increased from 45.5 nm to a longer wavelength of 48.9 nm. Meanwhile, the corresponding bandwidth and reflectivity decreased greatly, that is, the bandwidth decreased from 5.83 to 3.12 nm and the peak reflectivity decreased from 39.0 to 16.9%. It was demonstrated that increasing the Sc thickness ratio could effectively reduce the bandwidth of a Sc/Si multilayer while the reflectivity would drop. Figure 1B shows the theoretical reflectivity of Sc/Si multilayers with a d-spacing of 22.90–25.25 nm and a fixed working wavelength of 46.5 nm. When Γ_{Sc} was 0.65, the bandwidth decreased to less than 4.0 nm and the peak reflectivity was 31.8%. Based on these simulations, the Sc/Si multilayer with a d-spacing of 23.38 nm and Γ_{Sc} = 0.65 was opted to achieve a narrow bandwidth and relatively high reflectivity. In order to draw comparisons with this narrowband multilayer design, a conventional Sc/Si multilayer with Γ_{Sc} = 0.35 was designed. Schematics of the designed multilayer are depicted in Figure 2. Without considering the interlayer, the number of bilayers was 20.

3 Experiments

According to the designed results, Sc/Si multilayers with Γ_{Sc} = 0.65 and Γ_{Sc} = 0.35 were deposited by direct-current magnetron sputtering. The base pressure was less than 7.0×10^{-5} Pa. High-purity Ar (99.999%) was used as the sputtering gas and the Ar pressure was maintained at 0.160 Pa during the deposition. The layer thickness was confined by varying the residence time of the substrate as it passed over each sputtering target. The sputtering power of the Sc and Si targets was 30 and 80 W, respectively. The multilayers were deposited on 20×20 mm^2 super-polished silicon wafers with a root-mean-square roughness of 0.2 nm.

The structure of the samples was characterized by grazing incidence X-ray reflectometry (GIXR) with the 2theta-omega mode using an X-ray diffractometer (Bede, Durham, United Kingdom). The source was the Cu-Ka line at 0.154 nm. The GIXR measured curves were fitted by the software IMD using a two-layer model initially. However, compared with the intensity of the measured Bragg peaks, the simulated Bragg peaks had a lower intensity. According to previous literature, the measured curves were fitted with a four-layer model which took into account the Sc-Si mixtures at the interface. More information about the details of the multilayer structure is provided in Section 4.

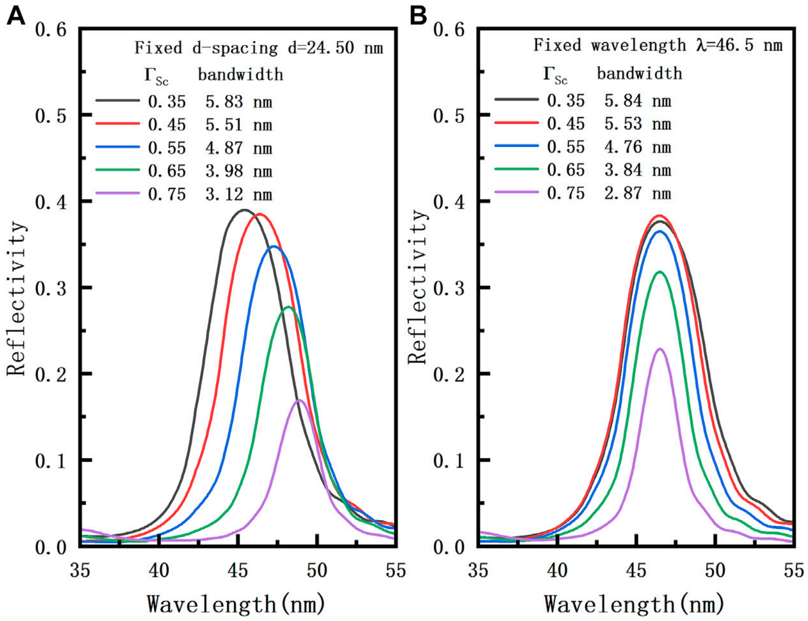

FIGURE 1
Theoretical reflectivity of the Sc/Si multilayers with different Γ_{Sc} values at a fixed d-spacing **(A)** and a fixed working wavelength of 46.5 nm **(B)**.

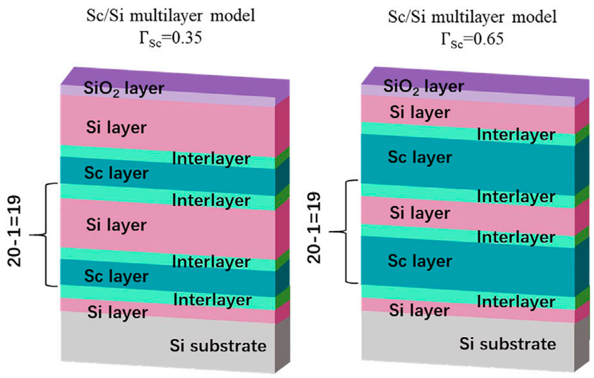

FIGURE 2
Schematic of the Sc/Si multilayer structures with Γ_{Sc} = 0.35 and Γ_{Sc} = 0.65.

Characterization of the crystallinity of multilayers was performed by X-ray diffraction (XRD, Bruker D8 Advance, Karlsruhe, GER). The detector scanned from 10° to 68° at a grazing incidence angle in the 2theta-omega mode. In this mode, the crystal plane parallel to the multilayer surface can be detected. The crystal phases can be obtained by matching the angular positions of the diffraction peaks with the powder diffraction file (PDF) of the International Center for Diffraction Data (ICDD). The average grain size perpendicular to the crystal phase direction was deduced by the Scherrer equation [18]:

$$D = \frac{\kappa\lambda}{B\cos(\theta)},$$

where D is the average grain size, κ is a dimensionless shape factor with a value of 0.89, λ is the wavelength of 0.154 nm, B is the full width at half maximum of the diffraction peak, and θ is the angular position of the diffraction peak.

In order to verify these results obtained by GIXR and XRD, the microstructures of multilayers were also investigated by transmission electron microscopy (TEM) using an FEI Talos F200X instrument (FEI, Hillsboro, OR, United States). It was equipped with a scanning TEM imaging with a nanoprobe for elemental contrast and an energy dispersive X-ray (EDX) spectrometer for elemental mapping. Selected area electron diffraction (SAED) measurements were used to characterize the crystallization of the multilayer. The profile of the layers along the growth direction was obtained by reading the gray value of the high-resolution TEM image using the software Digital Micrograph [19].

The EUV reflectivity of the Sc/Si multilayer with Γ_{Sc} = 0.65 was measured by Optics Beamline PM-1 at the BESSY-II facility. For the reflectivity measurement, the normal incidence monochromator was equipped with a grating of gl = 150 L/mm, and the beam stability was better than 0.1% [20]. The measurement was performed at an energy range of 22.3–33.5 eV (37.0–55.6 nm) and at a near-normal incidence angle of 4.60°.

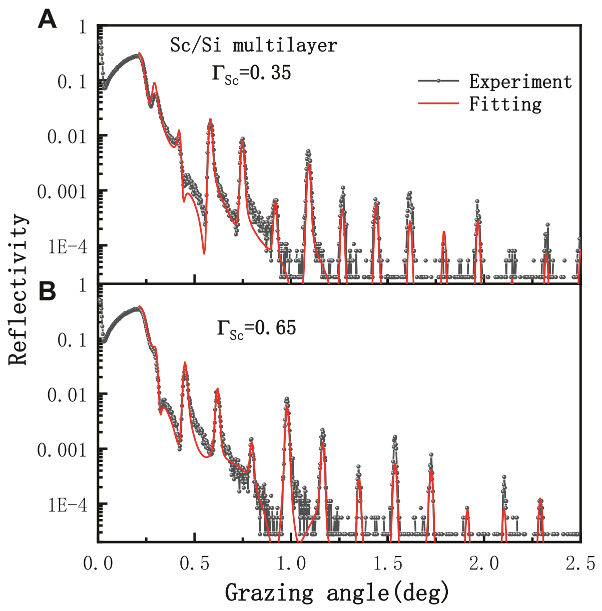

FIGURE 3
Measured GIXR and fitted results of Sc/Si multilayers with Γ_{Sc} = 0.35 **(A)** and Γ_{Sc} = 0.65 **(B)**.

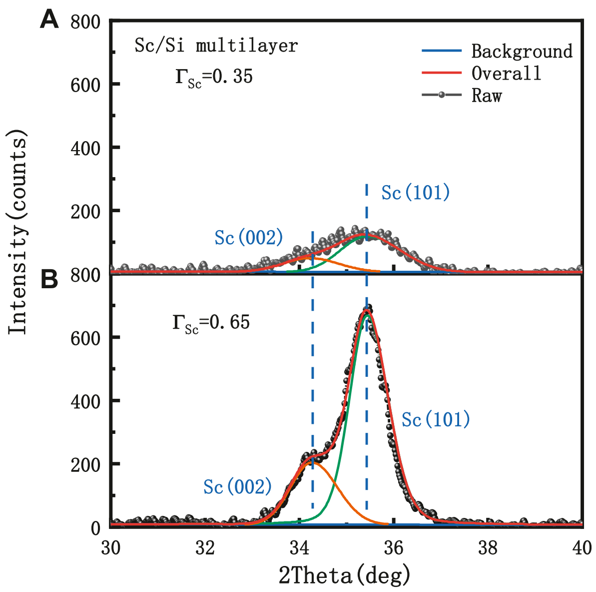

FIGURE 4
Measured XRD and fitted curves of Sc/Si multilayers with Γ_{Sc} = 0.35 **(A)** and Γ_{Sc} = 0.65 **(B)**.

TABLE 1 Sc/Si multilayer fitted parameters deduced from GIXR measurements.

Ratio	Layers	Thickness/nm	Roughness/nm	Ratio	Layers	Thickness/nm	Roughness/nm
Γ_{Sc} = 0.35	SiO_2	1.60	0.48	Γ_{Sc} = 0.65	SiO_2	1.65	0.45
	…	…	…		…	…	…
	Si	14.61	0.22		Si	6.86	0.22
	ScSi	2.96	0.49		ScSi	2.73	0.40
	Sc	5.99	0.38		Sc	12.26	0.35
	ScSi	1.30	0.30		ScSi	1.41	0.37
	…	…	…		…	…	…

4 Experimental results and discussion

4.1 Grazing incidence X-ray reflectometry analyses of Sc/Si multilayers

The measured and fitted GIXR curves of Sc/Si multilayers with Γ_{Sc} = 0.35 and Γ_{Sc} = 0.65 are shown in Figure 3. The measured curves were fitted with a two-layer model, but the fitted curves could not fit nicely with the measured curves and did not present details of the interfaces. According to previous studies, Sc-Si mixtures would be formed at the interface of Sc/Si multilayers, which were considered as ScSi compounds. Thus, ScSi interlayers were added to the fitted model as the four-layer model (Sc/ScSi/Si/ScSi). The theoretical reflectivity peaks and intensities were in good agreement with the experimental reflectivity. At a grazing angle range from 0.4° to 1.0°, there was a little deviation between the measured and fitted curves. This was mainly caused by surface oxidation and contamination. This deviation will not affect the fitted thickness value of the interlayer. Table 1 presents the fitted structure of Sc/Si multilayers, including oxidation of the silicon surface layer. It clearly exhibits the interlayer asymmetry in both Sc/Si multilayers. For the Sc/Si multilayer with Γ_{Sc} = 0.35 and a d-spacing of 24.86 nm, the Si-on-Sc interlayer thickness was 2.96 nm, while the Sc-on-Si interlayer thickness was smaller at 1.30 nm. For the Sc/Si multilayer with Γ_{Sc} = 0.65 and a d-spacing of 23.26 nm, the Si-on-Sc interface thickness was 2.73 nm, while the Sc-on-Si interface thickness was 1.41 nm. In both multilayers,

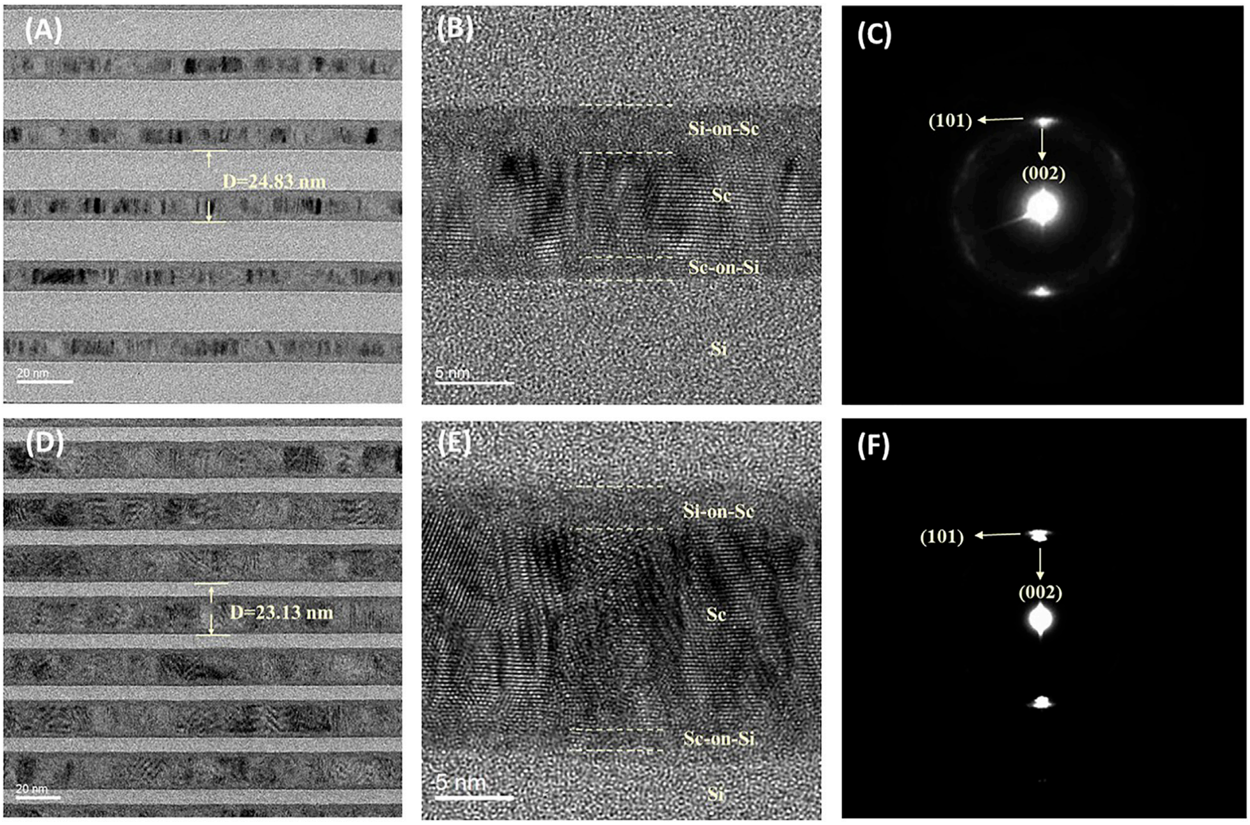

FIGURE 5
Bright-field TEM and SAED images of Sc/Si multilayers with Γ_{Sc} = 0.35 **(A–C)** and Γ_{Sc} = 0.65 **(D–F)**.

interdiffusion at the Si-on-Sc interface was wider than that at the Sc-on-Si interface. Interlayer asymmetry may be related to the crystallization of the Sc layers.

4.2 X-ray diffraction analyses of Sc/Si multilayers

Figure 4 shows the diffraction curves of the Sc/Si multilayers obtained by XRD in symmetrical reflection mode. The angular positions and the bandwidths of diffraction peaks were determined by fitting the peaks with a Gaussian profile. According to the PDF reference, the two peaks identified at diffraction angles of approximately 34.01° and 35.65° correspond to the Sc (002) and (101) crystal planes of a hexagonal close-packed structure, respectively. These crystal phases were also proposed by Zubarev [21]. Compared with the Sc/Si multilayer with Γ_{Sc} = 0.35, the diffraction peaks of the Sc/Si multilayer with Γ_{Sc} = 0.65 were narrower, and the intensity was increased. It was also clearly observed that the crystallization of Sc (101) was stronger than that of Sc (002). According to the Scherrer formula, the average grain size of the crystal phases was calculated. For the Sc/Si multilayer with Γ_{Sc} = 0.35, the average grain sizes perpendicular to the Sc (002) and (101) crystal phases were 5.9 and 5.5 nm, which were close to the Sc layer thickness. For the Sc/Si multilayer with Γ_{Sc} = 0.65, the average grain sizes perpendicular to the Sc (002) and (101) crystal planes were increased to 7.6 and 8.6 nm, respectively.

When the sputtered Si atoms were deposited on the crystalline Sc layer during the deposition, the crystal grains provided some diffusion channels and formed a thicker interlayer at the Si-on-Sc interface with Sc atoms [22]. When the sputtered Sc atoms were deposited on the amorphous Si layer, the underneath Si layer diffused into the growing Sc layer and formed another interlayer at the Sc-on-Si interface, which was thinner than that at the Si-on-Sc interface. Because the Sc layer was crystallized, while the Si layer was amorphous, the diffusion activities of Sc and Si atoms were different, which made the asymmetric interlayer at different interfaces.

4.3 Transmission electron microscopy analyses of Sc/Si multilayers

The microstructures of the Sc/Si multilayers with Γ_{Sc} = 0.35 and Γ_{Sc} = 0.65 were measured by TEM and SAED; the

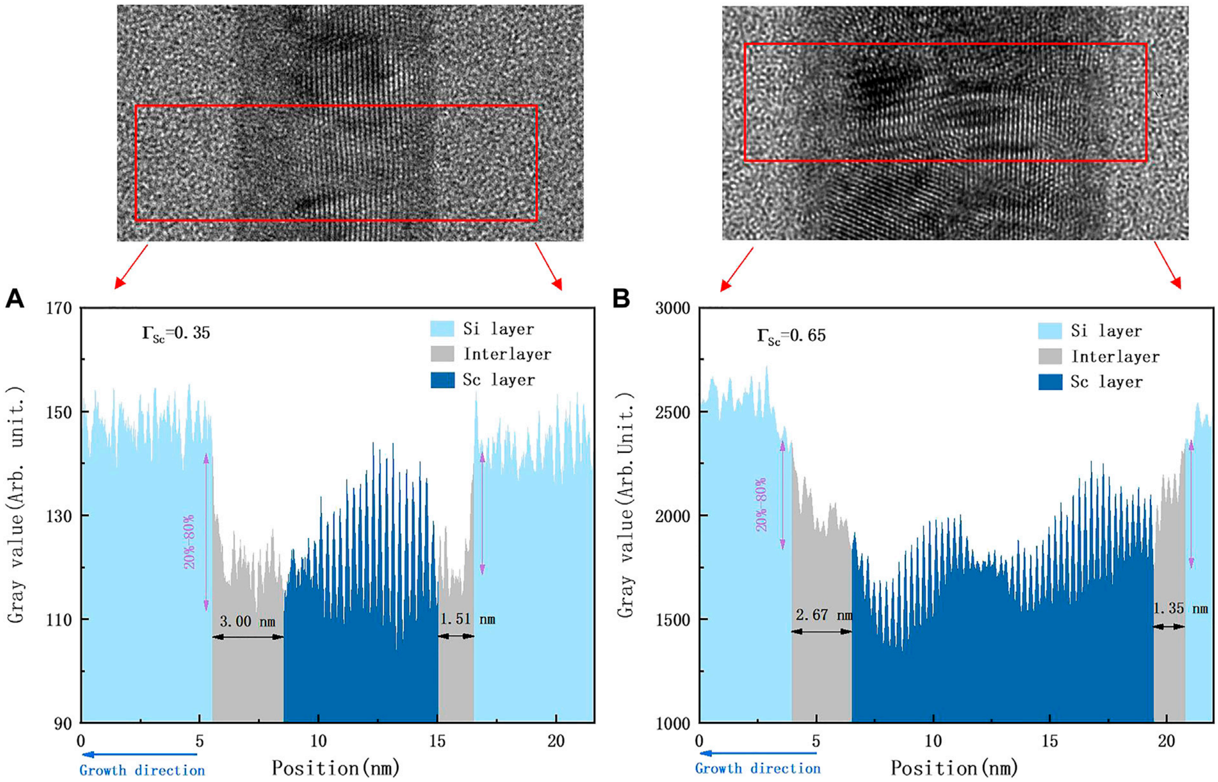

FIGURE 6
Gray-value profiles of Sc/Si multilayers with Γ_{Sc} = 0.35 **(A)** and Γ_{Sc} = 0.65 **(B)** derived from the selected area in the TEM images in Figures 5B and E (rotated by 90°).

measurements are shown in Figures 5A–F. Figures 5A and D are the bright-field TEM images and directly show the multilayer structure. The light and dark areas represent Si and Sc layers. A great number of grains obviously formed in the Sc layers. It was indicated that the Sc layers were partly crystallized. The thin gray area between the Sc and Si layers is Sc-Si mixtures, which can be observed more clearly in the high-resolution TEM images. Through Digital Micrograph software analysis, the d-spacings of the Sc/Si multilayer with Γ_{Sc} = 0.35 and Γ_{Sc} = 0.65 were 24.83 and 23.13 nm. This was almost consistent with the GIXR results. The bright-field high-resolution TEM images are shown in Figures 5B and E. The distribution of the Sc-Si mixtures and the different crystal orientations in the Sc layers are clearly observed. The average gray-value profile of the Sc/Si multilayers for one period was obtained from the same area later.

The selected area electron diffraction (SAED) images are shown in Figures 5C and F. The bright diffraction spots were both aimed at Sc crystal phases. The Si layer and interlayers were in the amorphous phase. For the Sc/Si multilayer with Γ_{Sc} = 0.35, there were diffraction spots in the longitudinal direction, which corresponded to the Sc (002) and (101) crystal planes. For the Sc/Si multilayer with Γ_{Sc} = 0.65, the diffraction spots were brighter. It was illustrated that the crystallization of Sc (101) and (002) crystal phases was enhanced, and most of the Sc grains grew along the direction of the multilayer growth.

The average gray-value profiles of the Sc/Si multilayers obtained near the middle of the multilayer are shown in Figure 6. The Y axis represents the average reading gray values along the growing direction of the multilayer. The X axis represents the observed position along the direction of the multilayer growth, and 20% of the peak and valley difference in the selected area was defined as the interface width [23]. The peak value was chosen from the Si layer near the edge, and the valley value was chosen from the internal Sc layer. The purple arrows marked the selected peak and valley values in Figure 6. At the top of the gray-scale curve was the selected area in the TEM images in Figures 5B and E, which were rotated by 90°. For the Sc/Si multilayer with Γ_{Sc} = 0.35, the thickness of the interlayer at the Si-on-Sc and Sc-on-Si interfaces was approximately 3.00 and 1.51 nm, respectively. For the Sc/Si multilayer with Γ_{Sc} = 0.65, the thickness of the interlayer at the Si-on-Sc and Sc-on-Si interfaces was approximately 2.67 and 1.35 nm, respectively. The asymmetrical interlayers were close to the fitted values of the GIXR results. The diffusion of Si atoms was easier along the grain boundaries of the Sc layer when Si atoms were deposited on it. Thus, the Si-on-Sc interlayer thickness was wider than the Sc-

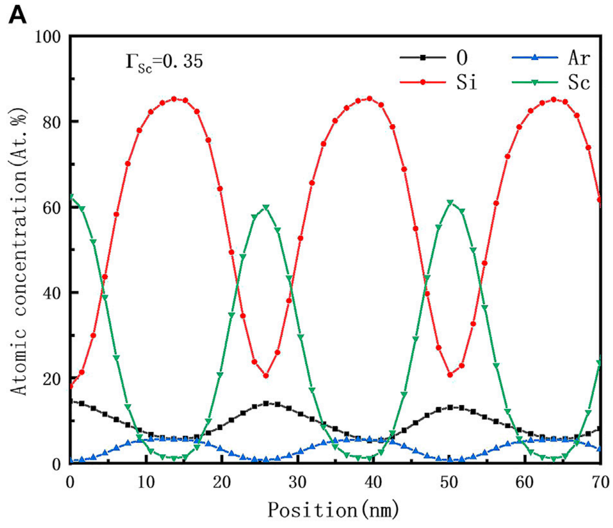

FIGURE 7
Depth distribution of the chemical elements of Sc/Si multilayers with Γ_{Sc} = 0.35 **(A)** and Γ_{Sc} = 0.65 **(B)**. Sc/Si reflectivity measurement by synchrotron radiation.

on-Si interlayer thickness. In addition to the asymmetrical interlayer, it was also found that the Si-on-Sc interlayer thickness decreased from 3.00 to 2.67 nm when Γ_{Sc} increased to 0.65. This was mainly caused by the crystallization enhancement of the Sc layer. With the increase of the Sc layer thickness, the crystallization of Sc increased and the defect in the Sc layer decreased, which inhibited the diffusion of Si atoms.

Energy dispersive X-ray (EDX) spectroscopy was performed to study the depth distribution of chemical elements heavier than carbon [24]. Figure 7 shows the depth distribution of chemical elements of both Sc/Si multilayers. It obviously presents a periodic oscillation of the concentration of each element. The asymmetrical distribution of Si shown in Figure 7A is evidence of interfacial diffusion, but not concrete diffusion, due to the resolution. There was a small amount of O and Ar detected in both multilayers. This can be explained by Sc possessing active chemical properties, and it would react with the only remaining O during the deposition. Ar atoms were probably incorporated from the sputtering gas. Gautier also found that Ar impurities mainly existed in the Si layers through a Rutherford backscattering test [13]. The existence of Ar and O was one of the reasons affecting the reduced reflectivity.

4.4 Sc/Si reflectivity measurement by synchrotron radiation

The optical performance of the Sc/Si multilayer with Γ_{Sc} = 0.65 was performed by Optics Beamline PM-1 at the BESSY-II facility. We used the four-layer model with the parameters obtained from GIXR to calculate the reflectivity curve at a near-normal incidence angle of 4.60°. Figure 8 shows the measured reflectivity of the Sc/Si multilayer in comparison with the theoretical reflectivity. The experimental peak reflectivity was 37.9% at 45.5 nm with a 3.68 nm bandwidth at a near-normal incidence angle of 4.60°. The theoretical peak reflectivity of the Sc/Si multilayer with Γ_{Sc} = 0.35 was 40.1% based on the fitted structure. To the best of our knowledge, this is the narrowest measured bandwidth of Sc/Si multilayers obtained so far.

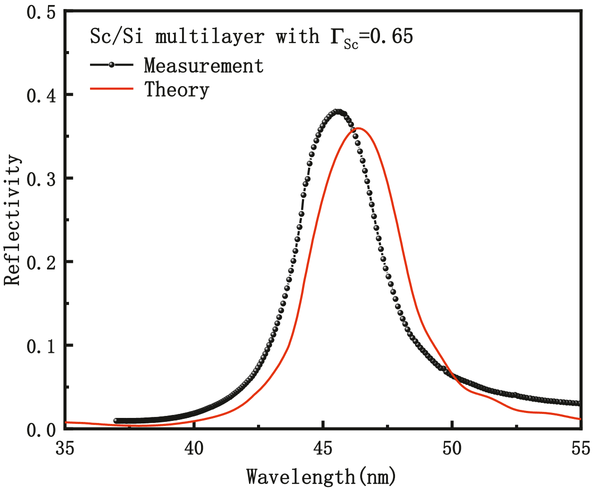

FIGURE 8
EUV reflectivity of the Sc/Si multilayer with Γ_{Sc} = 0.65.

However, there were differences between the measured and theoretical reflectivity. The wavelength of the measured peak reflectivity of the narrowband Sc/Si multilayer was 45.5 nm instead of 46.5 nm. This difference was due to uncertainties in the interlayer optical constants used in the calculation. These parameters might change in multilayers, especially in interlayers. The change in optical constant will affect the peak position of the reflectivity curve [25].

5 Conclusion

We studied the structure properties of the Sc/Si multilayer with $\Gamma_{Sc} = 0.35$ and $\Gamma_{Sc} = 0.65$ and further characterized the optical performance of the Sc/Si multilayer with $\Gamma_{Sc} = 0.65$. The GIXR measurement showed that the Sc-on-Si interlayer thickness was almost unchanged (~1.4 nm), whereas the Si-on-Sc interlayer thickness decreased from 3.0 to 2.7 nm when $\mathit{\Gamma}_{Sc}$ increased from 0.35 to 0.65. XRD measurements revealed that the Sc crystal phases were mainly Sc (002) and (101). This was consistent with SAED measurements. At the Si-on-Sc interface, the diffusion between Sc and Si was reduced by the increasing crystallization of Sc. In the EUV measurement, the peak reflectivity of the multilayer with $\Gamma_{Sc} = 0.65$ was 37.9% at 45.5 nm. The bandwidth was 3.68 nm, achieving the current narrowband requirement for observation.

Data availability statement

The original contributions presented in the study are included in the article/Supplementary Material; further inquiries can be directed to the corresponding author.

Author contributions

RQ and ZW conceived and designed the research work. JW analyzed the data and wrote the manuscript. ZZ and ZW contributed to helpful discussions to research and modification of the article. All authors have read and agreed to the published version of the manuscript.

Funding

This research was funded by the National Natural Science Foundation of China (12003016, 12027810, U2032169), the Strategic Priority Research Program of the Chinese Academy of Sciences (No. XDA15018400), and the Users with Excellence Program of Hefei Science Center CAS (2020HCS-UE005).

Conflict of interest

The authors declare that the research was conducted in the absence of any commercial or financial relationships that could be construed as a potential conflict of interest.

Publisher's note

References

1. Vernazza JE, Avrett EH, Loeser R. Structure of the solar chromosphere. III - models of the EUV brightness components of the quiet-sun. *ApJS* (1981) 45:635. doi:10.1086/190731

2. Tian H. Probing the solar transition region: Current status and future perspectives. *Res Astron Astrophys* (2017) 17:110. doi:10.1088/1674-4527/17/11/110

3. De Pontieu B, Title AM, Lemen JR, Kushner GD, Akin DJ, Allard B, et al. The interface region imaging spectrograph (IRIS). *Sol Phys* (2014) 289:2733–79. doi:10.1007/s11207-014-0485-y

4. Boerner P, Edwards C, Lemen J, Rausch A, Schrijver C, Shine R, et al. Initial calibration of the atmospheric imaging assembly (AIA) on the solar dynamics observatory (SDO). *Sol Phys* (2012) 275:41–66. doi:10.1007/s11207-011-9804-8

5. Wilhelm K, Curdt W, Marsch E, Schühle U, Jordan SD, Poland AI, et al. Sumer - solar ultraviolet measurements of emitted radiation. *Sol Phys* (1995) 162:189–231. doi:10.1007/BF00733430

6. Peter H, Judge PG. On the Doppler shifts of solar ultraviolet emission lines. *ApJ* (1999) 522:1148–66. doi:10.1086/307672

7. Del Zanna G, Bromage BJI, Landi E, Landini M. Solar EUV spectroscopic observations with SOHO/CDS: I. An in-flight calibration study. *A&A* (2001) 379: 708–34. doi:10.1051/0004-6361:20011220

8. Cheimets P, Caldwell DC, Chou C, Gates R, Lemen J, Podgorski WA, et al. SDO-AIA telescope design. *Proc Spie: Solar Phys Space Weather Instrumentation* (2009) III:74380G. doi:10.1117/12.830594

9. Rocca J-J, Frati M, Benware B, Seminario M, Filevich J, Marconi M, et al. Capillary discharge tabletop soft X-ray lasers reach new wavelengths and applications. *Comptes Rendus de l'Academie des Sci - Ser IV - Phys* (2000) 1: 1065–81. doi:10.1016/S1296-2147(00)01113-6

10. Seely JF, Uspenskii YA, Pershin YP, Kondratenko VV, VinogradovSkylab AV. Skylab 3600 groove/mm replica grating with a scandium-silicon multilayer coating and high normal-incidence efficiency at 38-nm wavelength. *Appl Opt* (2002) 41: 1846. doi:10.1364/AO.41.001846

11. Chakrabarti S, Kimble R, Bowyer S. Spectroscopy of the EUV (350–1400 Å) nightglow. *J Geophys Res* (1984) 89:5660. doi:10.1029/JA089iA07p05660

12. Yulin SA, Schaefers F, Feigl T, Kaiser N *Advances in Mirror Technology for X-ray*, 5193 (2004). p. 155–63. doi:10.1117/12.505582 Enhanced reflectivity and stability of Sc/Si multilayers*Proc SPIEEUV Lithography, Laser Other Appl*

13. Gautier J, Delmotte F, Bridou F, Ravet MF, Varniere F, Roulliay M, et al. Characterization and optimization of magnetron sputtered Sc/Si multilayers for extreme ultraviolet optics. *Appl Phys A* (2007) 88:719–25. doi:10.1007/s00339-007-4041-6

14. Zhu J, Zhang J, Jiang H, Zhu J, Zhu S, Li M, et al. Interface study on the effect of carbon and boron carbide diffusion barriers in Sc/Si multilayer system. *ACS Appl Mater Inter* (2020) 12:25400–8. doi:10.1021/acsami.0c03563

15. Lim YC, Westerwalbesloh T, Aschentrup A, Wehmeyer O, Haindl G, Kleineberg U, et al. Fabrication and characterization of EUV multilayer mirrors optimized for small spectral reflection bandwidth. *Appl Phys A Mater Sci Process* (2001) 72:121–4. doi:10.1007/s003390000723

16. Gautier J, Delmotte F, Roulliay M, Ravet M-F, Bridou F, Jerome A, et al. Performances and stability of Sc/Si multilayers with barrier layers for wavelengths around 46 nm. *Proc Spie: Adv Opt Thin Films* (2005) 5963:59630X. doi:10.1117/12.625030

17. Windt DL. IMD—software for modeling the optical properties of multilayer films. *Comput Phys* (1998) 12:360. doi:10.1063/1.168689

18. Shaw LL, Goberman D, Ren R, Gell M, Jiang S, Wang Y, et al. The dependency of microstructure and properties of nanostructured coatings on plasma spray conditions. *Surf Coat Tech* (2000) 130:1–8. doi:10.1016/S0257-8972(00)00673-3

19. Mitchell DRGDT. Electron diffraction software tools for DigitalMicrograph TM. *Microsc Res Tech* (2008) 71:588–93. doi:10.1002/jemt.20591

20. Feng Y, Huang Q, Zhuang Y, Sokolov A, Lemke S, Qi R, et al. Mo/Si lamellar multilayer gratings with high efficiency and enhanced resolution for the x-ray region of 1000-1700eV. *Opt Express* (2021) 29:13416. doi:10.1364/OE.422483

21. Zubarev EN. Reactive diffusion in multilayer metal/silicon nanostructures. *Phys -Usp* (2011) 54:473–98. doi:10.3367/UFNe.0181.201105c.0491

22. Pershyn YP, Zolotaryov A, Rocca JJ, Devizenko AY, Kondratenko VV, Artyukov IA, et al. Formation of periodic relief at Sc/Si multilayer surface under EUV laser irradiation. *Proc Spie: Damage Vuv, Euv, X-ray Opt VI* (2017) 10236: 102360J. doi:10.1117/12.2267292

23. Feng J, Huang Q, Wang H, Yang X, Giglia A, Xie C, et al. Structure, stress and optical properties of Cr/C multilayers for the tender X-ray range. *J Synchrotron Radiat* (2019) 26:720–8. doi:10.1107/S1600577519001668

24. Huang Q, Liu Y, Yang Y, Qi R, Feng Y, Kozhevnikov IV, et al. Nitridated Ru/B_4C multilayer mirrors with improved interface structure, zero stress, and enhanced hard X-ray reflectance. *Opt Express* (2018) 26:21803. doi:10.1364/OE.26.021803

25. Spiller E. *Soft X-ray optics*. Bellingham, Wash., USA: SPIE Optical Engineering Press (1994).

frontiers | Frontiers in Physics

TYPE Original Research
PUBLISHED 28 September 2022
DOI 10.3389/fphy.2022.915182

OPEN ACCESS

EDITED BY
Qiushi Huang,
Tongji University, China

REVIEWED BY
Riccardo Signorato,
S.RI. Tech s.r.l., Italy
Simon Alcock,
Diamond Light Source, United Kingdom
Yong Wang,
Shanghai Advanced Research Institute
(CAS), China
Maurizio Vannoni,
European X-Ray Free Electron Laser,
Germany

*CORRESPONDENCE
Fugui Yang,
yangfg@ihep.ac.cn

SPECIALTY SECTION
This article was submitted to Optics and Photonics,
a section of the journal
Frontiers in Physics

RECEIVED 07 April 2022
ACCEPTED 04 August 2022
PUBLISHED 28 September 2022

CITATION
Hu W, Cui X, Li M, Sheng W, Zhang W, Jia Q and Yang F (2022), Study on the X-ray mirror quality specification in advanced light source.
Front. Phys. 10:915182.
doi: 10.3389/fphy.2022.915182

Study on the X-ray mirror quality specification in advanced light source

Weishan Hu[1,2], Xiaowen Cui[1,2], Ming Li[1,2], Weifan Sheng[1,2], Weiwei Zhang[1], Quanjie Jia[1] and Fugui Yang[1]*

[1]Beijing Synchrotron Radiation Facility, Institute of High Energy Physics, Chinese Academy of Science, Beijing, China, [2]University of Chinese Academy of Sciences, Beijing, China

The influence of the X-ray mirror errors on the performance of the beamline increases as the X-ray beam's coherence improves in advanced light sources. The spatial dispersion of the X-ray beam is crucial for spatial resolution and field of view. However, selecting the appropriate merit function for expressing light distribution and identifying its relationship to optical error is very important in beamline design. We develop a high-efficiency wave-optics simulation platform and a deterministic analysis model to address this issue. The simulation experiments evaluated merit functions, including Strehl ratio, root-mean-square spot size, and encircled energy radius. We proved that the encircled energy radius is a good metric of the x-ray beam spatial dispersion, which matches the results of the Church-Takacs theory. In addition, it is found that limiting the contribution of the low frequency ($wavelength > \frac{1}{10}L$) error is effective for specifying the requirements of X-ray mirrors.

KEYWORDS

X-ray mirror, beamline design, simulation, surface error, synchrotron radiation facility

Introduction

X-rays emitted by advanced light sources, including free-electron lasers (FELs) and synchrotron radiation facilities, have advantages such as high flux and brightness. The fourth-generation synchrotron radiation source can achieve sub-micron spatial resolution. It can be used in many applications such as materials science, spectroscopy, chemistry, biology, etc. However, due to the high coherence of X-rays, various optical devices and equipment of beamlines will cause wavefront errors, which will reduce the system's spatial resolution or the peak intensity of beams. Therefore, these advantages of synchrotron radiation make high demands on optics quality for beamline transmission. For example, the surface shape accuracy of the High Energy Photon Source (HEPS)[1] for the X-ray nano-focusing mirror is required up to 2 nm peak-to-value (PV) or 0.5 nm root-mean-square (RMS), and the slope error is required to be better than 50 μrad RMS.

The influence of X-ray mirror shape errors have always been an essential issue in synchrotron radiation facilities. X-ray optical elements' specifications have been studied over the past few years. Church and Takacs [2] performed a systematic analysis of the errors of optical focusing elements as early as 1993, and they used the error statistics of the focusing elements to predict the imaging degradation of simple imaging systems. Church's article presents a model of errors and proposes two types of error, including the figure error left by the molding process during manufacturing and the finish error left by the finishing and polishing process. At the same time, R. Signorato and M. Sanchez del Rio[3] researched X-ray mirrors based on geometric ray tracing. They proposed that the power spectral density (PSD) does not contain all the information about the intensity and position of the light spot. On this basis, Pardini[4] finds that for diffraction-limited systems, within a critical spatial wavelength, the optical focusing element can appropriately relax the slope error requirements and still maintain a good light intensity distribution. Yashchuk[5] studied the effect of the specular error on the quality of the X-ray beam delivered to the sample location at different spatial frequencies. It shows that for a surface irregularity comparable to the mirror length, a significantly reduced photon flux density results in reduced beam quality. On the basis of the theoretical model, the power spectral density function[6–8], surface finish function[9,10] can be used to express the specific requirements of X-ray optical components.

According to the requirements for the manufacturing parameters of optical elements, adequate progress has also been made in manufacturing high-precision optical elements. Many researchers[11,12] have investigated high-precision optical components suitable for X-rays. But inevitably, high-precision optical components are expensive and difficult for manufacture. Also, not all experiments require highly coherent or diffraction-limited light, which means imperfect mirrors can suffice for application. For example, most conventional beamline experiments, including the experiment of small-angle scattering and absorption, only requires regular quality light spots. Westfahl [13] found that in the partially coherent beams of fourth-generation synchrotron radiation sources, use of mirrors with smaller errors caused wavefront distortions, but their coherence lengths were virtually unchanged. Moreover, in Church's article[2], it is also theoretically demonstrated that the imaging properties of surfaces with fractal errors perform well even if the fractal power spectrum diverges at low spatial frequencies.

In addition, how to implement the construction of such beamlines with low risk and low cost makes it necessary to carry out error evaluation of X-ray optical components for applications. With the improvement of the coherence of the light source, the application of wave optics is increasing, with the problems caused by the wave characteristics of light becoming the key to beamlines and experiments. The beamline simulation platform is important to study these problems. High-level beamline design requires a simulation platform that fully combines wave optics with traditional geometric optics tracing methods. The Ray tracing method can quickly evaluate the beamline's energy spectrum, the optics layout device's position, etc. Moreover, the existing simulation softwares are relatively mature, such as SRW, SHADOW, XRT [14,15]. Wave optics can more accurately evaluate the changes in coherence and wavefront errors caused by various device errors and vibrations. How to quickly carry out the wave simulation of optical problems is still difficult for many researchers. To slove the problem, we will introduce our simulation strategy.

As different applications have different requirements on the image quality, Figure 1 shows the HEPS strategy on the error solution in order to give the over-/under- specification of the optics. In this paper, we studied the focusing partially coherent light and give a simplified model of the beamline system. Based on the DABAM numerical simulation, we focus on the study of the energy spatial dispersion characterization of the focused beam, and giving the general requirements for the mirror quality of the beamlines.

Simulation methods

In order to give an explicit explanation, this paper focuses on the wavefront distortion and features of the beam spot on sample in a simplified optical system. The optical system is shown in the Figure 2, where the phase modulation function $t\ (x, y) = A\ (x, y)\ e^{i\phi(x,y)}$ is used to model the X-ray optics. The simplified system setup is beneficial for improving the simulation speed and performing theoretical calculations. Numerical simulation tools have been adopted to study the issues related to the X-ray optics imperfection. It has been proved that the insert device or bending magnet can be simulated with very high precision. Optimizing the source mainly depends on the energy spectrum requirement and has little relationship with the beamline issue we are concerned about in this paper. We will perform the simulation for the specified source.

In partially coherent light sources, the wave-optics calculation of beamline simulation software is very time-consuming, which also limits its applications in the study of beamline design engineering techniques. The physical basis of the simulation is to modulate the wavefront of the light source into the detected and received data through Fresnel diffraction and to perform calculation and analysis. It can be divided into four parts: model and calculation of the light source of the insert, model of optical components, optical wave-optics propagation, and data analysis. Among them, the first and third steps are the most time-consuming processes. Figure 3 shows our strategy for the simulation platform development. In order to improve the calculation efficiency, we integrated the mature software package (XRT/SRW) and adopted the following calculation strategies:

1) Optimizing light source and beamline set up separately. The source field by multiple electrons is calculated and saved to the local hard disk to avoid the repeated SR source calculations, which are time-consuming. In the beamline design stage, the data is loaded and used to perform

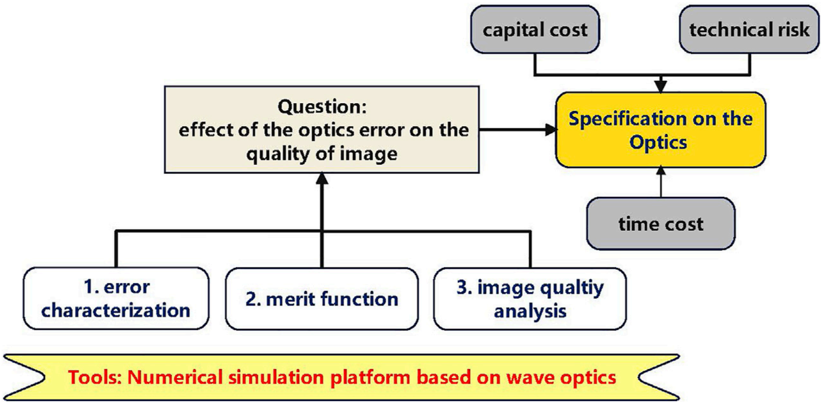

FIGURE 1
Issues related to the optics error problem.

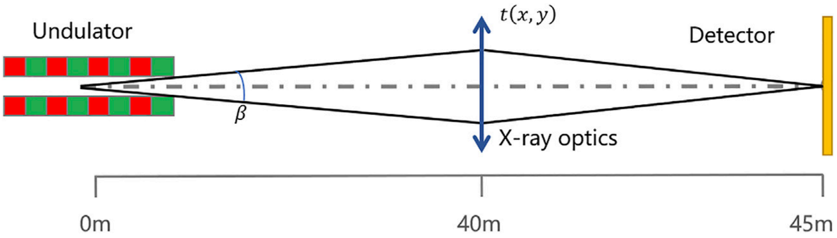

FIGURE 2
Scheme of the beamline system with focusing optics.

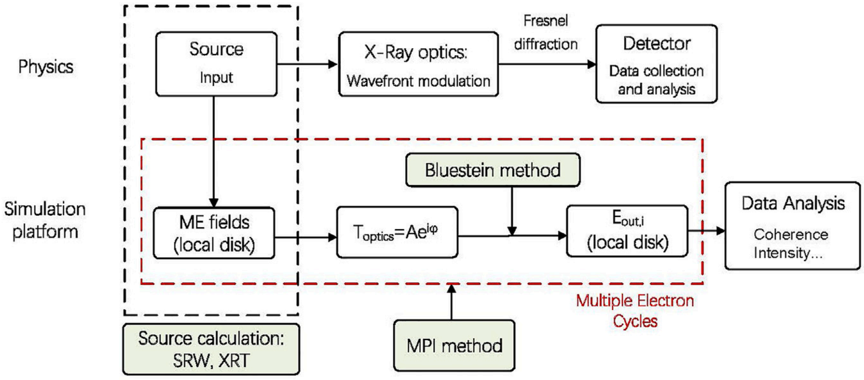

FIGURE 3
Roadmap of the calculation platform for partial coherence system simulation.

beamline simulation. Replacing numerical calculations with local data access also reduces the requirement on the large memory.

2) Optical wave propagation. Bluestein algorithm[16,17] is used to accelerate the Fresnel diffraction calculation. It can avoid the sampling issue in the traditional fast Fourier transform process.

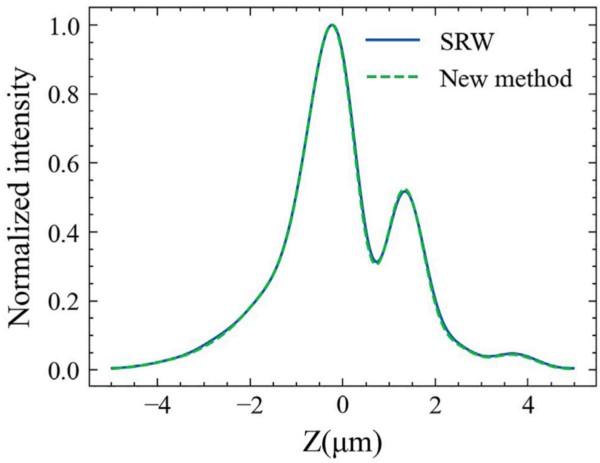

FIGURE 4
Comparison chart of SRW and new method.

TABLE 1 Parameters for the Storage and undulator.

Specification	Value
Circumference [m]	1,360
Electron energy (GeV)	6
Current (mA)	200
Electron energy spread	0.0011
Emittance horizontal/vertical [pm rad]	27.5/2.75
Horizontal/vertical size [μm]	8.8/2.3
Horizontal/vertical diver. [μrad]	3.1/1.2
Undulator	
period [mm]	16.8
number	175

TABLE 2 Parameters of X-ray light source at 10 keV for low beta beamline.

	x	z
Single electron radiation size [μm]	4.310	
Single electron radiation divergence [μrad]	5.636	
Source size [μm]	9.818	4.918
Source divergence [μrad]	6.320	5.636

3) MPI-based[18] parallel calculation for multiple electron loop. It has been successfully adopted in SRW.

Through these three optimization, this project's calculation time is significantly reduced. In modeling the optical element, the optical element error directly converts into wavefront error. Figure 4 shows the comparison of the SRW and our method in multi-electron simulation. The parameters of the undulator and X-ray light source are given by Table1, 2. In the debug process, the beamline parameters optimization (including sampling range, resolution, etc.) is suggested to be first carried out for single-electron calculation. After the debugging is completed, the multi-electron calculation is finally carried out.

Surface error analysis

Characterization of the surface error

Reasonable specification on the x-ray mirror quality should consider the features of the error data for real mirrors. In Church & Takacs [19] article, the specification of mirrors is studied based on their performance in the optical system. The Strehl Ratio (SR) and the power spectral density (PSD) of the mirror's surface error, is selected as a merit function of image quality. Because the PSD curve changes significantly with different mirrors, the RMS slope error, RMS height error, and PV height error are commonly used to specify the optics. The surface error statistical data (1D) is obtained from the DABAM database. By subtracting the original shape of mirrors, we extracted residual height and slope error.

As shown in the Figure 5, the raw data of height error (Figure 5A), slope error (Figure 5B) and the PSD (Figure 5C) of mirror M2 from DABAM database is displayed as an example with the coordinates of Figure 5C expressed in logarithmic form.

$$\sigma(f_{max}) = \sqrt{\int_{f_{\min}}^{f_{max}} psd(f)df} \tag{1}$$

$$\sigma_{Normalized}(f_{max}) = \sigma(f_{max})/\max(\sigma(f)) \tag{2}$$

Where there are equal interval df between sampling frequencies during the frequency range $f_{\min} = \frac{1}{L}$, $f_{\max} = \frac{1}{2df}$, with L the length of the mirror, dy the spatial interval between sampling points.

Figure 6 shows the $\sigma(f_m)$ calculated for the mirrors in the DABAM database. The $\sigma_{Normalized}$ values exceed 0.8 when the horizontal coordinate is 0.1 for all of the mirrors, which means that low-frequency error accounts for the major component of the total error. Further, we calculate the position f_m where the $\sigma_{Normalized}$ value reaches 0.8, the results are shown in Figure 6B demonstrating that the wavelength of the corresponding shape error is mostly greater than 0.1L. Figure 6) shows the relationship between PV and RMS of height error is approximately linear, which simplifies the analysis procedure later.

Deterministic analysis on the beamline performance

From the point of view of integration calculation, it is challenging to perform an analytical analysis of the low-frequency error. However, the physical rules behind the

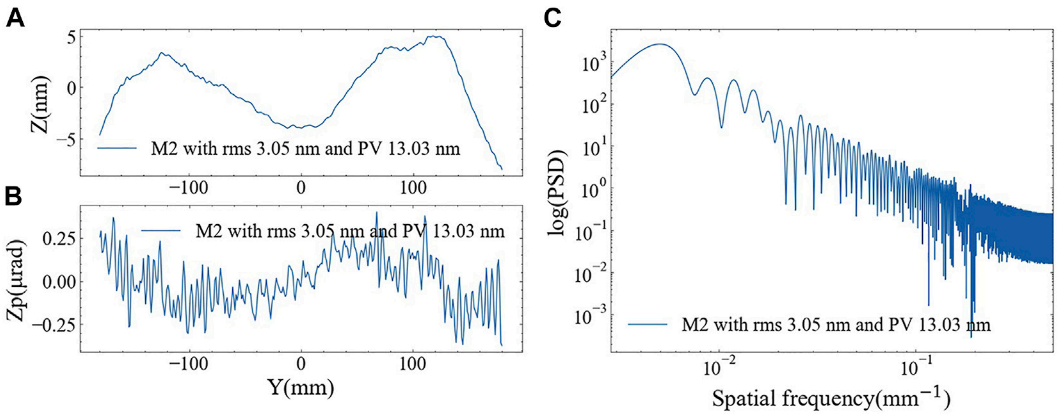

FIGURE 5
(A) The height error of mirror M2 in the DABAM database. **(B)** The slope error of mirror M2 in the DABAM database. **(C)** The PSD of the mirror in the DABAM database.

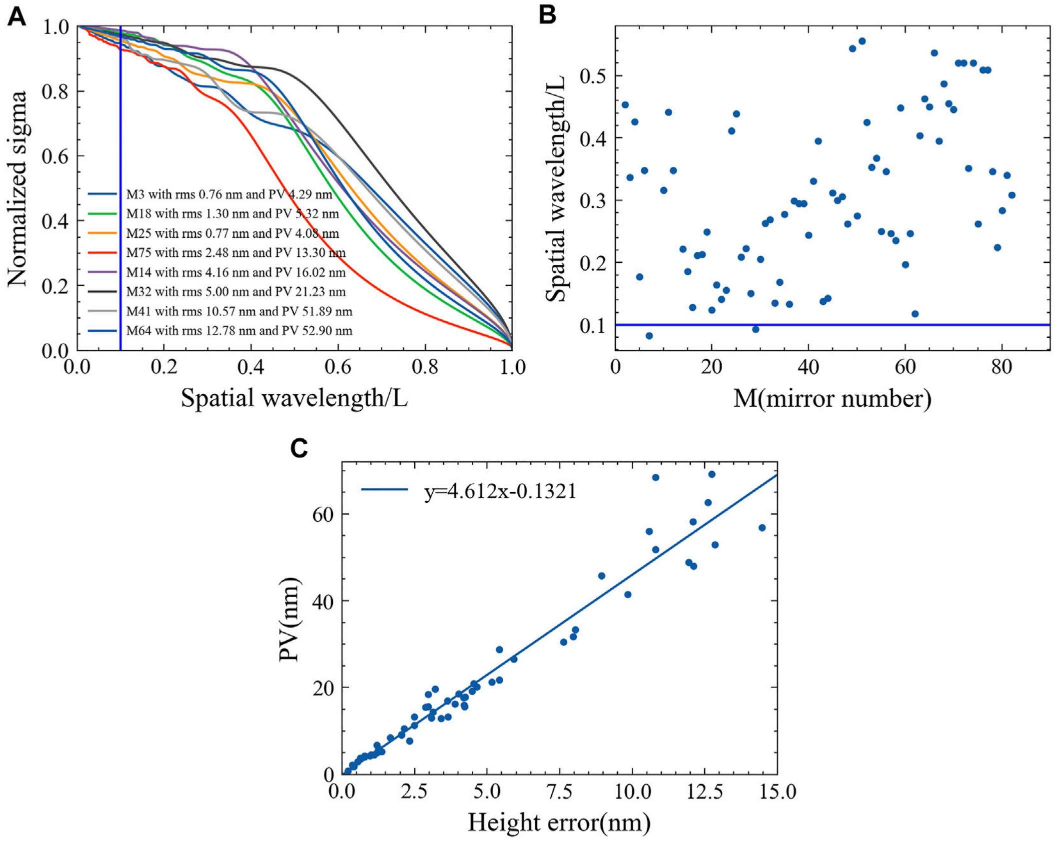

FIGURE 6
(A) The relationshape between $\sigma_{Normalized}$ with the spatial wavelength (/L).**(B)** the spatial wavelength (/L) of error for existing mirrors in DABAM when the $\sigma_{Normalized}$ reach 0.8.**(C)** the relationshape between PV with RMS of height error.

appearance are more important for practical beamline design work than simulation. In Section 2.2, it can be seen that the low-frequency error is the main component of the machining error. In order to study the influence of the spatial distribution characteristics of the surface shape error on the optical system performance, considering the statistical dilemma, here we develop the deterministic analysis method. In the case of a coherent light field, the entire aperture function $t\ (x_1)$ is divided into many segments, and the transmittance function in each segment can be expressed as

$$t_i(x_1) = rect\left(\frac{x_1 - c_i}{w_i}\right)f_i(x_1) \tag{3}$$

Where w_i and c_i are segment width and center position. $f_i(x_i) = exp[-j\frac{4\pi h(x_1)\sin\theta}{\lambda}]$ is error distribution function. *rect* $(\cdots)$is the rectangular function. It is easy to obtain the light field distribution on the focal plane as

$$U(x_0, y_0) = \frac{e^{jkz}e^{jk\frac{\left(x_0^2+y_0^2\right)}{2z}}}{j\lambda z}\mathcal{F}[U(x_1, y_1)]|_{f_x=\frac{x_0}{\lambda z}, f_y=\frac{y_0}{\lambda z}}$$
$$= C\sum_i exp(-j2\pi f_x c_i)[w_i sinc(w_i f_x)] * \mathcal{F}[f_i(x_i)]|_{f_x=\frac{x_0}{\lambda z}} \tag{4}$$

Where x_0 and y_0 are the coordinates of the focal plane, x_1 and y_1 are the coordinates of aperture, k is the wave number, z is the distance to the focal plane, $\mathcal{F}[\cdots]$ is the Fourier transform function, f_x is spatial frequency in the x-direction, and C is a constant. The intensity of the light field is given by

$$I(x_0, y_0) = U^*(x_0, y_0)U(x_0, y_0) \tag{5}$$

According to the Formulas 4 and 5, the final light field distribution can be divided into three contributions: [a]. Single slit diffraction factor $w_i sinc(w_i f_x)$. Slit width determines peak intensity and distribution width. [b]. Positional parameters *exp* $(- 2\pi f_x c_i)$ is the phase factor due to distance between slits. [c]. Diffraction modulation within each single hole $\mathcal{F}[f_i(x_1)]|_{f_x=\frac{x_0}{\lambda z}}$. Consider the Consine model, we have $f_i(x_1) = exp[j\frac{m}{2}cos(2\pi f_0 x_1)]$ and the Fourier transform function is

$$\mathcal{F}[f_i(x_1)]|_{f_x=\frac{x_0}{\lambda z}} = \sum_{q=-\infty}^{\infty}(j)^q J_q\left(\frac{m}{2}\right)\delta\left(f_x - qf_0, f_y\right) \tag{6}$$

$J_q(\frac{m}{2})$ is q-order Bessel function of the first kind, f_x is initial frequency. Each level component is shown in the Figure 7. Only the finite level can be considered when the error level is relatively low. As the height error increases, the higher-order contribution increases, leading to a dispersion of the light field over a large angular range. For general smooth surfaces, choosing the 0 and ± 1 order spreads of the Cosine wave is sufficient.

To demonstrate the effectiveness of this approach, Figure 8 presents the results of the piecewise approximation of the shape error under parallel light illumination for Mirror-34 from the DABAM database. It is shown that the piecewise approximation can generate the profile of the light field similar to the result by the nature error. It also verifies that the low-frequency error contributes to the structure in the focal spot. The structure feature can be well analyzed by a deterministic method using the segmented model with simple functions.

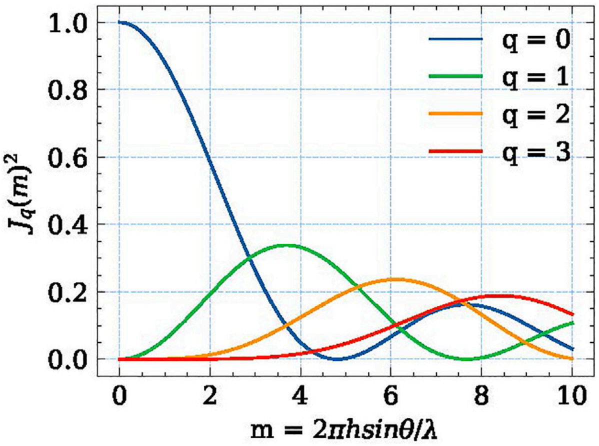

FIGURE 7
Contributions of different diffraction order versus the magnitude of the surface shape error under the cosine shape error model.

On the other hand, quantitatively, the simplest single-bump case can be considered to analyze the impact of low-frequency errors. The bump is set in the middle of the section. The width of the bump is w_0, the center position c_0, and the width of the entire aperture of the amplitude PV is w.

In the case of complete coherence, the distribution of the light spot on the focal plane is shown in the Figure 9 when considering the effect of position, width, height, and shape. The bump's position will cause the symmetry of the light field distribution, and the width will cause the intensity distribution of the interference fringes. The smaller the width of the bump, the smaller the error contribution of this part. As the height of the bump changes, multiple cycles of wavefront oscillations are formed in the bump, which also causes structural changes. Although the cosine distribution model is used in the above calculation, it does not affect the conclusion of the light field distribution structure compared with the calculation results of the parabolic and flat-topped model.

Merit function selection

In this section, we perform error experiments in a low-beta beamline of the HEPS light source. The parameters of the HEPS storage ring and the insert device are shown in Table 1, and the corresponding light source parameters are shown in Table 2. The Figure 10 uses the beamline tracing and mode decomposition modules to calculate the coherence and the angular distribution

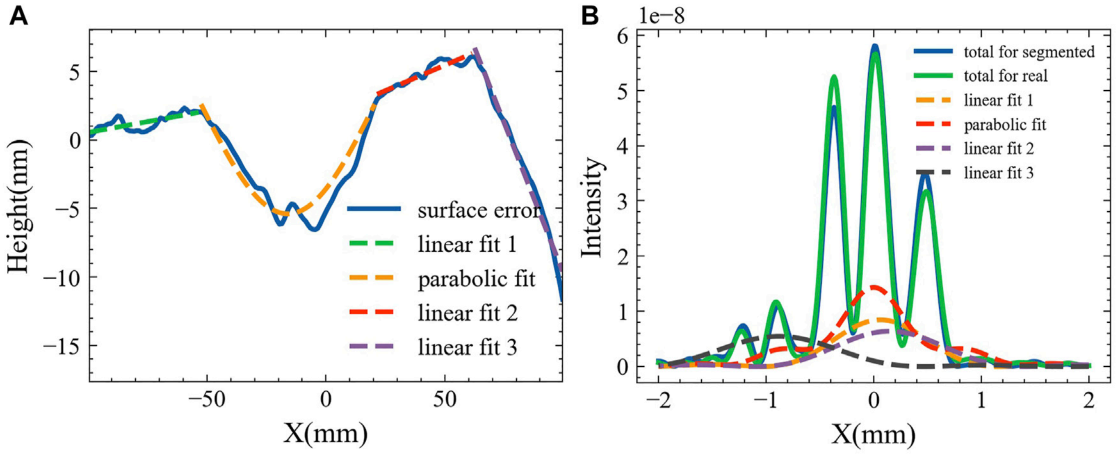

FIGURE 8
Verification of multi-segment decomposition approximation. **(A)** is shape fit of segmented surface error. **(B)** gives focused spot profile by different components and their interference.

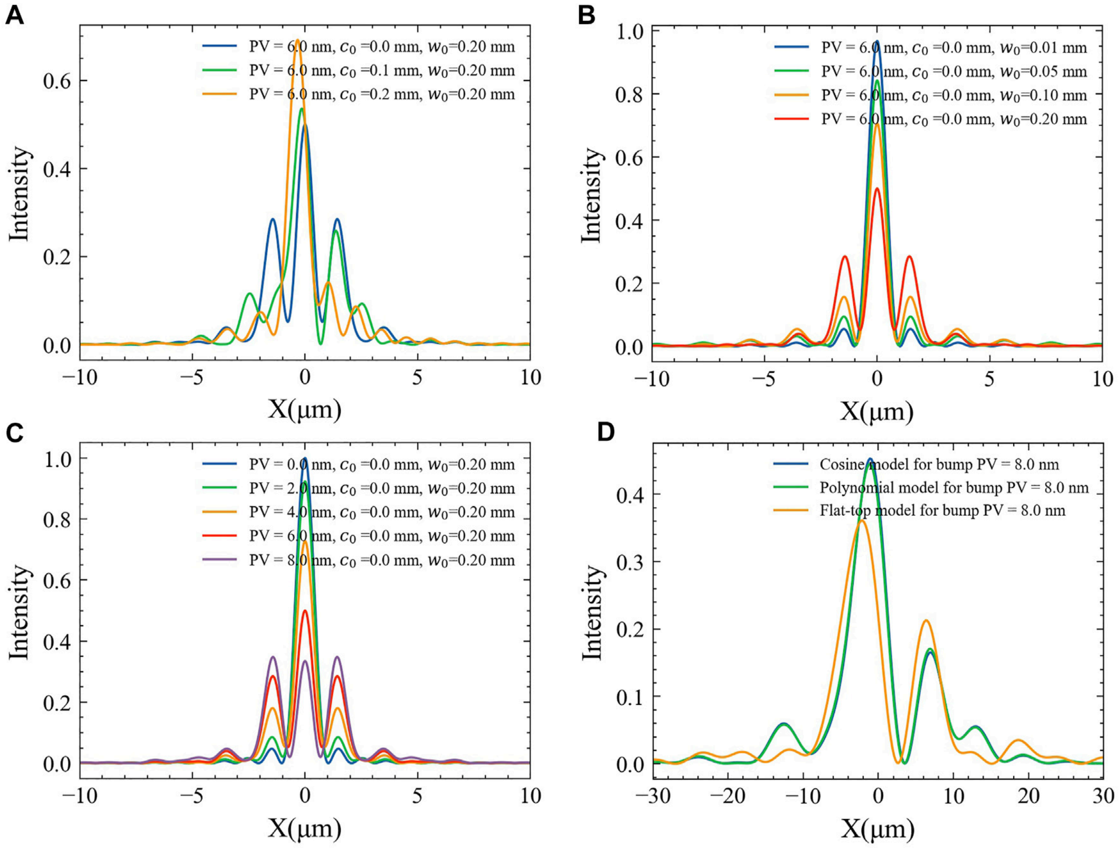

FIGURE 9
Bump model of simulation considering the effect of position **(A)**, width **(B)**, height**(C)**, and shape**(D)**.

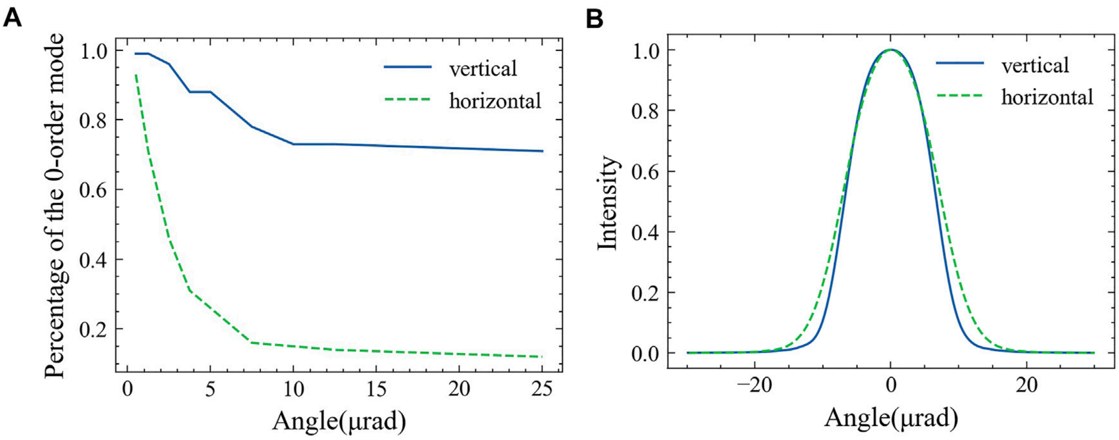

FIGURE 10
Coherence**(A)** and intensity**(B)** distribution of light field by the undulator source. Coherence is measured by the percentage of the 0-order mode.

of the light field in different angular ranges. The source can provide X-ray with perfect coherence in the vertical direction, and the coherence ratio in the horizontal direction is less than 20%. The focusing characteristics in these two directions can reflect the relationship between the degree of coherence and error characteristics. At the same time, considering the efficiency of the optical field flux, the acceptance angle range to be studied in this paper is 10 μrad in the vertical direction and 18 μrad in the horizontal direction.

Strehl ratio

SR is the illuminance ratio at the center of the system's Airy disk to the comparable value in an ideal imaging system. It is widely used as a standard function for diffraction limited systems. SR shows the degree of energy dispersion, the effect of diffraction and aberrations on the Airy disk. When SR is above 0.8, it is usually dependable in most optical system. The closer SR approaches to 1, the better the imaging quality are.

The relationship between the RMS optical path difference W_{rms} and SR is

$$D_s = e^{-\left(2\pi \frac{W_{rms}}{\lambda}\right)^2} = e^{-\left(2\pi \frac{2h sin\theta}{\lambda}\right)^2}$$

Where h is height of mirror. The aberration is relatively modest for SR > 0.8, and the SR can be approximated as

$$D_s = 1 - (2\pi)^2 \left(\frac{W_{rms}}{\lambda}\right)^2 \tag{7}$$

The surface error in the DABAM library is added on the horizontal and vertical directions in our simulation process, respectively. In the numerical experiment, the residual shape error is added on the vertical direction for the beamline acceptance angle $\beta = 10\,\mu rad$ and on the horizontal direction for $\beta = 18\,\mu rad$, which corresponds to the different coherence of the light field. Figure 11 is the SR of simulation in which we calculate the theoretical value of SR and the RMS height error using the Formula 7. SR scatter plots for 10μrad and 18 μrad receive angles in response to height error are shown in Figure 11A,B. When 1) and 2) are compared, it is clear that the 10 μrad results differ from the 18 μrad results. The 10 μrad results are more associated in theory than 18 μrad results. This demonstrates that, in good coherence, especially more than 0.8, the theoretical value of SR related to the height error can be utilized as a mirror selection criterion. We also noticed that the correlation between the theoretical and actual values reduces when the SR drops. Figure 11C,D give scatter plots of slope error versus SR value, which do not show a clear correlation between them. The above results show that the SR value can describe the dispersion degree of the light field only in the system close to the diffraction limit. SR is closely related to the height error.

Root-mean-square spot size

The extension of the spot is another measure of the energy or flux spread caused by the error. It should consider three contributions, including diffraction, geometric magnification, and the surface error given by

$$D_{geometry} = \sigma_{source} M \tag{8}$$

$$D_{Airy} = C\frac{2\lambda}{D} q \tag{9}$$

$$D_{error} = 2q\sigma_{slope} \sin\theta \tag{10}$$

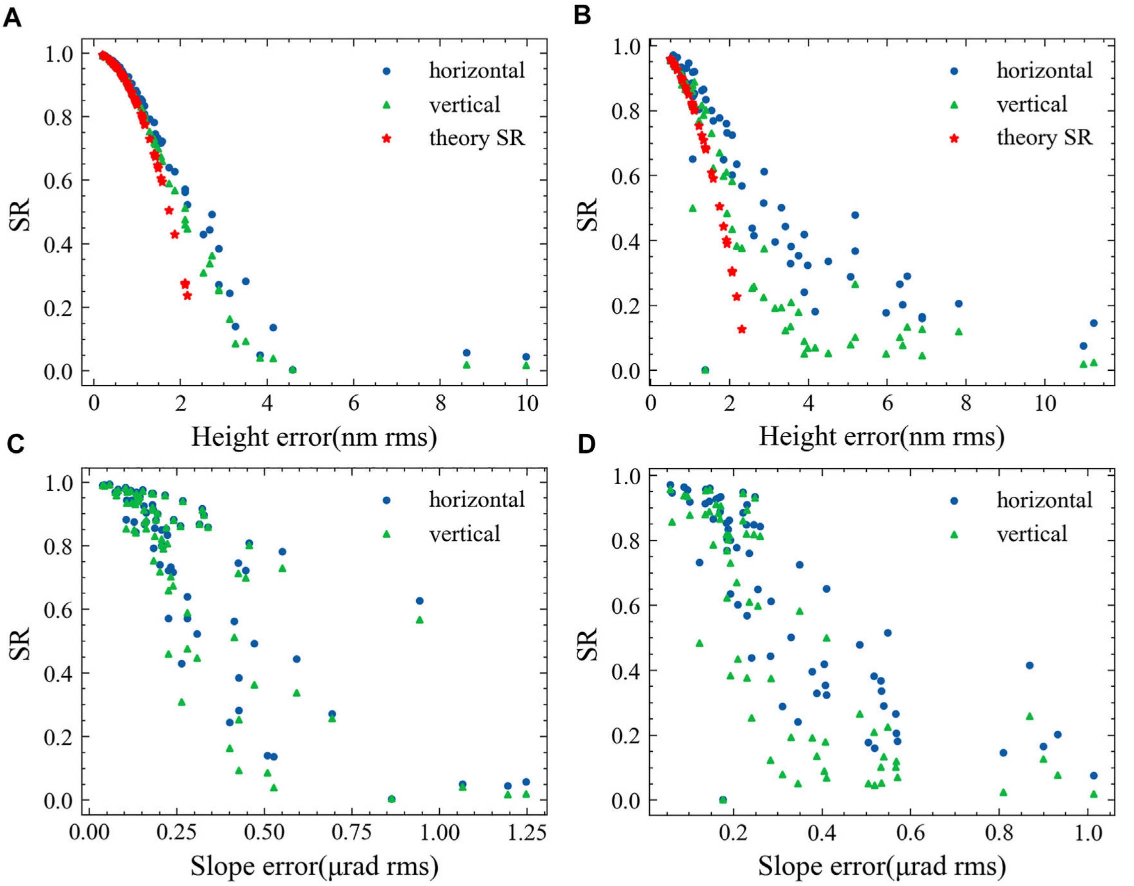

FIGURE 11
SR for Optical Simulation. **(A)** is the height error - SR scatter plot for 10 *μrad* acceptance angle, **(B)** is the height error - SR scatter plot for 18 *μrad* acceptance angle, **(C)** is the slope error - SR scatter plot for 10 *μrad* acceptance angle, **(D)** is the slope error - SR scatter plot for 18 *μrad* acceptance angle.

where $M = \frac{q}{p} = \frac{1}{8}$, q is image distance and p is object distance. C is a constant, D is aperture diameter, σ_{slope} is the residual surface error and θ is the gracing angle. The convolution of the three parts will all contribute to the final spot width:

$$D_{total} = \left(D^2_{source} + D^2_{error} + D^2_{Airy}\right)^{1/2} \tag{11}$$

For single slit diffraction, the distribution of the light field is$I(t) = sinc(t)^2, t = \frac{\pi D sin\theta}{\lambda} = \frac{\pi D x}{\lambda f}$. We pay attention to the positions of the first minimum $t_{1,min} = \pm\pi$. The position of half width is at $t_{FWHM} = \pm 1.39$, thus the FWHM is $x = 0.88\frac{\lambda f}{D}$. If the transformation relationship of 2.35 times between FWHM and sigma is defined according to the Gaussian distribution, there is a relationship of $\sigma_{spot} = 0.37\frac{\lambda f}{D}$. From the distribution of the real light field, the RMS size of the light field size is given by

$$\sigma^2_{spot} = \frac{\int I(t)t^2dt}{\int I(t)dt}$$

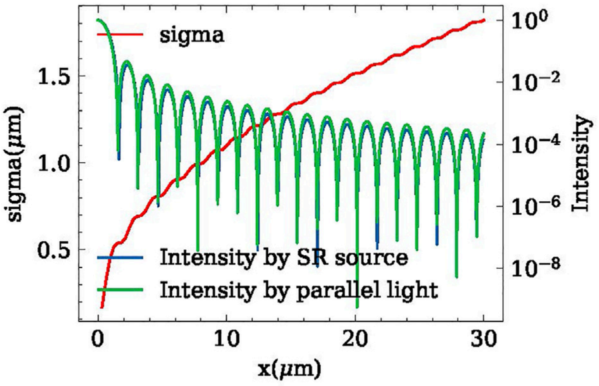

FIGURE 12
RMS spot size calculation for single slit diffraction.

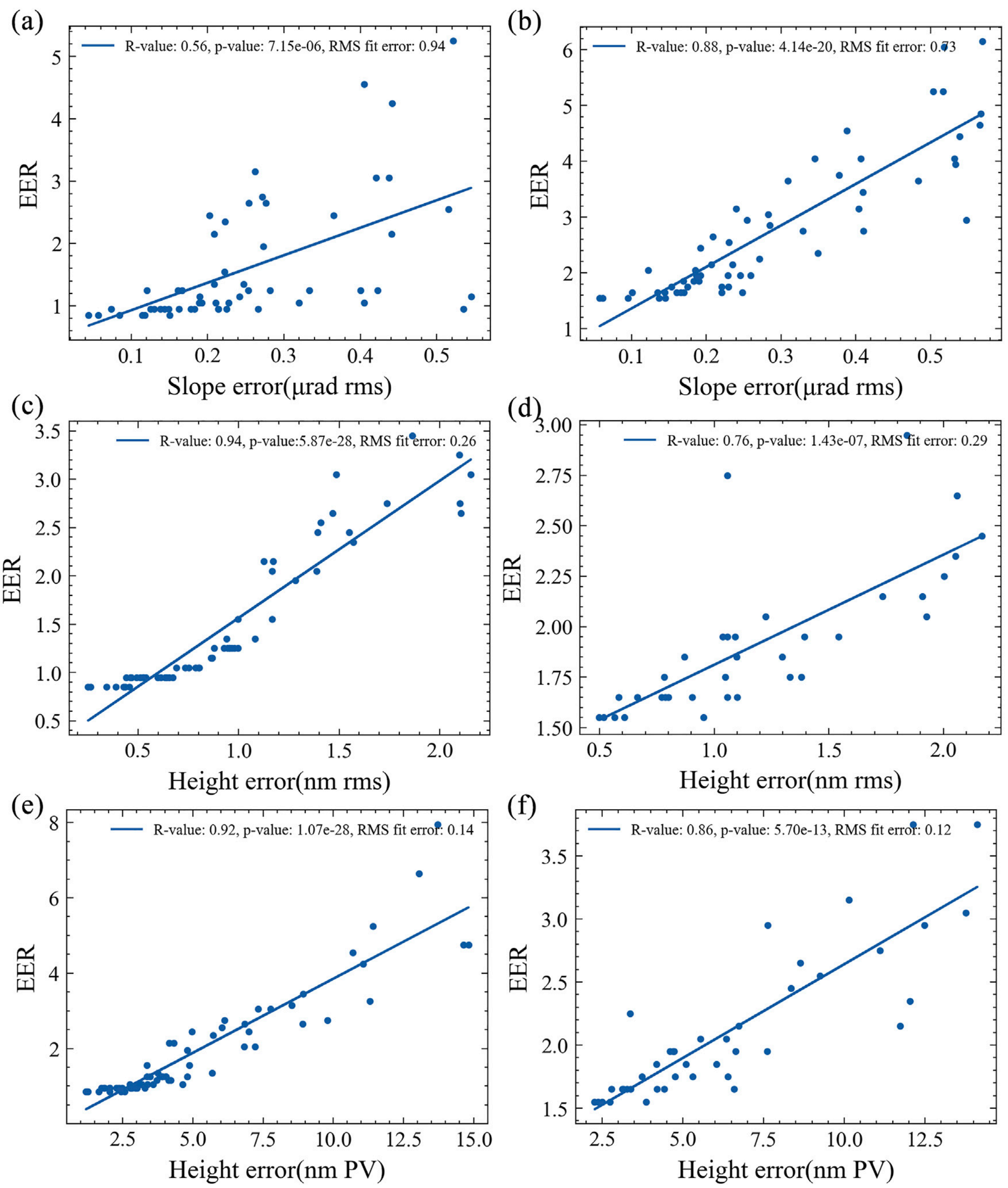

FIGURE 13

Encircled energy spot radius by values of RMS slope error**(A,B)**, RMS height error**(C,D)** and PV height error**(E,F)**. The left and right columns correspond to 10 *μrad* acceptance angle in vertical direction and 18 *μrad* acceptance angle in horizontal direction, respectively. The criterion for the encircled energy spot radius width is 70%.

The value of the integral spot size fluctuates with the range of the light field using this connection. We get $\sigma_{spot} = 0.4\frac{\lambda f}{D}$ for single slit diffraction if we limit it to the first principal maximum range, which is very close to the Gaussian assumption.

Then, we calculate the light SR field diffracted by the single slit, where the selected acceptance angle is 10 μrad. In the Figure 12, the first integral width sigma value is 0.538μm, the minimum position is 1.593μm, and the ratio is 0.538/1.593 = 0.33. It is consistent with the theoretical slit diffraction width characteristics. However, the integrated sigma value will increase significantly with the increase of the integration range. For example, the sigma value in this calculation is 1.8 μm over ±

30 μm. In practical applications, the experiment will configure a slit to block weak light from a large angle while only maintaining intense light in the central lobe, which already holds 90% of the light field energy and ensures a higher system spatial resolution at the same time. Unlike a Gaussian distribution, the spot's standard deviation size cannot accurately reflect the spot's energy dispersion in advanced light sources. As a result, we suggest that it is unsuitable for use as a light field standard.

Encircled energy radius

Encircled energy is another metric for specifying the performance of traditional optical systems, which is defined as the flux in a circle as a function of radius. However, it has not yet been studied and used in the SR beamline design. In this section, we will demonstrate that this metric is good for the spatial dispersion of the light field considering different coherence. The encircled energy distribution is calculated by integrating intensity from the center. When no specular error is loaded, the flux obtained by taking the FWHM of the intensity curve of focal plane as the encircling radius which is 70.6% for vertical direction and 72.2% for horizontal direction. And the ratio of the flux at the FWHM of the standard Gaussian distribution is 76%. Therefore, we calculated 76% flux of encircling energy radius.

In Figure 13, 76% encircled energy radius of the focus spot is plotted verse different surface error parameters with a linear regression fit performed. Figure 13B shows a more significant Pearson correlation coefficient and a smaller p-value for the hypothesis test compared to Figure 13A, indicating that the coordinate value of 18 μrad with 76% light intensity is more correlated with the slope error. Similarly, compared to Figure 13D, Figure 13C has a more significant Pearson correlation coefficient and a smaller p-value for the hypothesis test, indicating that the coordinate value of 10 μrad containing 76% of the light intensity is more correlated with the height error. This finding is similar to the result by Church & Takacs [19] that the performance is related to the height error for the coherent system while to the slope error for the low-coherence system. In addition, the PV and RMS height errors have shown no significant difference in the encircled energy radius in both cases, suggesting that both can be used to specify the mirror quality.

Conclusions

The influence of X-ray mirror error on beamline system performance is studied in this paper. We employ a simplified model and an accelerated simulation platform with improved computational efficiency for error analysis. It is investigated through the analysis of error characteristics and the simulation of beamline performance in order to identify more effective specification methods for various applications. As a result, we arrive at the following conclusion:

1) While the statistics of individual mirrors are highly debatable, the RMS and PV height error can be used together to constrain mirror errors. Low-frequency component with a period greater than 1/10 L is the major contributor to the fabrication error.
2) It is required to reduce the residual surface error to get an unstructured light spot. We discovered that a low-frequency mistake of more than 1/10 L period impacts system performance through the deterministic analysis and bump simulation.
3) The encircled energy spot size is a good measure for spatial energy dispersion for partial coherence application.

Through the calculation and analysis in this paper, it is helpful to determine the parameter requirements of low-risk optical components. On the other hand, the calculation method in this paper can also be used to study other problems, such as vibration, coherence control, and others, which require many wave calculations. In addition, some adaptive X-ray mirrors have been reported to control and correct low-frequency defects[20,21], and we hope to investigate such mirrors in the future.

Data availability statement

The raw data supporting the conclusions of this article will be made available by the authors, without undue reservation.

Author contributions

WS: taking part in the improvement on the paper work. QJ: calculation and discussion on the error feature. WZ: added frames and contents.

Funding

Youth Innovation Promotion Association of the Chinese Academy of Sciences (2019012); National Natural Science Foundation of China (11875059).

Conflict of interest

The authors declare that the research was conducted in the absence of any commercial or financial relationships that could be construed as a potential conflict of interest.

Publisher's note

References

1. Jiao Y, Xu G, Cui X-H, Duan Z, Guo Y-Y, He P, et al. The heps project. *J Synchrotron Radiat* (2018) 25:1611–8. doi:10.1107/s1600577518012110

2. Church EL, Takacs PZ. Specification of surface figure and finish in terms of system performance. *Appl Opt* (1993) 32:3344–53. doi:10.1364/ao.32.003344

3. Signorato R, del Rio MS. Structured slope errors on real x-ray mirrors: Ray tracing versus experiment. In: *Materials, manufacturing, and measurement for synchrotron radiation mirrors*, 3152. Washington, United States: International Society for Optics and Photonics (1997). p. 136–47.

4. Pardini T, Cocco D, Hau-Riege SP. Effect of slope errors on the performance of mirrors for x-ray free electron laser applications. *Opt Express* (2015) 23:31889–95. doi:10.1364/oe.23.031889

5. Yashchuk VV, Samoylova L, Kozhevnikov IV. Specification of x-ray mirrors in terms of system performance: A new twist to an old plot. In: *Advances in computational methods for X-ray optics III*, 9209. Washington, United States: SPIE (2014). p. 114–32.

6. Shi X, Assoufid L, Reininger R. How to specify super-smooth mirrors: Simulation studies on nano-focusing and wavefront preserving x-ray mirrors for next-generation light sources. In. 8th International Symposium on Advanced Optical Manufacturing and Testing Technologies: Subnanometer Accuracy Measurement for Synchrotron Optics and X-Ray Optics, 25 October, 2016, Suzhou, China, 9687. SPIE (2016). 9–19.

7. Church EL, Takacs PZ. Optimal estimation of finish parameters*Opt Scatter: Appl Meas Theor*, 1530. Washington, United States: International Society for Optics and Photonics (1991). p. 71–85.

8. Yashchuk YV, Yashchuk VV. Reliable before-fabrication forecasting of expected surface slope distributions for x-ray optics. *Opt Eng* (2012) 51:046501. doi:10.1117/1.oe.51.4.046501

9. Church EL. Fractal surface finish. *Appl Opt* (1988) 27:1518–26. doi:10.1364/ao.27.001518

10. Church EL, Takacs PZ. Instrumental effects in surface finish measurement. In: *Surface measurement and characterization*, 1009. Washington, United States: International Society for Optics and Photonics (1989). p. 46–55.

11. Krywka C, Last A, Marschall F, Márkus O, Georgi S, Müller M, et al. Polymer compound refractive lenses for hard x-ray nanofocusing. In: AIP Conference Proceedings, 30 August, 2016, Upton, NY, USA, 1764. AIP Publishing LLC (2016). p. 020001.

12. Mimura H, Takei Y, Kume T, Takeo Y, Motoyama H, Egawa S, et al. Fabrication of a precise ellipsoidal mirror for soft x-ray nanofocusing. *Rev Scientific Instr* (2018) 89:093104. doi:10.1063/1.5035323

13. Westfahl H, Jr, Lordano Luiz SA, Meyer BC, Meneau F. The coherent radiation fraction of low-emittance synchrotrons. *J Synchrotron Radiat* (2017) 24:566–75. doi:10.1107/s1600577517003058

14. Klementiev K, Chernikov R. Powerful scriptable ray tracing package xrt. In: *Advances in computational methods for X-ray optics III*, 9209. Washington, United States: SPIE (2014). p. 60–75.

15. Chubar O, Elleaume P. Accurate and efficient computation of synchrotron radiation in the near field region. In: proc. of the EPAC98 Conference; 22-26 June 1998; Stockholm, Sweden, 1177 (1998).

16. Bluestein L. A linear filtering approach to the computation of discrete fourier transform. *IEEE Trans Audio Electroacoust* (1970) 18:451–5. doi:10.1109/tau.1970.1162132

17. Hu Y, Wang Z, Wang X, Ji S, Zhang C, Li J, et al. Efficient full-path optical calculation of scalar and vector diffraction using the bluestein method. *Light Sci Appl* (2020) 9:119–1. doi:10.1038/s41377-020-00362-z

18. Dalcin L, Fang Y-LL. Mpi4py: Status update after 12 years of development. *Comput Sci Eng* (2021) 23:47–54. doi:10.1109/mcse.2021.3083216

19. Church EL, Takacs PZ. Specification of glancing-and normal-incidence x-ray mirrors [also erratum 34 (11) 3348 (nov1995)]. *Opt Eng* (1995) 34:353–60. doi:10.1117/12.196057

20. Signorato R, Hignette O, Goulon J. Multi-segmented piezoelectric mirrors as active/adaptive optics components. *J Synchrotron Radiat* (1998) 5:797–800. doi:10.1107/s0909049597012843

21. Goto T, Matsuyama S, Hayashi H, Yamaguchi H, Sonoyama J, Akiyama K, et al. Nearly diffraction-limited hard x-ray line focusing with hybrid adaptive x-ray mirror based on mechanical and piezo-driven deformation. *Opt Express* (2018) 26:17477–86. doi:10.1364/oe.26.017477

Frontiers in
Physics

Investigates complex questions in physics to understand the nature of the physical world

Addresses the biggest questions in physics, from macro to micro, and from theoretical to experimental and applied physics.

Discover the latest Research Topics

See more →

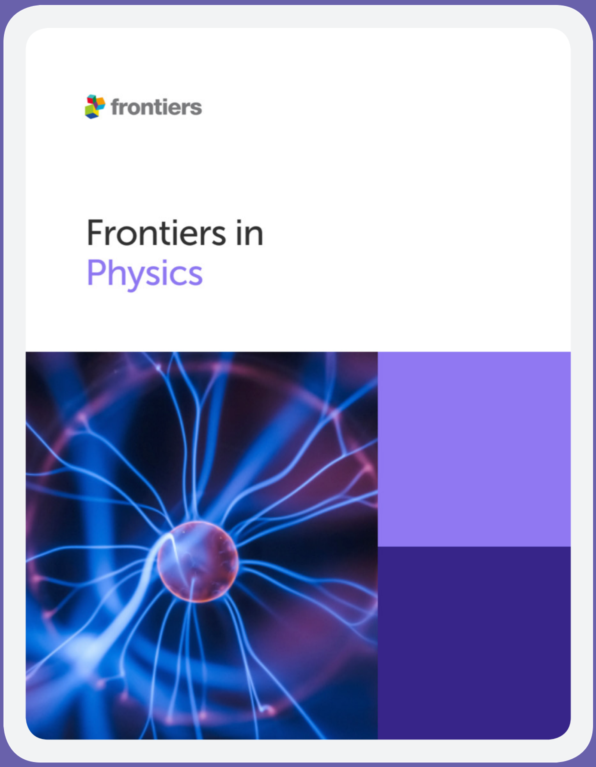

Frontiers

Avenue du Tribunal-Fédéral 34
1005 Lausanne, Switzerland
frontiersin.org

Contact us

+41 (0)21 510 17 00
frontiersin.org/about/contact